Static and Dynamic Magnetic Imaging of Different Magnetic Materials Using Scanning Electron Microscopy with Polarization Analysis

Dissertation
zur Erlangung des Grades
„Doktor
der Naturwissenschaften“
am Fachbereich Physik, Mathematik und Informatik
der Johannes Gutenberg-Universität
in Mainz

Daniel Schönke

geb. in Grünstadt
Mainz, 2020

Datum der mündlichen Prüfung: 19.02.2021

1. Berichterstatter: Prof. Dr. Mathias M. Kläui
2. Berichterstatter: Prof. Dr. Jairo Sinova

Abstract

In the field of spintronics the statics and dynamics of magnetic states in various materials and geometries are of high interest for finding new physics and mechanisms that could be employed in devices. Highly reliable states and switching pathways are required to encode information, as well as efficient switching mechanisms. Experimental research in this area uses different methods, including electrical transport measurements and magnetic imaging. The research progress strongly depends on the improvement of the instruments that are used for the sample fabrication and investigation. The ongoing trend of device miniaturization and high speed requirements ask for experimental techniques with high spatial and temporal resolution.

I improved a scanning electron microscopy with polarization analysis (SEMPA) to enable dynamic magnetic imaging with high spatial resolution. In addition to the novel time-resolved imaging mode, I employed a phase-sensitive detection (PSD) approach to detect small periodic magnetization changes. I determined the temporal resolution to be less than 2 ns and demonstrated a fivefold signal-to-noise ratio enhancement using PSD.

SEMPA with PSD was employed to probe current-induced surface spin accumulation in heavy metals (Pt, Ta) that can be used to switch efficiently magnetic states. SEMPA is especially suited for these experiments because it has a very high surface sensitivity. However, the unambiguous detection of spin accumulation was hindered by artefacts induced by an inhomogeneous sample potential if a current was applied.

Next I employed time-resolved SEMPA to investigate the magnetic switching and its reliability in two geometries: First, I demonstrated in a $Ni_{80}Fe_{20}$ half ring pair the ability to detect irregularities in the magnetization switching with a very small probability of 10^{-6} by a novel data analysis scheme. Further, the magnetic field-induced nucleation of vortex domain walls in curved wires proved to be one method to reliably generate vortex domain walls with a fixed chirality. Second, I demonstrated an angular dependence in the field-induced switching behaviour in asymmetric full rings. Depending on the field orientation with respect to the ring symmetry axis, either onion-to-onion state or vortex-to-onion-to-vortex state switching takes place. Thermal assistance was found to alter the probability of domain wall nucleation in the switching process.

Finally I studied new promising material classes with properties ranging from ferro- to antiferromagnetic. In general, SEMPA can not image antiferromagnets directly. However, I showed with three examples that for certain systems based on multilayers or ferrimagnets, SEMPA is a well-suited imaging technique. I demonstrated the dependence of the biquadratic coupling on the buffer layer and the smoothness of the films in a heterostructure. I further imaged skyrmion bubble domain walls in GdFeCo and Mn_2Au domains indirectly *via* an exchange-coupled Fe layer.

Overall, I show in this thesis different promising geometries and material systems that could be beneficial for the development of reliable and fast spintronic devices. At the same time I demonstrate the enhanced versatility of the newly developed time-resolved SEMPA imaging technique and discuss analysis approaches that provide additional information about the reliability of the observed dynamics.

Zusammenfassung

Auf dem Gebiet der Spintronik sind die magnetischen Zustände und die Magnetisierungsdynamik in verschiedenen Materialien und Geometrien von großem Interesse, um neue Physik und Mechanismen zu finden, die in neuen Technologien zur Anwendung kommen könnten. Zum Codieren von Informationen sind hochzuverlässige Zustände und Schaltwege sowie effiziente Schaltmechanismen erforderlich. Die experimentelle Forschung auf diesem Gebiet verwendet verschiedene Methoden, einschließlich elektrischer Transportmessungen und magnetischer Bildgebung. Der Forschungsfortschritt hängt stark von der Verbesserung der Instrumente ab, die für die Probenherstellung und -untersuchung verwendet werden. Der Miniaturisierungstrend und die hohen Geschwindigkeitsanforderungen erfordern entsprechende experimentelle Techniken mit hoher Orts- und Zeitauflösung.
Im Rahmen dieser Arbeit habe ich Rasterelektronenmikroskopie mit Polarisationsanalyse (SEMPA, engl. *scanning electron microscopy with polarization analysis*) weiterentwickelt, um eine zeitaufgelöste Bildgebung mit gleichzeitig hoher Ortsauflösung zu ermöglichen. Zusätzlich konnte phasensensitive Detektion (PSD) eingesetzt werden, um kleine periodische Magnetisierungsänderungen zu erkennen. Die ermittelte Zeitauflösung des Systems ist besser als 2 ns und bei Anwendung von PSD konnte eine fünffache Verbesserung des Signal-Rausch-Verhältnisses erzielt werden.
Mit SEMPA und PSD wurde die strominduzierte Oberflächenspinakkumulation in nichtmagnetischen Metallen (Pt, Ta) untersucht, mit der sich magnetische Zustände effizient schalten lassen. SEMPA ist hier aufgrund der Oberflächensensitivität besonders geeignet. Der eindeutige Nachweis der Spinakkumulation wurde jedoch durch Artefakte durch ein inhomogenes Probenpotential verhindert.
Als nächstes wurde zeitaufgelöste SEMPA eingesetzt, um feldinduzierte magnetische Schaltprozesse und ihre statistische Zuverlässigkeit in zwei Geometrien zu untersuchen: Zuerst zeigte ich am Beispiel von $Ni_{80}Fe_{20}$ Halbring-Paaren eine Möglichkeit, Unregelmäßigkeiten in der Magnetisierungsdynamik mit einer sehr geringen Wahrscheinlichkeit von 10^{-6} durch ein neues Datenanalyseschema zu erkennen. Gekrümmte Drähte erwiesen sich als nützliche Geometrie um Wirbeldomänenwände mit fester Chiralität zu nukleieren. Zweitens konnte eine Winkelabhängigkeit des feldinduzierten Schaltverhaltens in asymmetrischen Vollringen gezeigt werden. Abhängig von der Feldorientierung in Bezug auf die Ringsymmetrieachse beobachteten wir entweder einen Schaltvorgang zwischen den streufeldfreien Vortexzuständen unterschiedlicher Chiralität oder zwischen einem Vortex– und einem sogenannten Zwiebelzustand. Weiter wurde festgestellt, dass thermische Unterstützung die Wahrscheinlichkeit der Domänenwandnukleierung erhöht.
Schließlich wurden Schichtsysteme mit (quasi-)antiferromagnetischen Eigenschaften untersucht. Im Allgemeinen kann SEMPA Antiferromagnete nicht direkt abbilden. Anhand von drei Beispielen wird jedoch gezeigt, dass SEMPA für bestimmte Systeme, die auf Mehrfachschichten oder Ferrimagneten basieren, gut geeignet ist. Zunächst konnte die Abhängigkeit der biquadratischen Kopplung von der Pufferschicht und der Filmrauhigkeit in einem Mehrschichtsystem gezeigt werden. Außerdem nutzten wir die hohe Ortsauflösung von SEMPA, um Domänenwände in GdFeCo direkt und Mn_2Au-Domänen indirekt über eine austauschgekoppelte Fe-Schicht abzubilden.
Insgesamt zeige ich in dieser Arbeit verschiedene Geometrien und Materialsysteme, die für die Entwicklung zuverlässiger und schneller spintronischer Geräte von Interesse sein könnten. Dabei erweist sich die Vielseitigkeit der weiterentwickelten zeitaufgelösten SEMPA und Analysemethoden, die zusätzliche statistische Informationen über die Zuverlässigkeit der beobachteten Magnetisierungsdynamik liefern.

Contents

Introduction

The invention of computers has been a major technological breakthrough having a huge impact on industry, science and daily life. While the first industrial revolution around 1800 has changed the way physical work is done by the use of machines, the second and especially the third industrial revolutions changed drastically the way information is transmitted and processed [224]. The transformation of information into a code, for example with punch cards for telegraphy, the subsequent transmission of information and the final readout is still the basic concept of information processing: writing, storing or transporting, and readout. During the 20th century new communication and computing methods were invented. In 1941 Konrad Zuse built the first programmable, digital computer based on electromagnetic relays [315]. After the invention of transistors the first fully transistor-based computer was presented in 1954 at Bell Telephone Laboratories [120]. In the next decades the computing power of the devices increased strongly while their size decreased. The number of transistors in integrated circuits doubled approximately every two years according to Gordon Moore's prediction in 1965 [190]. Further developments in semiconductor-based electronics accelerated the third industrial revolution, also called the 'digital revolution', together with the invention of the internet and modern communication techniques. The rising computation and memory needs have been covered so far by downscaling and improvements in computation speed. However, the mentioned prediction from Moore is not only challenged by technical limits for fabrication, but has its physical limits, because the power density in devices increases and overheating becomes a decisive issue. Nevertheless the demand for computing is not saturating. The aimed at fourth industrial revolution [256] shall employ the internet of things and artificial intelligence to connect industrial production, information and communication systems. Scientific endeavours such as the Large Hadron Collider also generate big data and must process this using appropriate technologies [53]. Finally, also further technology developments for the private sector such as autonomous vehicles will need more computation resources. Beside the current demand for more computational and memory resources, the ecological impact of these technologies has to be considered. Currently the information and communication technology sector uses 11% of the global electricity production, but a very large amount of power in current electronic devices is wasted as heat [230].

The field of spintronics investigates the physics of the electron spin and the associated magnetic moment in different materials and aims to exploit it for reliable high-density and high-speed computing devices with low power consumption [60]. To achieve research progress in this field, one needs advances in the instrumentation for the fabrication of nanoscale structures as well as for the investigation of the spin structure and dynamics with high spatial and temporal resolution. For low-power devices highly efficient

switching of the magnetic bits is needed. A promising approach are spin-orbit torque (SOT) based magnetic random access memories (MRAMs) [95]. In SOT-MRAMs the efficiency strongly depends on the interconversion between charge and spin currents via the spin-Hall and inverse spin-galvanic effect [268].
Another non-volatile memory concept makes use of solitonic spin structures such as domain walls (DWs) and magnetic whirls called skyrmions that behave similar to single particles [222, 286]. Here the reliable nucleation and propagation of such magnetic features in different geometries play an important role and depend strongly on the detailed spin structure. Beside device design, spintronics requires the choice and engineering of materials with particular properties. Some materials such as heavy metals serve as good charge-to-spin converters, in others such as ferro- and ferrimagnets the magnetization is easily controllable, while antiferromagnets have high-frequency dynamics, for example. With the progress in thin film deposition and nano-fabrication techniques new material systems can be engineered in various ways. During the last years, especially the interest in antiferromagnetic spintronics has been growing.
In order to tackle some of the open issues, in this thesis we developed a novel nanosecond time resolution imaging method for scanning electron microscopy with polarization analysis (SEMPA) and employed phase-sensitive detection to detect small periodic magnetization changes with enhanced signal-to-noise ratio (SNR). The new technique was used to address open scientific questions such as a direct detection of surface spin accumulation in nonmagnetic metals with high spin-orbit interaction. We further imaged domain wall nucleation and propagation in curved systems that are of interest for devices and provide methods to analyse the reliability of these processes. Then the applicability of the technique was further tested by moving to the study of various material systems with (quasi-)antiferromagnetic properties.
The thesis is divided in 7 chapters:
Ch. 1 discusses the relevant theory for the research conducted in this thesis, including the origin of magnetism, magnetic order in the mean-field approximation, micromagnetism and magnetization dynamics with a special focus on curved geometries. Furthermore, we describe the physical mechanisms resulting in current-induced spin accumulation and finally magnetic interactions in heterostructures.
Ch. 2 describes the employed experimental techniques. In particular, the working principle of scanning electron microscopy with polarization analysis (SEMPA) is discussed.
In **Ch. 3** we present the development of time-resolved SEMPA imaging and the phase-sensitive detection (PSD) method. Then we determine the time resolution of the new SEMPA system and the increase of the signal-to-noise ratio by employing PSD.
Ch. 4 describes our attempt to detect directly current-induced spin accumulation in materials with high spin-orbit coupling (Pt, Ta) using conventional SEMPA and PSD. We discuss the origin of the measured signal and identify the importance of voltage-induced artefacts.
In **Ch. 5** we image the magnetization dynamics in $Ni_{80}Fe_{20}$ half ring pairs. We demonstrate the reliability of field-induced vortex wall nucleation with a fixed chirality in curved wires. Furthermore, we detect and identify rare events in the switching dynamics

by a novel analysis of the SEMPA data and present a method to quantify the reliability of switching processes using time-resolved SEMPA.
Ch. 6 discusses angle-dependent field-induced switching in $Ni_{80}Fe_{20}$ asymmetric rings. Depending on the field orientation with respect to the ring symmetry axis, we observed either onion-to-onion state or vortex-to-onion-to-vortex state switching. The switching was shown to depend on the probability of domain wall nucleation and can be tuned also via varying the temperature.
In **Ch. 7** we investigate novel material systems with ordering ranging from ferro- to antiferromagnetic. We demonstrate the dependence of the biquadratic coupling mediated by an oxide layer on the film smoothness. Furthermore, we succeeded to image with high spatial resolution chiral spin structures in the ferromagnet GdFeCo. Finally, we demonstrate that we can image antiferromagnetic domains in Mn_2Au indirectly by using an exchange-coupling ferromagnetic layer.
In **Ch. 8** we summarize the results and provide the reader with an outlook.

1 Theory

1.1 Magnetism and Magnetic Order

A possible classification of materials describes their response if they are exposed to an external magnetic field. In diamagnetic materials magnetic moments are induced, that oppose the applied field, while in paramagnetic materials the induced moments enhance the field. In contrast to purely diamagnetic and paramagnetic systems, ferromagnetic systems are characterized by a spontaneous magnetic order without an applied field with the magnetic moments either aligned parallel to each other (ferromagnetism) or antiparallel (antiferromagnetism or ferrimagnetism, if the moments of the sublattices are not equal). Spontaneous magnetization is based on the quantum-mechanical properties of the electron and is generated by the exchange mechanism between localized electron spin moments or the moments of itinerant electrons in the conduction band. The exchange interaction of localized electrons can result from a direct overlap of the wave function, but it can also be mediated *via* other ions ('superexchange') or *via* itinerant electrons near the Fermi edge.

1.1.1 Band Magnetism and Stoner Criterion

Spontaneous magnetization in the well-known magnetic elements Fe, Co and Ni and their alloys can be explained by the model of Stoner [277], which adds additional exchange energy I for every electron pair with opposite spin. We follow here the discussion in [117]. The energy of the electrons in the spin subbands is given by

$$E_{\uparrow,\downarrow}(\vec{k}) = E(\vec{k}) + I\frac{n_{\downarrow,\uparrow}}{n} \mp \mu_{\mathrm{B}}B, \tag{1.1}$$

with the energy eigenvalue $E(\vec{k})$ in the one-electron approximation and the number of up/ down spin electrons $n_{\downarrow,\uparrow}$. The energy shift due to the Pauli susceptibility is considered with the last term $\mp\mu_{\mathrm{B}}B$. Now we shift the zero energy $\tilde{E}(\vec{k}) = e(\vec{k}) + I/2$ and substitute $r = (n_\uparrow - n_\downarrow)/n$:

$$E_{\uparrow,\downarrow}(\vec{k}) = \tilde{E}(\vec{k}) \mp \frac{Ir}{2} \mp \mu_{\mathrm{B}}B. \tag{1.2}$$

In thermal equilibrium the chemical potential depending on the number of electrons n for subbands is equal. The difference between the number of electrons with opposite spins depends on the occupation probability of the subbands:

$$r = \frac{1}{n}\int \frac{D(E)}{2}(f[E_\uparrow(\vec{k})] - f[E_\downarrow(\vec{k})])\mathrm{d}E. \tag{1.3}$$

Here $f[E_{\uparrow,\downarrow}(\vec{k})] = 1/(e^{(E_{\uparrow,\downarrow}-\mu)/k_\mathrm{B}T}+1)$ is the Fermi function, which can be developed in orders of $Ir/2 + \mu_\mathrm{B}B$ and with further approximations we arrive at

$$r \approx \frac{D(E_\mathrm{F})}{2n}(Ir + 2\mu_\mathrm{B}B). \tag{1.4}$$

With the magnetization being $M = rn\mu_\mathrm{B}$, the susceptibility is given by

$$\chi = \frac{\mu_0 M}{B} = \frac{\mu_0\mu_\mathrm{B}^2 D(E_\mathrm{F})}{1-(ID(E_\mathrm{F})/2n)} = \frac{\chi_\mathrm{Pauli}}{1-(ID(E_\mathrm{F})/2n)}. \tag{1.5}$$

With increasing value of $ID(E_\mathrm{F})/2n$ the paramagnetic susceptibility increases until for $ID(E_\mathrm{F})/2n > 1$ spontaneous magnetization occurs. Large Stoner exchange parameters stronger reduce the energy in the case of spin alignment and thus ferromagnetism is favoured. In 3d ferromagnets (Fe, Co, Ni) the Stoner exchange parameter is of the order of 1 eV.

1.1.2 Magnetism in the Mean-Field Approximation

In this section different forms of magnetic order such as ferromagnetism, antiferromagnetism and ferrimagnetism are discussed in the mean-field approximation framework, following the description in Ref. [29]. We are considering localized moments in their magnetic environment, which acts on them as an effective field.

Ferromagnetism

In diamagnetic materials a magnetic moment is induced by an applied external magnetic field that is opposite to the field direction. This small negative magnetic susceptibility is inherent to all materials. The alignment of magnetic moments in an external field is the dominating effect in paramagnetic materials. The necessary condition for this behaviour, which leads to a positive magnetic susceptibility, is the existence of partially filled electron shells that yield net atomic magnetic moments. Ferromagnets exhibit a spontaneous magnetization even when no magnetic field is applied. Here all magnetic moments within a certain volume[1] are aligned. The dipole-dipole interaction can not account for this behaviour since the magnetostatic energy between typical atomic dipoles in a material is in the range of µeV and therefore compared to the thermal energy at room temperature vanishingly small. The Hamiltonian for a ferromagnet in a magnetic field comprises the Heisenberg exchange term and the Zeeman term:

$$\hat{\mathcal{H}} = \sum_{ij} J_{ij}^\mathrm{ex}\vec{S}_i \cdot \vec{S}_j + g\mu_\mathrm{B}\sum_j \vec{S}_j \cdot \vec{B}. \tag{1.6}$$

The first term with the exchange constant J_{ij}^ex is responsible for the spontaneous order of spins $\vec{S}_{i,j}$ while the second term describes the alignment of magnetic moments in an

[1] The concept and origin of magnetic domains is explained in Section 1.2.

external magnetic field $\vec{B}$. g is the gyromagnetic ratio and μ_B the Bohr magneton. We assume for now a system without orbital angular momentum ($L = 0$) and thus the total angular momentum is equal to the spin angular momentum ($J = S$). We approximate the molecular field experienced by the i^{th} spin as

$$\vec{B_{\mathrm{MF}}} = -2\frac{2}{g\mu_\mathrm{B}}\sum_j J_{ij}^{\mathrm{ex}}\vec{S}_j. \tag{1.7}$$

The resulting Hamiltonian for the i^{th} site is now analogous to a paramagnet in a magnetic field:

$$\hat{\mathcal{H}} = g\mu_B\sum_i \vec{S}_i \cdot (\vec{B} + \vec{B}_{\mathrm{MF}}), \tag{1.8}$$

where a new effective field is defined as the sum of the molecular internal field and the applied field. This equation holds for all sites assuming a periodic lattice of ions with the same magnetic moment. The Heisenberg exchange energy then equals the energy of a magnetic moment $\vec{\mu_i} = -g\mu_B\vec{S_i}$ in the molecular field $\vec{B}_{\mathrm{MF}}$. The molecular field can be parametrized by the molecular field constant λ_{MF} as a function of the magnetization:

$$\vec{B}_{\mathrm{MF}} = \lambda_{\mathrm{MF}}\mu_0\vec{M}. \tag{1.9}$$

The magnetization M can be expressed by the Brillouin function:

$$\frac{M}{M_S} = \mathcal{B}_J = \frac{2J+1}{2J}\coth(\frac{2J+1}{2J}y) - \frac{1}{2J}\coth(\frac{1}{2J}y). \tag{1.10}$$

M_s is the saturation magnetization and the dimensionless variable y is given by

$$y = \frac{g_J\mu_\mathrm{B}J|\vec{B}_{\mathrm{MF}}|}{k_\mathrm{B}T}. \tag{1.11}$$

For small y, $\mathcal{B}_J$ can be approximated by the second order of its power series and then the critical temperature can be calculated as

$$T_\mathrm{C} = \frac{g_J\mu_B(J+1)\lambda_{\mathrm{MF}}M_\mathrm{s}}{3k_\mathrm{B}}. \tag{1.12}$$

For a ferromagnet with $J = S = 1/2$, $g_J = 2$ and a Curie temperature $T_\mathrm{C} = 1000\,\mathrm{K}$ the molecular field corresponds to a very high energy:

$$B_{\mathrm{MF}} = \lambda_{\mathrm{MF}}M_\mathrm{s} = \frac{k_\mathrm{B}T}{\mu_\mathrm{B}} \approx 194\,\mathrm{meV}. \tag{1.13}$$

This is significantly higher than the thermal energy at room temperature, which is about 25 meV. The molecular field is not a real field but rather a convenient description of the strong Coulomb interactions within the material. The resulting temperature dependence of the magnetic order parameter is shown in Fig. 1.1 for different values of J and experimental values of the transition metal ferromagnets iron, cobalt and nickel.

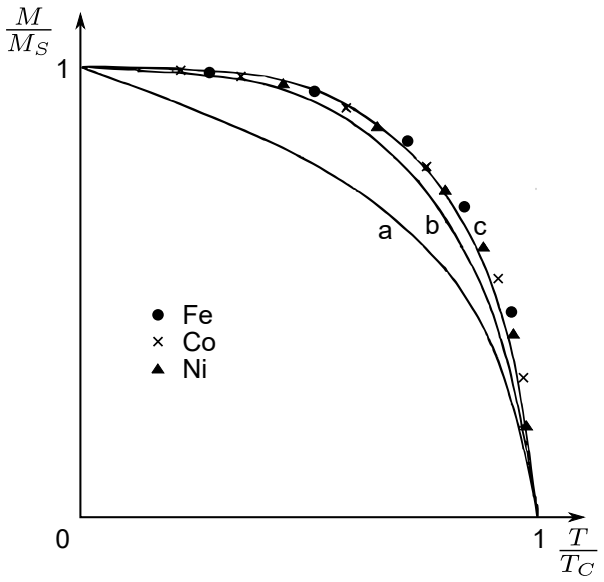

Figure 1.1: Spontaneous magnetization curves calculated for **a)** $J \to \infty$ ($\mathcal{B}_J = \tanh(x)$), **b)** $J = 1$ and **c)** $J = 1/2$. In addition experimental values for the 3d metals Fe, Co and Ni are plotted. (Graph adapted from [289]).

For $T > T_\mathrm{C}$ the magnetization is zero. The function is continuous but not differentiable at $T = T_\mathrm{C}$, indicating a second-order phase transition between the non-magnetic and the ferromagnetic phase. If a magnetic field is applied, the induced magnetization is always non-zero and the phase transition disappears. For low magnetic fields the paramagnetic susceptibility above T_C is proportional to $1/(T - T_\mathrm{C})$ (Curie-Weiss law). So far we only considered the case $J = S = 1/2$, which is reasonable for 3d ions such as Fe, Co and Ni with a strong crystal field interaction resulting in orbital quenching ($L = 0$). However, for 4f ions such as the rare earth elements gadolinium and dysprosium the unfilled electron orbitals are closer to the nucleus and the crystal field has less impact. Here S is not a good quantum number, but needs to be replaced by $(g_J - 1)J$. Thus the molecular field scales with

$$\lambda_\mathrm{MF} = \frac{2zJ^\mathrm{ex}(g_J - 1)^2}{ng_J^2\mu_\mathrm{B}^2}, \tag{1.14}$$

with z being the number of nearest neighbours and n the number of atoms per unit volume. Accordingly T_C can be written as

$$T_\mathrm{C} = \frac{2z(g_J - 1)^2 J^\mathrm{ex}}{3k_\mathrm{B}}(J(J + 1)), \tag{1.15}$$

with the de Gennes factor $(g_J - 1)^2 J(J + 1)$ [54].

Antiferromagnetism

For antiferromagnetic materials, J^{ex} is negative and therefore neighbouring moments align antiparallel to each other. Many antiferromagnets can be considered as two interpenetrating lattices with opposite magnetic moments. Mn_2Au, the antiferromagnet that was imaged indirectly *via* an exchange-coupled iron layer within this thesis, is one such material [32]. While Mn_2Au has a broken inversion symmetry, we consider here, for the sake of simplicity, an antiferromagnet where the nearest neighbours all belong to the sublattice with the opposite magnetic moment so that the molecular field experienced by a magnetic moment is proportional to the magnetization of the other sublattice, when considering just inter-sublattice interactions:

$$\vec{B_{\mathrm{MF},\pm}} = -|\lambda_{\mathrm{MF}}|\mu_0\vec{M_{\mp}}, \tag{1.16}$$

λ_{MF} is the negative molecular field constant. More advanced models can b developed that consider additionally intra sublattice interactions. The magnetization for each sublattice is again described by the Brillouin function:

$$\frac{M_{\pm}}{M_{\mathrm{s}}} = \mathcal{B}_J(x), \tag{1.17}$$

with $x = -g_J\mu_{\mathrm{B}}J|\lambda_{\mathrm{MF}}|M_{\mp}$. This is analogous to the ferromagnetic case with the critical temperature being the Néel temperature

$$T_{\mathrm{N}} = \frac{g_J\mu_{\mathrm{B}}(J+1)|\lambda_{\mathrm{MF}}|M_{\mathrm{s}}}{3k_{\mathrm{B}}}. \tag{1.18}$$

Since the net magnetization $M_+ + M_-$ is zero for all temperatures also below T_{N}, the relevant magnetic order parameter is here the so-called staggered magnetization, defined as $M_+ - M_-$ with the Néel vector $\vec{L} = (\vec{M}_+ - \vec{M}_-)/2$. The susceptibility of an antiferromagnet is proportional to $1/(T + T_N)$. In general the following relation holds

$$\chi \propto \frac{1}{T - T_{\mathrm{crit}}}, \tag{1.19}$$

with $T_{\mathrm{crit}} = 0$ in the case of a paramagnet, $T_{\mathrm{crit}} = T_{\mathrm{C}}$ for a ferromagnet and $T_{\mathrm{crit}} = -T_{\mathrm{N}}$ for an antiferromagnet. The inverse susceptibilities for these magnetic materials are plotted against temperature in Fig. 1.2a).
Below T_{N} the magnetic susceptibility strongly depends on the direction of the applied field, as shown in Fig. 1.2b). If the field is applied along the magnetization direction of one of the two sublattices at $T = 0$, the susceptibility $\chi_{\parallel}$ is zero. A perpendicular field, however, results in a tilt of the magnetic moments of both sublattices towards the field direction ($\chi_{\perp} \neq 0$). With increasing temperature below T_{N}, the staggered magnetization is reduced and a field applied along the magnetization of one sublattice results in a net magnetization $M_+ + M_- \neq 0$. Now let us consider the effect of a strong magnetic field below T_{N} on a uniaxial antiferromagnet. If the field is applied perpendicular to the magnetization axis of the sublattices, the magnetization is just bent towards the field

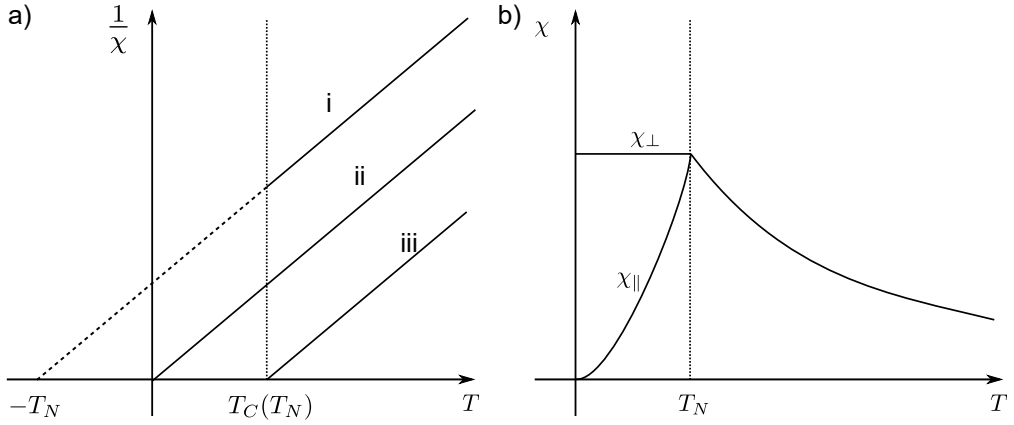

Figure 1.2: a) Inverse susceptibility as a function of temperature for i) an antiferromagnet, ii) a paramagnet and iii) a ferromagnet. **b)** Parallel ($\chi_\parallel$) and perpendicular ($\chi_\perp$) components of the antiferromagnetic susceptibility.

axis. If the field is parallel to the magnetization of one sublattice, nothing happens ($\theta = 0$, $\phi = 180°$) until a critical field B_{SF}, the so-called spin-flop field, is reached. In the spin-flop phase $\theta = \phi$. The existence of the spin-flop phase depends strongly on the strength of the magnetic anisotropy. If this is very high, a spin-flip of the sublattice with the opposite magnetization direction occurs.
There are different types of antiferromagnetic order and many known antiferromagnetic materials. Considering collinear order in a primitive cubic lattice, as shown in Fig. 1.4, there is only one possible ferromagnetic configuration (B-type) and the others are antiferromagnetic. One example is the type G antiferromagnet $LaFeO_3$. Here the nearest neighbours are always coupled antiferromagnetically because of the super-exchange interaction through the oxygen atoms.
The only elemental antiferromagnet at room temperature is chromium. We find antiferromagnetic materials that are insulating, semiconductors, semimetals and metals [17]. Detailed reviews of metallic antiferromagnetism can be found in Ref. [173, 266]. In the early period of their research, antiferromagnets were considered as a highly interesting but useless class of materials [126]. This view changed with further progress of the research and technology. In 1970 Louis Néel received the Nobel prize "for fundamental work and discoveries concerning antiferromagnetism and ferrimagnetism which have led to important applications in solid state physics." [204, 207]. Compared to ferromagnets, antiferromagnets and compensated ferrimagnets have zero stray fields and much higher resonance frequencies up to the THz range [214]. The former property is advantageous for the miniaturization of devices, the latter for high-speed computing applications [176]. Furthermore these materials are far less sensitive to external magnetic fields [177]. In this thesis we investigate the domain pattern of metallic Mn_2Au. It has a centrosymmetric tetragonal structure, as shown in Fig. 1.5. The two magnetic sublattices A and B form spatial inversion partners with the central Au atom as symmetry centre. Along the

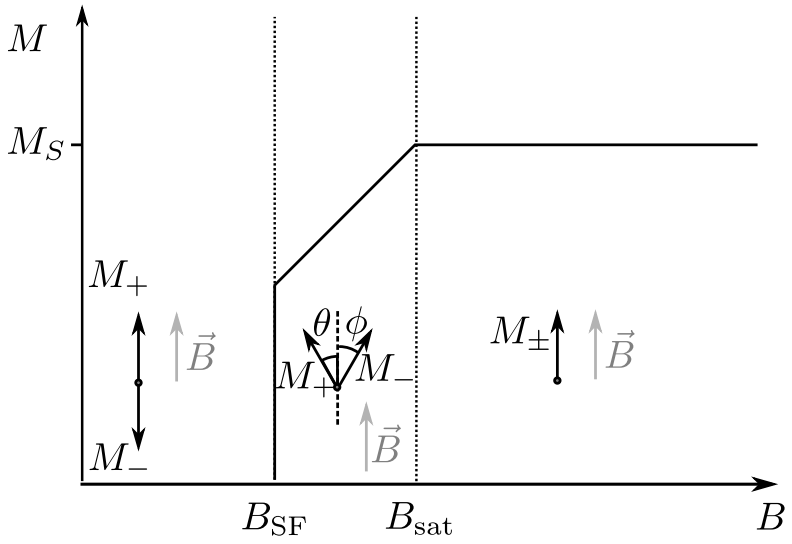

Figure 1.3: Net magnetization of a uniaxial antiferromagnet as a function of a parallel applied magnetic field. At the spin-flop field B_{SF} the net magnetization jumps and then increases until it saturates at B_{sat}.

[001] axis the inversion symmetry is locally broken. In antiferromagnets with this symmetry Néel spin orbit torques can be used for switching the magnetic state [30, 307, 308], which is highly interesting because it is very difficult to manipulate antiferromagnets by conventional magnetic fields. So far only a few materials with this symmetry have been found, CuMnAs [308], Mn_2Au [30] , CuMnSb [264] and $MnPb_2$ [263].

Ferrimagnetism

In ferrimagnets the magnetic moments of both sublattices M_A and M_B in general are not equal and a net magnetization below the critical temperature remains. Here we consider besides inter-sublattice interactions also intra-sublattice interactions with the molecular field constants $\lambda_{\mathrm{MF},AB}$ and $\lambda_{\mathrm{MF},AA}$ [51, 312]. The molecular field without an external magnetic field is given by

$$\vec{B}_{\mathrm{MF},A} = \lambda_{\mathrm{MF},AA}\mu_0\vec{M}_A + \lambda_{\mathrm{MF},AB}\mu_0\vec{M}_B. \tag{1.20a}$$

$$\vec{B}_{\mathrm{MF},B} = \lambda_{\mathrm{MF},BA}\mu_0\vec{M}_A + \lambda_{\mathrm{MF},BB}\mu_0\vec{M}_B \tag{1.20b}$$

The interaction between the sublattice magnetizations $\lambda_{\mathrm{MF},AB}$ is negative. Again the magnetization of the sublattices can be described by the Brillouin function $\mathcal{B}_J$. While there is in general a remaining net effective magnetization, the two sublattice magnetizations can cancel depending on the inter- and intra-sublattice interactions, as shown in Fig. 1.6. At the compensation temperature the ferrimagnet exhibits some of the properties of an antiferromagnet. As such, temperature and stoichiometry are tools to tune the

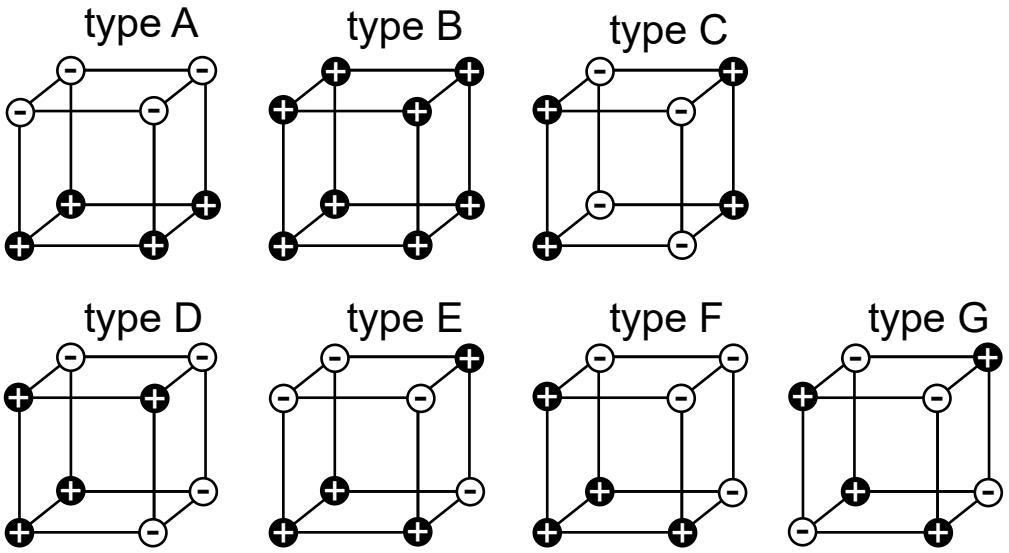

Figure 1.4: Possible collinear magnetic configurations in a primitive cubic lattice. + and − correspond to opposite spins of the two sublattices.

interaction of both sublattices and change the ferromagnetic character of the material to an antiferromagnetic one.
Well-known ferrimagnets are yttrium-iron garnet (YIG) $Y_3Fe_5O_{12}$ and magnetite Fe_3O_4. Here Fe ions are placed on the two different crystallographic sites A and B. In this thesis we investigated the ferrimagnetic amorphous alloy GdFeCo. It consists of the rare-earth (RE) element gadolinium (Gd) and the transition metals (TM) iron and cobalt. The net magnetization $\vec{M}_{\text{net}} = \vec{M}_A + \vec{M}_B = \vec{M}_{\text{RE}} + \vec{M}_{\text{TM}}$ is determined by the stoichiometry of the alloy and the temperature. The Landé factors of the materials are different ($g_{\text{RE}} \neq g_{\text{TM}}$) and thus compensation points of the magnetization $T_{\text{comp},M}$ and angular momentum $T_{\text{comp},L}$ exist [109]. The magnetization and the angular momentum are coupled *via* the gyromagnetic ratio $\gamma_{\text{TM/RE}} = g_{\text{TM/RE}}\,\mu_{\text{B}}/\hbar$ [123]:

$$\vec{L} = \vec{L}_{\text{TM}} + \vec{L}_{\text{RE}} = \frac{\vec{M}_{\text{TM}}}{\gamma_{\text{TM}}} + \frac{\vec{M}_{\text{RE}}}{\gamma_{\text{RE}}} \tag{1.21}$$

Ferrimagnetic systems have very interesting dynamic properties at the angular momentum compensation point that allow, for example very high domain wall velocities [133, 273]. Furthermore, around $T_{\text{comp},L}$ the skyrmion Hall effect is reduced or even avoided in ferrimagnetic systems exhibiting skyrmionic spin structures [110]. Therefore ferrimagnetic systems can be a useful route towards the understanding of antiferromagnets.

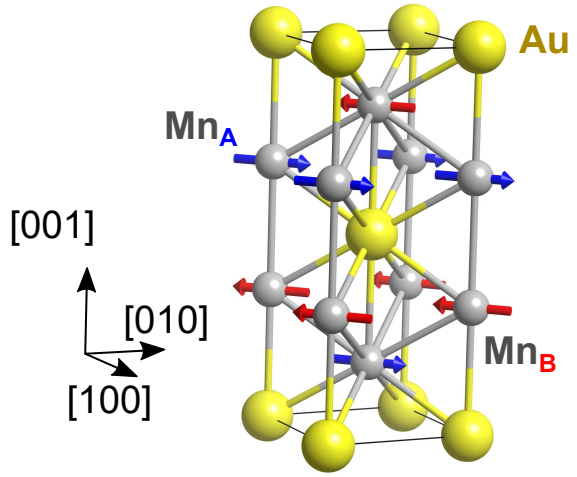

Figure 1.5: Mn_2Au centrosymmetric tetragonal unit cell with the Au atoms (yellow) and the Mn atoms of sublattices A and B with opposite magnetization.

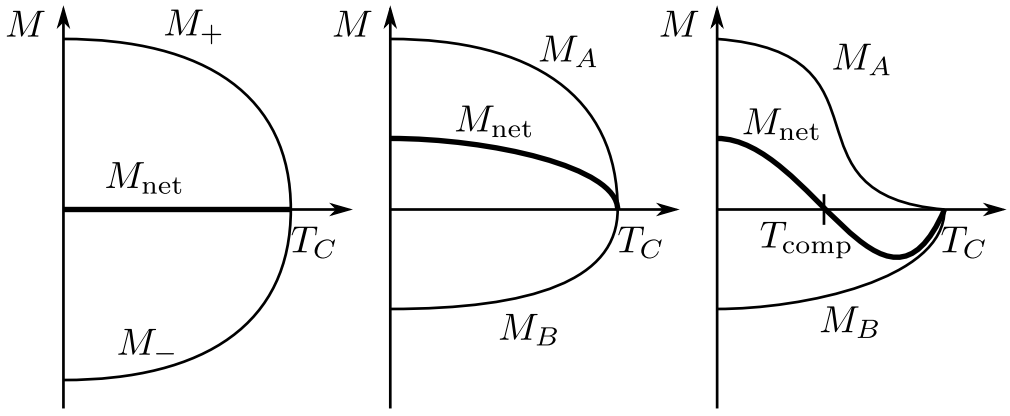

Figure 1.6: Sublattice magnetization of an antiferromagnet (left), a ferrimagnet with $|\lambda_{\mathrm{MF},AB}| >> |\lambda_{\mathrm{MF},AA}|, |\lambda_{\mathrm{MF},BB}|$ (centre) and a ferrimagnet with $|\lambda_{\mathrm{MF},BB}| >> |\lambda_{\mathrm{MF},AB}|, |\lambda_{\mathrm{MF},AA}|$ (right). At the compensation temperature T_{comp} the net magnetization M_{net} is zero.

1.2 Micromagnetism

A magnetic system in its environment (open system) with a constant temperature, a constant volume and no change in the number of particles is described by the Gibbs free energy:

$$G = U - TS - V\vec{B}_0\vec{M}. \tag{1.22}$$

A spatially varying magnetization $\vec{M}(\vec{r})$ of the system is chosen, so that the free enthalpy is minimized (local or global minimum). To allow a micromagnetic approach we assume the size of the system to be larger than the atomic distance and neglect quantum effects. Further the temperature is well below T_C, so that $M = M_s = const.$ Then the magnetization is a continuous function of the position in our description and no longer a system of discrete single spins.

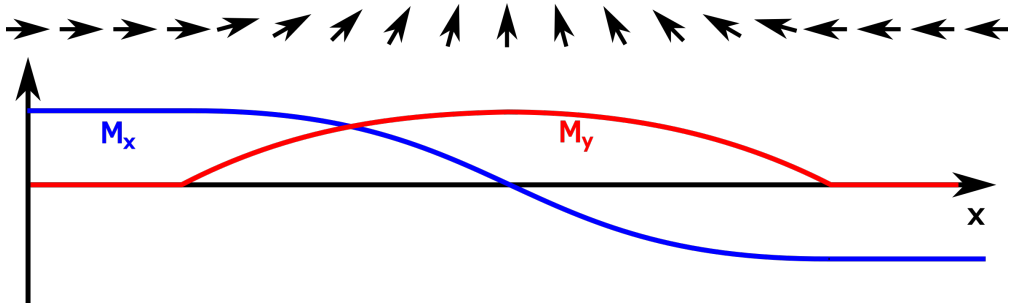

Figure 1.7: Micromagnetic continuous approximation of discrete magnetic moments.

In the description of the energy terms we follow the explanation in Refs. [51, 234].

1.2.1 Zeeman Energy

First a magnetic field leads to a change of the system energy. You can distinguish between external "Zeeman" fields and stray fields generated by the system itself . For the first case the energy term is given by

$$E_{\text{Zeeman}} = -\int_V \vec{B}_0\vec{M}(\vec{r})d^3r. \tag{1.23}$$

If the magnetic field is homogeneous and unidirectional, the energy does not depend on the shape of the sample, but only on the average magnetization. If the magnetization is not aligned with the field, it experiences a torque. In a multi-domain structure the new equilibrium state is one where the domains pointing in the direction of the applied field are enlarged with increasing field, as shown in Fig. 1.8a) for a $4 \times 3.5\,\mu\text{m}$ $Ni_{80}Fe_{20}$ rectangle.

1.2.2 Stray Field Energy

A magnetic sample generates a stray field H_d by dipole-dipole interaction. Starting from the Maxwell equation

$$\nabla\vec{B} = \nabla(\mu_0(\vec{H}_\mathrm{d} + \vec{M})) = 0, \tag{1.24}$$

and assuming $\vec{B} = 0$, the demagnetizing field is given by the divergence of the magnetization

$$\nabla H_\mathrm{d} = -\nabla\vec{M}, \tag{1.25}$$

and the relevant energy term is

$$E_\mathrm{d} = \frac{\mu_0}{2}\int \vec{H}_\mathrm{d}^2 dV = -\frac{\mu_0}{2}\int \vec{H}_\mathrm{d}\cdot\vec{M}(\vec{r})d^3r. \tag{1.26}$$

H_d is generated by effective surface $\sigma = \vec{n}\cdot\vec{M}$ and volume charges $\rho = -\nabla\vec{M}$:

$$H_\mathrm{d} = \int_V \frac{(\vec{r}-\vec{r'})\rho(\vec{r'})}{|\vec{r}-\vec{r'}|^3}dV' + \int_S \frac{(\vec{r}-\vec{r'})\sigma(\vec{r'})}{|\vec{r}-\vec{r'}|^3}dS'. \tag{1.27}$$

Here the shape of the magnetic body enters and hence this contribution is sometimes also called shape anisotropy. The stray field minimization is the reason for inhomogeneous magnetization and domain formation. Fig. 1.8a) shows a Landau domain pattern in a $4\times 3.5\,\mu\mathrm{m}$ $Ni_{80}Fe_{20}$ rectangle that considerably reduces the stray field compared to a single domain state. The stray-field interaction is long range and the energy is proportional to M_s^2.

1.2.3 Exchange Energy

In the micromagnetic approach we approximate the Heisenberg energy term by an integral:

$$E_\mathrm{ex} = \frac{1}{2}\sum_{ij} J_{ij}^\mathrm{ex}\vec{S}_i\cdot\vec{S}_j \approx \frac{A_\mathrm{ex}}{M_\mathrm{s}^2}\int(\vec{\nabla}\vec{M}(x))^2 d^3r. \tag{1.28}$$

Here A_ex is the exchange stiffness, which is proportional to the Curie temperature T_C, the exchange constant J^ex and the saturation magnetization M_s. The exchange length is given by

$$l_\mathrm{ex} = \sqrt{\frac{A_\mathrm{ex}}{\mu_0 M_\mathrm{s}^2}}. \tag{1.29}$$

The exchange interaction is very strong with a strength comparable to $k_\mathrm{B}T_\mathrm{C}$, but is short range compared to the dipolar stray-field interaction.
In certain bulk materials and multilayers with broken inversion symmetry and high spin-orbit coupling there is, in addition to the symmetric Heisenberg exchange interaction, an asymmetric term called Dzyaloshinskii-Moriya interaction (DMI) [70]. The DMI favours perpendicular orientation of adjacent spins. A strong DMI can result in chiral spin structures such as skyrmions. A broken inversion symmetry is found in non-centrosymmetric bulk crystals such as B20 compounds [197] and can also be designed at interfaces for thin films. The interaction is depicted in Section 1.6.1.

1.2.4 Magnetic Anisotropy

Magnetic anisotropy originates mainly from spin-orbit interaction. For materials with a magnetic anisotropy the magnetization favours orientation along certain directions, as shown in Fig. 1.8b) for a biaxial anisotropy in a FeSi rectangle on lead magnesium niobate-lead titanate (PMN-PT). Different effects contribute to the anisotropy, such as magneto-crystalline anisotropy, surface anisotropy and magnetoelastic anisotropy. In the case of uniaxial magnetic anisotropy the energy term is given by

$$E_{\mathrm{A}} = K_{\mathrm{u}} \sin^2\theta. \tag{1.30}$$

K_{u} is the anisotropy constant and θ the angle between the magnetization and the anisotropy axis, which in the case of $K_{\mathrm{u}} < 0$ is a hard axis and for $K_{\mathrm{u}} > 0$ an easy axis. The latter is the case, for example, in thin films with a perpendicular magnetic anisotropy (PMA), where the magnetization orients out of the plane. Another example is cubic magneto-crystalline anisotropy with the energy contribution

$$E_{\mathrm{A}} = K_0 + K_1(\alpha_1^2\alpha_2^2 + \alpha_2^2\alpha_3^2 + \alpha_3^2\alpha_1^2) + K_2(\alpha_1^2\alpha_2^2\alpha_2^2) + ... \tag{1.31}$$

$\alpha_{1,2,3}$ are the cosines of the magnetization angle with respect to the three cubic crystal axes $\langle 100 \rangle$. Higher order energy terms can be neglected in general. If $K_1 > 0$, easy axes are along the $\langle 100 \rangle$ directions. Mathematical expressions for other magneto-crystalline anisotropies are provided in [116]. Permalloy, which we used in our time-resolved magnetization dynamics, is usually polycrystalline with negligible intrinsic magnetocrystalline anisotropy and behaves as an isotropic material.
Perpendicular anisotropy K_{u} can be the consequence of either an easy axis perpendicular to the film plane or a strong surface anisotropy in the case of very thin films [202]. The surface anisotropy K_{s} results from the coupling of the surface atoms to the crystal field generated by the anisotropic environment at the film surface. The total energy E_{tot} consisting of the stray field energy and the anisotropy energy is given by:

$$E_{\mathrm{tot}} = K_{\mathrm{u}} \sin^2\theta + \frac{1}{2}\mu_0 M_{\mathrm{s}}^2 \cos^2\theta. \tag{1.32}$$

θ is the angle between the film plane normal and the magnetization. E_{tot} is minimal if $2K_{\mathrm{u}}/\mu_0 M_{\mathrm{s}}^2 > 1$. This is only the case for materials with strong magnetocrystalline anisotropy, strong surface anisotropy $K_{\mathrm{u}} = K_{\mathrm{s}}/t$ in thin films with thickness t or materials with a low M_{s}. If $2K_{\mathrm{u}}/\mu_0 M_{\mathrm{s}}^2 < 1$, a worm-like domain pattern is formed with equal areas of up and down magnetization at zero external field to reduce the stray field. By applying a magnetic field perpendicular to the film plane the stripe domains break up and bubble domains can form.
Micromagnetic calculations as employed in simulation tools such as MicroMagnum [3] minimize the free energy usually for $T = 0$. If the requirements for a micromagnetic approach are not satisfied, an atomistic model may be required [55].

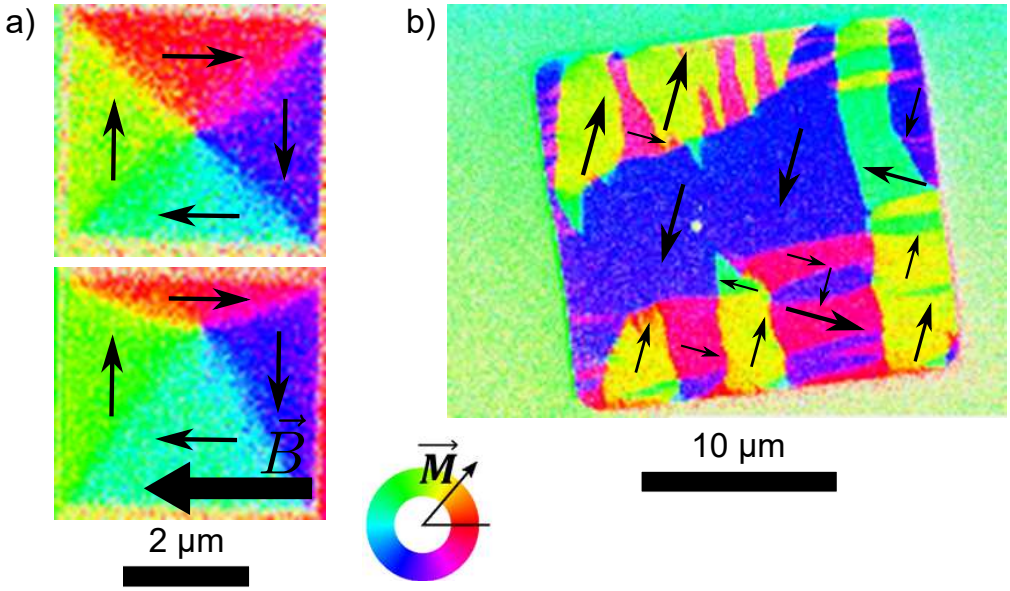

Figure 1.8: **a)** Landau domain pattern in a $4 \times 3.5\,\mu m$ $Ni_{80}Fe_{20}(10\,nm)$ rectangle without applied field (top) and with applied field (bottom). The flux-closure Landau pattern minimizes the stray field. When a magnetic field is applied, the domain with the magnetization oriented along the field direction is enlarged to minimize the Zeeman energy, while the opposing domain shrinks. **b)** Fourfold magnetic anisotropy in a large FeSi(18 nm) rectangle on lead magnesium niobate-lead titanate (PMN-PT). The magnetization in the domains is oriented along four different orthogonal directions.

1.3 Magnetization Switching and Dynamics

In this section we will discuss magnetization switching in single domain particles and in more complex magnetic system following Ref. [234]. In particular we will consider magnetic field-induced dynamics in mesoscopic ring geometries. Magnetic states can change under changing external conditions such as temperature and pressure. Electrical currents can also apply torques to the magnetization. These spin-transfer and spin-orbit torques have been investigated intensively during the last decade. In particular, magnetic fields can induce changes of the magnetization to minimize the Zeeman energy. Single domain particles are small objects where the exchange energy contribution dominates. Stoner, Wohlfarth and Néel developed a classical description of coherent magnetization rotation assuming such a single domain magnetic system with uniaxial anisotropy [201, 278]. This approach was generalized by Thiaville [284]. Anisotropy and Zeeman terms form the expression for the total energy:

$$E_{\mathrm{tot}}(\vec{h}) = F(\vec{m}(\theta)) - 2\vec{h} \cdot \vec{m}(\theta). \tag{1.33}$$

The reduced magnetic field is given by $\vec{h} = \vec{H}/H_{\mathrm{k}} = \vec{H}M_{\mathrm{s}}/(2K)$. The direction of the

magnetization is given by the magnetization unit vector $\vec{m} = \vec{M}/M_s = (\cos\theta, \sin\theta)$, and $F(\vec{m})$ is the anisotropy energy density divided by the anisotropy constant K. E_{tot} has either one or two minima, resulting in hysteretic behaviour. Magnetization switching occurs when the system swaps from one minimum to the other one, *i.e.* $\mathrm{d}^2E_{tot}/\mathrm{d}\theta^2 = 0$. The reduced critical field is given by

$$\vec{h}_c = \frac{1}{2}\left(\frac{\mathrm{d}F}{\mathrm{d}\theta}\vec{e} - \frac{\mathrm{d}^2F}{\mathrm{d}\theta^2}\vec{m}\right), \tag{1.34}$$

with $\vec{e} = (-\sin\theta, \cos\theta)$ being the unit vector orthogonal to $\vec{m}$. In the case of a uniaxial anisotropy $F(\theta) = K_u\sin^2\theta$ the critical field $h_c = (-\cos^3\theta, \sin^3\theta)$ has the form of a square astroid, as shown in Fig. 1.9a). Three different field sweep lines are also shown with the corresponding magnetization response shown in Fig. 1.9b). If the magnetic field is applied only along the easy axis, the switching field is maximum and equals the coercive field. If the field is swept along the hard axis, no sudden switching is seen but a continuous rotation of the magnetization.

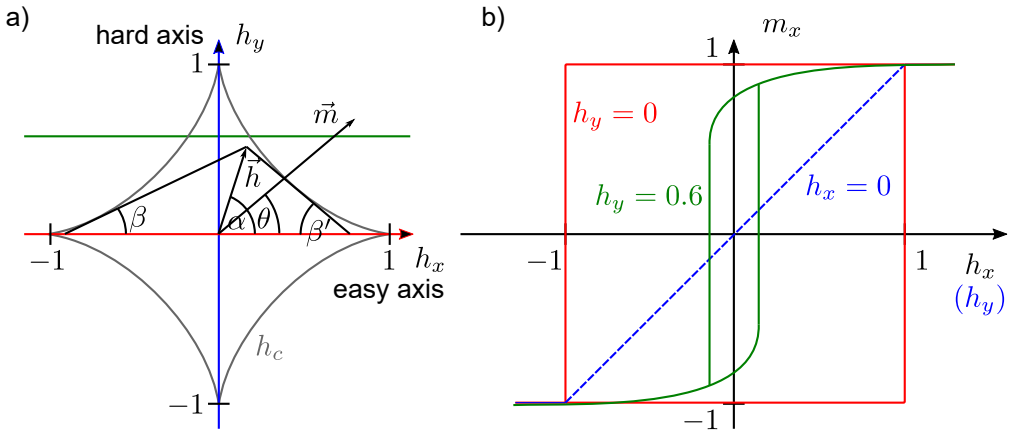

Figure 1.9: a) Stoner-Wohlfarth switching fields for a small thin-film element with uniaxial anisotropy with the easy axis along the x direction. The critical field h_c is indicated by the astroid line. The equilibrium magnetization direction θ can be determined by the tangent construction from the applied field $\vec{h}$. The coloured lines indicate the magnetic field sweeps corresponding to the hysteresis curves in b). **b)** Hysteresis curves with sweeping in-plane magnetic fields.

In equilibrium, no torque is applied by the effective field $\vec{H}_{eff}$ to a magnetic moment $\vec{m} \times \vec{H}_{eff} = 0$. If there is a finite torque, the dissipationless temporal evolution of the magnetic moment is given by

$$\dot{\vec{m}} = \frac{\partial\vec{m}}{\partial t} = \gamma\vec{m} \times \vec{H}_{eff}. \tag{1.35}$$

The magnetization precesses around the magnetic field while the angle between magnetization and field is always maintained. Dissipation is introduced by the phenomenological

Gilbert damping constant α:

$$\dot{\vec{m}} = \vec{m} \times (\gamma \vec{H}_{\text{eff}} - \alpha \dot{\vec{m}}). \tag{1.36}$$

With advancing time the magnetization aligns with the effective field. Another equivalent mathematical expression if $\alpha << 1$ is given by the Landau-Lifshits formula:

$$\dot{\vec{m}} = \gamma_{\text{LL}} \vec{m} \times \vec{H}_{\text{eff}} - \alpha_{\text{LL}} \vec{m} \times (\vec{m} \times \vec{H}_{\text{eff}}). \tag{1.37}$$

Above we discussed magnetic switching *via* coherent rotation. However, if the critical field for another reversal mode is lower, this switching pathway is taken. For example, in a spheroid different reversal modes have been found [8]: Fig. 1.10 shows schematically the exchange energy dominated coherent rotation, as well as the curling mode *via* the formation of vortex structures inside the particle minimizing the stray field and the buckling mode in a single-domain ellipsoid of revolution. The latter mode reduces the stray field with alternating surface charges.

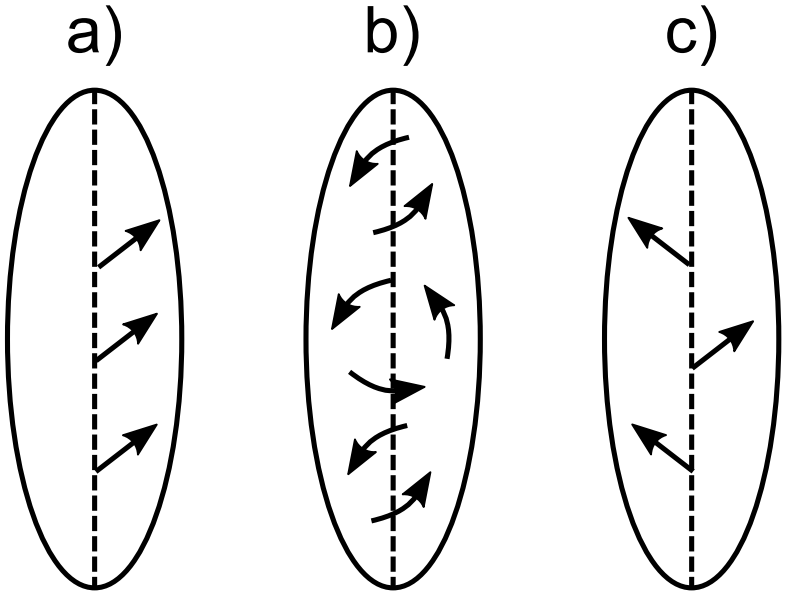

Figure 1.10: Different reversal modes in a homogeneous ellipsoid: **a)** Coherent rotation, **b)** curling, **c)** buckling.

In multi-domain systems the reversal is more complicated and several processes can occur, including

1. coherent or non-coherent rotation of spins,
2. domain and domain wall nucleation,
3. domain wall motion,
4. domain and domain wall annihilation.

1.4 Magnetic States and Dynamics in Ferromagnetic Rings

In this section a short overview is given on magnetic states and switching in mesoscopic and nanoscale magnetic rings, since a major part of this thesis deals with magnetization dynamics in (half)ring geometries.
In the last decades, magnetic rings in the micrometre and nanometre range have been investigated intensively. The geometry is an ideal test system for studies of domain walls since their field-induced nucleation is easy compared to straight wires [139, 151]. Magnetic rings also have been proposed as a basic geometry for spintronic devices such as magnetoresistive random access memory [332, 333], spin-based field effect transistors [92, 161], sensors [188] and logic elements [118]. The magnetic ground state is the so-called vortex state where the magnetization is aligned along the edges. Two configurations with the same energy but opposite chirality exist - either clockwise (cw) or counter-clockwise (ccw). These degenerate states can be used as a binary memory. In a symmetric ring the stray field of these configurations is zero, in contrast to magnetic disks which possess in the vortex state an out-of-plane vortex core [265]. Due to the high exchange energy contribution of a vortex core to the free energy [239], the vortex state in magnetic disks is not as stable as in rings. This is of particular importance considering the continuing trend of down-scaling for devices. A uniform state with the magnetization within the whole ring pointing in one direction is energetically unfavourable in a ring due to the extra stray field contribution associated with the central hole [305]. By applying a unidirectional magnetic field the magnetic configuration can change into a so-called onion state with opposite circulation of the magnetization in each half of the ring. This state is metastable, thus it is usually maintained after relaxation of the field. The onion state contains two DWs at the top and bottom: a head-to-head DW and a tail-to-tail DW. Depending on the ring width and thickness different domain wall types are preferred [139]. In narrow wires transverse walls (TWs) are energetically favoured compared to vortex walls (VW). In a roughly triangular TW the magnetization rotates by 180° in the plane, as shown in the left micromagnetic simulation in Fig. 1.11a). In a VW, as shown in the right of Fig. 1.11a), the magnetization circulates around a vortex core where the magnetization is pointing out of the plane. The TW has a significant stray field that is strongly reduced by the circulation in the VW. Fig. 1.11b) shows phase diagrams correlating the occurrence of the DW types with the ring width w and thickness t. The left phase diagram contains experimentally measured values in $Ni_{20}Fe_{80}$ rings, the right one a comparison of the experimental measurements, micromagnetic simulations and analytical calculations. The difference between the stray field energies of both DW types can be estimated as [183]

$$\Delta E_{\mathrm{d}} \approx -\frac{1}{8}\mu_0 M_{\mathrm{s}}^2 t^2 w. \tag{1.38}$$

The main contribution to the difference of the exchange energy is due to the vortex in the VW:

$$\Delta E_{\mathrm{ex}} \approx 2\pi t A \ln\frac{r_{\max}}{r_{\min}}, \tag{1.39}$$

with A being the exchange constant and r_{max}/r_{min} the outer respectively inner radius of the vortex. Thus the phase boundary is approximately given by $wt \approx$ const [183].

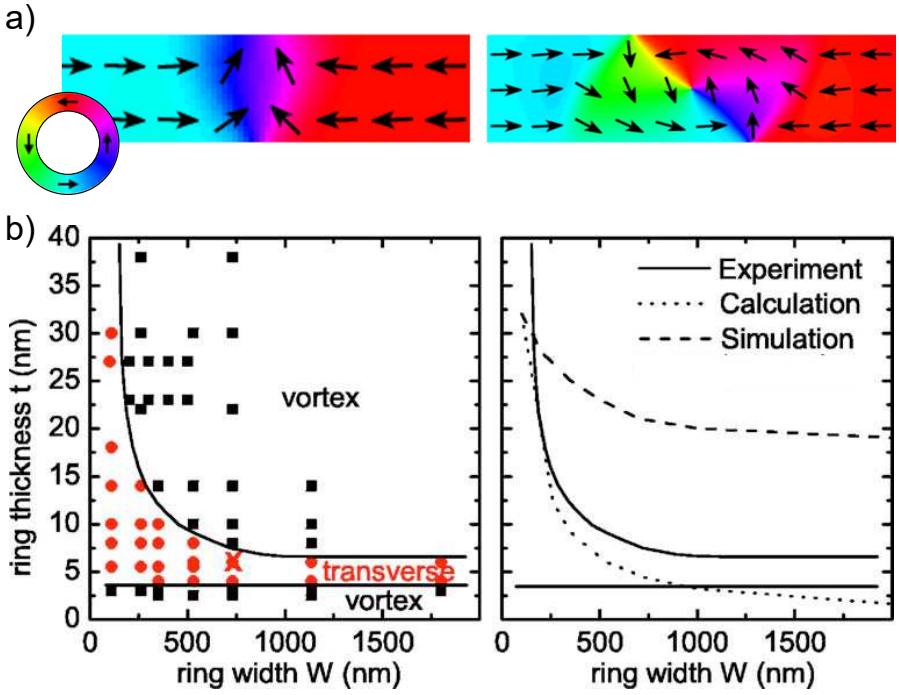

Figure 1.11: a) Micromagnetic simulations of a transverse domain wall (TW) and vortex domain wall (VW). **b)** Left: Experimental phase diagram for the occurrence of TWs and VWs in $Ni_{80}Fe_{20}$ rings. Black squares indicate VWs and red circles TWs. The phase boundaries are shown as solid lines. Right: A comparison of the upper experimental phase boundary (solid line) with results from calculations [102] (dotted line) and micromagnetic simulations (dashed line).

Magnetization switching in mesoscopic rings from one high-remanence onion state to the opposite onion state can occur *via* different pathways. Fig. 1.12 shows three hysteresis loops and schematically the corresponding magnetization configurations of polycrystalline Co rings with different outer (d_{out}) and inner (d_{in}) diameter and thickness. We observe single step switching without a metastable intermediate state, and double and triple switching *via* intermediate spin configurations [141]. We discuss them in turn in the following [142]

a) The single-step switching can occur *via* two mechanisms: In thin films a reverse domain can be nucleated at the edge of the ring and then expand until the opposite onion state is formed. Alternatively the switching can occur *via* pure DW propagation with both DWs moving either clock- or counter-clockwise until the opposite onion state is formed. This switching has been achieved by tailoring the field carefully [26, 27].

b) Double-step switching is mainly caused by asymmetries in the ring [140]. With decreasing field first the fully magnetized state transforms into the onion state and then one DW depins first and propagates toward the other one, where they annihilate, so that an intermediate vortex state is formed. With increasing field in opposite direction new DWs are nucleated.
c) In very wide and thick rings triple switching can be observed. As in the case described before, with decreasing field a vortex state forms, but then with the increasing field in the opposite direction a vortex core is nucleated. The vortex core reduces the Zeeman energy and with further increasing field strength it is expelled at the perimeter of the ring.

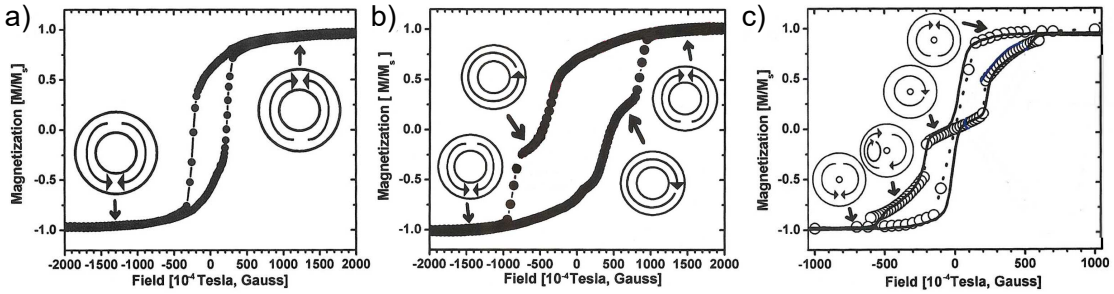

Figure 1.12: Hysteresis loops of polycrystalliine Co rings. The magnetization states are shown schematically. (Adapted from [141] with permission.). **a)** Single switching from the onion to the reverse onion state in thin rings ($d_{\mathrm{out}} = 1700\,\mathrm{nm}$, $d_{\mathrm{in}} = 1250\,\mathrm{nm}$, $t = 4\,\mathrm{nm}$). **b)** Double switching from the onion to the reverse onion state *via* the vortex states ($d_{\mathrm{out}} = 1200\,\mathrm{nm}$, $d_{\mathrm{in}} = 950\,\mathrm{nm}$, $t = 15\,\mathrm{nm}$). **c)** Triple switching in very wide and thick rings *via* vortex and vortex core state ($d_{\mathrm{out}} = 1700\,\mathrm{nm}$, $d_{\mathrm{in}} = 300\,\mathrm{nm}$, $t = 32\,\mathrm{nm}$).

Instead of a uniaxial field also a rotating field can be used to switch the onion state in a magnetic ring [26]. The DWs tend to align with the field axis to reduce the total energy. The switching dynamics is now not only determined by the field amplitude but also the rotation frequency. Interestingly, even below the so-called Walker breakdown where the DW type alternates (VWs and TWs), the DW velocity is not constant for a constant rotation frequency due to periodic small spin structure changes [26]. In asymmetric rings with gradually changing ring width this effect can be mitigated by a tailored width gradient [235]. The vortex state to onion state switching *via* the nucleation of DWs using a uniaxial field was investigated *via* time-resolved XMCD scanning transmission X-ray microscopy in Ref. [236]. The switching occurs in three steps: First a ripple-like pattern similar to the buckling mode discussed before appears in the ring half, where the magnetization direction opposes the field direction. Then the ripples transform into two DWs and propagate to the ring vertices to align with the field direction. This DW nucleation and propagation process in shown in Fig. 1.13.
Furthermore, asymmetric rings even allow for switching from one vortex state to the vortex state with opposite chirality using simple uniaxial fields [181, 229, 331]. To this

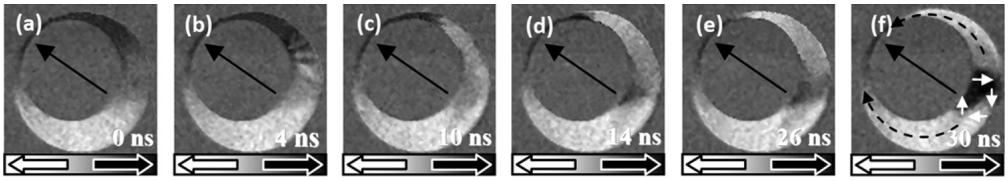

Figure 1.13: Time-resolved scanning transmission X-ray microscopy of DW nucleation in an asymmetric $Ni_{20}Fe_{80}$ ring ($d_{out} = 5.5\,\mu m$) using a 37 ns long uniaxial, non-rotating field pulse. The switching from the vortex state to the onion state occurs *via* three steps: **(a)**-**(b)** formation of a ripple-like domain structure, **(c)** DW formation and **(d)**-**(f)** DW propagation and alignment with the field direction. (Reprinted with permission from [236].)

end, first an onion state is generated by a static field pulse. As soon as the field is switched off, the DWs move along the width gradient toward the narrowest part of the ring, since the spatially dependent DW energy landscape has a maximum at the widest part of the asymmetric ring and a minimum at the narrowest part [235]. This DW propagation process, shown in Fig. 1.14, is called automotion. Finally the two domain walls annihilate and a vortex state is formed. The chirality of this newly formed vortex state depends on the field direction. Switching between vortex states with opposite chirality could be applied in logic devices [35] and reversing the direction of the onion state is applied in a proposal of a lateral giant magnetoresistance device [121]. Automotion of DWs can be induced by a wire width gradient, but also by current-induced spin structure changes [42] and curvature gradients, where the degree of nanowire bending is gradually increased [322]. Automotive DW propagation could be useful for low-energy interconnects in spintronic logic devices [206].

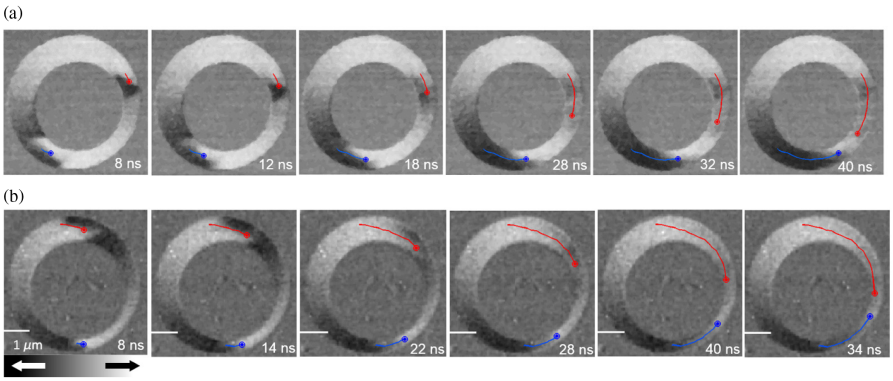

Figure 1.14: Time-resolved scanning transmission X-ray microscopy of DW automotion switching the magnetic state of an asymmetric $Ni_{20}Fe_{80}$ ring ($d_{out} = 5.5\,\mu m$) from an onion to a vortex state in the case of **a)** equal VW chirality and **b)** opposite VW chirality. (Reprinted with permission from [181].)

1.5 Spin Hall Effect

An electrical current in materials with high spin-orbit coupling can cause a transversely flowing pure spin current with the polarization of the electrons orthogonal to the electrical and spin current orientation, as shown in Fig. 1.15. This effect is called the spin Hall effect (SHE). A recent review on this topic can be found in Ref. [268]. The family of spin dependent Hall effects includes the SHE, the anomalous Hall effect where an applied current leads to transverse charge separation in magnetic materials and the inverse spin Hall effect (ISHE), which is a reciprocal effect according to the Onsager principle with a spin current generating a transverse charge current [244, 298]. The SHE was predicted theoretically almost 50 years ago in 1971 by Dyakonov and Perel [68]. From the Mott scattering experiment it was known that the scatter direction of an electron in vacuum depends on its angular momentum, its spin [196]. This effect was considered as an explanation for the anomalous Hall effect (AHE) that has been observed in 1881 [101]. 1999 the prediction of the SHE was revived by Hirsch with a proposal for its experimental detection by using the inverse spin Hall effect (ISHE) [111]. However, even though the SHE shares underlying physics with the AHE [198], the simultaneous generation using the SHE and electrical detection with the ISHE is difficult, since the spin decays and dephases as it is not a conserved quantity like the charge. The first detection of the SHE was realized by Kato *et al.* in the semiconductor GaAs using Kerr microscopy [128]. The first experiment demonstrating in parallel SHE and ISHE succeeded with the semiconductor HgTe in 2010 [39]. Kimura *et al.* demonstrated electrical detection of spin currents generated by the SHE in metals [135]. Optical detection methods have been considered as being insufficiently sensitive for imaging the spin accumulation in metals [112]. A key parameter for the efficiency of the conversion from a charge current to a spin current is the so-called spin-Hall angle (SHA). However the spin accumulation not only depends on this charge-to-spin conversion ratio but also on the spin diffusion length λ_s of the material. While in semiconductors λ_s can be in the range of µm [130], it is considerably smaller in metals being only in the range of a few nm [272]. Spin relaxation of conduction electrons can occur *via* different mechanisms [78]: The Elliott-Yafet mechanism is relevant in systems with inversion symmetry and the spin-flip time τ_s is proportional to the momentum scattering time τ_p [75]. Here spin-orbit band mixing with phonon and impurity scattering results in spin relaxation [85]. The spin relaxation *via* Dyakonov-Perel mechanism occurs *via* spin precession *via* an effective spin-orbit magnetic field, which is a consequence of the band splitting due to the spin orbit interaction in materials with inversion asymmetry and is characterized by an anti-proportional dependence between τ_s and τ_p [69]. Current-induced spin polarization is also very relevant from a technological point of view. The generated spin currents can be injected into adjacent ferromagnetic layers and switch the magnetization *via* spin-transfer torque [170, 189] and/ or spin-orbit torque [47, 156]. Similar torques can switch staggered antiferromagnets such as CuMnAs [308] or Mn_2Au [30]. Further, spintronic devices that do not rely on ferromagnetic materials are highly desirable to guarantee faultless function even in the presence of external magnetic fields. Only recently have full non-magnetic lat-

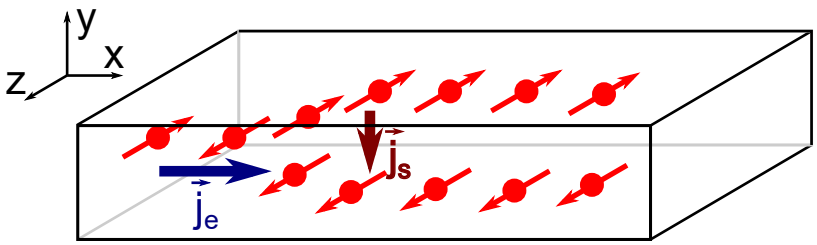

Figure 1.15: A charge current in a material with strong spin orbit interaction induces a transverse spin current that generates a spin accumulation at the surfaces of the material. The direction of the spin current is determined by the direction of the charge current and the sign of the spin Hall angle.

eral spin valves been realized using the SHE as the spin current generator instead of a ferromagnetic spin current injector and the ISHE for the detection [43, 320].

1.5.1 Contributions to the SHE

Three different mechanisms are responsible for current-induced spin accumulation in a non-magnetic metallic conductor with high spin-orbit coupling. Here these mechanisms are discussed following Sinova *et al.* [268]. A typical classification of those mechanisms separates them according to their dependence of the spin Hall conductivity σ_{xy}^{SH} on the momentum scattering time τ_p. σ_{xy}^{SH} determines the generated spin current by the applied field $j_s = \sigma_{xy}^{SH} E_x$. One needs to keep in mind that this is a phenomenological classification and that different microscopic mechanisms can have the same τ_p dependence. Skew scattering is proportional to τ_p, while the other two mechanisms do not depend on the conductivity ($\sigma_{xy}^{SH} \propto \tau_p^0$).

Intrinsic spin-Hall effect

The intrinsic contribution which is defined by the linear dependence on τ_p depends only on the band structure of the ideal crystal. Bands connected by spin orbit interaction near the Fermi energy provide the largest contributions to the spin Hall conductivity σ_{xy}^{SH}. The Bloch electrons are accelerated in an electric field and precess around the induced momentum-dependent field. The mechanism is here exemplarily described by the two-dimensional Rashba Hamiltonian following [267]:

$$H = \frac{p^2}{2m} - \frac{\lambda}{\hbar}\vec{\sigma} \cdot (\hat{z} \times \vec{p}), \tag{1.40}$$

with the eigenvalues

$$E_{\pm} = \frac{p^2}{2m} \pm \lambda |p|. \tag{1.41}$$

The second term in the Hamiltonian describing the spin-orbit coupling can also be expressed in terms of the spin momentum $\vec{S} = \frac{\hbar}{2}\vec{\sigma}$ and the angular momentum $\vec{L} = \hbar\vec{l} =$

$(\vec{r} \times \hbar\vec{k})$ of the electron [93]:

$$H = \frac{p^2}{2m} + \xi(r)\frac{\vec{\sigma}}{2} \cdot \vec{l} \tag{1.42}$$

with the spin-orbit parameter $\xi = \langle \xi(r) \rangle$ being proportional to Z^4. Thus elements with a high atomic number Z are needed to obtain high spin-orbit coupling.
The Bloch equation describes the dynamics of an electron spin in a time-dependent magnetic field that is induced by the motion of the spin in momentum space.

$$\frac{\hbar d\hat{n}}{dt} = \hat{n} \times \vec{\Delta}(t) + \alpha \frac{\hbar d\hat{n}}{dt} \times \hat{n}. \tag{1.43}$$

$\hat{n}$ denotes the spin direction, α is the damping, and the Zeeman coupling is given by $-\vec{s} \cdot \vec{\Delta}/\hbar$ with $\vec{\Delta} = 2\lambda/\hbar(\hat{z} \times \vec{p})$. Solving this equation results in a z-component of the spin direction:

$$n_z(t) = \frac{\hbar}{\Delta_1^2}\frac{d\Delta_2}{dt}, \tag{1.44}$$

with $\Delta_{1,2}$ being the in-plane components of the Rashba effective field. If an electric field is applied, as shown in Fig. 1.16b)-c), the momentum of the electrons changes by $\dot{p_x} = -eE_x$ and thus the momentum-dependent effective magnetic field also changes. The z-component of the spinor depends linearly on the p_y:

$$n_{z,\vec{p}} = \frac{-e\hbar^2 p_y E_x}{2\lambda p^3}. \tag{1.45}$$

The resulting spin current in y direction is given by

$$j_{s,y} = \frac{-eE_x}{16\pi\lambda m}(p_{F+} - p_{F-}), \tag{1.46}$$

with p_{F+} and p_{F-} being the Fermi momenta of the minority and majority Rashba bands. The generation of the spin current is illustrated in real space in Fig. 1.15. The spin accumulation at the surface depends on the spin Hall conductivity $\sigma_{xy}^{SH} = \frac{-j_{s,y}}{E_x}$ and the spin diffusion length λ_s.
The spin Hall conductivity of the intrinsic SHE can be calculated accurately considering the band structure of the materials by using *ab initio* methods [86]. This is of particular importance since the intrinsic mechanism is the main contribution in heavy metals such as Pt [282] and Ta [243]. Adjacent bands connected *via* spin-orbit coupling give the largest contributions to σ_{xy}^{SH} [99]. Another interesting feature is the sign change of the spin Hall angle for 5d transition metals on progressively filling the band. Thus Ta has a negative spin Hall angle while for Pt it is positive. This was first predicted theoretically [282] and then confirmed by ferromagnetic resonance (FMR) measurements [310]. Due to the inherent τ_p dependence the spin Hall angle can be tuned by varying the resistivity *e.g. via* different thin film growth [242, 243]. In addition to the band-structure dependent intrinsic mechanism there are two other mechanisms, which also lead to a spin current.

Skew scattering

This mechanism shares the physics with Mott scattering of relativistic electrons [196]. Here the electrons experience disorder-induced chiral scattering in the presence of spin-orbit interaction. If the skew scatter contribution dominates, the spin Hall conductivity σ_{xy}^{SH} is proportional to the longitudinal conductivity σ_{xx} of the material. However, this mechanism only plays a subordinate role compared to the intrinsic mechanism for heavy metal materials such as Pt, W and Ta, which have been investigated in this thesis [334].

Side jump mechanism

The side jump mechanism is simply defined as the missing component that results in the total spin Hall conductivity σ_{xy}^{SH}. In materials with high spin orbit interaction this contribution consists of an intrinsic and extrinsic part. The intrinsic contribution is described by the spin-orbit-coupled term of the Bloch electron wave function at the scalar potential without spin orbit coupling, while the extrinsic side jump results from the scattering of the non-spin-orbit-coupled term of the wave-packet induced by spin-orbit-coupled disorder. The intrinsic contribution is significant in heavy metals like Pt and Ta.

1.5.2 Inverse Spin-Galvanic Effect

Current-induced spin polarization can be induced also by another spin-orbit based mechanism. In contrast to the SHE in the bulk of the material the inverse spin galvanic effect (ISGE) requires broken inversion symmetry at surfaces or interfaces. The spin galvanic effect was first demonstrated by Ganichev *et al.* [94]. The local electric field due to the inversion asymmetry and the redistribution of scattered electrons on the Fermi surface with spin-dependent texture leads to the nonequilibrium spin density. The Hamiltonian describing this effect is again the Rashba Hamiltonian [93], as for the intrinsic SHE.

1.5.3 Spin Diffusion

In this thesis direct imaging of the current-induced surface spin accumulation in non-magnetic metals was attempted. However, not only does the spin Hall angle need to be high for a sizeable signal but also the spin diffusion length λ_s of the material. The spin accumulation due to the SHE can be calculated considering drift-diffusion of the spin current to the film surface. We follow here Ref. [327] and [174]. The spin diffusion equation is given by [299]

$$\nabla^2 \delta\mu_N = \frac{1}{\lambda_s^2}\delta\mu_N. \tag{1.47}$$

$\delta\mu_N$ is the difference of the electrochemical potential due to the spin accumulation. The ohmic current and the diffusive spin current are given respectively by

$$\vec{j_c} = \sigma_{xx}\vec{E} \text{ and } \vec{j_s} = -\left(\frac{\sigma_{xx}}{2e}\right)\nabla\delta\mu_N, \tag{1.48}$$

with the total charge and spin currents

$$\vec{J_c} = \vec{j_c} + \theta_{\mathrm{SH}} \left(\frac{\vec{j_c}}{|\vec{j_c}|} \times \vec{j_s} \right), \tag{1.49}$$

$$\vec{J_s} = \vec{j_s} + \theta_{\mathrm{SH}} \left(\frac{\vec{j_s}}{|\vec{j_s}|} \times \vec{j_c} \right). \tag{1.50}$$

θ_{SH} is the spin-Hall angle describing the ratio between spin-Hall and charge conductivity. Solving the differential spin-diffusion equation leads to the z-dependent spin accumulation, which is polarized along the y-axis:

$$\delta\mu_N(z) = 2e\theta_{\mathrm{SH}}\rho_{xx}\lambda_s j_c \frac{\sinh\left(\frac{z}{\lambda_s}\right)}{\cosh\left(\frac{t}{2\lambda_s}\right)}. \tag{1.51}$$

The spin diffusion length is given by λ_s, the resistivity by ρ_{xx}, while t is the thickness of the wire. θ_{SH} can also be expressed by the spin-Hall conductivity σ_{xy}^{SH} and the electrical conductivity σ_{xx} of the sample. Thus the spin accumulation can be estimated by using *ab initio* calculations of σ_{xy}^{SH}.

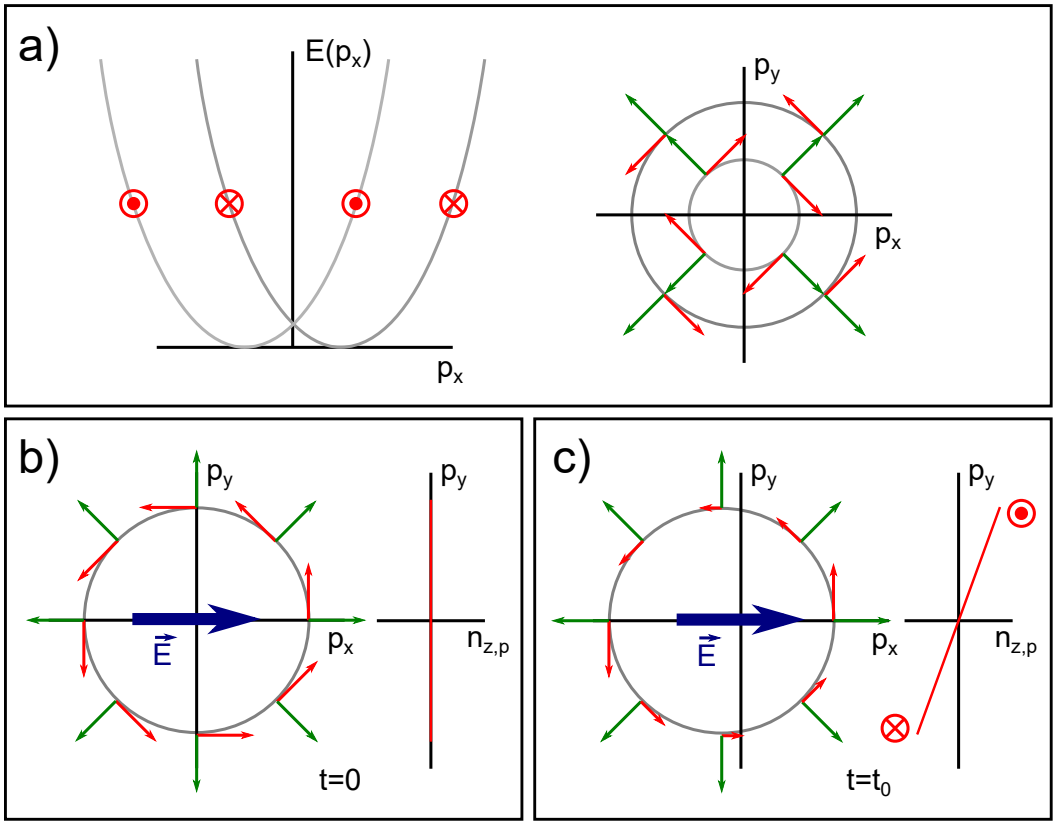

Figure 1.16: **a)** The eigenstates of a 2D Rashba system in equilibrium. The conduction band is split into two parabolas for the two spin states $\pm\frac{1}{2}$. The eigenspinors are orthogonal to the momentum. **b)** Rashba spin texture for one chiral state when an electric field is switched on ($t = 0$) and c) after the field being switched on for $t = t_0 < \tau_p$. The electric field shifts the Fermi circle and induces an effective torque on the electron spin so that the spins tilt up for $p_y > 0$ and down for $p_y < 0$. The generated spin current flows in y direction, orthogonal to the net spin direction and the electric field orientation, as shown in Fig. 1.15.

1.6 Magnetic Interactions in Heterostructures

With the development of thin film deposition techniques such as thermal evaporation and sputtering multilayers consisting of magnetic and nonmagnetic thin films have been in the focus of intense research motivated by a better understanding of the underlying physics and exploiting their rich properties for possible applications. Different magnetoresistive effects playing a big role in spin transport, such as the giant magneto-resistance [15, 24] and tunnel magneto-resistance [125] were discovered and employed in devices. The coupling of ferromagnets to antiferromagnets was investigated and the exchange bias effect employed to fix the magnetization direction in spin valves [231]. In the last part of this thesis, Ch. 7, we investigate spin structures in certain heterostructure systems by SEMPA imaging, where the domains and the DW spin structure crucially depends on the interaction of the magnetic moments of the different layers. In the following sections the basic physics of these interactions is described.

1.6.1 Dzyaloshinskii-Moriya Interaction

Dzyaloshinskii-Moriya interaction (DMI) in general is not confined to spin-spin interactions between layers of different materials but also occurs in compound materials [70, 197]. The necessary condition is spatial inversion asymmetry. In this section we focus on interfacial DMI and discuss several typical spin structures occurring in DMI systems. By choosing the different layer materials and thickness, interfacial DMI can be engineered depending on the requirements. In the discussion of DMI we follow here mainly the review by Fert *et al.* [80].
The spin-orbit coupling leads to a spin interaction term that is described by the DMI Hamiltonian:

$$\mathcal{H}_{\mathrm{DMI}} = \sum_{i<j} \vec{D}_{ij}(\vec{S}_i \times \vec{S}_j). \tag{1.52}$$

In the case of interfacial DMI $\vec{D}_{ij}$ is given by $\vec{D}_{ij} = D_{ij} \cdot (\hat{\vec{n}} \times \hat{\vec{u}}_{ij})$ with $\hat{\vec{n}}$ being the unit vector perpendicular to the film plane and $\hat{\vec{u}}_{ij}$ the unit vector pointing from site i to j. D_{ij} is proportional to the spin-orbit interaction. To minimize the DMI energy the spins tend to be orthogonal. In a ferromagnet this results in a rotation of the spins either clockwise or counter-clockwise, depending on the sign of D_{ij}. $\vec{D_{ij}}$ lies in the x-y-plane and the overall effect of the DMI on the magnetization can be described by the energy term

$$E = D \cdot (m_z \partial_x m_x - m_x \partial_x m_z + m_z \partial_y m_y - m_y \partial_y m_z), \tag{1.53}$$

where D is the global DMI constant, which is inversely proportional to the film thickness if it is pure interfacial effect [321].
The sign and magnitude of the DMI is controlled by the 3d ferromagnet´s orbital occupation and the spin-flip mixing processes with the spin-orbit active 5d states of the heavy metal [21]. The DMI can be measured experimentally with different methods including Brillouin light scattering [58, 205], chiral domain wall motion/ bubble expansion [159]

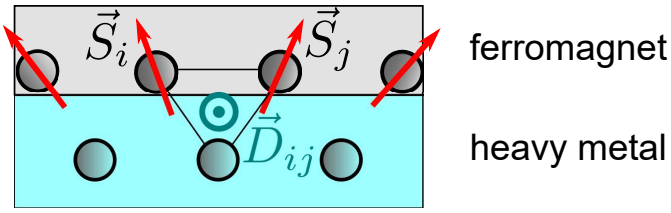

Figure 1.17: Interfacial Dzyaloshinskii-Moriya interaction (DMI) in a heavy metal/ ferromagnet bilayer. The asymmetric exchange interaction is mediated by the heavy metal atoms. The DMI energy is minimized by a non-collinear arrangement of adjacent spins, with the chirality determined by the direction of the DMI vector $\vec{D}_{ij}$.

and domain nucleation [228]. The DMI can be effectively enhanced by putting the ferromagnetic layer in between two heavy metals where the interfacial DMI constant has the opposite sign [191].
The DMI energy contribution can significantly affect the DW spin structure. In general in films with perpendicular magnetic anisotropy, Bloch DWs with the magnetization rotating in the plane are favoured, since magnetic charges and demagnetization fields are avoided (Fig. 1.18a)-b)). However, above a critical value for the DMI constant, $D > D_c = 4\lambda_{DW}K/\pi$, the Néel configuration will be favoured, where the magnetization rotates within the plane of the domain magnetization [285]. Here λ_{DW} is the DW width [164] and K the anisotropy constant.
A strong DMI guarantees a fixed chirality. This is a necessary prerequisite for stable whirl-like spin structures called skyrmions, in contrast to other bubble-like domains that are stabilized only by dipolar interactions. A measure of the winding of the normalized local magnetization $\hat{\vec{m}}$ is given by the topological winding number S [80]:

$$S = \frac{1}{4\pi} \int \hat{\vec{m}} \cdot (\partial_x \hat{\vec{m}} \times \partial_y \hat{\vec{m}}) \mathrm{d}x\mathrm{d}y = \pm 1. \tag{1.54}$$

For skyrmions, the full sphere (4π) is covered if the magnetization is mapped on a sphere. Skyrmions are topologically protected, *i.e.* the spin structure can not be changed continuously into a configuration with different S. There are Néel and Bloch type skyrmions, depending on the DMI vector, as shown in Fig. 1.19. The solitonic nature of skyrmions makes them very interesting for storage devices such as the skyrmion race track memory [286] and also stochastic logic devices [325]. Skyrmions were first seen experimentally in non-centrosymmetric single crystals with bulk DMI [197, 324] and later in ferromagnetic layers on heavy metals with interfacial DMI [107]. More recently, a strong interest is found in the investigation of materials with antiferromagnetic properties that host skyrmions [163, 328].

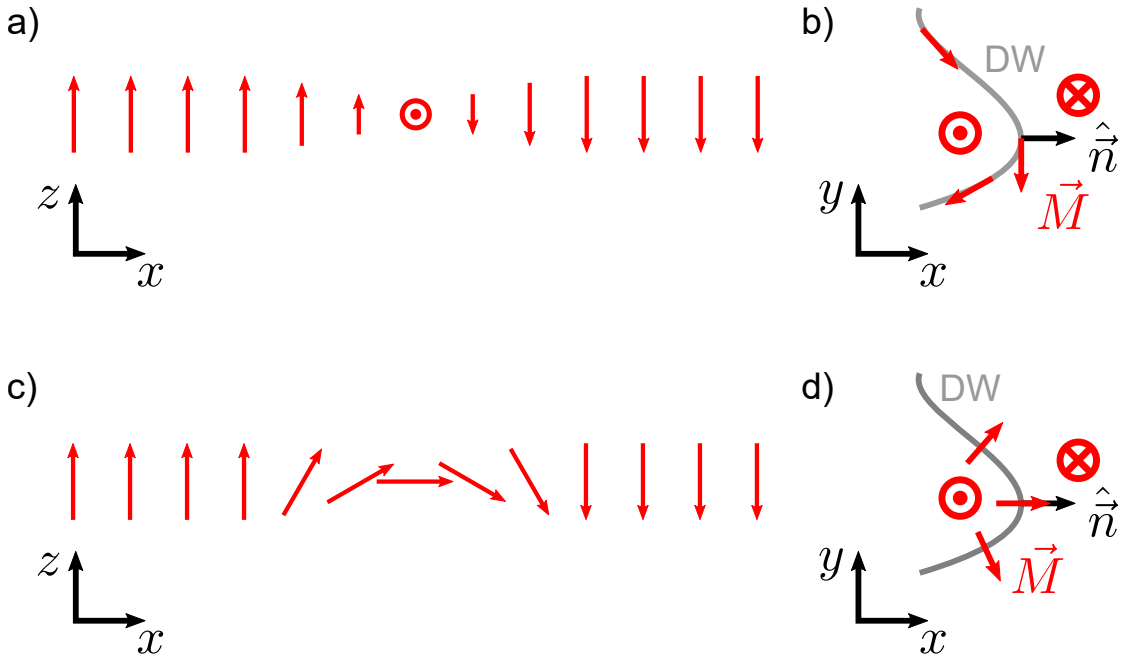

Figure 1.18: **a)** Projection of the Bloch wall spin structure into the x-z plane. **b)** Bloch DW in the x-y plane. The magnetization in the DW is perpendicular to the DW normal $\hat{\vec{n}}$. **c)** One-dimensional Néel wall spin structure in the x-z plane. **b)** Néel DW in the x-y plane. The magnetization in the DW is collinear with the DW normal $\hat{\vec{n}}$.

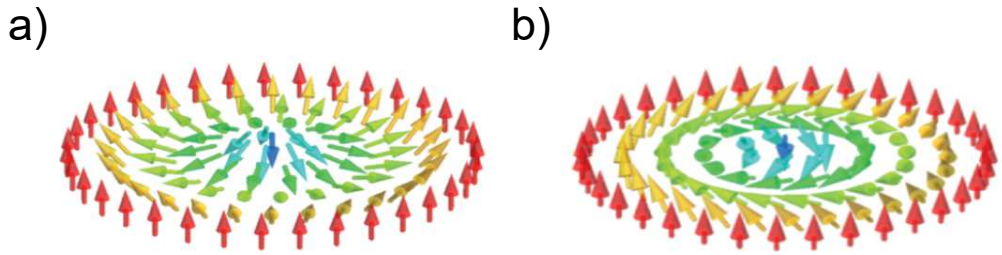

Figure 1.19: **a)** Néel skyrmion and **b)** Bloch skyrmion (Reprinted with permission from [80]).

1.6.2 Indirect Exchange Coupling

Bilinear exchange

The bilinear coupling energy of two ferromagnetic layers separated by a non-magnetic layer is determined by the orientation of the magnetization in the magnetic layers and the coupling constant:

$$E = -A_{12}\vec{M}_1 \cdot \vec{M}_2 \tag{1.55}$$

Various experiments demonstrated a spacer thickness dependency of A_{12}. For example, the sign of A_{12} changes up to 60 times by variation of the interlayer thickness between 0 and 80 monolayers in a Fe/Au/Fe system. Experimentally this behaviour was discovered by measuring the giant magnetoresistance of these multilayers [221]. By using a wedged spacer, as shown for a Fe/Au/Fe system in Fig. 1.20, SEMPA imaging is very well suited to investigate the dependence of the coupling on the spacer thickness [293, 295], although it can not be used for quantitative determination of the coupling strength since it is difficult to apply magnetic fields during imaging. Similar to RKKY-coupling, the origin of this oscillatory behaviour is explained by sharp cut-offs in k-space due to the Fermi surface of the spacer layer. At interfaces electrons get reflected. In a trilayer you have two interfaces where electrons are reflected. The superposition of these waves in the spacer leads to interference effects. Resonances in the case of constructive interference (also called quantum-well states) shift with varying thickness of the spacer t_s. The periodic crossing of the Fermi energy by these resonances is the reason for the oscillatory behaviour of the coupling [275]. It is important to take the discrete nature of the spacer into account that can lead to aliasing effects due to undersampling of the oscillating coupling [50]. The observed change between ferromagnetic and antiferromagnetic coupling allows the fabrication of artificial antiferromagnets.

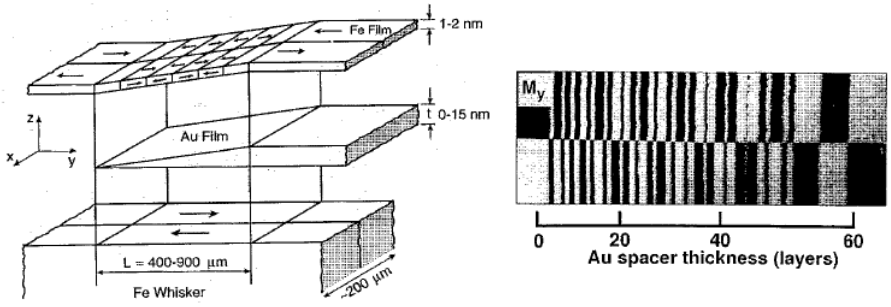

Figure 1.20: Oscillatory bilinear coupling in Fe/Au/Fe(100) depending on the thickness of the Au spacer. The schematic drawing shows the sample geometry and the magnetization orientation in the domains of the Fe whisker substrate as well as in the Fe film on top of the spacer. The top layer magnetization is imaged using SEMPA (right image) [295].

Another possible origin for bilinear coupling is stray fields. In ideal samples with perfectly smooth interfaces and uniformly in-plane magnetized layers, no stray fields are

generated. This no longer holds in the case of rough interfaces. If the normal vectors of both interfaces are collinearly aligned, *i.e.* the thickness of the spacer layer is uniform, but the interfaces are rough, the stack prefers ferromagnetic coupling. This type of interaction is called orange-peel coupling. The coupling energy $A_{12,\mathrm{OP}}$ can be calculated by applying the original Néel model [150, 203]:

$$A_{12,\mathrm{OP}} = \frac{\pi^2}{\sqrt{2}}\frac{\delta_\mathrm{s}^2}{\lambda}\mu_0 M_\mathrm{s}^2 \exp(-\frac{\pi}{\sqrt{2}}\frac{t_\mathrm{s}}{\lambda}), \tag{1.56}$$

δ_s is the surface roughness, λ the average period of the roughness and t_s the thickness of the nonmagnetic spacer. Using typical values for these variables, $A_{12,\mathrm{OP}}$ can be in the order of the overall coupling constant A_{12} reinforcing ferromagnetic coupling.

Biquadratic exchange

Ignoring for the moment crystallographic anisotropy, the total energy per unit interfacial area for a system of two magnetic layers separated by a non-magnetic layer in between in a magnetic field $\vec{H} = H\hat{e_z}$ is given by [73]

$$E_{tot} = -(d_1\vec{M}_1 + d_2\vec{M}_1)\cdot\vec{H} - \frac{A_{12}}{|\vec{M}_1|\cdot|\vec{M}_2|}(\vec{M}_1\cdot\vec{M}_2) - \frac{B_{12}}{|\vec{M}_1|\cdot|\vec{M}_2|}(\vec{M}_1\cdot\vec{M}_2)^2. \tag{1.57}$$

Here we consider both magnetic layers to have the same thickness $d = d_1 = d_2$ and the same magnetization $M = |\vec{M}_1| = |\vec{M}_2|$. The magnetization vector can also be expressed by the angle of the magnetization $M_{1,2} = (\sin(\theta_{1,2}), 0, \cos(\theta_{1,2}))$:

$$E_{tot} = -Md(\cos(\theta_1) + \cos(\theta_2))H - A_{12}\cos(\theta_1 - \theta_2) - B_{12}\cos^2(\theta_1 - \theta_2). \tag{1.58}$$

If $B_{12} > 0$ the second term of the interaction energy just enforces the collinear magnetization alignment of the two ferromagnetic layers. However, if $B_{12} < 0$, you have to distinguish different cases. First let us consider the case for magnetic layers with an easy axis along $\hat{e_x}$ and $\hat{e_z}$ and without applying a magnetic field [57]. Further we assume the magnetocrystalline energy to be larger than B_{12}, as is the case in *e.g.* Ref. [241]. Then only three states are possible: antiferromagnetic coupling, ferromagnetic coupling and biquadratic coupling, in other words: 180°, 0° and 90° orientation of the magnetization. The coupling phase diagram for this system is shown in Fig. 1.21. If $B_{12} < 0$ and $|A_{12}| < -B_{12}$ the magnetization of the two layers is 90°-coupled. Now we consider the case $A_{12} < B_{12} < 0$ and a variable magnetic field $H \geq 0$. Then $A_{12} - B_{12} < 0$ and $-A_{12} - B_{12} > 0$. For ferromagnetic coupling ($\theta_1 = \theta_2$) the total energy is given by $E_\mathrm{FM} = -A_{12} - B_{12} - 2MdH$, for antiferromagnetic coupling ($\theta_1 = -\theta_2$), $E_\mathrm{AFM} = A_{12} - B_{12}$ and in the case of biquadratic 90°-coupling, $E_{90°} = -MdH$. The energy dependence on the applied field and the critical fields $H_1 = -(A_{12} + B_{12})/(Md)$ and $H_2 = -(A_{12} - B_{12})/(Md)$ leading to a transition between two phases is shown in Fig. 1.22. Without applied field the magnetization of the two layers is antiparallel. With increasing field above H_2 the system shows biquadratic coupling and for $H > H_1$ the magnetic moments of both layers align along the field direction. The phase transition

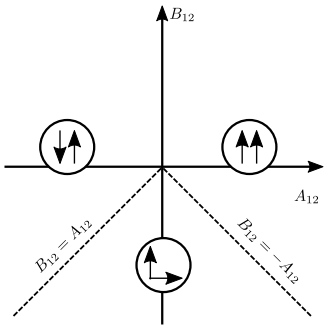

Figure 1.21: Phase diagram of two equal magnetic layers with dominating fourfold anisotropy coupling through a nonmagnetic spacer layer without applied magnetic field.

can be clearly seen in $M(H)$ loop measurements, as shown in Fig. 1.22b). The plateau length with $M_{\parallel}/M = 0.5$ is given by $H_{\mathrm{P}} = H_1 - H_2$. After removing the hysteresis effect the coupling constants A_{12} and B_{12} can be determined [248][2].
Various mechanisms have been considered as an explanation for the biquadratic coupling that has been previously introduced phenomenologically. Comprehensive reviews can be found in [73] and [275].

Intrinsic mechanism

For a simple free-electron model of a trilayer with perfect interfaces, biquadratic coupling appears if higher order terms of the angle between the magnetization are considered [74]. In general, these terms are small and can be neglected. Nevertheless there are theoretical calculations for Co/Cu/Co(001) indicating a significant contribution from the intrinsic biquadratic coupling if interface roughness is taken into account [66].

Fluctuation mechanism

If the oscillation period of the intrinsic bilinear coupling A_{12} is about two monolayers, A_{12} changes sign at a position where the interlayer thickness varies by one monolayer. If in addition the average size of interlayer areas with the same thickness is smaller than the domain wall width in the ferromagnetic layers, the magnetization is not able to align parallel or antiparallel, but will take some intermediate value. Energy minimization results in an average angle between the layer magnetization of 90° [269].

'Loose spin' model

For some systems like Fe/Al/Fe [100] or Fe/Au/Fe [91] the effective biquadratic coupling decreases quickly with increasing temperature, which is not expected from the fluctu-

[2] In the case discussed before ($B_{12} < 0$, $|A_{12}| < -B_{12}$) only the sum $A_{12} + B_{12}$ can be determined, since there is only one jump in the magnetization loop visible ($E_{\mathrm{AFM}} > 0$)

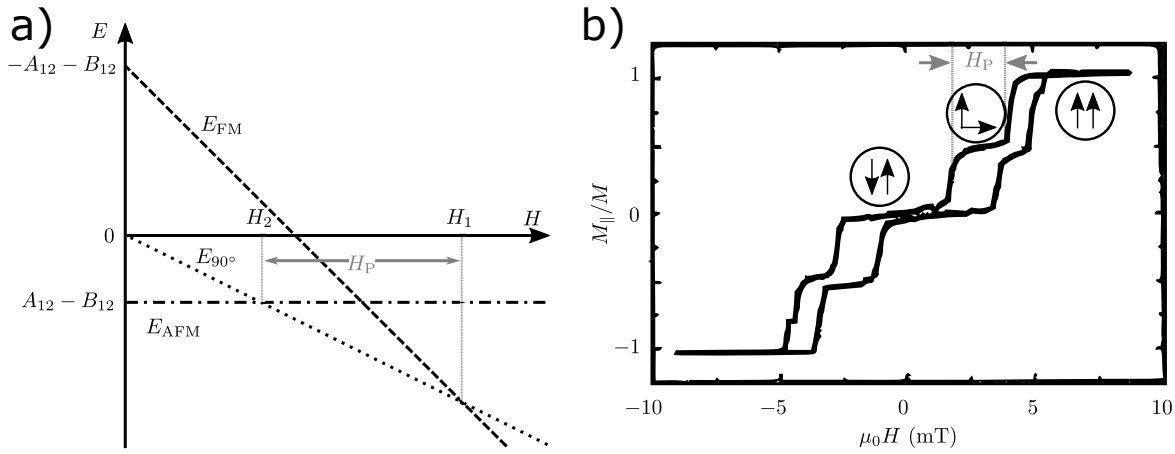

Figure 1.22: **a)** Schematic plot of the energies $E_{\mathrm{AFM}}(H)$, $E_{\mathrm{FM}}(H)$ and $E_{90°}(H)$ for $A_{12} < B_{12} < 0$ [73]. **b)** Magneto-optical Kerr effect hysteresis loop for Fe(1.5 nm)/Ag(1.85 nm)/Fe(1.5 nm). The different levels indicate the different field-dependent coupling phases (adapted with permission from [248]).

ation mechanism. Magnetic impurities in the nonmagnetic spacer layer which are not directly coupled *via* exchange to the magnetic layers were proposed to be the source for this kind of noncollinear coupling with a strong temperature dependence [270]. In an experiment with a low density of intentionally inserted Fe in an Ag spacer, this theory was supported [248]. Another explanation for this strong temperature dependence is given in the pin-hole model which applies when the interfaces are rough [105]. With increasing temperature the magnetization in the thin magnetic bridge decays and B_{12} decreases.

Magnetostatic coupling

A perfectly flat ferromagnetic layer has no significant stray field outside itself in contrast to a rough layer. This can lead to two kinds of coupling mechanism. A rough surface generates magnetic poles at the surface if the exchange interaction within the layer is strong enough to prevent alignment of the spins parallel to the local surface. If the roughness of both interfaces in a trilayer is correlated, *i.e.* the surface normals are parallel to each other, then the so-called 'orange-peel effect' occurs, which has already been described in Section 1.6.2. However for systems with uncorrelated surface roughness there is also a contribution to biquadratic coupling [56] since the intralayer exchange is finite and allows fluctuations in the magnetization direction. The energy is minimized for 90° alignment, as for the fluctuation mechanism.

2 Experimental Techniques

Besides scanning electron microscopy with polarization analysis, which will be discussed in detail in the next chapter, several other techniques were employed to either fabricate the samples or characterize them further. These techniques and their modes of operation are presented and short explained here.

2.1 Electron-Beam Lithography

The production of the patterned samples produced in this thesis was performed *via* a standard two-step electron-beam lithography lift-off process, as shown in Fig. 2.1. For patterned samples we use usually undoped naturally oxidized Si wafers as the substrate with a resistivity of $>1000\,\Omega$cm. To avoid charging due to e-beam exposure during SEMPA imaging we do not use highly insulating MgO or Al_2O_3. For wide and thick ($> 60\,$nm) structures such as contacts and striplines we use a double layer resist. In this case, after cleaning the substrate (acetone, isopropanol, water), the substrate was spin-coated with MMA (methyl methacrylate) and baked for 90 s at 180°C. Then an additional layer of PMMA (polymethyl methacrylate) was spin-coated and the sample was baked again with the same parameters. The time and speed of the rotation determines the thickness of the resist. The sample geometry was designed with the Raith Pioneer CAD software and the exposure performed with the corresponding e-beam system. In the case of an positive resist, such as used here, the electron beam exposure breaks the cross linking of the acrylate [274]. Depending on the size of the structure, the appropriate size of the aperture is chosen: For geometries on the order of µm, apertures between 30 and 60 µm are a good compromise between beam current (i.e. exposure time) and resolution. A higher voltage allows a better focussing of the beam. The dose applied to the resist depends mainly on the exposure time and the beam current. The exposed resist is dissolved in a bath of methyl isobutyl ketone (MIBK). The development is stopped with isopropanol. The material deposition can be done using molecular beam evaporation (Section 2.2) or sputtering (Section 2.3). After material deposition the lift-off is done using solvents such as acetone or NEP (N-ethylpyrrolidone). For successful lifting, it is important that the developed areas in the resist have a significant undercut and the material deposited on the substrate is not connected to the material on the remaining resist. This can be achieved using a resist double-layer, such as the one described above (MMA-PMMA) or by making use of the proximity effect in single layers. Depending on the geometrical position of the sample in the evaporation or sputter chamber, as well as the deposition technique side deposition can also hinder the results. The lift-off can be facilitated by heating the solvent (acetone max. 50°C, NEP 120°C). Furthermore,

it is important for the lift-off that the temperature of the sample does not exceed the glass-transition temperature of the resist, *e.g.* during bake-out of the deposition UHV system. If, as in our case, a second layer with different geometry (and material) is needed, it is important to pattern markers during the first step that can be used for proper alignment of the sub-micro scale structures on top of the first layer. In other respects, the processing of the second layer is similar to the first one. We used for our smaller and thinner structures (for example the heavy metal wires or the curved ferromagnetic structures) a single PMMA layer resist. For the exposure an aperture of 10 or 15 µm and a beam voltage of 20 kV instead of 10 kV was selected.

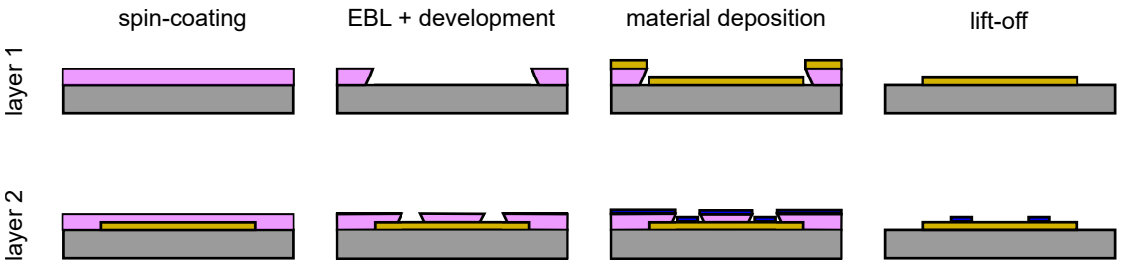

Figure 2.1: 2-step electron beam lithography (EBL): First the substrate (grey) is spin-coated with a resist (pink), then the resist is exposed to high energy electrons in the EBL system and the chemical bonds in the resist are weakened. During the development the exposed areas of resist are removed so that a mask is formed. Subsequently the material (yellow) is deposited and in the last step the remaining resist is removed (lift-off) to leave the designed structure. In the second stage this procedure is repeated with a different material (blue).

2.2 Thermal Evaporation

A widely applied material deposition technique is thermal evaporation [108]. The evaporator consists of an electron-emitting filament (thorium-doped tungsten) and the target material, either in the form of a rod (as shown schematically in Fig. 2.2). If the material melts first under this pressure and temperature, a crucible with pellets of the material is needed. The evaporator has a water-cooling housing. The deposition needs to take place in UHV conditions (10^{-9} mbar). The low gas pressure in the chamber allows for the deposition of high-purity films and provides highly directional deposition of the material, making this technique advantageous for patterning with lift-off. A filament current of about $I = 2\,\mathrm{A}$ is used to thermally emit electrons which are accelerated towards the target due to the application of a high positive voltage U_{HV} of several hundreds volts. The material sublimates or evaporates into the vacuum and travels towards the sample. The amount of deposited material is measured by measuring the change in resonance frequency of a quartz crystal due to the change in mass on material deposition.

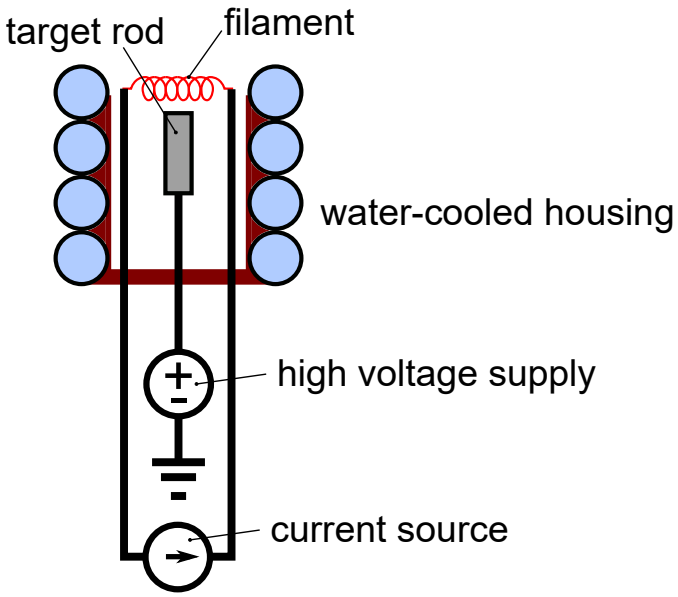

Figure 2.2: Schematic drawing of a thermal evaporator cell. With a high current electrons from the filament are released by thermionic emission and accelerated by the high voltage difference toward the target rod, heating it up locally. The material sublimates and is deposited on the sample.

2.3 Sputter Deposition

An alternative deposition technique is sputtering [261]. In contrast to evaporation this technique is widely used for fast industrial fabrication processes. Especially for materials like Pt, Ta and W, which can not be easily thermally evaporated, sputtering is the method of choice. Moreover optimized recipes allow the deposition of very smooth while at the same time thick films, which proved crucial for certain experiments conducted in the frame of this thesis. The operating principle is described following Ref. [52] and is sketched in Fig. 2.3. Before starting the deposition, the vacuum chamber is flooded with a so called process gas, typically Ar, so that a desired working pressure is reached. A strong electric field between the target (Pt, Ta, etc.), serving as the anode, and the substrate holder, ignites a plasma of the process gas. The ionized gas atoms accelerate towards the target and target atoms as well as secondary electrons are released. The target atoms move ballistically towards the anode and deposit on the substrate, while the secondaries are accelerated again by the field and sustain the ionization by random collisions with the process gas. The sputter efficiency can be increased by using magnets under the target in order to confine the plasma in a process known as magnetron sputtering. This leads to a longer path of the secondary electrons and more ionizing events.

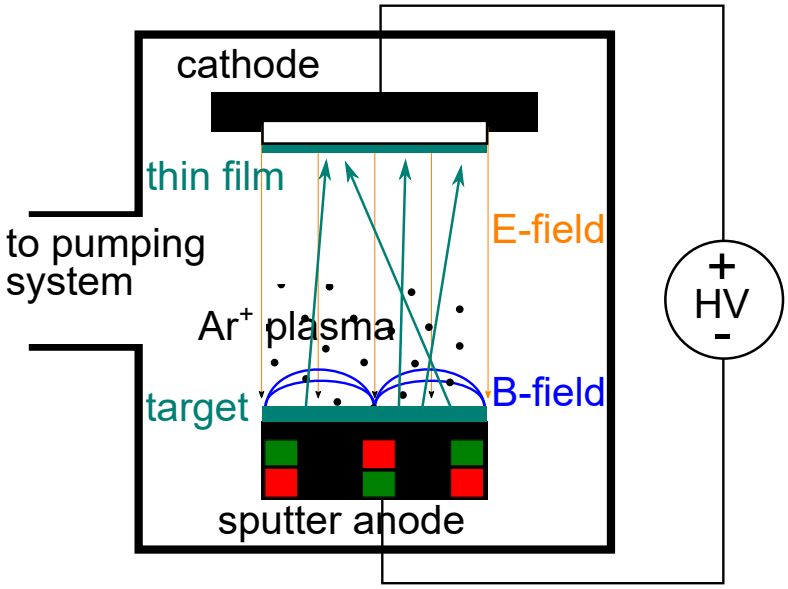

Figure 2.3: Schematic drawing of the sputter process. A strong electric field between the target material serving as anode and the cathode ignites the plasma. The Ar^+ ions release the target atoms, which move towards the anode and deposit on the substrate. The magnetic field confines the plasma and increases the sputter efficiency.

2.4 Atomic Force Microscopy

A common technique for topographic microscopy with nanometre resolution is atomic force microscopy (AFM) [72]. A schematic drawing of the operating principle is shown in Fig. 2.4. The AFM consists of a spring-like cantilever with a tip at its bottom that very close to the sample surface. The upper surface of the cantilever reflects the light of a laser source towards a 4-quadrant photo detector, thereby detecting the displacement of the cantilever with respect to its equilibrium position. While scanning the surface of the sample in the standard contact mode measurement the distance between the tip and sample is kept constant by a feedback loop from the detector to a z-axis piezo driver. In the contact mode the tip is kept in the repulsive regime of the Lennard-Jones potential [165] of the surface atoms. The cantilever reacts against the surface topography following Hooke´s law. Within this thesis AFM measurements were performed to determine the thickness and the surface roughness of the deposited materials. For high resolution imaging of the samples investigated in this thesis, Bruker SNL-10 tips [1] were used.

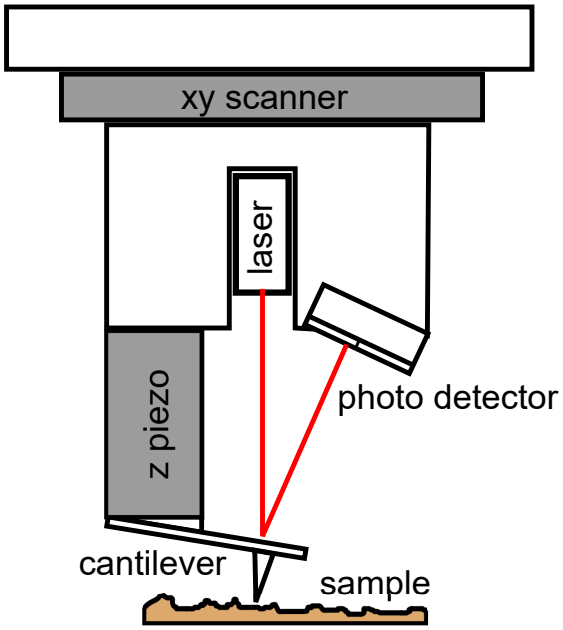

Figure 2.4: Schematic drawing of the operating principle of an atomic force microscope (AFM). The cantilever reacts against the surface topography while scanning the sample. This is detected by the reflection of a laser beam on its upper surface.

Fig. 2.5 shows an example AFM image of an asymmetric half ring on top of a stripline. Using the software Gwyddion [2], profile plots can be generated (line 2 in Fig. 2.5). These can be used to determine the height of the different layers in patterned devices. The roughness can be determined quantitatively from line scans (e.g. line 1 in Fig. 2.5).

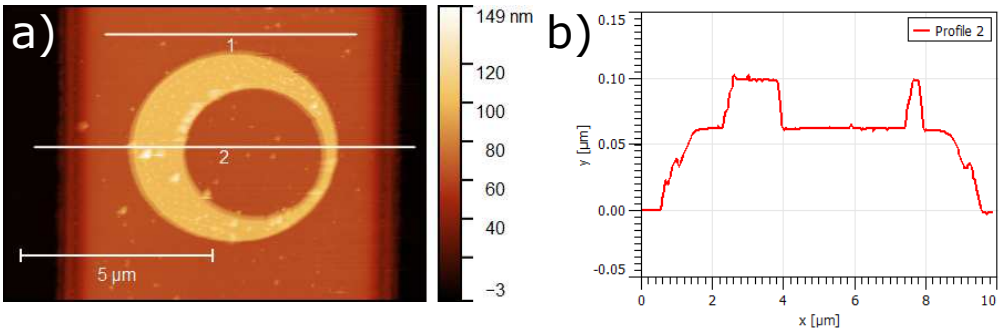

Figure 2.5: **a)** AFM image of an asymmetric ring on top of a stripline. Line 1 can be used to calculate the roughness of the stripline and in **b)** the height profile for line 2 is shown. Three main height levels are seen corresponding to the substrate, stripline and patterned ring.

2.5 Microwave spectroscopy

As described in Ch. 1, a magnetic moment $\vec{M}$ precesses around an effective magnetic field $\vec{H}_{\text{eff}}$ and on longer timescales is damped and aligns with $\vec{H}_{\text{eff}}$ (Equation 1.37). The resonant frequency f_{FMR} of a magnetic film exposed to an in-plane field $\vec{H}_{\text{ext}}$ and a small modulated field in the microwave range (which can be produced by a current through a coplanar waveguide below the sample) is given by:

$$f_{\text{FMR}} = \frac{\gamma}{2\pi}\sqrt{|\vec{H}_{\text{ext}}|(|\vec{H}_{\text{ext}}| + M_{\text{s}})}, \tag{2.1}$$

with M_{s} being the saturation magnetization [138]. In this way in a ferromagnetic resonance (FMR) experiment, M_{s} can be determined. Usually the resonance frequency is kept constant and the external field is swept. From the measured absorption spectra the Gilbert damping parameter α can be determined by the full width at half maximum ΔH of the resonance peak [71]:

$$\Delta H = \frac{4\pi\alpha}{\gamma} f_{\text{FMR}} + \Delta H_0. \tag{2.2}$$

Here the additional term ΔH_0 results from field and sample inhomogeneities [71].

2.6 Scanning Electron Microscopy with Polarization Analysis (SEMPA)

2.6.1 Magnetic Imaging Techniques

Within the range of experimental investigation techniques in the field of micro- and nanomagnetism, magnetic imaging techniques play an important role. They have helped in the interpretation of electrical measurements based on magneto-resistive effects that depend on the magnetic configuration [144, 254]. Furthermore they have enabled a deeper understanding of switching processes in magnetic materials detected indirectly with other methods such as hysteresis measurements based on the Kerr effect [14], superconducting quantum interference device (SQUID) magnetometry [124] and vibrating sample magnetometry [83]. In 1932 Francis Bitter published one of the first direct observation methods for magnetic domains [28]. He used small magnetic particles suspended in a fluid covering the sample surface that would align in the stray-field of the sample to make the magnetic state visible. Since then a broad variety of magnetic imaging techniques have been invented and used. An overview of these is given in a recent review chapter [233]. The different imaging techniques rely on the measurement of various physical quantities such as the stray field or the magnetization and can therefore be seen as complementary. One workhorse of modern magnetic imaging techniques is Kerr microscopy [84, 182]. It is a quick tool to investigate directly the domain pattern of ferromagnetic samples without complex sample preparation. However, the spatial resolution of optical techniques is limited in general by the wavelength of light to several hundred nanometres. This

drawback has become more significant in the last years with the advances in lithography and the associated progress in miniaturization of spintronic devices. On the other hand, magneto-optical methods allow for the detection of ultrafast processes [20, 182]. Another widely used technique is magnetic force microscopy (MFM) [257]. The setup is similar to an atomic force microscope, but the tip is magnetic and interacts with the stray field of the sample. The spatial resolution, at a few tens of nanometres, is high and allows for imaging small magnetic textures like domain walls and skyrmions. However, in addition to a good spatial resolution a high temporal resolution is also strongly desired since for potential devices not only the static but also the dynamic magnetic properties need to be understood. MFM only provides a very poor time resolution. Static spin-polarized scanning tunnel microscopy (SP-STM) can resolve even atoms [317], while systems with picosecond time resolution so far sacrifice the very high spatial resolution [67, 281]. If high spatial and temporal resolution are required simultaneously for magnetic imaging, one in general needs to apply for costly beamtimes at larger synchrotron facilities and employ techniques such as scanning transmission x-ray microscopy (STXM) [131] or photoemission electron microscopy (PEEM) [276]. Here the magnetization dynamics can be investigated directly with a temporal resolution of about 50 ps. One specific advantage of x-ray microscopy is the sensitivity to selected elements by tuning the wavelength to specific absorption edges. Electron microscopy offers an alternative technique with high spatial and temporal resolution for magnetic imaging in the laboratory. Lorentz transmission electron microscopy (LTEM) [41, 82, 240] can resolve magnetic features down to 10 nm and has a time resolution of 700 fs. The disadvantage of transmission experiments like STXM or LTEM is the difficult sample fabrication using growth on membranes or thinning techniques. On the other hand, these techniques can be used for 3-dimensional imaging using holography or tomography [64, 65, 186]. Another electron microscopy technique is scanning electron microscopy with polarization analysis (SEMPA) or spin-SEM, which is the tool employed throughout this thesis. Beside the good spatial resolution in the nanometre range, conventional SEMPA offers simultaneous 2-dimensional vector imaging of the magnetization.

2.6.2 Conventional SEMPA

Scanning electron microscopy with polarization analysis (SEMPA, alternatively spin-SEM) was proposed by T. H. DiStefano in 1978 [63] and J. Unguris *et al.* in 1982 [292] and first realized by Koike *et al.* in 1984 [147]. Reviews of this technique have been written by K. Koike [146] and the other early pioneers M. R. Scheinfein [250] and R. Allenspach [9]. It is an SEM-based magnetic imaging technique, which relies on the detection of the polarization of secondary electrons emitted from the sample. Compared to many other high-resolution imaging techniques such as PEEM and STXM it is laboratory-based. The spatial resolution is below 30 nm and for some systems a spatial resolution down to 3 nm has been demonstrated [146]. In contrast to Lorentz microscopy, SEMPA is not a transmission mode imaging technique. SEMPA is just sensitive to the upper first few nanometres of the material under investigation. This is advantageous for imaging multilayer stacks of thin films but also means a very clean surface and therefore

a careful sample preparation is required. SEMPA is a rather slow imaging technique. In particular the low efficiency of the spin detector is primarily responsible for the long beam exposure needed with SEMPA imaging. While research efforts have been made to improve the efficiency of the spin detector by looking for new spin-filter materials and detector designs, we have developed and investigated a software-based approach to improve the measurement efficiency for certain types of measurements with temporally modulated magnetization. A further drawback of SEMPA until recently was the missing possibility for time-resolved imaging. Very recently, another group presented a method allowing for dynamic measurements using microchannel plate electron multipliers [89]. In the course of the project we developed together with the new detection scheme a setup that is able to acquire magnetic images with a high temporal resolution of $< 2\,\mathrm{ns}$.

Spin-Polarized Secondary Electron Emission

In 1976 Chrobok and Hofmann demonstrated spin-polarized secondary electron emission from a ferromagnetic material excited by an unpolarized primary electron beam [48]. This motivated the development of a scanning electron microscope detecting the spin-polarization of the secondary electrons. First we will describe secondary electron emission in a metal and then explain the spin polarization of secondary electrons emitted from a 3d ferromagnet such as iron, cobalt or nickel.

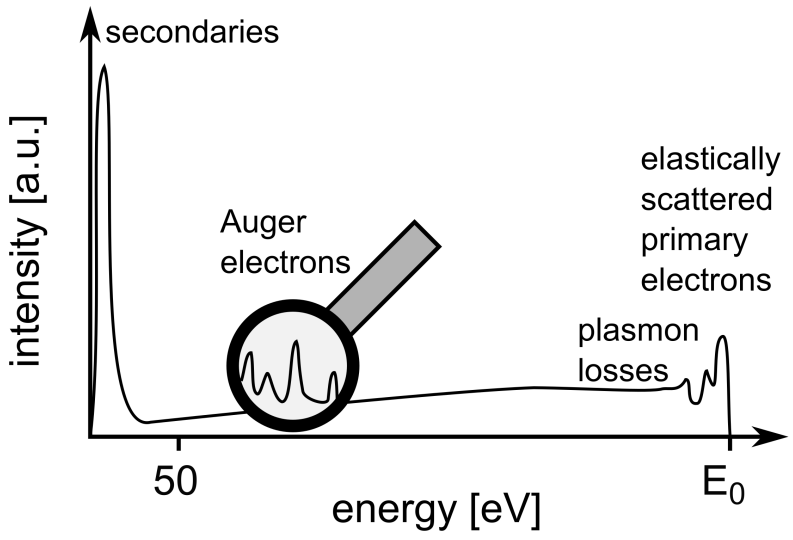

Figure 2.6: Intensity spectrum of electrons emitted from a surface that is bombarded with electrons of a primary energy E_0. The magnified peaks correspond to Auger processes. The spin-polarized electrons used for SEMPA imaging are the secondaries below 50 eV.

Incident electrons transfer energy to valence electrons, which are then excited to unfilled states in the conduction band. Different processes can occur [211, 292]: Firstly

the primary electron can be elastically scattered back. In the intensity spectrum of all detected electrons, as shown in Fig. 2.6, these electrons can be found at the high energy end of the spectrum. Next to it is the signal of inelastically scattered electrons with low plasmon losses (collective longitudinal charge-density waves of excited conduction or valence electrons). Small local maxima in the spectrum correspond to Auger processes at different energies. A maximum at low energies below 50 eV corresponds to the secondary electrons. Their intensity is so high because of the cascade process of multiple inelastic scattering events. Consider a high-energetic primary electron releasing an inner-shell bound electron into the continuum as a so-called secondary electron, as shown in Fig. 2.7a). This electron can initiate another cascade scatter process or leave the material directly. Another bound electron can then relax from a higher energy state into the vacant position and transmit the released energy to an Auger electron. The backscattered primary electrons, the released secondary electrons and the excited Auger electrons can again scatter before they are emitted into the vacuum or become thermalized. This generates an avalanche of low energy secondary electrons resulting in the high intensity peak at low energies in the spectrum.

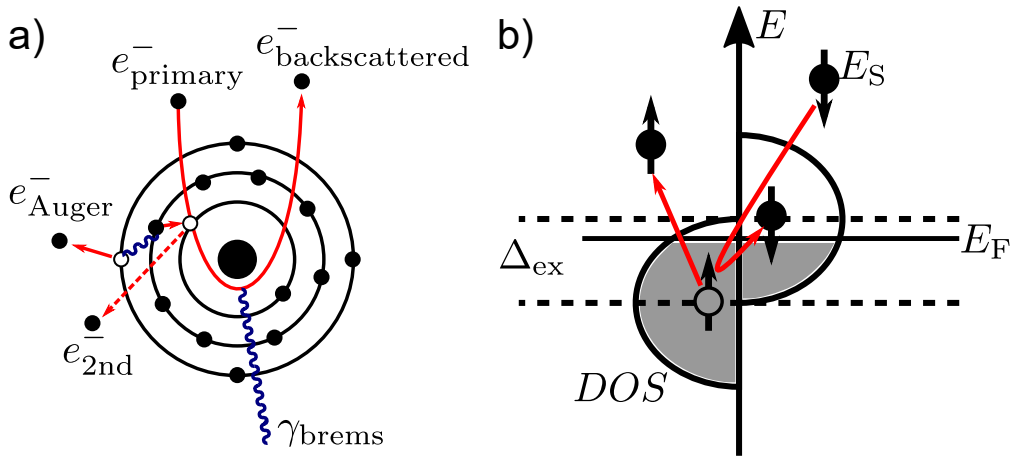

Figure 2.7: a) Interaction of a primary electron e^-_{primary} with an atom leading to secondary electron emission e^-_{2nd}, the subsequent emission of an Auger electron e^-_{Auger} and backscattered electrons alongside the emission of bremsstrahlung γ_{brems}. **b)** Stoner excitation in a ferromagnet resulting in the enhancement of the spin polarization for low energy secondary electrons.

Now let us consider the case of an itinerant ferromagnet following Ref. [211]. It was found that the polarization of the secondary electrons is enhanced at low energies below 30 eV. Above this value it approximates asymptotically the average d-band polarization [136]. The highest spin polarization values for low energy secondary electrons were measured for iron, followed by cobalt and then nickel [114, 137]. The high spin polarization and the simultaneous high intensity at low energies is advantageous for measurements. The

origin of the spin polarization is explained by considering the spin-dependent density of states of ferromagnets shown schematically in Fig. 2.7b). A minority electron with an energy E_S that is above the Fermi energy E_F scatters elastically with a d-band majority electron of the ferromagnet. After the scattering process the released majority electron has almost the initial energy of the incoming minority electron. Meanwhile this minority electron is now located in the d-band with an energy just above E_F and forms an electron-hole pair with the generated hole in the majority band. This process looks like an inelastic scattering process with an energy loss $E_S - \Delta$ and associated spin-flip if the incoming and released electrons are considered only. In a ferromagnet the described process is more probable than the opposite one emitting a minority electron due to the exchange splitting of the d-bands at E_F. In this Stoner excitation process the spin reversal is always accompanied with a loss of energy, which explains the increasing spin polarization of the secondary electrons with decreasing energy. The average energy loss equals the exchange splitting of the d-bands Δ_{ex} [136]. Another model was presented by Schönhense and Siegmann [252] who relate the enhancement of the spin polarization of the low energy cascade electrons to the number of holes in the d-bands and the corresponding spin-dependent mean free path in ferromagnetic materials. This model is even able to describe the mean free path of low energy electrons in nonmagnetic transition metals by a general correlation of the cross section of low energy electrons to the number of holes in the d-bands.

Spin Polarization Detection

While scanning electron microscopy is a widely used technique in the scientific community, the spin detector is more exotic since it requires a UHV SEM. Different types of detectors have been suggested. The first SEMPA system used a Mott detector [147]. Here the secondary electrons are accelerated by a high voltage of 20-100 kV and scatter at the nucleus of an atom of a heavy-metal foil target such as gold. The spin-orbit interaction leads to a backscattering of the polarized electrons under an angle of $\pm 60°$ with respect to the incident electrons which depends on the electron spin polarization. To shield the high voltages the Mott detector must be quite bulky. Two other detectors using lower voltages were proposed afterwards. The low-energy diffuse scattering (LEDS) detector [249] employs diffuse scattering of low energy electrons of 150 eV from evaporated polycrystalline gold targets. The detector used in our SEMPA system is based on low-energy electron diffraction (LEED) [87]. Here the target is a W(001) single crystal where the electrons are scattered with different probabilities depending on their spin orientation in different directions, as indicated in Fig. 2.9a). The diffracted electrons in the four (2, 0) LEED beams are counted and based on that the asymmetry components $A_{x,y}$ calculated, which is related to the in-plane magnetization at the sample surface:

$$A_{x,y} = \frac{\dot{N}_{\rightarrow,\uparrow} - \dot{N}_{\leftarrow,\downarrow}}{\dot{N}_{\rightarrow,\uparrow} + \dot{N}_{\leftarrow,\uparrow,\downarrow}}, \tag{2.3}$$

where $\dot{N}_{\rightarrow,\leftarrow,\uparrow,\downarrow}$ is the number of electrons scattered to the particular direction in a certain time. The sensitivity S can be given in analogy to the Sherman function determined

for Mott detectors [129]. If a monochromatic incoming beam with 100% spin polarization would be detected by the detector, the measured asymmetry would be S. For Mott and LEED detectors S is around 25% while the sensitivity for a LEDS detector is lower at approximately 11% [211]. However, the efficiency of a detector is not only determined by the sensitivity, but also by the reflectivity R of the detector material. The statistical error of the polarization measurement in a discrete electron counting experiment is given by

$$\Delta P = \frac{1}{\sqrt{NS^2}}. \tag{2.4}$$

The number of counted electrons N depends on the reflectivity R. Therefore the figure of merit as a measure of the detector efficiency is calculated as the product $2RS^2$. This value is around 10^{-4} for the above mentioned detector systems and compared to a conventional SEM very low since the reflectivity is just about 0.1% for the W(001)-based LEED detector [88]. This results in very long acquisition times for a reasonable signal-to-noise ratio (SNR), requiring stable conditions of the detector and sample. A drawback of the LEED detector is the surface contamination over time [172]. For a pressure of 10^{-10} mbar the detector operation is maintained for roughly one hour. After this time the tungsten crystal has to be flash-heated to remove adsorbents from the tungsten crystal surface. Various cleaning protocols are pre-set and can be selected at the control rack [172, 323]. After a system venting and bakeout a longer flash cycle of approximately 30 min is used to clean the crystal. In between the measurements, every few hours, a short heating of about 30 s up to 2300 K removes tungsten oxides from the crystal. Recent detector developments based also on the LEED principle, but using a Au-passivated Ir(001) crystal [153, 304] or an oxygen passivated Fe film grown on a W crystal [5, 77] demonstrated progress concerning the issue of detector stability as well as efficiency. With a modification of the electron optics even the third polarization component is accessible [49, 145], paving the way for the investigation of out-of plane magnetized materials. The spin-polarized LEED detector was optimized thoroughly for the application with SEMPA [88] and the best working conditions were found under a scattering energy of 102.5 eV. Our detector is equipped with the Channeltron electron multipliers from Photonis. This signal is fed into a discriminator that transforms the pulses to low-voltage (2.5 Vpp) transistor-transistor logic (TTL) pulses with a pulse width of 100 ns that can be counted by conventional electronic pulse counters. Typical count rates per channel are between 0.5 and 2 million counts per second. The pulse width determines the dead time of the counter that results in an underestimation of the true counts for statistically generated pulses with a high average frequency, as is the case for typical SEMPA measurements [258]. Other systems use multichannel plates [87, 89]. These do not degenerate quickly, in contrast to the Channeltron multipliers which have a very limited lifetime and need to be replaced approximately every 1.5 years if the system is used on a daily basis.

The SEMPA UHV System

The SEMPA measurements presented in this thesis were performed in a commercial UHV system from Omicron (today Scienta Omicron GmbH) consisting of two main UHV chambers. A photograph of our system is shown in Fig. 2.8. The UHV system is pumped by a turbo pump, three ion pumps and two titanium sublimation pumps. The base pressure is in the range of 10^{-11} mbar. The samples are loaded *via* a small load lock chamber into the preparation chamber, where the sample can be milled with energetic Ar ions between 0.6 kV and 5 kV to remove the oxide layer and restore the magnetic contrast. During milling the sample current is measured and there is also the possibility to monitor the resistance of the sample for contacted samples. Furthermore the chamber is equipped with three thermal evaporation cells. This allows deposition of a thin mirror layer of cobalt or iron to enhance the magnetic contrast [303]. Another use could be for capping measured samples with gold to prevent oxidation if the sample should be taken out from the chamber for further investigation at a different setup. After the preparation the sample is transferred to the investigation chamber. There up to 12 samples can be stored. An attached magnetization stage allows one to magnetize the sample in the out-of-the-plane as well as transverse in-plane direction with a magnetic field of > 100 mT by applying a current through an electromagnetic coil.

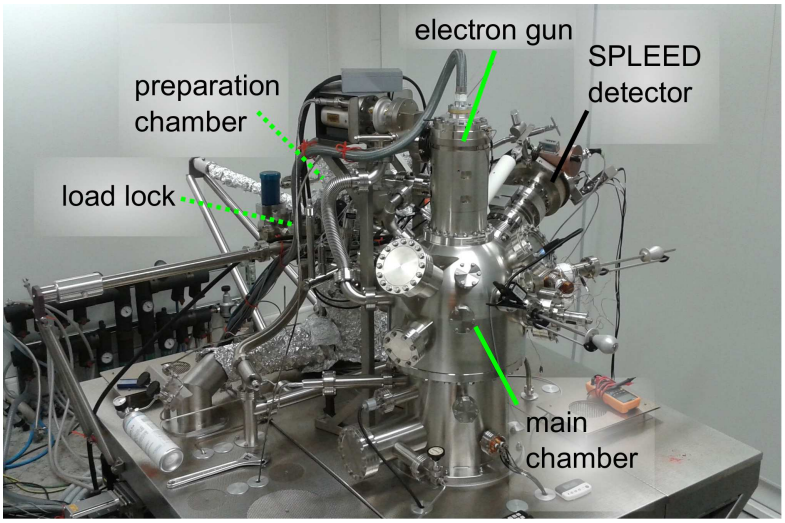

Figure 2.8: Photography of the SEMPA system in Mainz with the main investigation chamber in the forefront and the preparation chamber in the background.

The rotatable main stage is just below the electron gun. The stage is equipped with a Helium flow cryostat and a sample heater. Sample temperatures between 30 K and several hundred degrees centigrade can be reached. The sample stage can be tilted by 60° to align the sample plane with the plane of the tungsten crystal in the spin detector. The sample stage can be moved in x, y and z direction with a piezo-driver. 4 contacts can be

used to apply currents to the sample. During the work on the setup we have changed the wiring of the stage to allow for high frequency pulses as will be described later. The UHV Gemini electron column is based on a conventional Zeiss Gemini system [122] and uses the same electron optics, but modified materials and sealing techniques to allow baking up to 180°C. The electrons are emitted by a tungsten thermal field emitter (1800 K), which is coated with Zirconium oxide to achieve a lower work function and a defined tip radius. The beam is then focused by the electron optics onto a small spot of the sample surface. Due to the above-mentioned low sensitivity of the detector a high beam current is needed to excite as many secondary electrons as possible. Our system operates in general with an aperture of 90 µm and a beam current of 3 nA. The typical spatial resolution of our system is approximately 20 nm [232]. The EHT voltage can be varied by the user, depending on the requirements for spatial resolution. Typical values are between 3 keV and 15 keV. Lower primary beam energies down to below 1 keV in general provide higher yield of secondary electrons, at the expense of spatial resolution [148]. The electron column part of the chamber is pumped by an additional vibration free ion pump and can be separated from the rest of the chamber volume for maintenance purposes by a column valve. The spin-polarized LEED detector, which is described in more detail above, is attached under an angle of 60° with respect to the electron gun. For imaging the sample is usually tilted to be parallel to the detector plane, *i.e.* to the tungsten crystal. In our system the detector is rotatable around its mounting axis, which allows one to select the magnetization axis for the sample under investigation.

SEMPA Imaging Example

Here we present two examples of SEMPA imaging and explain the post-processing leading to the colour-coded magnetization vector maps. Fig. 2.9a) shows a schematic representation of the SEMPA experiment. The primary unpolarized beam scans the field of view (FOV), the secondary electrons are collected by the LEED detector and diffracted at the W(001) crystal towards the channeltron electron multipliers depending on the beam polarization, while inelastically scattered electrons and secondaries from the tungsten crystal are repelled by retarding grids. The spin polarization of the released secondary electrons has the opposite sign compared to the sample magnetization. Summing up all four detector counts during the acquisition time results in the 'sum' or 'topography' image. The asymmetry components are calculated as described by Equation 2.3 and shown in Fig. 2.9b) for a 4×3 µm $Ni_{80}Fe_{20}$ rectangle. The $A_{x,y}$ values of each pixel are plotted in a scatter plot (Fig. 2.9c)). In this case we know the magnetization is oriented fully in-plane and there are four clearly separated domains with distinguishable magnetization direction. First the centres of the point clouds are determined after k–means clustering the points (indicated by crosses) [171]. Next an ellipse is fitted to these centre points. In the ideal case it should be a perfect circle without distortion placed symmetrically around the origin. However, in general there are detector imbalances due to geometrical misalignments, unequal detection efficiencies of opposing electron counters and misalignments in the electron optics that need to be corrected. After correcting for those imbalances the angular position of the pixels in the scatter plot can be encoded by

a circular colour-map covering the angular range from 0° till 360°. For the calculation of a reliable colour-map the in-plane component of the magnetization must be constant over the whole area. Furthermore, the covered angular spectrum of magnetization directions in the sample needs to be sufficiently large to allow for fitting an ellipse to the asymmetry values. If there is not such a clear domain pattern as that in the shown rectangle, for example in a magnetic disk exhibiting a continuous vortex magnetic structure, all points in the scatter plot have to be considered for the ellipse fit.

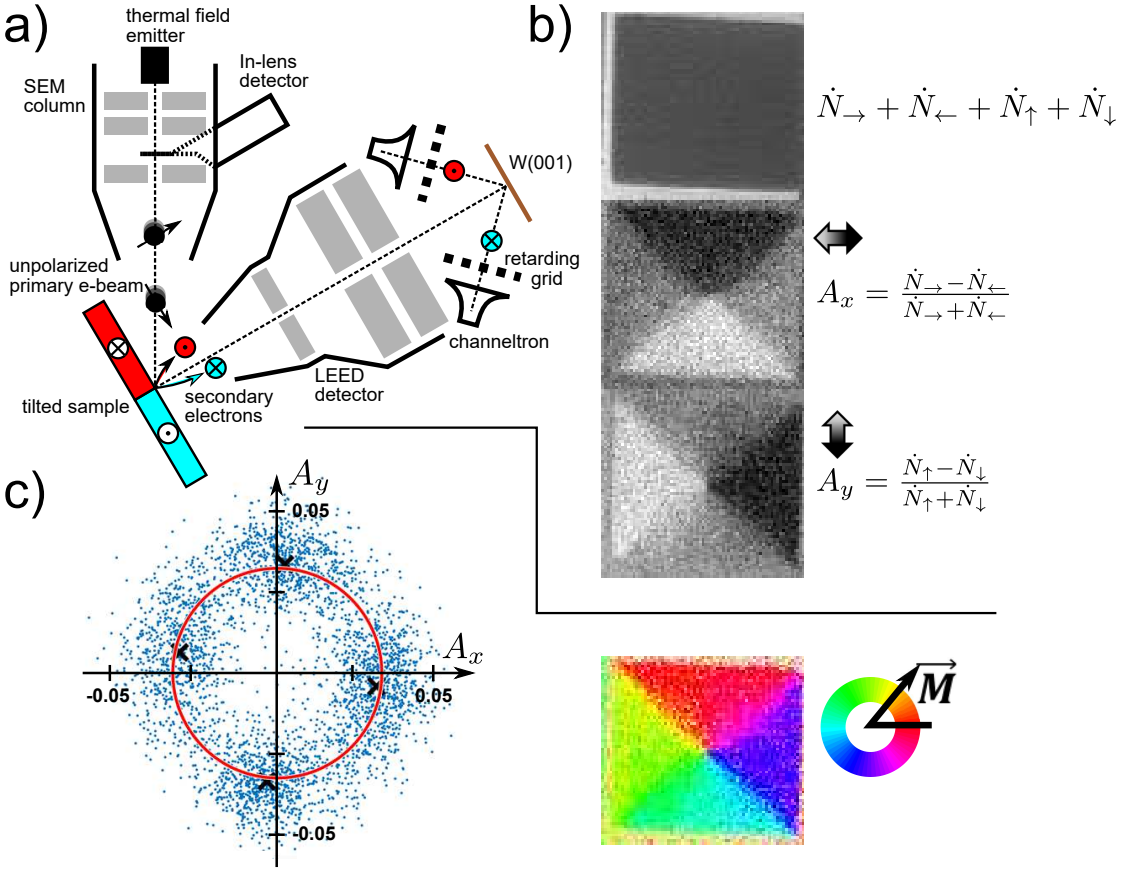

Figure 2.9: **a)** Schematic drawing of the SEMPA imaging principle (description see text). **b)** SEMPA images of a $4 \times 3\,\mu m$ $Ni_{80}Fe_{20}$ rectangle: The topographic sum image is calculated by adding the counts of all four channels during the acquisition time. The asymmetry values $A_{x,y}$ are related to the local in-plane magnetization. **c)** The colour-coded in-plane magnetization image is obtained by plotting all $A_{x,y}$ pairs for every pixel from the magnetic area in a scatter plot, fitting an ellipse to it and correcting for detector imbalances.

SEMPA is not only able to determine the magnetization direction but also allows for a comparison of the spin polarization of different materials at the sample surface. The absolute value of the asymmetry $\sqrt{A_x^2 + A_y^2}$ equals the radius of the resulting circle

fit and is approximately proportional to the spin polarization generated by the spin splitting of the d-bands if the magnetization is oriented in the plane. If materials with a low spin polarization are investigated one can deposit a very thin mirror layer of iron on top of the sample in-situ [303]. Iron has the highest spin polarization among the itinerant 3d ferromagnets. In Fig. 2.10 the contrast enhancement by a thin Fe layer of 0.5 nm on $Ni_{80}Fe_{20}$ (30 nm) is demonstrated. Before the first measurement the sample was prepared by Argon ion milling to remove the oxide layer. After the first imaging, the sample was transferred back into the preparation chamber and 0.5 nm of Fe were evaporated thermally on top. The signal increase can already be noticed from the asymmetry images by the naked eye. The difference is even clearer visible in the scatter plot: The point clouds corresponding to the domains are more separated due to the higher spin polarization of Fe. With the Fe layer the measured asymmetry is almost 6% while it is only about 3% without it. If the Fe layer does not modify the magnetic properties of the sample as is seen to be the case here, this method is well suited to reduce measurement time and increase the image quality. The high surface sensitivity of SEMPA is advantageous here.

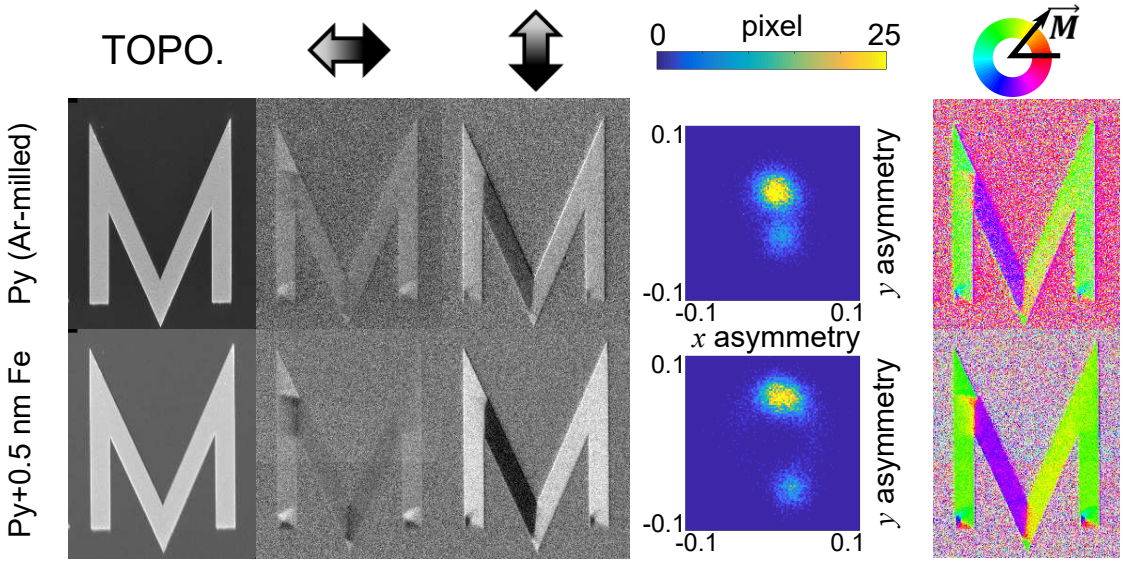

Figure 2.10: Contrast gain by in-situ deposited Fe mirror layer. Both acquisitions used the same settings (7.5 kV, $t_{\mathrm{dwell}} = 2.5\,\mathrm{ms}$). The greyscale asymmetry images have the same contrast settings and the enhancement of the SNR by the 0.5 nm Fe is clearly visible. The measured asymmetry is larger with the Fe dust layer (approx. 6%) compared to the pure Py structure (asymmetry approx. 3.5%) and thus the point clouds in the scatter plot are more separated due to the higher spin polarization of Fe compared to Ni.

3 Time-Resolved SEMPA

Magnetic imaging is a very informative tool in the investigation of magnetic materials. The possibility of time-resolved imaging greatly extends the range of information that can be obtained. However, typical processes in ferromagnetic dynamics occur in the GHz frequency range. This requires a temporal resolution on the order of nanoseconds or lower. So far most SEMPA have been employed for static imaging. For imaging with high spatial and temporal resolution mainly synchrotron-based X-ray imaging has been used. The lab-based SEMPA technique would be more attractive if its application area could be extended by the possibility of time-resolved imaging and other imaging modes. We set out to develop a new time-resolved SEMPA system by modification and addition of hardware and software components. We further extend the time-resolved imaging modes with a phase-sensitive detection (PSD) scheme to extract excitation-correlated changes in the signal. This technique is in particular of interest if the expected signal is very small. The time-to-digital converter (TDC) and the associated C++ software were provided by Surface Concept GmbH. My contributions were the coordination of the project, the adaptation of the LabVIEW measurement program and the interface to the TDC software as well as the hardware modifications of the stage. We first describe the hardware modifications, then the software, and finally we discuss the different possible imaging modes providing an estimate of the temporal resolution and the efficiency of the PSD mode.

3.1 Hardware Modifications

The new acquisition types allowing for the investigation of magnetization dynamics require hardware changes. First the electrical connection of the sample had to be modified to be compatible with fast current pulses. Second the incorporation of a the time-to-digital converter (TDC) to the system is the core hardware upgrade that makes time-resolved imaging and phase-sensitive detection possible.

High Frequency Sample Connections

To fully exploit the capabilities of our new measurement scheme with nanosecond time resolution the cabling to the sample had to be high frequency compatible. With the commercial stage, pulses with short rise and fall times in the nanosecond regime were distorted. To improve this, first the original single-ended BNC feedthroughs were replaced by two-side SMA feedthroughs. Then the cables within the chamber were also exchanged. For application in SEMPA several requirements had to be fulfilled for the cabling in addition to the high frequency suitability (50 Ohm impedance matching):

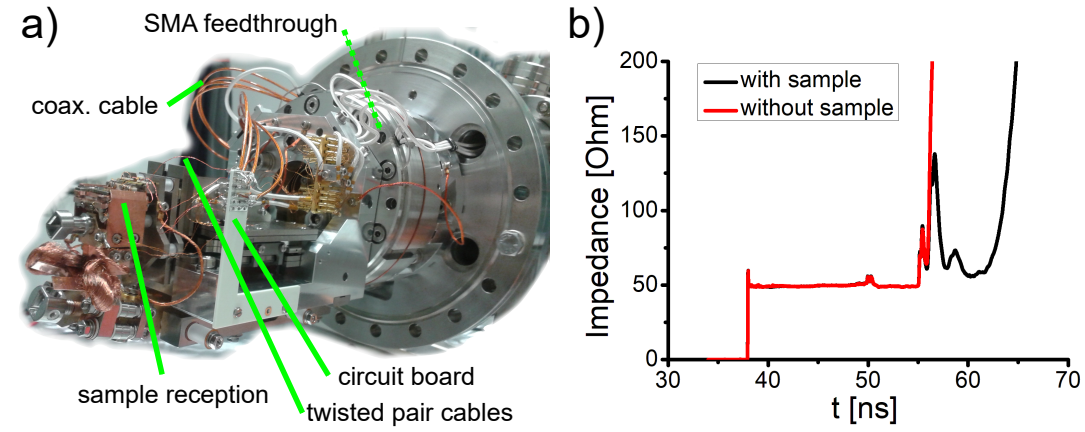

Figure 3.1: a) Photograph of the sample stage. The original cabling was replaced by highly flexible coaxial cables from the SMA feedthrough to a circuit board. The spring contacts at the sample reception are connected *via* twisted pair cables with the circuit board. **b)** Electrical characterization using time-domain reflectometry.

The material must be ultrahigh vacuum compatible, *i.e.* it must not outgas and support bake-out temperatures $\geq 150\,^{\circ}\mathrm{C}$. The permissible current has to be higher than 100 mA and the cable must be very flexible to allow the rotation of the sample stage. The best fitting coaxial cable was found to be the Allectra 311-KAP50S-RAD, a high flexibility multi strand cable with a total diameter of 1.47 mm (inner diameter 0.24 mm). It is Kapton insulated, allows 0.5 A maximum current and a maximum temperature of 300 °C. Nevertheless this coaxial cable is still too stiff to directly fix the end at the front of the sample reception since the position of this part of the stage is driven by a piezo motor. The motion would be affected and even limited by the tension of the cables. The developed solution provides a compromise between high-frequency compatibility and flexibility: A small circuit board was mounted at one side of the sample stage, the coaxial cable soldered to it using lead free solder and from there a very thin (diameter 0.1 mm) twisted pair cable goes to the sample reception, allowing free motion of the front part of the stage. The small circuit board is a Rogers 4350B (1.55 mm, 35 µm Cu) board, which is UHV compatible since it is fabricated without a solder mask and thereby has a lead free surface. The material is also bakeable, but it is not oxygen-resistant above 105 °C. This is no problem, since baking of the system is anyway started after prepumping to 10^{-6} mbar because of the sensitivity of the channeltron electron multipliers in the SPLEED detector. The entire soldering process of the cables to the circuit board is kept at or below the 4350B glass transition temperature of 280 °C [98]. The shield of the coaxial cables must have a connection at the circuit board to have good high frequency performance. A picture of the modified sample stage is shown in Fig. 3.1a). The electric circuit was characterized by time-domain reflectometry (TDR). This method enables one to localize reflection sources that reduce the quality of high frequency waveform

transmission. In Fig. 3.1b) two TDR curves are shown, the first one with a sample plate in the sample reception and two contacts on the sample plate connected and a second one without a sample plate. In the latter case the impedance diverges at 56 ns due to this open circuit. The peak just before corresponds to the change from the coaxial cable to the twisted pair at the circuit board. The hump due to the SMA feedthrough is comparably low. The main limiting factor remains the electrical connection of the sample to the sample reception, as visible in the first curve. In the current design it is realized as springs sliding onto contact pads on the sample holder. Further increases in performance would need to start with improving this sample connection by using high frequency contacts such as coaxial SMC ('SubMiniature version C') pins [238].

The Time-to-Digital Converter

The core part of the additional setup is the time-to-digital converter (TDC). It detects the delay of the detector pulses with respect to a synchronization pulse and thereby enables dynamic measurements. The TDC is integrated in the SEMPA measurement setup as shown in Fig. 3.2. The interfaces with the other components of the setup are discussed below.
The device is based on the model SC-TDC-1000/08 S from Surface Concept GmbH and is customized for our particular requirements. Inside the TDC chip GPX from ACAM [6] is installed. A sophisticated control-, start- and streaming-logic is built in with a field programmable gate array (FPGA), which has a high-speed USB 3.0 interface to connect to a computer. A schematic layout of the TDC is shown in Fig. 3.3.
The TDC allows for simultaneous time measurements on 8 different 'stop' channels with a time resolution of 82.3 ps and a thermal stability of < 10 fs/K. The dead time of a single stop input is 5.5 ns, *i.e.* two subsequent pulses must be separated by this time in order that both are detected properly. A schematic layout of the device is shown in Fig. 3.3. The 'stop' signals are fed into the TDC chip and the synchronization with the excitation frequency is put into 'Ext. Start'. The highest possible 'start' frequency of the ACAM chip is 7 MHz. However an additional programmable frequency divider makes frequencies up to 100 MHz possible. All 'stop' channels provide 32-fold multi-hit capability as an input buffer, so that bursts of many pulses in short time intervals can be detected. However, the internal output registers and the maximum reading speed from the chip are a bottleneck. With those, average count rates of up to 40×10^6 pulses per second are possible, which is sufficient for 4 channels of up to 4×10^6 counts/s and possibly a fifth channel for synchronization with the excitation frequency driving the magnetic system under investigation. The arrival times of the 'stop' pulses are either detected with respect to the 'Ext. Start' input signal or the last 'stop' pulse of any of the 'stop' input channels. The acquisition dwell times for time data from the TDC are settled within the FPGA by a quartz stabilized time gate in an interval from 1 ms to 1193 h. The start and the end of the acquisition are either triggered by a software input or by sending a TTL pulse into the 'Sync. In' channel. The end of the measurement is indicated by a pulse signal at 'Sync. Out'. In the present application with SEMPA not only is temporal synchronization needed with respect to the driving excitation, but

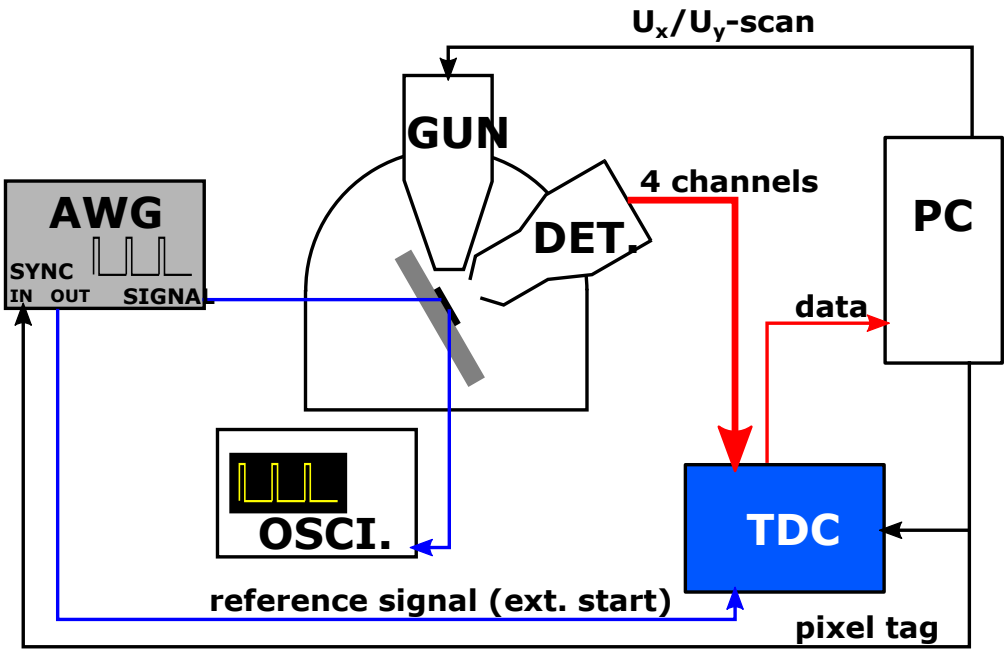

Figure 3.2: The integrated SEMPA setup: In the centre the main investigation chamber of the SEMPA UHV system is drawn schematically with the electron gun (GUN) and the LEED detector (DET.) The 4 detector signal channels are fed into the TDC where they are processed and forwarded to the computer. This image data stream is drawn in red. The control lines from the PC (black) include the deflection voltages (U_x/U_y scan) and the pixel tag provided to the TDC and if desired also to the arbitrary waveform generator (AWG). The AWG generates the excitation pulse, which is monitored by an oscilloscope (OSCI.) (Reprinted with permission from [253].).

the signal must be also affiliated to the correct x and y pixel position in the scan of the FOV. To this end, a pulse that is synchronous to a change in the deflection voltage of the primary electron beam is fed into the 'Tag' input. This signal triggers an internal up-counter, which reinitializes the number of counts to zero at the start of each acquisition block. A TDC-internal FIFO (first-in-first-out) buffer guarantees a high reliability of data transfer with a data loss probability of less than 0.01%. The software is described in the next section.

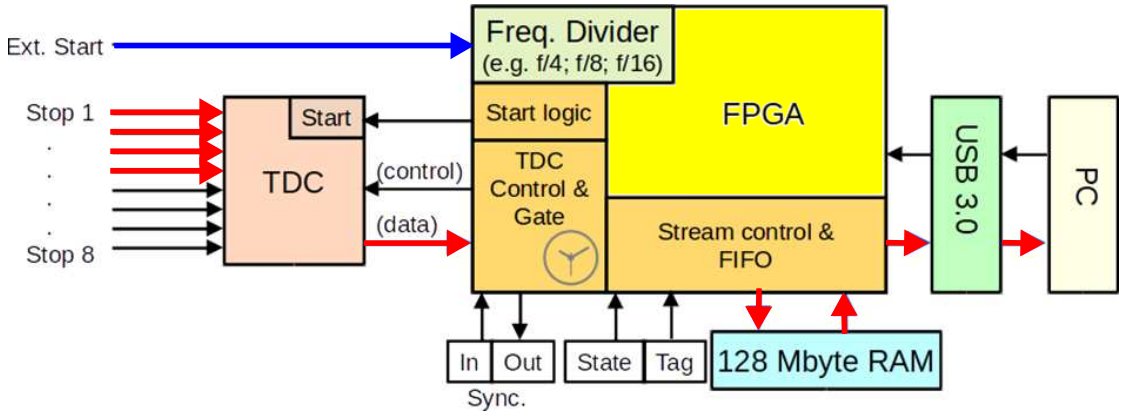

Figure 3.3: Components and data flow in the TDC. The left block represents the ACAM TDC chip GPX with the stop inputs where the counts measured by the detector are fed into and the start input detecting the reference frequency. The yellow block in the centre represents the control-, start- and streaming logic handling the data flow (red) and pre-processing the excitation reference signal (blue) before transferring it to the ACAM chip. For our application 'In' and 'Out' synchronization as well as the 'State' channel are not used. The 'Tag' input synchronizes the TDC with the pixel clock of the electron column. (Reprinted with permission from [253].)

3.2 Control Software and Interfaces

The electron column is controlled with the commercial SmartSEM software using a Windows XP computer. Here the beam is switched on/off, the beam is focused on the sample and the magnification can be set based on the image obtained with a conventional in-lens SEM detector. From this computer SEMPA measurements can also be started with commercial software based on ImageJ. However, this program is not very flexible as it, for example, does not allow to change the aspect ratio. To allow for more customized acquisitions a second computer with a data acquisition (DAQ) card (National Instruments PCIe 6343) was installed in the lab that can also control the experimental setup *via* a LabVIEW control software. A first version of this software had the task of the electron beam and spin detector control and direct read-out of the four detector channels. The scanning of the FOV by the electron beam is realized by increasing the deflection voltage stepwise *via* an external scan control. Two analogue voltage outputs of the PCIe card are used for the x and y direction. The counter channels of the card were used as input for the LEED detector signals, postprocessed and stored as sum and asymmetry images from the LabVIEW program. The communication with the detector control to switch the channeltron voltages on and off is realized with a GPIB interface. To allow for time-resolved imaging, in the newly developed experimental setup the detector counts are not directly fed into the DAQ card and read-out by the LabVIEW program, but are handled by the TDC, streamed to the computer *via* USB 3.0 and processed by C++ software.

The LabVIEW code then calls the C++ dynamic link library (DLL) and reads only the data that is set in the C code for display in the graphical user interface on the LabVIEW front panel - typically the first time frame of the movie. The DLL provides the data storage. One counter channel of the DAQ card is now used as an output, sending pulses synchronized to the changes in the e-beam deflection voltage to the 'Tag' input of the TDC. If only static measurements need to be done, this signal can also be split using a fan-out box and can serve as the 'Ext. Start'. The additional amount of data that needs to be handled requires the use of LabVIEW in the 64-bit version instead of the 32-bit version. In the following part we want to describe the functionality and the various measurement options possible with the new software. After focussing the beam and moving to a desired FOV on the sample by using the piezo position control of the stage, a quick square overview image is acquired. Then a region of interest (ROI) of arbitrary shape can be selected. Various possibilities are provided by the vision development module from LabVIEW including rectangles, circles, annuli and free-hand regions. This new feature can reduce significantly the acquisition time for certain geometries, which is of high interest for this slow imaging technique. Subsequently the user changes from the 'Config. Capture' tab to the 'Capture' tab, where it is possible to specify the spatial resolution and the pixel dwell time by setting the scan frequency. An additional feature compared to the commercial software is the multi-scan option, allowing for a specified number of subsequent faster scans of the selected ROI to avoid distortions in the image due to thermal drift of the sample, which is in particular important for very small structures, materials with low magnetic contrast and therefore long acquisition times or measurements at elevated or reduced temperatures when it can take a long time for the system to fully thermalize. To avoid the object of interest moving out of the ROI, a drift correction was implemented into LabVIEW based on the pattern recognition modules provided by the vision development module from LabVIEW. The first scan is used as a reference image and if for a subsequent scan the position of the selected object has changed, the deflection voltages controlling the scan position of the e-beam are adapted corresponding to the position change. The statistical noise is proportional to the square root of the pixel dwell time and in turn the number of scans in the multi-scan mode. The possible settings for time-resolved imaging are given in the respective sections below where the operation of the new acquisition modes is described and tested. The development of the new system is also reported in our publication [253] and part of this chapter is published there.

3.3 Imaging Modes

With the development of the SEMPA setup three different imaging modes based on time-resolved imaging are possible. In this section these imaging modes are described. We also determine the temporal resolution of the system and demonstrate the signal-to-noise ratio enhancement in the phase-sensitive detection mode.

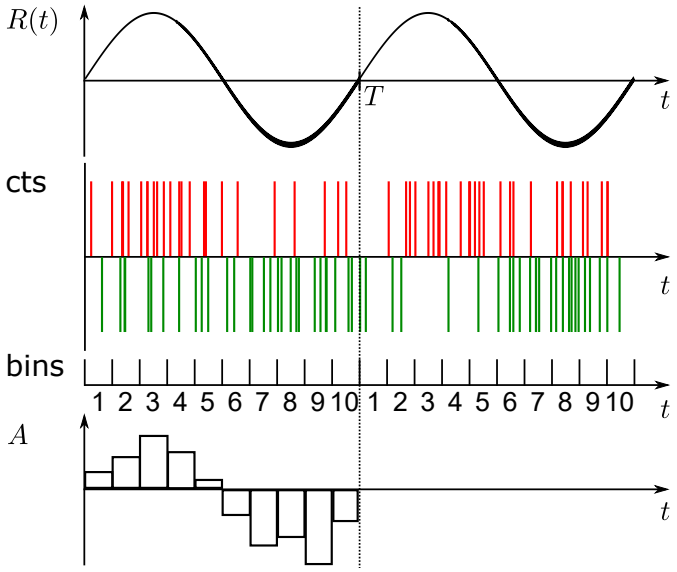

Figure 3.4: A schematic explanation of the time-resolved measurement principle: The upper graph shows a sinusoidal excitation signal $R(t)$ with a period length T_A. In the second line the pulses generated in two opposing channeltrons in the spin detector are shown (red and green). For this measurement the number of time frames n_f is set to be 10, which are equally distributed over T_A. The asymmetry $A_{x,y}$ is calculated from all the counts during all periods during the pixel dwell time. (Reprinted with permission from [253].)

3.3.1 Full-Period Time-Resolved Imaging

This acquisition mode images the magnetization dynamics during the full excitation period. While in conventional pump-probe techniques only the detector signal of a short defined time interval within the period is processed at once and then the delay needs to be changed, we image simultaneously all time frames while the beam is located at a certain position on the sample. If the dwell time per pixel is longer than the period length, the counts of equivalent time intervals are summed up. The net acquisition time scales, therefore, with the number of time frames n_f dividing the period length in n_f time intervals, which can be specified by the user. A schematic drawing illustrating the measurement principle is shown in Fig. 3.4.
The arrival time of detector counts with respect to the excitation signal is detected by the TDC and the signal is affiliated with the corresponding time interval of the n_f time frames. Typically the dwell time on a pixel exceeds the period length of the excitation, so first the counts of each channel and each time bin are added and then the asymmetry values for the pixel are calculated considering the counts during all excitation cycles at this beam position. The excitation of the sample can lead to significant shifts of the FOV due to field-induced deflections of the primary electron beam. This is corrected in the postprocessing step using an autocorrelation plugin based on the software ImageJ [287].

Considering the technical capabilities of the TDC, t_f can be increased until the time bin length reaches the minimal limit of 82.3 ps. However, the overall time resolution is not limited by the TDC but by the jitter in the electron optics. The time-resolved SEMPA of the Hamburg group was shown to have a temporal resolution of 700 ps [89]. In contrast to this SEMPA system our detector is equipped with channeltrons instead of multichannel plates. This is expected to have an impact on the time resolution. We determined the overall time resolution of our system with the same method as it is presented in [89]. To this end the edge of a rectangular $Ni_{80}Fe_{20}$ test structure with a size of $4 \times 3\,\mu m^2$ on a stripline was first imaged using conventional SEMPA imaging. Then the resolution under the current settings was determined in the sum image by fitting a Gaussian error function to the edge of the rectangle and determining its width $2\sigma_0$ as shown in the upper image of Fig. 3.5a). During a subsequent time-resolved SEMPA measurement of the same structure a sinusoidal current of 120 MHz was driven through the stripline leading to an oscillation shift of the FOV mainly parallel to the stripline axis. The number of frames during an excitation cycle was set to be $n_\mathrm{f} = 50$. The absolute field-induced shift was determined by cross-correlating the frames. The x and y displacement is shown in Fig. 3.5b). The edge blurring was also determined in the image frame where the displacement velocity of $v(t) = 201 \pm 13\,\frac{\mathrm{m}}{\mathrm{s}}$ due to the field was the highest (lower image of Fig. 3.5a)). The measured blurred width of the edge during the excitation can be expressed mathematically as the Euclidean sum of the resolution $2\sigma_0$ and the blurring due to the motion $2\sigma_t v(t)$, where $2\sigma_t$ denotes the time resolution:

$$2\sigma(t) = \sqrt{(2\sigma_0)^2 + (2\sigma_t v(t))^2}. \tag{3.1}$$

The measured widths are $2\sigma_0 = 45 \pm 30$ nm and $2\sigma(t) = 370 \pm 60$ nm. From this the time resolution can be calculated to be $2\sigma_t = 1.8 \pm 0.4$ ns. As expected the jitter in the channeltrons results in a slightly worse temporal resolution compared to multichannel plates. However, it is still of the required order of magnitude to image typical dynamic processes like nucleation and motion of magnetic domain walls thereby intensely expanding the applicability of SEMPA.

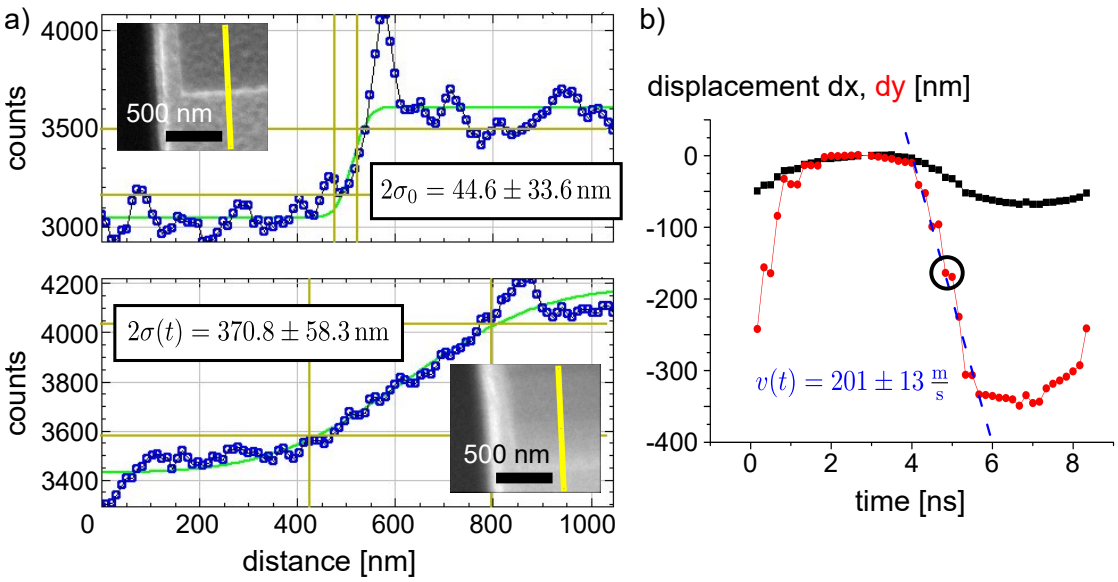

Figure 3.5: Determination of the overall time resolution of our SEMPA system. **a)** Determination of the apparent edge width in a static SEMPA sum image without excitation ($2\sigma_0$), upper image and graph) and during 120 MHz sinusoidal excitation ($2\sigma(t)$) in the movie frame corresponding to the highest velocity $v(t)$ measured (indicated by the circle in b)). Field-induced **b)** x and y displacement of the rectangle edge. The blue linear fit was used to determine the velocity $v(t) = 201 \pm 13\,\frac{\mathrm{m}}{\mathrm{s}}$.

We demonstrate full period time-resolved imaging using a test sample of a magnetic $Ni_{80}Fe_{20}$ disk with a thickness of 30 nm and a diameter of 4.3 µm placed on a copper stripline. The thickness of the stripline was 120 nm plus 5 nm Au capping. By applying a sinusoidal current through the stripline with a frequency of 48 MHz, an oscillating Oersted field with 0.5 mT amplitude was generated at the position of the disk. The magnetic ground state in a disk of this size is a vortex [152] where the magnetization is aligned with the edges to minimize the stray-field energy and in the centre points out of the plane. This so-called vortex core is displaced to minimize the Zeeman energy if an external field is applied. We imaged the vortex oscillation using the presented measurement scheme with the number of time frames being $n_\mathrm{f} = 10$. Every second frame of the x asymmetry component is shown in Fig. 3.6a). The estimated resonance frequency for this geometry is between 45 and 67 MHz [301]. From the plot of the vortex core position in Fig. 3.6 we see the motion is off-resonant since mainly the y position is changing due to the field while the x position is rather stable.

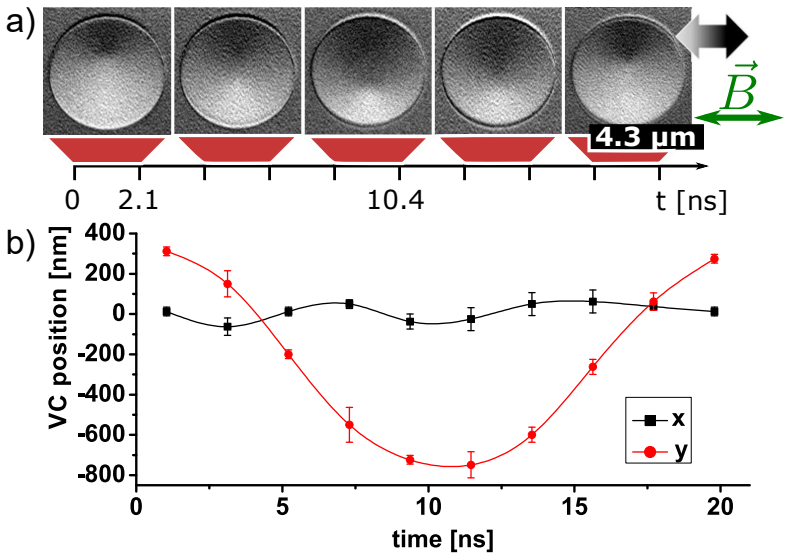

Figure 3.6: a) Full period time-resolved SEMPA imaging of a 4.3 µm permalloy disk during an oscillating magnetic field of 48 MHz. Each of the shown x component asymmetry image frames covers a time interval of 2.1 ns. The arrow indicates the magnetization direction. **b)** The relative x and y position of the off-resonant vortex core (VC) oscillation. (Reprinted with permission from [253].)

The overall acquisition time including the scan time and the processing of the data, *i.e.* saving all time frames for each scan and correction of the beam deflection voltages after determining the image drift, was 211 minutes. Roughly half of the time was used for processing since in this case the synchronization pulse was fed into a fifth stop input of the TDC. If for this purpose the 'Ext. Start' input is used, the processing of the computer can be significantly reduced.

3.3.2 Selected Time-Window Imaging

A second imaging mode allows to set the delay time and the width of the time window. Up to four such time windows can be defined. In contrast to the above-described imaging mode these intervals can have different lengths and can also overlap. We demonstrate the functionality of this mode by imaging permalloy rectangles with a width of 4 µm and different aspect ratios during a rectangular excitation that switches the field direction at a frequency of 50 kHz. A schematic plot of the excitation is shown in Fig. 3.7a), where the two time windows are indicated by red and green colour. The current through the stripline induces an Oersted field of 1.25 mT perpendicular to the stripline axis. The sample geometry as well as the magnetic contrast SEMPA images are shown in Fig. 3.7b). The magnetization direction in the two larger rectangles reverses if the current is reversed to minimize the Zeeman energy. For the narrowest rectangle the stray-field contribution to the free energy is still dominant for the used field strength because of the higher shape

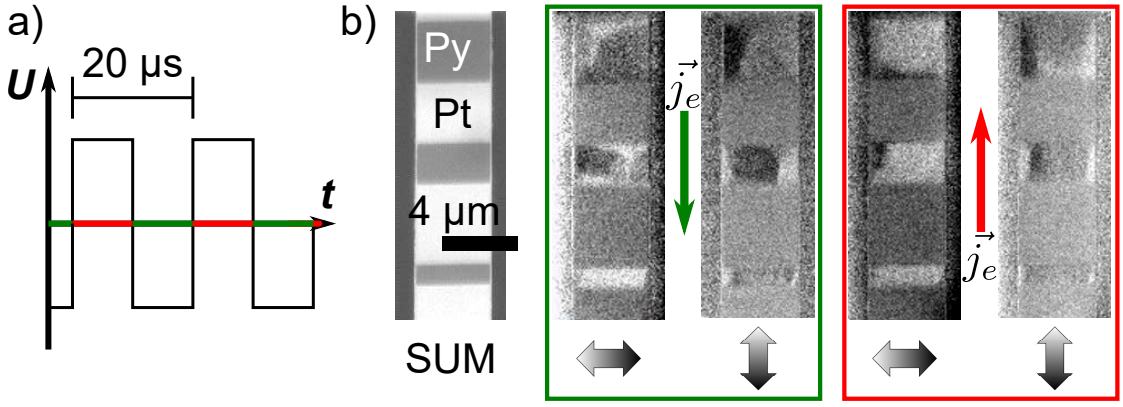

Figure 3.7: **a)** Schematic drawing of the rectangular excitation pattern with a frequency of 50 kHz. The two user-defined time windows are indicated by the colours red and green. **b)** At the left a SEMPA sum image of the sample is shown. Three Py rectangles of 10 nm thickness with different sizes are placed on a Pt(10 nm) stripline. The green and red framed images show the x and y components of the SEMPA asymmetry images during the two defined time intervals within the excitation with opposite applied field direction.

anisotropy, which hinders switching.
The presented measurement used a rather low-frequency excitation. If the frequency is increased the time window needs to be placed very carefully considering runtime delays of the pulses in the cables. To determine these phase shifts between the excitation and detection, a full-period time resolved movie of the structure is acquired. From the field-induced displacement the delays can be calculated.

3.3.3 Phase-Sensitive Detection

As described above, the main drawback of SEMPA is the low efficiency of the spin detector. Several new designs of detectors have been presented recently [77, 153]. In connection with the development of the new SEMPA system we have implemented and tested a software-based approach that can increase the SNR for certain types of measurements. This phase-sensitive detection (PSD) method is similar in its functionality to a lock-in amplifier [335]. The general working principle of the lock-in technique is shown for continuous functions in Fig. 3.8. This technique can be applied if the response $A(t)$ of the device under test (DUT) has the same frequency as the excitation and it acts to filter out unwanted noise of other frequencies, thereby enhancing the SNR. The oscillating signal excites the DUT - in our case the magnetization of the sample. The measured response is then mixed by multiplication with the reference signal $R(t)$, which equals the normalized excitation waveform. Fig. 3.8 demonstrates that if the frequencies of excitation and response coincide, the resulting signal (magenta) has twice the frequency $\omega_A + \omega_R$. However, if the frequencies differ even slightly, as shown in the right plot in Fig. 3.8b), the resulting high frequency is modulated by a lower frequency

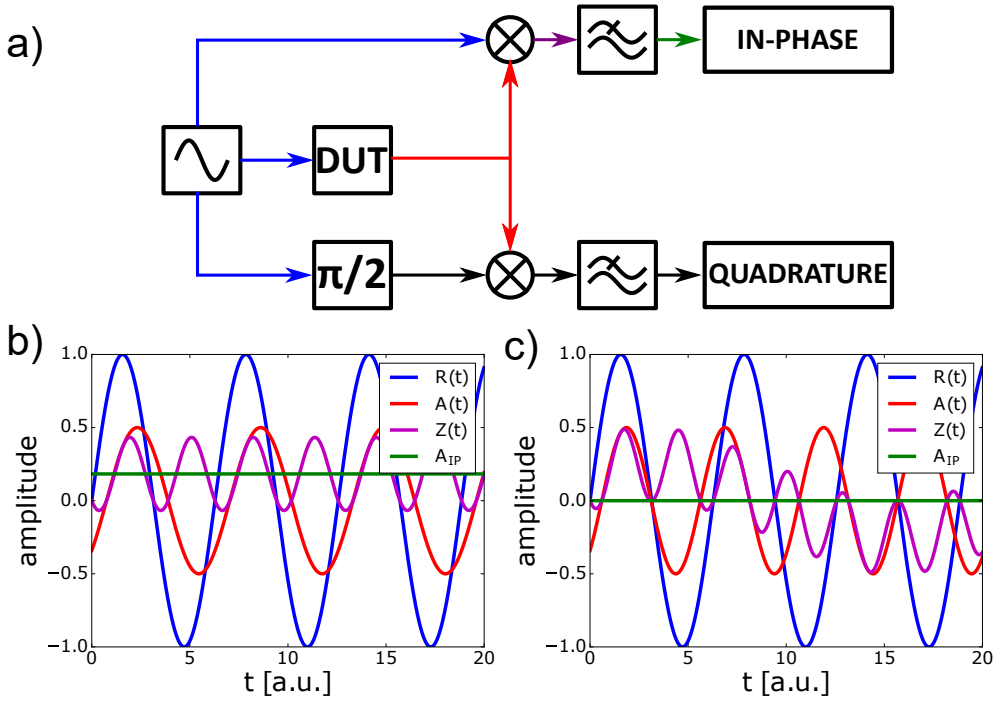

Figure 3.8: a) Processing steps in phase sensitive detection. In the first step the reference signal $R(t)$ (blue) is mixed in-phase and also 90° phase-shifted with the response $A(t)$ of the device under test (DUT). The resulting signal is then filtered, removing high-frequency components. **b)** The filter effect for unwanted frequencies is demonstrated for the in-phase component. In the plot at the left side $\omega_A = \omega_R$, while in the right one $\omega_A \neq \omega_R$. The resulting A_{IP} value is indicated by the green line.

$\omega_A - \omega_R$. In the next step a low-pass filter is applied which can be in the simplest case just an averaging over the period. For more complex low-pass filters like digital RC, Chebychev or Butterworth [311] it is important to take into account sufficient periods due to the settling time. The resulting in-phase component A_{IP} is a finite number which is not equal to zero if there is a frequency component of the response signal that has the same frequency as the excitation and reference signal. The quadrature component A_{Q} is obtained similarly in this dual-phase down-mixing approach by just using the reference signal with a phase shift of 90°.
In our case the phase sensitive detection has to work with discrete data in terms of the electron counts. The reference period T_R is split into n_{f} time bins with a length τ. The bth bin therefore starts at the time $t_b = \tau(b-1)$. After mixing the time-dependent asymmetry values $A(t_b)$ with the total complex reference signal $R_{\mathrm{tot}}(t_b) \approx \exp(-i\omega_R t_b)$

the oscillating in-phase $A_{\mathrm{IP}}(t_b)$ and quadrature $A_{\mathrm{Q}}(t_b)$ components are given by:

$$A_{\mathrm{IP}}(t_b) = A(t_b) \times \sin(\frac{b-0.5}{n_{\mathrm{f}}} \times 2\pi), \tag{3.2}$$

$$A_{\mathrm{Q}}(t_b) = A(t_b) \times \cos(\frac{b-0.5}{n_{\mathrm{f}}} \times 2\pi). \tag{3.3}$$

The dual-phase complex mixing results in terms with the sum and the difference of the frequencies ω_R and ω_A:

$$Z_{\mathrm{tot}}(t_b) = A(t_b) \times R_{\mathrm{tot}}(t_b) = A(\exp(i(\omega_A - \omega_R)t_b) + \exp(i(\omega_A + \omega_R)t_b)). \tag{3.4}$$

As described above and demonstrated in Fig. 3.8, the first term becomes constant. The second one can be filtered out by averaging or more advanced low-pass filtering methods. Following the first mentioned approach as described in [38], the complex value of Z_{tot} is obtained by calculating

$$Z_{\mathrm{tot}} = A_{\mathrm{IP}} + iA_{\mathrm{Q}} = \frac{2}{n_{\mathrm{f}}}(\sum_{b=1}^{n_{\mathrm{f}}} A_{\mathrm{IP}}(t_b) + i\sum_{b=1}^{n_{\mathrm{f}}} A_{\mathrm{Q}}(t_b)). \tag{3.5}$$

The final output of the phase-sensitive processing is the amplitude

$$|Z_{\mathrm{tot}}| = \sqrt{A_{\mathrm{IP}}^2 + A_{\mathrm{Q}}^2}, \tag{3.6}$$

and the phase corresponding to the phase shift of the asymmetry signal compared to the reference

$$\theta = \arctan(\frac{A_{\mathrm{Q}}}{A_{\mathrm{IP}}}). \tag{3.7}$$

In our case the set of time-dependent asymmetry values of each pixel has to be processed in this way.

First we apply the phase-sensitive detection algorithm to the shift-corrected raw data of the full period time-resolved measurement of the magnetic disk shown in Fig. 3.6. While the raw data is time resolved, the final amplitude and phase images are not. These are shown in Fig. 3.9 ('AMPL.' and 'PHASE'). In the amplitude image the highest intensities are found in the centre of the magnetic disk and at the upper and lower edges of the disk. However, the reason for this increased contrast is different. First we consider the centre region of the disk. The vortex core position oscillates with the frequency of the excitation signal so that in the centre the magnetization direction oscillates too. This signal is detected by the above described algorithm and extracted. The areas where the magnetization direction does not change are dark. The increased intensity of the edges is an artefact due to the imperfect shift-correction. The shift is mainly in the y direction, as we have seen in Fig. 3.5, and thus the signal is increased in particular at the upper and lower edges of the disk. The right image in Fig. 3.9 shows the phase correlation of the amplitude signal for every pixel. The phase image is colour-coded. If there is no correlation, neighbouring pixels have on average very different colours while for an area

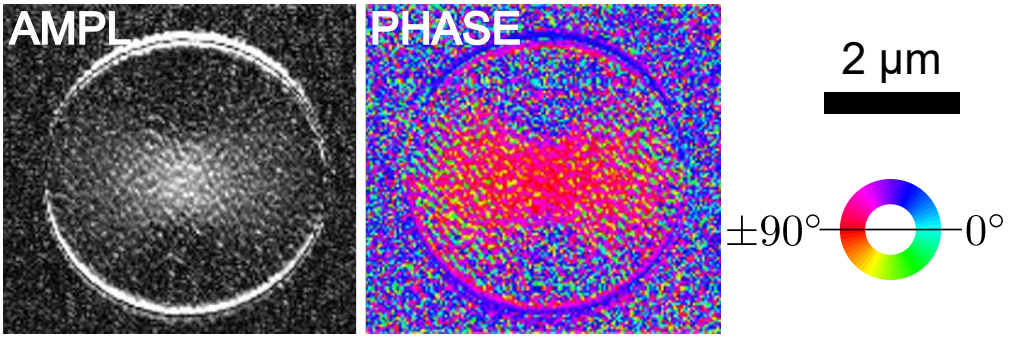

Figure 3.9: Resulting amplitude and phase images of the time-resolved vortex core motion movie of a magnetic disk processed using the phase-sensitive detection technique. In the amplitude image bright pixel values indicate a high amplitude. The phase image is colour-coded. (Reprinted with permission from [253].)

with strong correlation the colour in neighbouring pixels is very similar. The absolute value of the phase has to be considered with caution since runtime delays can lead to an artificial phase shift.
A more quantitative test of this detection method was performed using a test sample consisting of a $1 \times 10\,\mu\text{m}$ permalloy rectangle on top of a stripline and aligned along the stripline axis. If a current is flowing through the stripline, an Oersted field perpendicular to the long axis of the rectangle is generated, as shown in the schematic drawing in Fig. 3.10a). To minimize the stray field energy the magnetization in the rectangle is oriented along its long axis. The Oersted field results in a tilt of the magnetization. Fig. 3.10b) presents static SEMPA asymmetry images confirming the alignment of the magnetization along the long axis of the Py rectangle when no current is applied. The next SEMPA acquisition is performed while a DC current of 30 mA is flowing through the stripline (Fig. 3.10c)). The contrast change in the x component due to the field-induced tilt of the magnetization is not recognizable with the naked eye. Remarkably, the contrast on the y asymmetry is reduced. A possible reason could have been the modified sample potential. The low voltages around $U \approx 1\,\text{V}$ should not affect the spin-sensitivity of the detector significantly [88] but for samples with a high resistance this effect must be considered. The detected count rates during the acquisition without an applied current and $I = 30\,\text{mA}$ do not deviate strongly either. The images in Fig. 3.10d) show the amplitude and phase images calculated for a full period time-resolved acquisition of the x and y asymmetry during a sinusoidal excitation with $I_{\text{max}} = 30\,\text{mA}$ and 10 kHz. The period length was sampled with $n_{\text{f}} = 32$ time bins. The scan frequency was 10 pixel/s, resulting in a total acquisition time of about 20 min. The x component amplitude image shows as expected a high intensity for pixels in the magnetic rectangle, indicating a strong response of the magnetization to the excitation. Since the y component of the magnetization does not oscillate with the same frequency, the pixels in the y-amplitude are dark. The high correlation of the magnetization oriented transversely to the rectangle

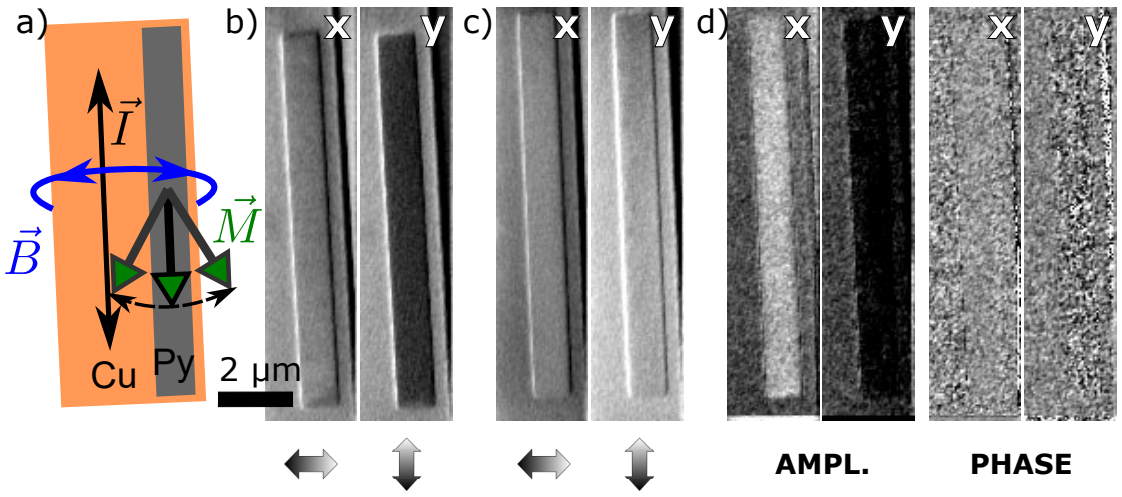

Figure 3.10: Quantitative determination of SNR improvement using phase-sensitive detection. **a)** Schematic drawing of the stripline with the permalloy rectangle. The current generates an Oersted field that tilts the magnetization in the rectangle away from the easy axis. **b)** Static SEMPA asymmetry images without current flowing through the stripline, confirming the magnetization orientation along the long axis of the rectangle. **c)** Repetition of the SEMPA measurement with a DC current of 30 mA. **d)** Amplitude and phase images of the x and y asymmetry. The x amplitude image in d) shows the magnetization tilt with an SNR improvement of a factor 5 better compared to the x asymmetry image in c).

main axis to the driving signal is confirmed by the reduced noise level in the area of the Py rectangle in the x-phase image. In the phase image based on the y asymmetry SEMPA data the noise is even increased in this area, indicating a predominant response at a distinct frequency. This will be discussed in more details further below. First we determine the gain in SNR. The signal is defined as the difference between the mean value of the pixels of the magnetic material and the pixels of the stripline. The noise is calculated *via* the standard deviation of the pixel values. Comparing the x component phase images in Fig. 3.10c) and d), it turns out that the phase-sensitive detection approach can improve the SNR by a factor of 5. This enhancement of the SNR has been confirmed for excitation frequencies of 10, 100 and 1000 kHz. While this is still a careful assessment of the SNR enhancement, since the current during the acquisition of Fig. 3.10d) reached 30 mA only at its maximum, in contrast to the constant current of 30 mA in c), the noise reduction strongly depends on the measurement and in particular on the frequency spectrum of the noise.
In a similar experiment we investigated further the response of the magnetization in the y asymmetry component. While the x component oscillates with the excitation frequency ω_{exc}, the y component should oscillate with twice the excitation frequency $2\omega_{\mathrm{exc}}$. This is tested by applying the PSD algorithm using a reference frequency of $\omega_R = 2\omega_{\mathrm{exc}}$. To this end we image the centre region of a rectangle with the same geometry as shown in

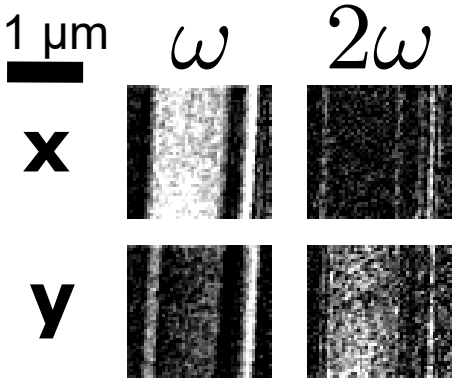

Figure 3.11: PSD amplitude images of the centre region of a $1 \times 10\,\mu$m permalloy rectangle with an excitation frequency $\omega_{\mathrm{exc}} = 5\,$kHz, comparing the results for $\omega_R = \omega_{\mathrm{exc}}$ and $\omega_R = 2\omega_{\mathrm{exc}}$. While the x component of the magnetization oscillates with the excitation frequency, the y component oscillates with twice the frequency.

Fig. 3.10, again while applying an oscillating current of 5 kHz. Fig. 3.11 shows the x and y component PSD amplitude images with the same contrast settings using $\omega_R = \omega_{\mathrm{exc}}$ and $\omega_R = 2\omega_{\mathrm{exc}}$. For $\omega_R = \omega_{\mathrm{exc}}$ the results described above are confirmed: The x component shows a high signal while the intensity of the pixels of the y component in the magnetic area is dark. This however changes if $\omega_R = 2\omega_{\mathrm{exc}}$ is used as reference frequency. Then the response at $\omega_A = \omega_{\mathrm{exc}}$ is filtered out and the asymmetry oscillations with $\omega_A = 2\omega_{\mathrm{exc}}$ are extracted. This is the reason for the higher intensity in the y amplitude.
In conclusion the new measurement schemes developed broaden the investigation possibilities of the SEMPA technique significantly. Time-resolved imaging of magnetization dynamics such as domain wall nucleation and motion with a high spatial resolution is possible in the laboratory without having to access big accelerator facilities. This technique was explored by studies on switching pathways in half ring pairs, as described in Ch. 5, and domain wall dynamics in asymmetric rings (Ch. 6). The PSD technique was employed for an attempt to image directly current-induced spin accumulation at the surface of heavy metals as described in Ch. 4. I added further minor functionalities accompanying the developments of the new SEMPA system including the multi-scan imaging mode with automatic tracing of the structure that have proved to be very useful for long time acquisitions of systems with very low magnetic contrast *e.g.* systems which are capped with a thin nonmagnetic layer for the purpose of preventing oxidation or inducing DMI.

4 Feasibility of Imaging Current-Induced Spin Accumulation with SEMPA

In spintronics spin currents are used to transport spin angular momentum and thus the generation, propagation and the detection of spin currents are all of great interest, not only for scientific reasons but also for possible applications [174]. Diffusive pure spin currents can be generated by injection from a ferromagnetinto materials with a long spin diffusion length [213]. Other possible generation methods include the spin-Hall effect [268], spin pumping [11] and the spin-Seebeck effect [290]. In this project the goal was the direct detection of spin currents in nonmagnetic metals generated by the spin-Hall effect using SEMPA imaging.

4.1 Imaging of Spin Accumulation in the Literature

Current-induced spin accumulation in non-magnetic materials can be detected using different methods. It has been measured indirectly by non-local injection into a second metal with long diffusion lengths [297, 298], by measuring the associated spin-orbit torques [170, 220] or spin-pumping experiments [195, 244]. Comparing the results of these different techniques, huge deviations in the charge-to-spin conversion efficiency for the same materials are found. The origin of these diverging results is attributed to different deposition techniques with different cleanliness and growth modes of the heavy metals [242], different experimental methods [268] and different experiment geometries and interfaces used [316]. Therefore there is a very high desire to detect the spin accumulation directly in a system without interfaces contributing to the result. One possibility is to use single metal H-shaped lateral spin valves, however this approach is confined to materials with high spin-orbit coupling and long spin diffusion lengths, which are conflicting demands [43, 187]. Another option is magnetic imaging. An overview of previous research in this field is shown in Tab. 4.1. Several attempts have been made in recent years with optical methods, but these measurements are highly debated [237, 272, 279, 302]. Current-induced heating leads to artefacts in the Kerr signal [79]. In the last years synchrotron-based X-ray imaging techniques have been successfully used to detect directly spin currents [61, 155, 166]. Here the elemental sensitivity is very useful to determine the origin of the measured signal. A disadvantage is the need of large scale accelerator facilities to perform these experiments. As well as a so far not realized proposal to use magnetic force microscopy to detect spin accumulation [223], another technique which uses spin-polarized positrons was applied to measure spin polarization directly on the surface of heavy metals [326]. The authors relate the unexpected high

signal seen with their surface sensitive technique to be a consequence of the Rashba-Edelstein effect, also called inverse spin-galvanic effect [93]. Since the surface sensitivity of SEMPA is also below the spin diffusion length of the materials of interest, it should be well suited to attempt imaging of current induced spin accumulation. So far SEMPA has been only employed without success to detect spin accumulation generated by spin injection [185]. We attempted to detect a signal of current-induced spin accumulation using conventional SEMPA and SEMPA imaging in combination with our newly developed phase-resolved detection mode which has the potential of increasing the signal-to-noise ratio, as required based on the low expected signals. Such phase sensitive detection has proved to be a key enabling factor in other optical [302] and X-ray imaging [33, 155] detection schemes of such spin accumulation.

Ref.	Generation	Detection Method	Detectable Signal	Pt	Ta	W	Fe	Cu	Al
[194]	SI	XMCD	No					$< 0.01\%$	
[185]	SI	SEMPA	No					$<1\%$ (estim. $1.4 \times 10^{-4}\,\mu_B$)	
[166]	SP	XMCD	Yes					$Cu_{75}Mn_{25}$: 0.02% ($2.5 \times 10^{-3}\,\mu_B$)	
[155]	SI	XMCD	Yes					$3 \times 10^{-5}\,\mu_B$ ($4 \times 10^{-3}\,\mu_B$)	
[326]	SHE	polarized positrons	Yes	$11 \pm 2\%$	$\alpha : -12 \pm 3\%$ $\beta : -7 \pm 2\%$	$\alpha : -6 \pm 2\%$ $\beta : -9 \pm 2\%$		0	
[302]	SHE	Kerr	Yes	1.3 mdeg (25×10^8 A/m^2)		-20 mdeg (8×10^8 A/m^2)	150 mdeg (M switch.)		<0.1 mdeg (25×10^8 A/m^2)
[237]	SHE	Kerr	No	<0.05 mdeg	<0.05 mdeg	<0.05 mdeg			
[279]	SHE	Kerr	No	<0.08 mdeg		β: <0.08 mdeg (estim. 0.1 mdeg/10^{12} A/m^2)			
[272]	SHE	Kerr	Yes	15 nrad (theory $10^{-5}\,\mu_B$)		-30 nrad			<5 nrad
[61]	SP	XMCD	Yes					$2 \times 10^{-4}\,\mu_B$	

Table 4.1: Summary of different attempts to image spin accumulation generated by spin injection (SI), the spin-Hall effect (SHE) or spin pumping (SP). Depending on the measurement technique the spin accumulation is measured in different units: In Kerr measurements the rotation angle of the polarization axis is given, XMCD-based imaging provides a percent value and theoretical calculations provide the spin polarization per atom in the units of μ_B. There is wide divergence in the size of the reported signals.

4.2 Investigated Spin-Hall Materials and Sample Overview

Three standard elemental spin-Hall materials have been investigated for the measurements: the 5d metals platinum (Pt), tungsten (W) and tantalum (Ta), which all have high spin-Hall conductivities [268]. While Pt has a positive spin-Hall angle, Ta and W have negative spin-Hall angles [282] which allows one to distinguish the spin-Hall signal from other effects like current-induced Oersted fields. Pt is especially advantageous for imaging with SEMPA because of its high secondary electron emission, while W and Ta emit much fewer secondaries [62]. The materials were deposited *via* sputtering on naturally oxidized Si substrates in our industrial Singulus Rotaris deposition system. Previously significant spin-Hall conductivities were measured in devices fabricated with the same method and in the same chamber [259], which is important to know since it was shown that different deposition techniques and conditions have a high impact on the charge to spin conversion [242, 243]. The thickness was chosen so that it exceeds clearly the spin diffusion length of the respective material to avoid a partial compensation of the spin accumulation at the sample surface: Since for Pt spin diffusion lengths between 3 nm [169] and 11 ± 3 nm [272] were measured at room temperature, the thickness of the wire was between 20 and 25 nm. The thickness of the Ta samples was 10 nm, since Ta has a spin diffusion length of only 2.7 ± 0.4 nm [169]. The samples were fabricated in a two step lithography process using a single PMMA layer to mask the deposition of the heavy metal. Before imaging, the samples were Ar^+ ion milled with 1 kV to clean the surface. The milling times and estimated final thicknesses of the spin-Hall materials are given in detail in Ch. 8.
Since the current-induced surface spin polarization in a non-magnetic conductor is expected to be homogeneous for a homogeneous current density in the wire, the sample has to be designed in a way that a reference area is given. Three different types of wire geometries were used: U-shaped, S-shaped and I-shaped wires. The sample geometry was adapted in the course of the project to elaborate the origin of the measured signal and therefore their geometry is pictured and described in more detail in the next section.

4.3 Experiment and Results

The first sample had a U-shaped geometry and a wire width of 2 µm where the two wire arms were parallel. The two arms are expected to show opposite asymmetry indicating a spin polarization perpendicular to the wire edges in the SEMPA images since the current is flowing in opposite directions. Fig. 4.1a) shows a MicroMagnum simulation of the current density distribution in the wire [3]. The left image just displays the geometry and the other images the two components of the current density. The amplitude of the spin accumulation is expected to be proportional to the current density so that the grey-scale coded simulation corresponds to the expected ideal SEMPA $A_{x,y}$ images without noise or other artefacts. From the difference of the asymmetry values between the upper and lower arm of the wire in the SEMPA A_y image it should be possible to determine the spin accumulation. The experimental imaging was performed while the

sample was cooled using the He flow cryostat to low temperatures between 20 and 40 K to avoid electro-migration of the wires due to the very high current densities. Indeed preliminary SEMPA measurements, as shown in Fig. 4.1b) for both current directions, showed contrast in the images: If the electrons flow from the top to the bottom, as in the set of SEMPA images in the first row, the upper wire in the A_y image is darker than the lower one. This reverses when the current direction is inverted. A quantitative analysis is shown in Fig. 4.1c). The difference between the mean $A_{x,y}$ values of both wire arms is plotted against the current density. The error bars plotted are given by the standard deviation of the asymmetry values in the considered ROIs. While for ΔA_y a clear trend is visible, the horizontal asymmetry component A_x does not show this trend, as expected. However, the changes in A_x are of the same size, which calls for an explanation.

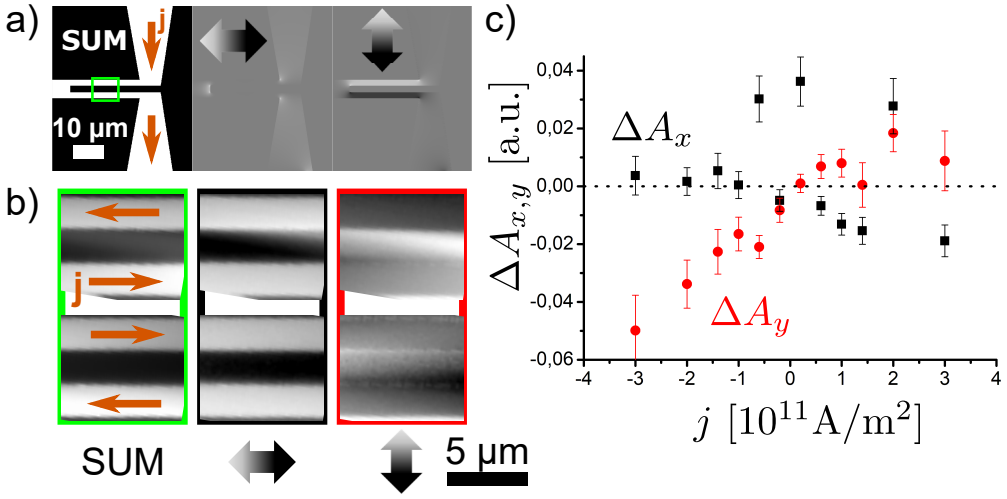

Figure 4.1: **a)** MicroMagnum simulation of current density distribution in a U-shaped Pt(25 nm) wire [3]. The current-induced spin accumulation is expected to be proportional to the current density. The left image displays the geometry, the other two images the x and y component of the expected spin accumulation amplitude. The electron flow is indicated by arrows. The grey scale corresponds to the expected SEMPA signal from a SHE signal for Pt. **b)** SEMPA images (sum, A_x, A_y; $U_{\mathrm{EHT}} = 5\,\mathrm{kV}$, $T = 33 - 34\,\mathrm{K}$, $t_{\mathrm{dwell}} = 500\,\mathrm{ms}$) of the Pt(25 nm) wire with DC current of $+/-15\,\mathrm{mA}$ applied (electron flow indicated by brown arrows). **c)** Difference between the average asymmetry values $\Delta A_{\mathrm{x,y}}$ of the upper and lower arm of the U-wire depending on the current density.

A possible verification of the signal is a comparison experiment with a spin-Hall material with negative spin-Hall angle such as Ta. For an easier identification during sample handling the Ta U-shaped wires were patterned with the bow pointing to the right. The SEM images as well as the SEMPA A_y images are shown in Fig. 4.2a) for currents of +5 mA and -5 mA. The asymmetry change in the shown images is stronger for the Ta,

but this could easily be explained by the lower thickness of the wire and the accordingly higher current density. Again the asymmetry difference ΔA_y between the upper and lower wire is plotted (Fig. 4.2b)). For a positive current the upper wires are darker in both cases, *i.e.* for Pt and Ta, but since the orientation is the opposite, also the current direction is inverted. Thus as expected the resulting slope for the Ta sample has the opposite sign compared to the Pt sample.

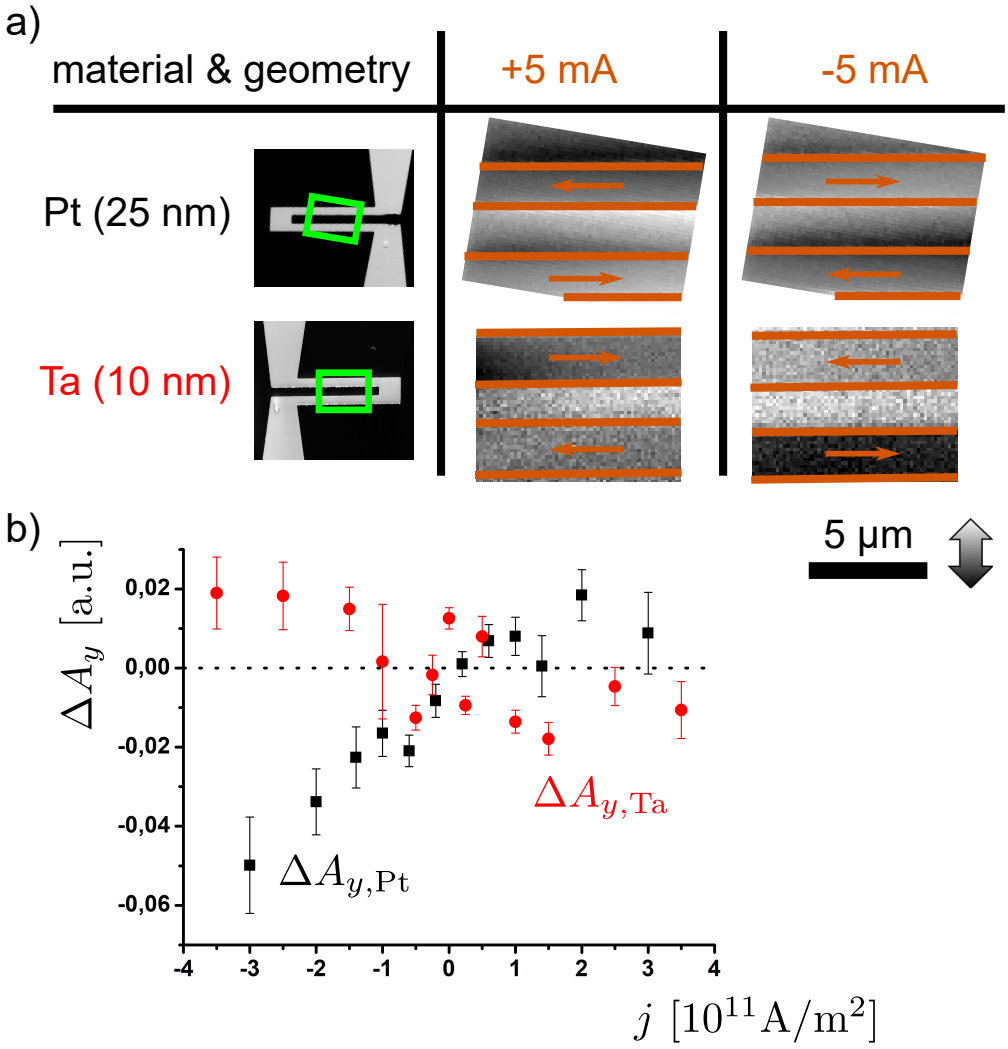

Figure 4.2: **a)** SEM of U-shaped Pt(25 nm) and Ta(10 nm) wires and SEMPA A_y images of the indicated ROI ($U_{\mathrm{EHT}} = 5\,\mathrm{kV}$, $T = 33 - 34\,\mathrm{K}$, $t_{\mathrm{dwell}} = 500\,\mathrm{ms}$). The SEMPA images are acquired during applied current in the positive and negative direction. The electron current flow is indicated by arrows and the wire edges by brown lines. **b)** Difference between the average asymmetry values ΔA_y of the upper and lower arm of the U-wire depending on the current density for Pt and Ta.

In an additional experiment we attempted to verify these results showing that the orientation of the 'U' does not influence the result. To this end, U-shaped Pt wires were patterned with both orientations, as shown in the schematic images in the left column of Fig. 4.3. In contrast to the measurements so far we used here an asymmetric driving potential resulting in a virtual ground at the wire centre to keep the potential difference between the sample and the detector close to the optimim of 102.5 V [88]. However, the sign of the measured symmetry values in the SEMPA A_y images did not invert for the differently orientated U-wires. For a positive current the upper wires of both samples appear darker and for a negative current they are brighter. The measured asymmetry therefore clearly does not result from the current-induced spin accumulation.

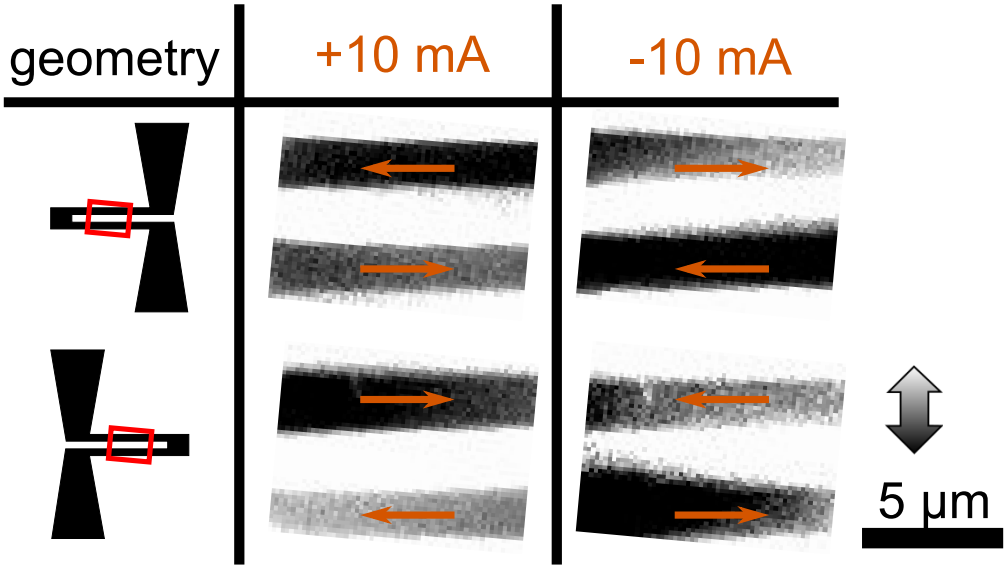

Figure 4.3: SEMPA A_y images of U-shaped Pt(20 nm) wires ($U_{\mathrm{EHT}} = 3\,kV$, $T = 22 - 23\,K$, $t_{\mathrm{dwell}} = 500\,ms$) with opposing orientation. The ROI position is indicated by the red rectangle in the left column.

To investigate the origin of this signal we fabricated new samples with an S-shaped wire geometry with a wire width of 2 µm. The expected signal in the SEMPA images was again simulated qualitatively by simulating the spatial distribution of the current density. The result is shown in Fig. 4.4a) for a current where the electrons flow from the top to the bottom. The parallel wire arms alternate between bright and dark in the A_x image. In Fig. 4.4b) the corresponding SEMPA images are presented with the current flowing in the same direction. Obviously the asymmetry A_x does not alternate in the wire arms, but rather changes gradually along the wire. In this example this gradual change is clearly visible even in the sum and A_y image. Thus the origin of the so far measured signal is to be found in the electric potential variation along the wire. Depending on the potential, the reflectivity of the detector changes causing a gradient

in the sum image. The artificial asymmetry in both components might be the result of the non-constant asymmetry function of the SPLEED detector, which varies slightly with the scattering potential [88].

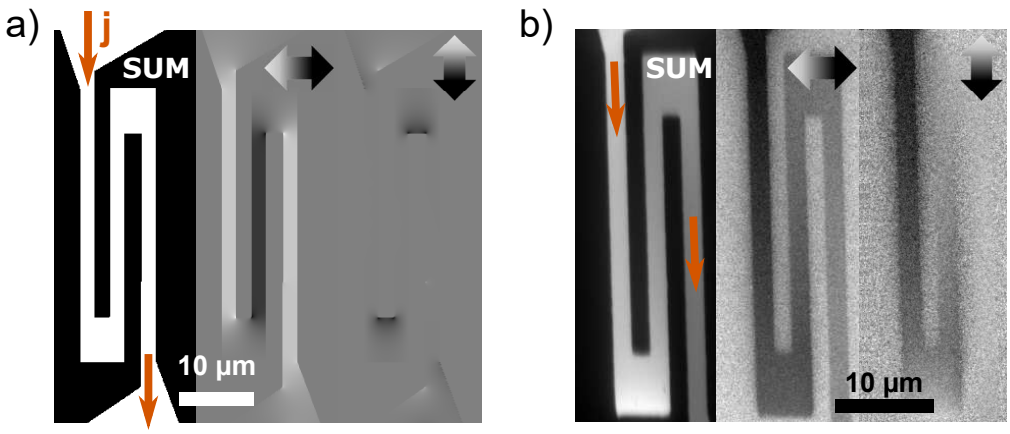

Figure 4.4: **a)** Simulation of current density distribution in an s-shaped Pt wire using MicroMagnum [3] The spin accumulation is expected to be proportional to this. The left image displays the geometry, the right images the x and y component of the current density. The electron flow is indicated by arrows. The grey scale corresponds to the expected SEMPA signal from a SHE signal for Pt. **b)** Experimental SEMPA images (sum, A_x, A_y; $U_{\mathrm{EHT}} = 3\,\mathrm{kV}$, $T = 24\,\mathrm{K}$, $t_{\mathrm{dwell}} \approx 4\,\mathrm{ms}$) of a Pt(20 nm) wire with a current of $+14.5\,\mathrm{mA}$. The asymmetry changes gradually along the wire in the A_x and the A_y images.

To demonstrate unambigously the dependence on the sample potential the imaging was repeated with a Cu sample of the same geometry and a thickness of 25 nm. The spin-Hall angle of Cu is negligible [268] and therefore no spin accumulation signal is expected. Without an applied current the measured asymmetry along the Cu wire is constant, as shown in Fig. 4.5a). However, with an applied DC current of $\pm 14\,\mathrm{mA}$ and again using an asymmetric driving voltage of $\pm 1.3\,\mathrm{V}$ ($\Delta V = 2.6\,\mathrm{V}$), a clear gradient of the contrast in particular in the A_y component is visible. Due to the lower resistivity of Cu the potential gradient along the wire is smaller than for Pt, but the effect is still detectable.

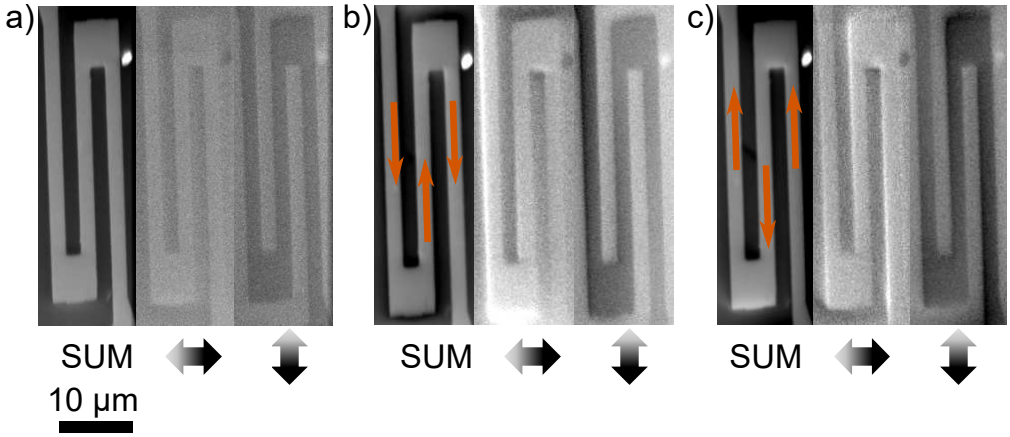

Figure 4.5: SEMPA images (sum, A_x, A_y; $U_{\mathrm{EHT}} = 3\,\mathrm{kV}$, $T = 23\,\mathrm{K}$, $t_{\mathrm{dwell}} \approx 6\,\mathrm{ms}$) of an s-shaped Cu(25 nm) wire **a)** without applied current, **b)** with applied current of +14 mA and **c)** -14 mA. In this case an asymmetric potential is applied The electron flow direction is indicated by arrows. While the grey value is constant in A_x and A_y along the wire length in a), with an applied current the grey value changes along the wire and the gradient reverses with reversing the current direction.

Summing up the results obtained with the U- and S-shaped samples so far, it is clear that the signal due to the electric potential is much larger than a possible signal of the spin accumulation. Ideally the resistance of the sample should be as low as possible to minimize the required driving voltage and reduce this unwanted effect. To this end, a third sample geometry was tested consisting of a simple short wire ('I-shape') so that long meandering wires with higher resistance were avoided. While in the U- and S-shaped sample the contrast was determined by comparing the signal in the two wire arms with opposite current direction, we used in this geometry a reference pad of the same material just beside the wire, as shown in Fig. 4.6a). The reference pad was grounded explicitly to avoid charging or any unspecified floating potential. The Pt wire had a nominal width of 500 nm and a thickness of 20 nm. At a temperature of 23 K the resistance was about 90 Ω. Again a constant asymmetric driving potential was applied resulting in a DC current of 4 mA corresponding to a current density of $j_{\mathrm{c}} \approx 4 \cdot 10^{11}\,\mathrm{A/m^2}$. The A_x images for positive and negative currents are shown in Fig. 4.6b). In addition, profile plots along the wire and crossing the reference pad and the wire are shown. The average A_x value of the reference pad is set to zero (black horizontal line in the plot). For both current directions the asymmetry in the wire is lower than in the reference pad and no significant difference between the two current directions was observed. However, in contrast to the measurements so far, no gradient is seen along the wire (orange profile plot in Fig. 4.6b)). Therefore we must conclude that conventional SEMPA imaging is not sensitive to the possibly small enhancement of spin polarization due to the spin-Hall effect and/ or the inverse spin-galvanic effect.

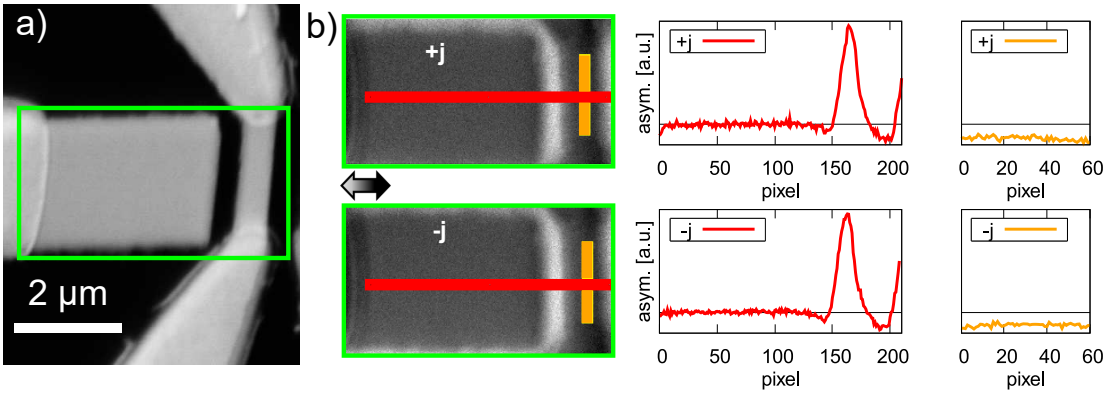

Figure 4.6: **a)** SEM image of the I-shaped sample geometry with grounded reference pad of the same material (Pt(20 nm)) at the left. **b)** Experimental A_x SEMPA images ($U_{\mathrm{EHT}} = 7.5\,\mathrm{kV}$, $T = 23\,\mathrm{K}$, $t_{\mathrm{dwell}} \approx 70\,\mathrm{ms}$) of the Pt wire and reference pad with a current of $\pm 4\,\mathrm{mA}$. Again an asymmetric driving potential with a virtual ground was used. At the right profile plots across and along the Pt wire are shown. The lines are indicated in the A_x images.

Finally, we employ the newly developed phase-sensitive detection (PSD) method which offers enhanced signal-to-noise ratio due to noise suppression to image spin accumulation in an I-shaped Pt wire, as shown in Fig. 4.8a). Before imaging the sample was milled with Ar^+ ions of 1 kV for 15 min to prepare a clean surface. The imaging and PSD analysis technique is described in detail in Ch. 3 and was successfully tested using ferromagnetic systems. Here we use an AC excitation of a fixed frequency and detect changes in the asymmetry that are correlated to the excitation by filtering out components of the signal that have not the same frequency as the excitation. Fig. 4.7 shows a schematic drawing of the electrical circuit.

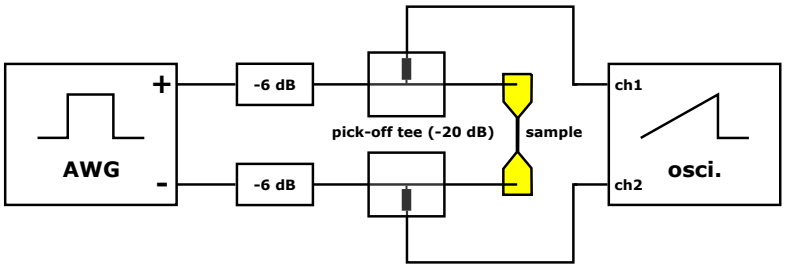

Figure 4.7: Schematic drawing of the electrical circuit used for the phase-sensitive approach to image directly spin accumulation using SEMPA. The arbitrary waveform generator (AWG) provides the differential signal, the attenuators (-6 dB) protect the AWG, the voltage is tapped using two -20 dB pick-off tees and monitored on the oscilloscope.

The arbitrary waveform generator (Tektronix AWG4162) provides the differential si-

nusoidal signal with $U_{\mathrm{AWG}} = 0.72\,\mathrm{Vpp}$ and $f_{\mathrm{exc}} = 100\,\mathrm{kHz}$. The attenuators (-6 dB) protect the AWG, the voltage is tapped using two -20 dB pick-off tees and monitored on the oscilloscope. The excitation signal is plotted in Fig. 4.8b). The maximum voltage difference between the two channels is 36 mVpp corresponding to a maximum current density in the wire of about $5 \cdot 10^{11}\,\mathrm{A/m^2}$. Stamm *et al.* [272] calculated using both ab initio methods and the spin diffusion equations (see Section 1.5.3) an induced effective magnetic moment of $(5.0 \pm 0.6) \cdot 10^{-5}\,\mu_{\mathrm{B}}$/atom for the surface Pt layer at room temperature. Thus the effective spin polarization is still a factor 10^{-5} lower than in Fe [283]. However, the current density can not be increased further because of heating and electromigration. During the excitation and imaging the sample was cooled down at 26 K to avoid electromigration. The scan frequency of the electron beam was 5 kHz and 620 scans were acquired subsequently to avoid image distortions due to thermal drift. The total dwell time per pixel was 124 ms. The excitation period of $T = 10\,\mu\mathrm{s}$ was divided in 10 time bins of 1 µs length. During post-processing all scans were aligned *via* a cross correlation algorithm [287] and finally the PSD algorithm was applied to the time-resolved asymmetry image data. The amplitude images of the PSD analysis for the x and y component of the asymmetry images are shown in Fig. 4.8c). The expected signal due to current-induced spin accumulation would be a higher intensity in the x component amplitude image in the area of the Pt wire while in the y component the intensity should be homogeneous. Further the intensity should be lower in the part of the Pt wire where it is widening towards the contact pad because the current density is lower there due to the higher cross section of the conductor and thus the spin accumulation is also expected to be proportionally reduced. The profile plots along the lines indicated in Fig. 4.8a))(averaging over 20 pixels) show this expected behaviour. First we consider the x component (image and plots in the left of Fig. 4.8c)): The intensity in the Pt wire is higher than in the reference pad and is enhanced where the wire is narrow. The signal is just above the noise level, but is consistent with an interpretation by a spin accumulation proportional to the current density in the wire. In the y component no such signal is visible, as expected.

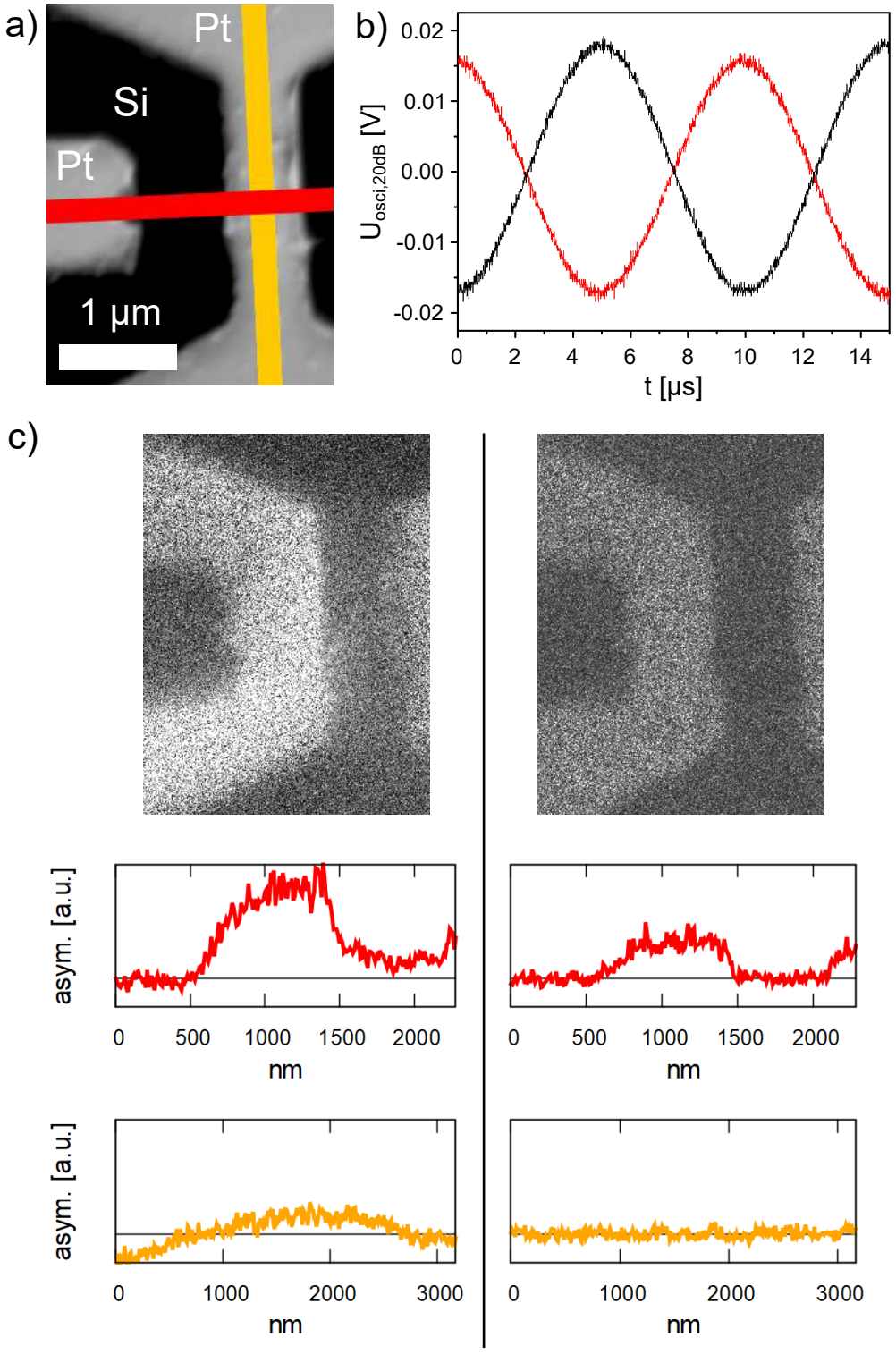

Figure 4.8: **a)** SEM image of the I-shaped sample geometry with grounded reference pad of the same material (Pt(20 nm)) at the left. The orange and red lines indicate the position of the profile plots in c). **b)** Sinusoidal excitation of the sample with 100 kHz. The measured peak-to-peak voltage corresponds to a current density of $j_c \approx 5 \cdot 10^{11}\,\mathrm{A/M^2}$. **c)** Amplitude result of the phase-sensitive detection approach applied on the SEMPA A_x frames (left) and A_y frames (right). The position of the profile plots shown below is indicated in a). The contrast scaling of both images is the same and the asymmetries shown in the graphs can be directly compared (asymmetry range (y axis): 1%).

While these observations again confirm the functionality of the PSD approach, the result is not unambiguous. The highest intensity in both amplitude images we find for the pixels that belong to the substrate. The origin of this signal needs to be understood to unequivocally ascribe the measured intensity in the wire to the expected spin accumulation. Furthermore, the absolute size of the signal is clearly higher than expected. The y range of the profile plots shown in Fig. 4.8 covers an asymmetry amplitude of 1%. Thus the signal is 1-2 orders of magnitude smaller than the signal for Fe (for comparison: Fig. 7.17 in Ch. 7). However, we would expect an asymmetry amplitude in the range of $10^{-5}...10^{-4}$ (Tab. 4.1) that could not have been resolved even with a five times higher SNR that was demonstrated in Ch. 3.
The second result of the PSD mode is the phase image. The colour-coded phase results of the x and y component are shown in Fig. 4.9a). In Fig. 4.9b) the occurrence of the phase values in the full FOV is shown. While the y component does not show any correlation to the excitation frequency, the x component exhibits a clear peak at $\theta \approx 53°$. The phase shift results most probably from run-time delays because of different cable lengths of the excitation reference and detector signal in the measurement setup. From the colour-coded x component phase image it can be seen that the correlation is clearly higher in the narrow part of the wire than in the widening part. However, if we consider only the Pt reference pad, as done in the histogram plotted in Fig. 4.9c), the correlation in the x component is still clearly visible, which is not expected, since this area is always at ground potential. This result also needs to be understood before claiming that spin accumulation is the origin of the main signal observed the wire.

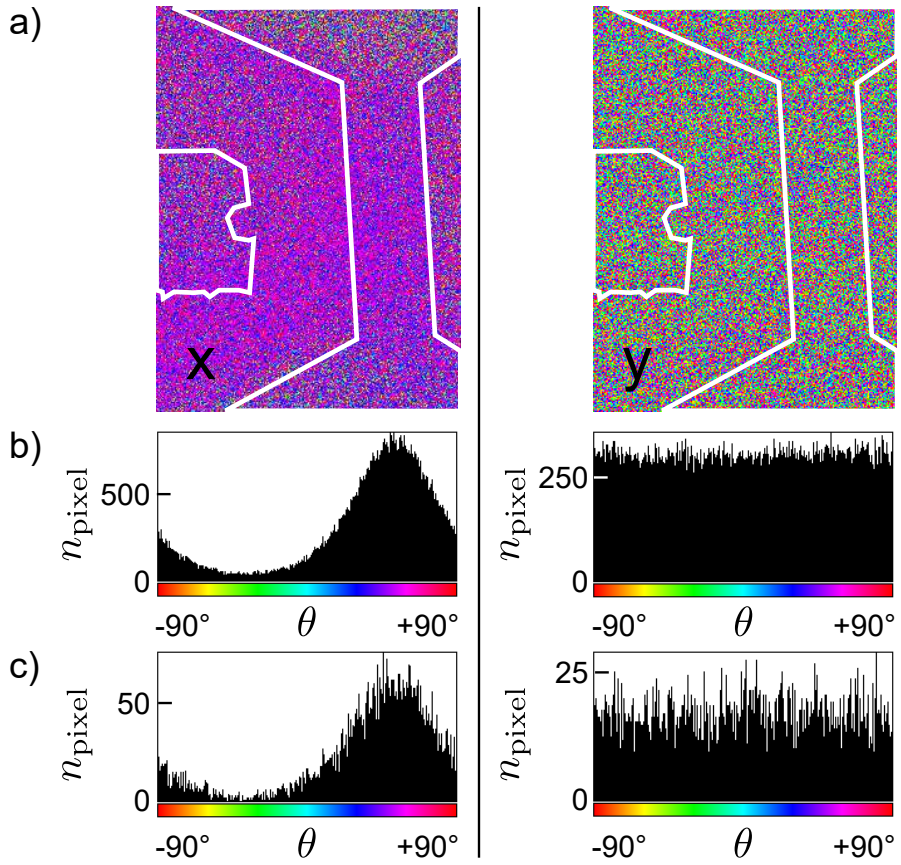

Figure 4.9: **a)** Phase images of the x (left) and y (right) asymmetry component. The white lines indicate the geometry of the Pt structure. The phase angle θ is colour-coded with the key given in b) and c). **b)** Histogram with the number of pixels n_{pixel} per phase value θ containing all pixels in the FOV. **c)** Histogram containing only the phase values in the Pt reference pad.

4.4 Conclusion and Outlook

While SEMPA imaging has several advantages compared to other imaging techniques, such as high surface sensitivity, also significant disadvantages became visible during this study. One has to be careful in the analysis not only if external fields are applied, but also if high currents are used. High current densities can lead to local heating and therefore to distortions by thermal drift, if the system is not in equilibrium [291]. However, even if the system is in equilibrium, the measured asymmetry depends sensitively on the scattering energy of the secondary electrons and therefore on the electrical potential of the sample. Therefore high currents through highly resistive conductors result in a gradual artefact signal, depending on the potential, as described above for the SEMPA

imaging while applying high DC currents. A first step to deal with that problem is the use of a differential excitation with a virtual ground in the wire centre. Using the differential AC excitation with the PSD approach, we could get on the one hand the promising result of an excitation-correlated asymmetry in the Pt wire, confirming again the functionality of the new detection mode. On the other hand open questions still remain because so far we are not able to explain the enhanced signal in image regions where no current is flowing. Local substrate heating and the interaction of the secondaries with the generated Oersted field might be possible explanations. If these questions are solved, the detection mode can be improved further using specific low-pass filters to increase increase the signal-to-noise ratio. For now, despite their own challenges, other techniques such as magneto-optical Kerr and X-ray-based imaging are ahead of SEMPA if pure spin currents should be detected directly.

5 Competing Magnetic States and Switching Pathways in Curved Nanowires

In this chapter we present a study of typical magnetic device components that consist of widely investigated basis geometries, in particular curved wires with width variations. The work investigates the complex magnetization dynamics of the systems. While conventional pump-probe imaging techniques usually only show the overall switching pathway in the magnetic system we demonstrate here that with time-resolved SEMPA imaging and a novel analysis approach, much more information can be extracted revealing competing switching pathways. The analysis allows for determining the probabilities of the competing pathways quantitatively and can identify even rare events leading to changes between the observed switching pathways that can not be detected by conventional pump-probe schemes. The analysis is supported by micromagnetic simulations. Possible spintronic devices must demonstrate high reliability before they are ready for the market. Especially the encoded magnetic states must be thermally stable. Further control of the switching dynamics needs to be guaranteed. The switching process must also work error-free over many switching cycles. In a simple single domain device the switching occurs *via* coherent [255, 260] or incoherent [160, 215] magnetization rotation. However, many devices are based on geometries that show multi-domain states where switching relies on domain wall nucleation and domain wall motion [139, 234]. Domain wall motion can be driven by current-induced torques [22, 175], but the most straightforward approach is *via* the application of magnetic fields to nucleate and move domain walls [103, 219]. This technique is employed already in commercial sensing devices [59]. Domain wall motion can further be induced or supported by using a width or curvature gradient [181, 322] that can lead to automotion of the walls. If a device consists of many basic geometry units packed closely, stray fields will in addition influence the switching processes and the magnetic states [104, 158, 210]. All these effects must be controlled reliably in memory [222], logic [10, 218] and sensor [34] applications based on magnetic domains and domain walls. In the test geometry that is investigated in this study all mentioned effects play a role. The results demonstrate that time-resolved SEMPA allows one to detect the pathways and simultaneously analyse deviations from stable operation that occur very rarely in only every millionth cycle. In addition the detailed mechanism of curvature- and field-dependent chirality selection is investigated by time-resolved imaging. Highly reliable chirality-selective nucleation is of particular interest for chirality-encoded logic [217, 218]. Chirality selection has been realized *via* geometrical features such as edges [216], wire ends [318] and notches [37]. Alternative approaches used electric fields [44] or a combination of tailored magnetic field and geometry [167]. However, the reliability of the proposed mechanisms for chirality selection

has mostly not been investigated. In this study we integrate the signal over billions of cycles and thus have a measure of the reliability of the processes.

5.1 Sample Fabrication

The studied geometry consists of two mesoscopic magnetic half rings oriented with their vertices towards each other. The width of the wires changes gradually along the wire length. The ferromagnetic half rings (HRs) were fabricated on top of a conducting stripline. By applying a current through this wire an Oersted field is generated that manipulates the magnetization in the magnetic structures. The stripline was patterned in the first lithography step using a double-layer resist (MMA/PMMA) and has a width of 8 µm. First we fabricated a Cu(130 nm)/Au(4 nm) stripline grown on a naturally oxidized undoped Si substrate using thermal evaporation. Au capping prevents the oxidation of the Cu underneath. Since thermally evaporated Cu did not yield smooth surfaces, a special recipe designed for tunnel magneto-resistance stacks composed of alternating CuN and Ta layers was used, deposited in the Singulus Rotaris sputter system. The low surface roughness is important to minimize pinning effects in the magnetic material deposited on top of the stripline. The detailed lithography and deposition recipes are found in Section 8.2. With AFM measurements the root mean square roughness $R_q = \sqrt{\frac{1}{N_{px}} \sum_{j=1}^{N_{px}} r_j^2}$ of the stripline surface has been determined to be about 0.3 nm for Cu/Au and 0.1 nm for the CuN/Ta stack. N_{px} is the number of pixels in the AFM line scan in Fig. 5.1 and $r_j = z_j - |z|$ the height deviation from the average z value in the line scan. The AFM acquisitions as well as the lines used for roughness determination are shown in Fig. 5.1.
For the dynamics measurements we had to change the thickness of the stack for better impedance matching. This is necessary to achieve proper current pulse shapes and minimize the reflections in the system. For the push-pull circuit, as described in Section 5.2, an impedance of 100 Ω is ideal. To achieve this, we used a thinner stripline composed of Ta(4 nm)[CuN(16 nm))Ta(4 nm)]×3, resulting in a stripline DC resistance of about 80 Ω. As the ferromagnetic material we used soft-magnetic $Ni_{80}Fe_{20}$, also called Permalloy (Py). This material has a negligible magneto-crystalline anisotropy and is a standard material if soft magnetic properties are needed. 30 nm of Py were thermally evaporated in one of our MBE chambers with a deposition rate of about 4-6 nm/h as has been done for other related studies in the past [26, 181]. The base pressure during evaporation was in the range of 10^{-9} mbar. Sputter deposited Py was also attempted but this led to problems during lift-off due to side-deposition as a result of the much higher pressure in the chamber during material deposition. The material deposition techniques are described in detail in Section 2.2 and Section 2.3. For the patterning we used a single PMMA resist layer recipe as described in Section 2.1.
The HRs have an outer diameter of 5.5 µm and an inner diameter of 4 µm. The width of the HR is gradually decreased along the wire length. The narrower end is tapered while the wider end is rectangularly shaped. An SEM image is presented in Fig. 5.2. 10 HR

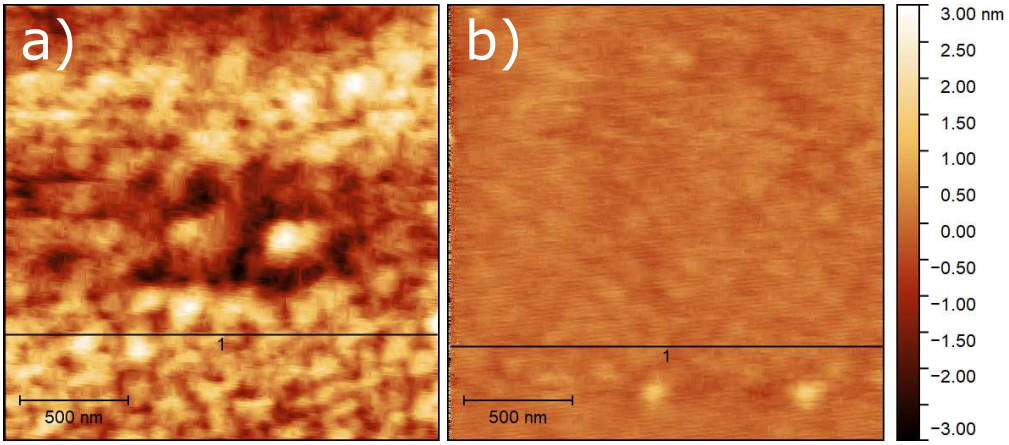

Figure 5.1: AFM images with a FOV of 4 µm^2 of **a)** Cu(130 nm)/Au(4 nm) and **b)** Ta(5 nm)/[CuN(20 nm)/Ta(5 nm)]×5. The average height is set to 0 nm and the colour scale as shown on the right is the same for both images, demonstrating the higher roughness in a). The indicated lines are the line scans used for quantitative roughness determination, as described in the text.

name	HR1	HR2	HR3	HR4	HR5	HR6	HR7	HR8	HR9	HR10
symmetry	axis	point	axis	point	axis	point	axis	point	axis	point
$w_{\min}$ [nm]	500	500	400	400	300	300	200	200	100	100

Table 5.1: Half ring (HR) samples and their geometric properties: symmetry and narrowest width $w_{\min}$ (excluding the tapered end).

pairs were placed on the stripline with a separation of about 15 µm between each pair. Alternating HRs are arranged in axis or point symmetry. The HR pairs were patterned with 5 different width gradients, so that the narrowest width is between 500 nm and 100 nm (100 nm steps). The geometry assigned with the sample name HR1-10 is given in Tab. 5.1. Odd numbers indicate axis symmetry while even numbers correspond to point symmetry.
HR1&2 and HR5&6 were imaged in detail using time-resolved SEMPA imaging, whereas all samples were imaged statically. In the wide end of the HRs an end vortex forms due to stray field contribution, as shown in the colour-coded static SEMPA images in Fig. 5.3. The tapered end, in contrast, can not host a vortex spin structure. The lowest energy state of the HR is a quasi-uniform half-vortex state with the magnetization in general parallel to the HR edge. There is a second possible remanent state: By applying a transverse in-plane magnetic field, DWs can be placed at the vertices of the HRs, to form a so-called half-onion state. For the dimensions used in this case, vortex walls are favoured energetically [158].

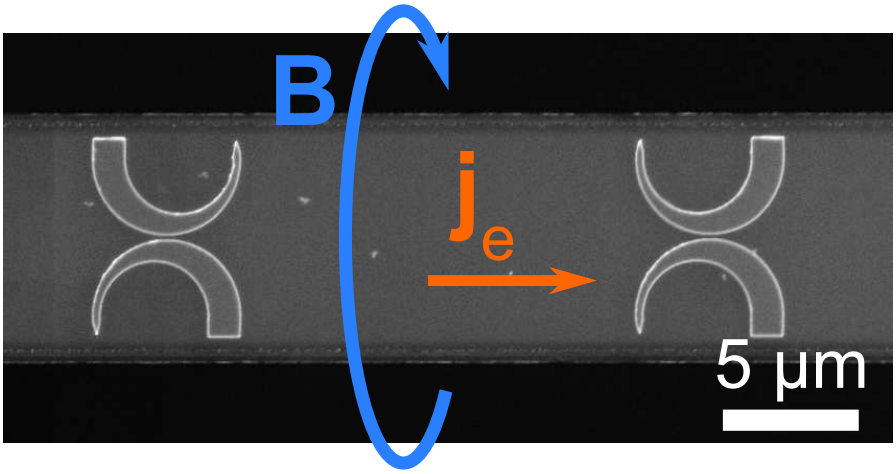

Figure 5.2: SEM image of the CuN stripline with two HRs (HR5& 6) with different symmetry. The current j_e flowing through the stripline induces a transversal Oersted field.

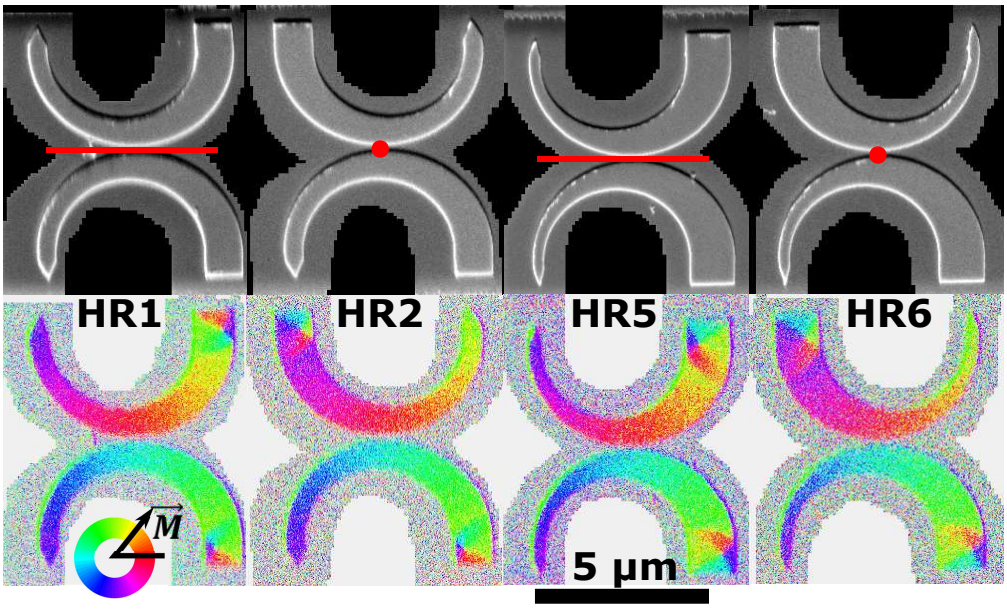

Figure 5.3: Topography and static magnetic images of HR1&2 and HR5&6 before the excitation. The symmetry of the HR pairs is indicated by the red line or the point. The magnetization is colour-coded (colour wheel at the bottom left).

5.2 Experiment

The electrical circuit used for the excitation of the magnetic system is shown in Fig. 5.4. A Tektronix AWG4162 arbitrary waveform generator (AWG) was used to generate the pulses. It has two channels with opposite polarity outputs. During SEMPA imaging it is important to keep the sample always at the same potential using a virtual ground (c.f. Ch. 4) so that the kinetic scattering energy of 102 eV is kept constant. Otherwise the detector count rates decrease significantly and the asymmetry of the detector also changes [88].
Another advantage of the asymmetric driving voltage is the reduced deflection of the primary electron beam [89]. Therefore the circuit is symmetric from both sample sides. The output of the pulser (positive and negative output of channel 1) is amplified by a Mini–Circuits LZY-22+ amplifier (+45 dB) that has the necessary bandwidth (f_{min} =0.1 MHz, f_{max} =200 MHz) to properly amplify the pulses which have a rise/ fall time of about 8 ns and a pulse width (FWHM) of 21 ns. The lower limit of the pulse rising time can be estimated by $\tau \approx 1/(3 \cdot f_{\mathrm{max}}) \approx 2\,\mathrm{ns}$, for the maximum allowed pulse width it requires $\Delta_{\mathrm{FWHM}} \approx 1/(10 \cdot f_{\mathrm{min}}) \approx 1\,\mu\mathrm{s}$ to have a flat-topped pulse shape. To protect the amplifier from reflections, high-power compatible 6 dB attenuators were connected in series. These attenuators also serve to reduce the disturbing reflections due to the high voltage free standing ratio in the amplifier output at low frequencies [4]. Bias tees were used in the case of comparison measurements using conventional pulsing from only one side of the sample while the other side was grounded. Without the bias tees, the zero voltage level of the pulse generator output would be shifted by the AC amplifier in a way that its mean output would be zero. The pulse was monitored using a two-channel real-time oscilloscope tapping the voltage before and after the sample with two pick-off tees (-30 dB). The bias and pick-off tees were fabricated to be compatible with the high power and the used frequency and kindly provided by Dr. Rolf Heidemann and Dr. Hermann Stoll. Knowing the sample resistance and by monitoring the pulses we can calculate the maximum magnetic field from the stripline to be 15 mT if the AWG output peak–to–peak voltage is set to 210 mVpp. To avoid biasing the amplifiers, in the final experiment an excitation pattern of two pulses of the same height and width, but opposite direction was used. The two pulses have a separation of 75 ns and the cycle length is 150 ns, as shown in Fig. 5.5. The delay between the opposite pulses was chosen so that there is still a time window without applied field between the pulses to observe possible field-free automotion of the VWs along the width gradient, as has been observed in [181]. Further these off-times avoid excessive heating. Nevertheless, with the application of this pulse cycle the sample temperature increased from room temperature to 340 K. The temperature was measured at the sample holder using a Pt100 sensor and a LakeShore 330 controller.

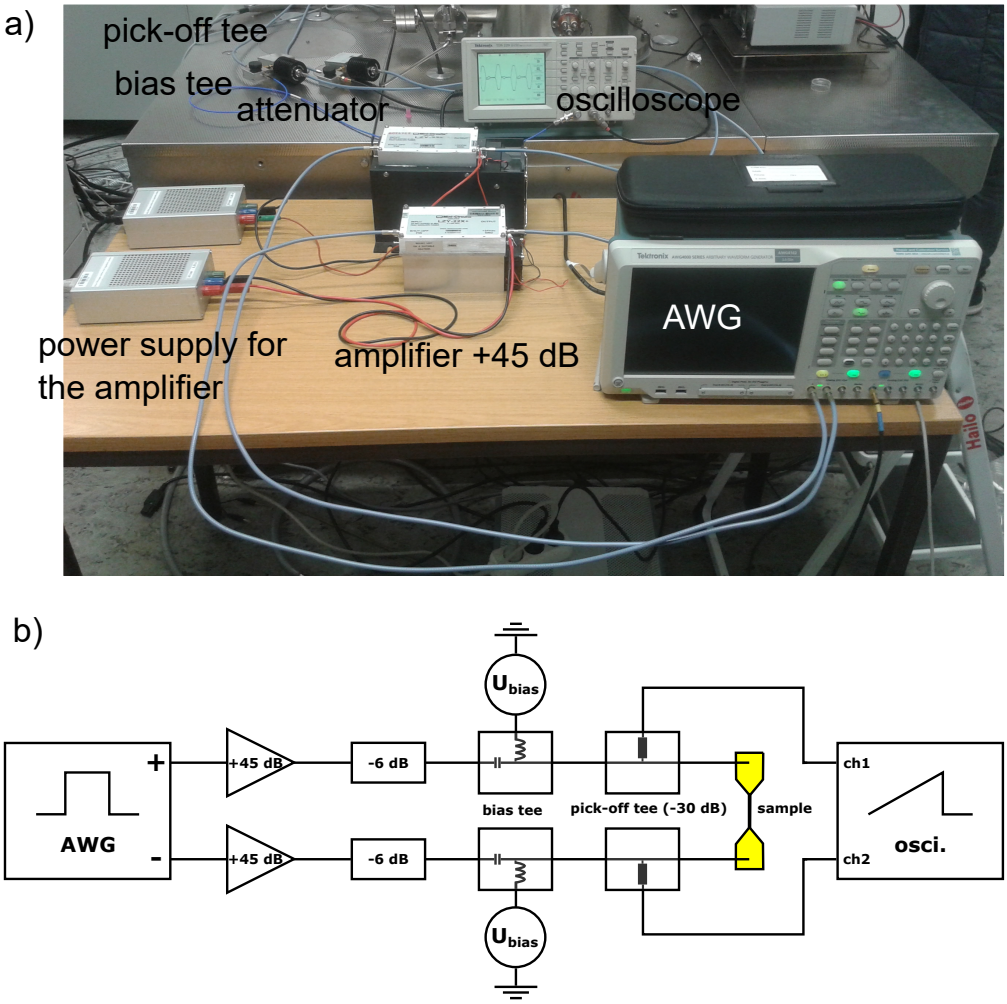

Figure 5.4: **a)** Photography of the electrical circuit for the pulse excitation. **b)** Circuit diagram of the push-pull excitation consisting of an arbitrary waveform generator, symmetrically arranged amplifiers, attenuators, bias & pick-off tees, the sample and a monitoring 2-channel oscilloscope.

We use direct dynamic SEMPA imaging to investigate the switching pathways in the HR pairs. The technique is described in Ch. 3. The TDC was synchronized with the excitation by a short 20 ns pulse of $U_{\max} = 2.5\,\mathrm{V}$ every 150 ns from the second channel of the AWG. The full period is subdivided in 75 time intervals of 2 ns, corresponding to the system´s time resolution, as measured in Ch. 3. To have a comparable SNR in every single frame to that in a conventional static SEMPA image, the dwell time per pixel must be multiplied by the number of frames. A 75 times longer dwell time per pixel is not feasible due to thermal drifts of the sample over the total acquisition time of approximately ten hours. To avoid blurring from the drift, the FOV was scanned

several hundred times with a rather high scan frequency of 500 pixel/s. The measurement software recognizes the drift and by applying pattern recognition the system is able to adapt the FOV after every frame. To save measurement time, an irregular ROI was chosen that just contained the two HRs. By scanning just this selected area, the measurement time could be reduced by 25%. The FOV of 6.9 µm width was divided in 256×306 pixels so that the set resolution approximately matched with the resolution of the system. The EHT voltage of the primary electron beam in SEMPA was set to 7.5 kV and the beam current to 3 nA. Before imaging the samples were Ar^+ ion milled at an energy of 1 kV and then 0.5 nm Fe was deposited on top to enhance the magnetic contrast [303] (c.f. Section 2.6).
The post-processing included a drift correction of the several hundred subsequent scans using an ImageJ plugin [287]. In a second step also the shift of the FOV due to the excitation was corrected for the 75 video frames. The asymmetry images were colour-coded using a self-written MATLAB routine. Due to a small misalignment of the sample plane compared to the detector plane the y-scale had to be rescaled for proper position determination of certain magnetization features like vortices.

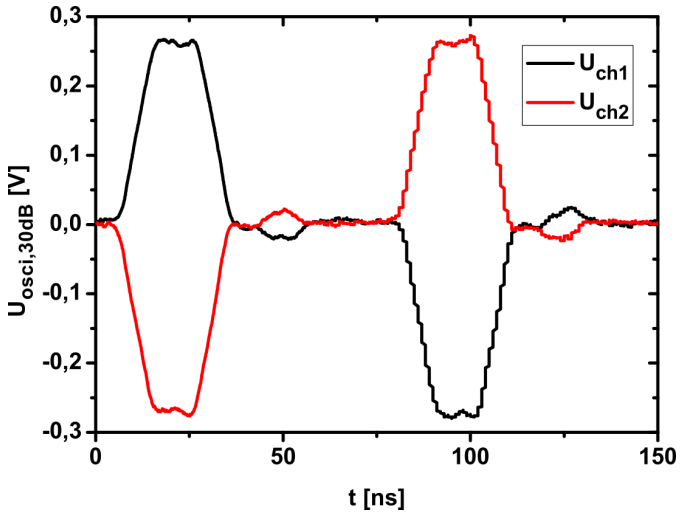

Figure 5.5: The pulse cycle used to generate the Oersted field measured with an oscilloscope and two 30 dB pick-off tees before (black) and after (red) the sample.

5.3 Simulation

The simulations corresponding to the experimental measurements were performed using the open-source Python-based MICROMAGNUM software [3]. The initial magnetization states were set roughly by defining the x orientation of each HR and then the system was allowed to relax to the lowest energy state without an applied field until the torques due to the stray-field were below a certain limit. In the experiment the rectangular end

hosted a vortex that did not nucleate automatically during the relaxation, but needed to be initialized by intention with a given chirality, as shown in Fig. 5.6. In the experiment the non-zero temperature helps the nucleation of the vortex. In the following text we will refer to the geometry and the experiment with HR1, HR2, etc., and if a specific simulation is addressed we will use HRS1, HRS2, etc.

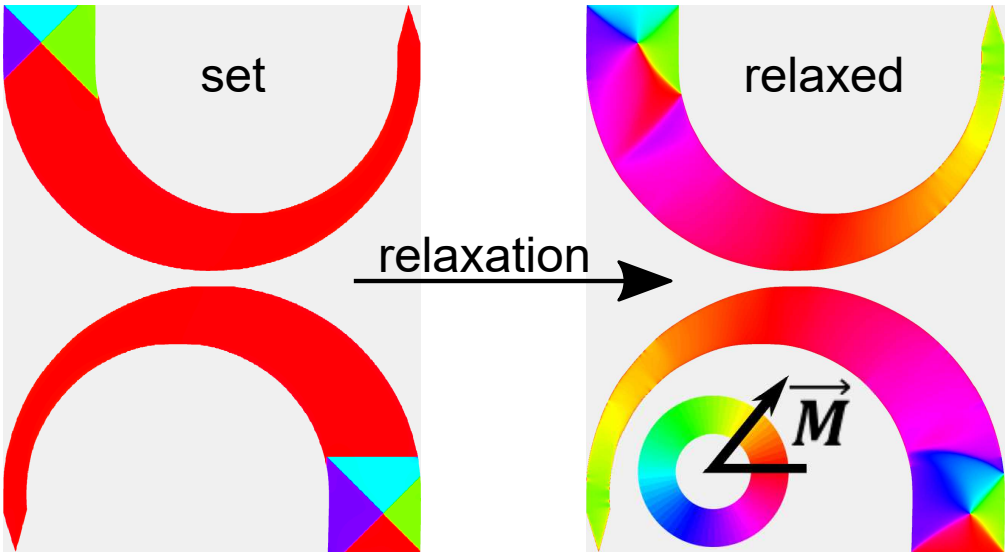

Figure 5.6: Two-step initialization of the magnetic state by defining the x-direction of the magnetization and the vortices and subsequent relaxation.

The dimensions in the simulations equal the dimensions of the samples. To simulate the dynamics in the HRs, the typical material parameters of Permalloy have been used: Exchange stiffness $A = 1.3 \times 10^{-11}$ J/m, saturation magnetization $M_S = 800 \times 10^3$ A/m, damping parameter $\alpha = 0.008$, no magnetocrystalline anisotropy, and the cell size of $5 \times 5 \times 30\,\mathrm{nm}^3$ [181]. To accelerate the simulations, computation was performed using parallel computing with a graphics card.

5.4 Curvature Dependent Chirality of Nucleated Vortex Walls

For chirality-based logic devices the reliable control of the vortex wall chirality is required. Different methods have been proposed as possible approaches. Besides using external factors such as electrical fields [19, 44] and magnetic fields [167] mainly tailoring the geometry serves for this purpose: Introducing notches [37], wire ends [318] and edges [216] lead to chirality rectification. In our experiment we observe the chirality rectification in edges/ strongly curved structures and at wire ends. Further down we also discuss and compare shortly the reliability of these methods.
First we look at the movie frames t_A and t_B just before the next pulsed field excitation that show the steady-state of the magnetization. The colour-coded images are shown

in Fig. 5.7. The temporal position of the shown images t_A and t_B is indicated in the plot of the pulse shape in Fig. 5.8. If automotion of the two interacting DWs always occurred, we would have expected to see a half-vortex state in each of the HRs after the assumed relaxation by field-free DW motion due to the width gradient of the wires. Instead we see in general in Fig. 5.7 a half-vortex state only after one of the pulses and after the other one a clear half-onion state. This raises the question of the origin of this asymmetric behaviour for an otherwise very symmetric scenario.

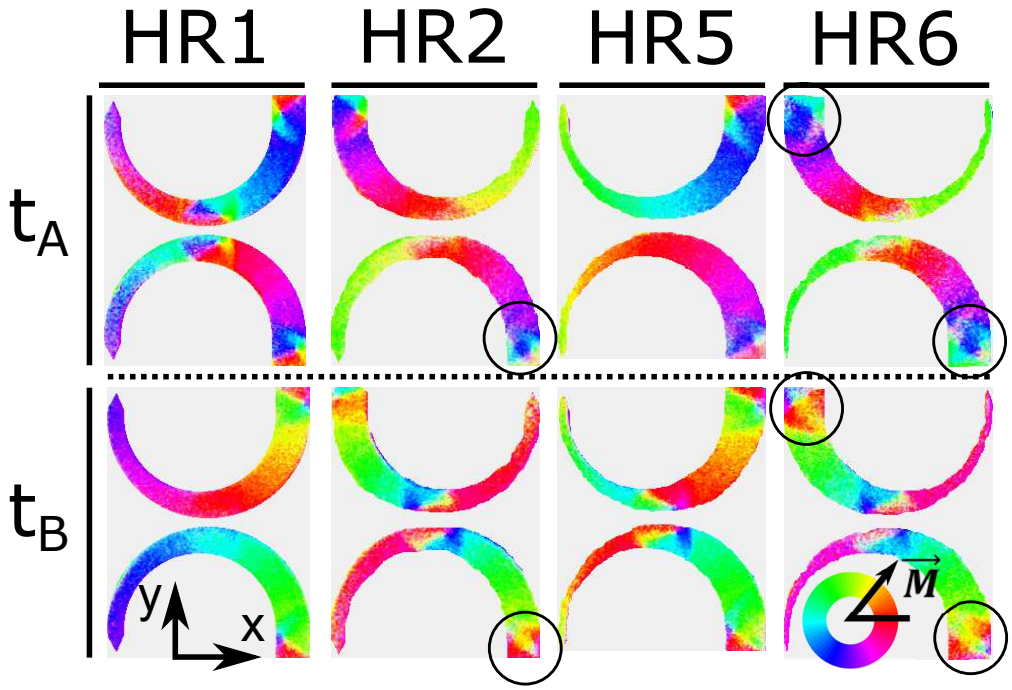

Figure 5.7: Steady-state magnetization just before the positive field pulse $+B_y$ (t_A) and the negative field pulse $-B_y$ (t_B). The shown magnetic images are frames of the SEMPA movie that was dynamically acquired. The encircled end domains do not show clear end vortices but non-physical domain patterns that indicate a superposition of different unstable domain states. In the centre at the HR vertex a clear vortex forms only after one of the two pulses, however, for HR2 and HR6 a weaker contrast vortex can be recognized also in frame t_A.

The switching pathway is examined in detail in Section 5.5. Before that we correlate the spin structure of the nucleated VWs with the sample geometry and the nucleation field. After one of the two magnetic field pulses (for HR1 after the negative pulse at t_A, for HR2 and HR5&6 after the positive pulse at t_B) a vortex wall with an fixed chirality is positioned at the HR vertex. Since we can only see the integrated magnetic signal over all excitation cycles during the whole measurement time, this indicates a very high reliability of a vortex wall nucleation with exactly this chirality. Highly reproducible nucleation

processes are technologically highly important for applications *e.g.* in chirality-based logic [217, 218]. As can be seen in Fig. 5.7, the chirality of the nucleated VW depends on the HR curvature and the direction of the nucleating magnetic field. The curvature is defined in this context as $\hat{\kappa} = +1$, if the wire turns to the left from the perspective of the nucleating DW and as $\hat{\kappa} = -1$, if it turns to the right. A magnetic field pointing in the direction of the VW motion is assigned with a $\hat{B} = +1$, and accordingly $\hat{B} = -1$ for the opposite case. Then the resulting spin structure with clockwise (cw: $\hat{c} = +1$) and counter–clockwise (ccw: $\hat{c} = -1$) chirality can be determined by simple multiplication of the field direction and the sign of the curvature. The VWs in the lower HR for sample HR2, HR5 and HR6 show at t_B always the same clockwise (cw) chirality since for all lower HRs curvature $\hat{\kappa} = +1$ and field direction $\hat{\kappa} = +1$ are equal. Looking at HR1, only at t_A is a VW clearly visible. The curvature is still the same, but the field direction has changed. The VW chirality has also changed to counter-clockwise (ccw). Considering now also the upper HR where the HRs are arranged in axis symmetry, the same VW chirality is found as in the lower HRs of the same HR pair. The curvature and the field direction relative to the curvature are just opposite for the upper HR compared with the lower HR. In HR2 and HR6 VWs can also be seen after the negative B_y pulse at t_A, but with the opposite chirality compared to t_B, where the negative field has been applied. The role of the curvature can be seen by comparing HR1 and HR2 at t_A. While the lower HRs in both cases turn toward the left, the upper HRs have the opposite curvature. Consequently, the chirality of the VWs in the vertex of the lower HRs is the same while it is the opposite for the upper HRs of HR1 and HR2. The simulations reveal the same behaviour and are consistent with the experiment. The fact that the VWs nucleate always in the wider part of the wire is the reason why in general the axis symmetry HRs always have the same overall chirality in the upper and lower HR and the point symmetry HRs have the opposite overall chirality. Only for significantly higher magnetic fields does one have to consider the possibility of VW nucleation in the narrower part of the HR. In simulations with 24 mT instead of 15 mT VW nucleation could be observed even in the narrower part of the HR.

To sum up the observations in a nutshell: The chirality of the VWs always equals the overall chirality of the HR magnetization before the nucleation of the VW, *i.e.* the magnetization along the inner HR edge is always continuously transforming from the wider part of the HR, where the wall is nucleated, into the VW. This is the case for all investigated samples. The mechanism to nucleate VWs with a selected chirality has been demonstrated in [216]. What we show here in addition, is the very high reliability of this process. The images shown in Fig. 5.7 show the average magnetization pattern for more than 50000 repetitions of the excitation cycle. It is further important to note that the chirality of the nucleated VW does not depend on the chirality of the end vortex. This excludes pure DW motion as the switching mechanism, which is described further down in Section 5.5. While the chirality of the VWs at the vertices is highly reliable, the chirality of the end vortices is not. It is expected to be protected as well [318], but the mechanism is not as reliable compared to the nucleation mechanism described above. This can be seen by comparing the initial state before the excitation in Fig. 5.3

and the steady-state in the frames t_A and t_B of the SEMPA movie in Fig. 5.7, which show the magnetic state after around 40 ns without field just before the next field pulse. While the static images show clear end vortices for all HRs, the rectangular ends for HR2 and HR6 show clearly domain patterns that would not be expected to be stable in the mentioned frames in the time-resolved SEMPA acquisition (encircled in Fig. 5.7). The appearance of these unphysical states results from the fact that we are summing up the signal from more than 50000 pulse cycles. If the magnetic state is not highly reliable, the final image shows a superposition of all acquired magnetic states and corresponding unphysical states. This explanation is supported by abrupt contrast changes in the end domains resulting in bright or dark stripes in the single scan images, as shown later in Fig. 5.10. The instability of the end vortex chirality increases in the case of the wider wire end.

5.5 Switching Pathways

In this section the switching pathway is investigated in detail by having a closer look at the acquired SEMPA movie, as well as at the micromagnetic simulations of HR5. In Fig. 5.8 the characteristic stages of the switching mechanism are shown for both experiment and simulation. We start with describing the magnetization dynamics for an initial half-vortex state with the boundary domain of the end vortex pointing in the same direction as the overall magnetization in the HR, as is the case for the upper HR at t_1. As soon as the magnetic field is applied, the leading edge 90° Néel-DW moves towards the vertex of the HR and the domain of the end vortex with the magnetization pointing in the field direction extends. For this geometry, switching usually does not occur *via* simple DW motion. It is a complex process consisting of the subsequent nucleation of several vortices with opposite chiralities. The vortices are indicated by arrows in the simulation images in Fig. 5.8b). At around the half way point towards the HR centre, the leading edge DW splits up into a vortex–antivortex pair [27] with the nucleated vortex chirality opposite to the chirality of the end vortex (t_2 in Fig. 5.8). The leading edge 90° Néel-DW of this new vortex then splits again into a vortex–antivortex pair with a clockwise chirality (t_3). The last nucleated vortex then travels along the outer edge of the wire until it reaches the centre of the HR where it is expelled so that a transverse DW forms (t_4). After the magnetic field pulse, the vortex forms again with the previous chirality (t_5).

While the subsequent nucleation of these two additional vortices always occurs, only one vortex with the 'correct' chirality prevails, as discussed before: The chirality of the VW in the centre equals the overall chirality of the half-vortex magnetization in the HR. If this is the case already for the chirality of the end vortex, in some cases this end vortex can unpin from the end, travel towards the vertex and even prevail over the newly nucleated vortex that then annihilates during the switching process.

Now we consider the case with the end vortex chirality opposite to the preferred chirality due to curvature and field. This is the case for the lower HR in Fig. 5.8. Then the second appearing vortex prevails and moves along the outer perimeter towards the HR vertex

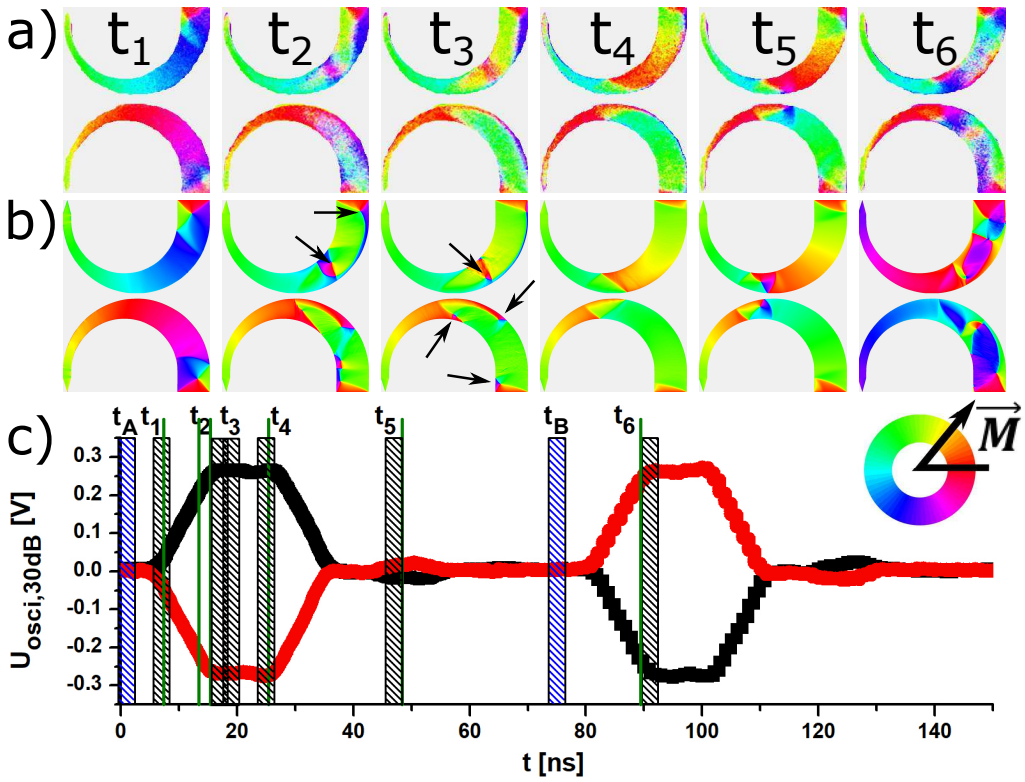

Figure 5.8: Switching pathway of HR5. **a)** Selected frames t_1-t_6 from the time-resolved SEMPA imaging of HR5. **b)** Corresponding frames from the micromagnetic simulation with $B_{\max} = 15\,\mathrm{mT}$. The end vortex as well as the nucleated vortices are indicated by black arrows. **c)** Excitation pulse shape as shown in Fig. 5.5, but with the time windows t_1-t_6 corresponding to the frames in a), green lines indicating the times of the simulation images in b) and blue areas indicating the times of the steady-state image frames in Fig. 5.7.

while the third vortex with opposite chirality is expelled at the inner edge of the HR. In some of the simulations the initial state already possesses two vortices of opposite chirality in the wide end of the wire with the main end vortex having opposite chirality to the overall chirality in the HR. In this case the smaller vortex near the inner edge of the HR with the appropriate chirality is just driven directly to the HR vertex.
To sum up the VW nucleation dynamics, we observe that always three vortices including the end vortex appear with alternating chirality, but only one vortex with the chirality equal to the initial overall chirality of the magnetization in the HR prevails. This geometry thus provides a very reliable nucleation method of VWs with a selected chirality.
In the experimental SEMPA movie the DW is pinned at the vertex after the nucleation pulse, it only changes its type back from a TW during field application to a VW by re–nucleation of the vortex, as shown at t_4 and t_5 in Fig. 5.8a). However in some

simulations, as for instance with HRS5, the VW is not pinned and starts to travel towards the narrower end driven by the width gradient (t_5 in Fig. 5.8b)). This so–called automotion [181] is not directly observed in the experimental images.
During the next pulse with opposite field direction, the VW in the SEMPA images is expelled at the inner edge of the HR and the magnetization returns back to the quasi–vortex state without a VW at the vertex, leading to the in-general observed behaviour of alternating half-onion and quasi–vortex states after the field pulses. This holds as long as the VW in the centre of the wire is pinned. In the simulations where we see automotion of the VW away from the vertex into the narrower part of the HR, the second field pulse is also able to nucleate a new VW *via* the same mechanism and thus the reverse half-onion state is generated. This behaviour is promoted for the samples with a higher width gradient, such as HRS5 and HRS6, as shown in Fig. 5.9 (the simulations corresponding to HR5 and HR6). If VW automotion starts directly after the magnetic field pulse is off, the relaxed magnetic state before the next reversed pulse is again a half-vortex state, but with reversed chirality in the HRs. This is observed in the case of HRS5. However, it is not necessary that the VW moves until the tapered end and annihilates there before the reversed field sets in. This is the case for the lower HR of HRS6 ('HRS6L'). It moves a bit further than the vertex but is stopped by the attractive stray field interaction that leads to an alignment of the edge half antivortices of the adjacent VWs. While for the upper HR ('HRS6U') the VW moves back from the vertex towards the wider end during the reversed pulse, the VW in the lower HR is moved by the field towards the tapered end. In the upper wire of HRS6 a half-vortex state with the same chirality as before the first pulse forms again while the lower HR switches from one half-onion state to the opposite half-onion state. These two simulations point to effects that potentially can influence the magnetization dynamics in our geometries significantly.
Motivated by this observation in the simulations, we have again a closer look at the experimental data to see if there are signatures of DW automotion. In Fig. 5.7 half-onion states are not only visible after one of the two pulses, *i.e.* either at t_A or at t_B, but at least for HR2 and HR6 the images indicate the presence of VWs after the $-B_y$ pulse at t_A. However, the contrast is weaker than in the corresponding frame t_B. The reason is to be found in the pump-probe measurement type that is averaging over many excitation cycles. Non-physical domain patterns, as we have seen in the case of the end vortices, as well as reduced contrast indicate the superposition of competing magnetic states. By using the conventional analysis approach, it is not possible to reveal further details about the competing magnetic states, to quantify their probabilities and to determine the mechanism resulting in a change of the magnetic state. However in the next section we devise a new analysis approach that indeed allows for both by extracting additional information from the single scan images.

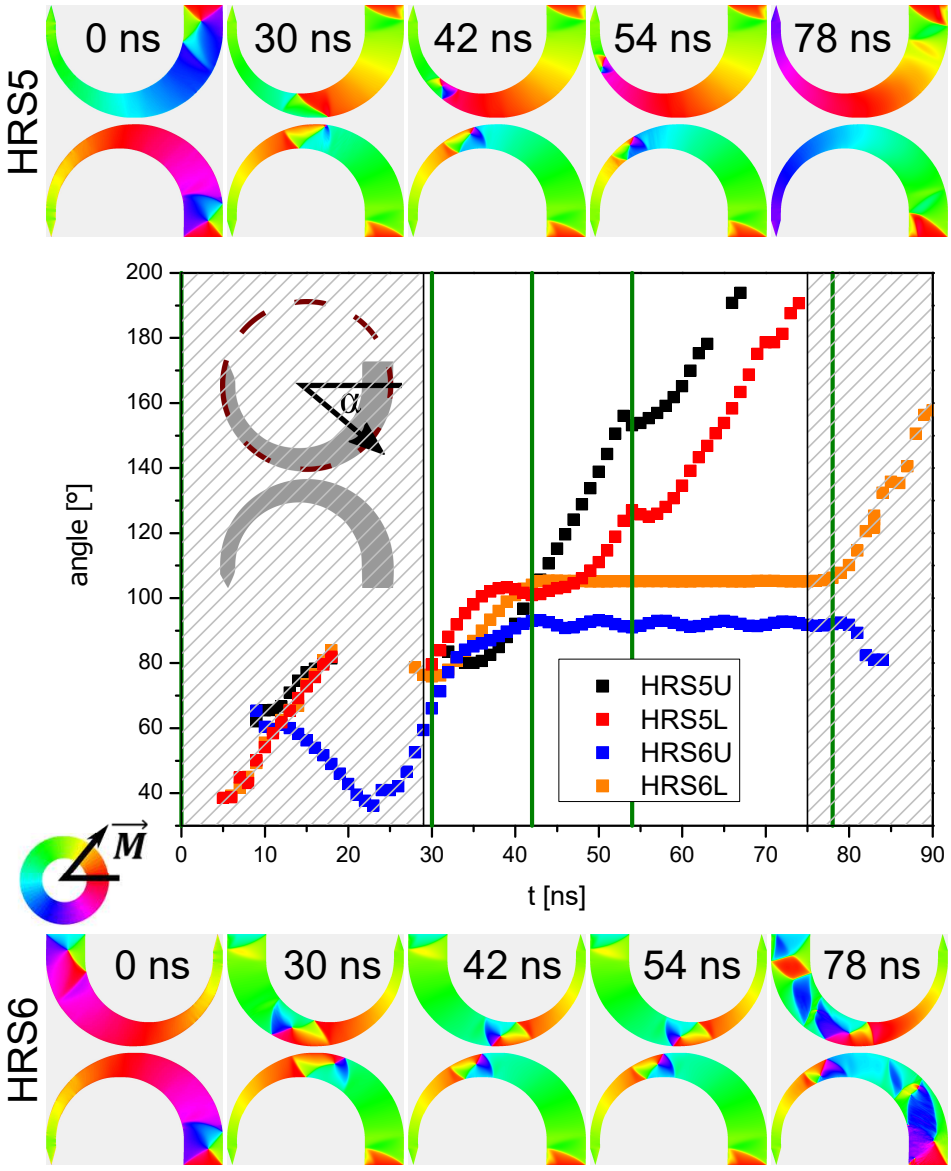

Figure 5.9: Automotion in the simulations HRS5 and HRS6 corresponding to the geometries of HR5 and HR6. The graph in the centre shows the angular VW position as defined by the vortex core position and the images on top/ bottom show some selected time frames of the magnetization dynamics. The times are indicated by green lines in the plot. The hatched area indicates the time of the pulse application.

5.6 Prevalence of Different Pathways Depending on Geometry and Temperature

To bring a spintronic device to market maturity a high functional reliability must be guaranteed. To this end the reliability must be confirmed over many repetition cycles and quantified. For further device development and optimization, all possible switching pathways must be understood, as well as the events that lead to changes between the possible pathways. To this end, in this section a new analysis approach is developed that provides vital insights into just these issues. In conventional acquisition modes disentangling the different pathways using a pump-probe technique is not possible. However, we can extract additional information from the many subsequent single scans that are acquired to avoid blurring of the imaged object because of thermal drift. The final movie contains the information of all those scans by summing up all counts of every time frame after aligning the scans using cross-correlation and subsequent calculation of the asymmetry images. Now we do the analysis the other way around: We do not add the information of all scans and keep the time frames separate, but instead we look at every single scan separately while having all information in the time frames of this scan added up. In this case the asymmetry images show the magnetization averaged over the whole excitation period. Since the electron beam dwell time per pixel is 2 ms, details of single pathways stable over more than several tens of milliseconds are captured, giving access to a wealth of additional information.
First we look at three subsequently acquired single scan x asymmetry images of HR1, shown in Fig. 5.10a). The wider part of the ring has a similar intermediate grey value to the non-magnetic background, indicating an equal superposition of magnetization with positive and negative x–component (since the alternative interpretation of fully y directed magnetization is ruled out by the corresponding y component magnetization images), while the narrower part is either bright or dark indicating a stable magnetic state. This is consistent with the pathway described above that switches between quasi–vortex and quasi–onion state with every pulse. However, we can also see a change of the magnetization direction in the narrow part of the HRs by comparing the scans labelled 'pw2' and 'pw1' in Fig. 5.10a). This change corresponds to a change between two possible switching pathways and is attributed here to a change from one switching pathway ('pw2') to another pathway ('pw1'), which occurred during the acquisition of frame 'pw2/1', as can be seen in the abrupt change of contrast during the scan of the lower HR. The end domains of the HRs also show strong contrast indicating a preferred chirality. This is consistent with the clearly visible end vortex in HR1 in Fig. 5.7. However, even for HR1 the vortex chirality is not fully reproducible, as can be recognized by the abrupt contrast changes in the magnified picture of the end vortex of scan 'pw2/1'. We know already by looking at the single frames that the changes of the pathway and of the end vortex chirality are not directly correlated and can postulate they are largely independent of each other, since the frequency of changes differs considerably for both effects, which is already valuable information. Plotting the occurring pathway over the measurement time, as shown in Fig. 5.10b), allows us to quantify the number and frequency of the

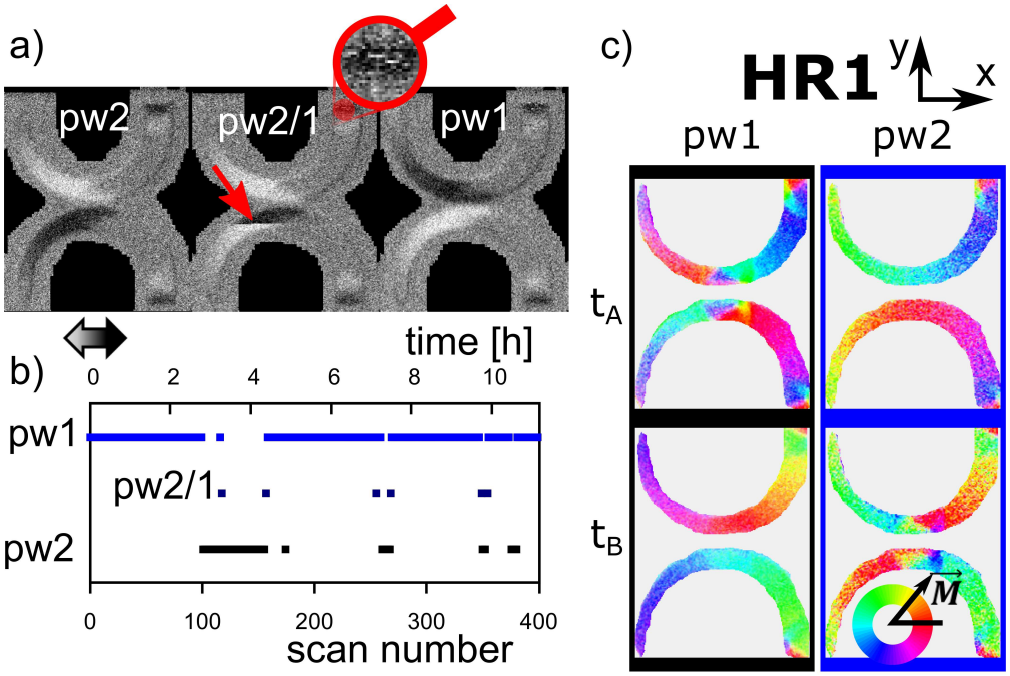

Figure 5.10: **a)** Three subsequent single scan SEMPA x-component magnetic images of HR1 acquired during the application of the continuous excitation. The information of all time frames is added up in this case. The first and the third image show the opposite magnetization direction in the narrower part of the HRs. During the acquisition of the second scan the change between the pathways occurred, resulting in an abrupt change in contrast (arrow). The end domain also shows these abrupt jumps but at a higher frequency as shown in the magnified excerpt. **b)** The chosen pathways are shown in this graph for every scan during the 11 h long acquisition of the data for the magnetization dynamics movie. **c)** The low frequency of changes allows for disentanglement of the pathways. Here the steady-state frames of pathway 1 (pw1) and pathway 2 (pw2) are shown, in analogy to Fig. 5.7.

events leading to changes of the pathway. After sorting the scans we are able to make two movies showing the disentangled dynamics of the two different pathways. Using this method we are able to detect also the pathway with a lower probability, which would be hidden in conventional analysis. In both pathways switching occurs between the half-vortex and half-onion state; only the phase is different, as shown in Fig. 5.10c) in analogy to Fig. 5.7. We also find confirmation for the predicted field and curvature dependence of the VW chirality (Fig. 5.7).
Now we are able to extract and compare information about the vortex positions and velocities in the same wire with the end vortex having the same and the opposite circulation direction as the overall magnetization in the HR. The vortex position is determined using a MATLAB script by repeated clicking on the vortex centre in the image to extract the position of the pixel and calculating the average position with respect to the HR

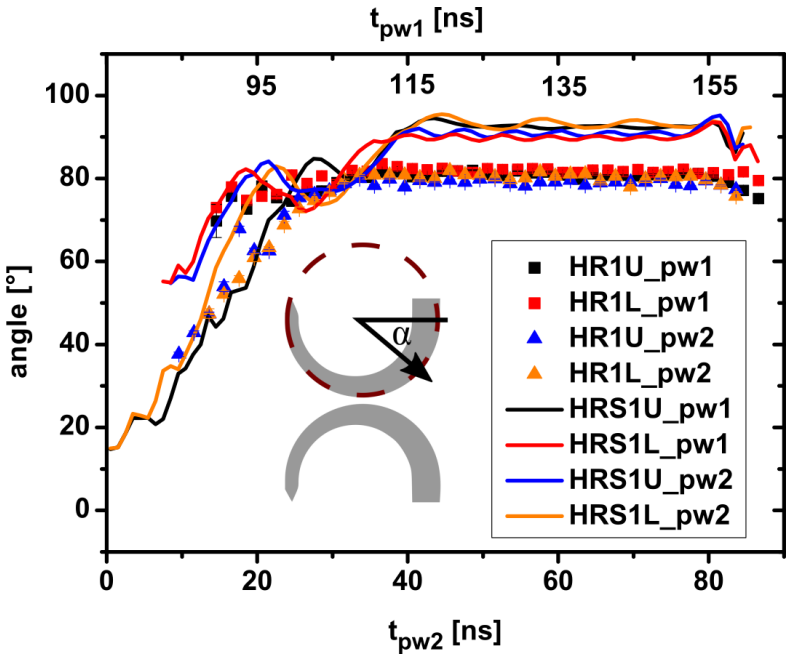

Figure 5.11: Angular positions of the emerging vortex cores in the upper ('U') and lower ('L') HRs in the experiment (HR1) and the simulation (HRS1) for pathway 1 (pw1) and pathway 2 (pw2). The data for pw1 is plotted with a temporal shift of 75 ns, since in this case the VW nucleation occurs during the negative field pulse.

position. The angular position of the prevailing vortex is shown for both pathways (pw1 and pw2) and both the upper 'U' and lower 'L' HR in Fig. 5.11. The experimental data is labelled with HR1 etc., while the data extracted from the simulations is labelled with HRS1 *etc.* Here we look at the switching dynamics initiated by the pulse that switches the HR from the half-vortex to a half-onion state. Considering the lower HR, in 'HR(S)2Lpw2' (orange in Fig. 5.11) the second and third vortex appear earlier than in 'HR(S)2Lpw1' (red), and the second vortex prevails, while in pw1 the third vortex prevails. This is the reason why the red trajectory starts delayed but at a higher angle compared to the orange one. The third vortex in pw1 reaches the centre region of the HR earlier than the second one in pw2, despite the latter being nucleated earlier in time. From the determined initial slope of the domain wall position *vs.* time the average VW velocity during field application in pw2 in the lower HR was calculated to be 100 ± 20 m/s in the experiment. In the simulation the DW velocity was 230 ± 60 m/s. The significant difference can be attributed to pinning by material imperfections. A deviating damping parameter as discussed in the next chapter could also modify the DW velocities. In the simulation the VW travels until it reaches the HR centre at around 90°. In the real samples pinning stops the VW earlier.

Influence of the HR Width Gradient

The next step is the identification of the mechanism that leads to the change of the pathway. To get more insight, we investigate the frequency of the changes by comparing HRs with different width gradients, look for the influence of arranging the HRs in different symmetries and perform the dynamic measurement at lower temperature. In Fig. 5.12a) a topographic image of HR5 is shown with an overlay of the x asymmetry SEMPA image in the narrower parts of the HRs. In the upper HR the x component of the magnetization is mainly negative (white), in the lower one it is mainly positive (black). This is a signature of pathway 2. However, the homogeneous contrast is interrupted by dark or bright stripes in the upper/ lower HR, respectively. This indicates a change between pathways on a much shorter timescale to that observed before for HR1. For HR1 changes take place on the order of minutes or hours, for HR5 there are changes after several tens of ms. In this case the disentanglement of both pathways is not possible. Of course it is possible to reduce the dwell time, but only at the cost of SNR. This limits the individual determination of the switching pathways. In general, depending on the spin polarization and the amount of secondary electrons emitted by the investigated material, dwell times even in the µs range are feasible.
As mentioned before, the micromagnetic simulation HRS5 show automotion after the field pulse in contrast to HRS1 where the VWs remain at the vertices of the HRs and annihilate during the following reversed field pulse. Thus automotion is a possible mechanism that can change between the two possible pathways. Another candidate would be rarely occurring VW nucleation in the narrower part of the wire. The observation of a higher frequency of changes between pathways for HRs with a stronger width gradient supports the first proposed mechanism, since nucleation is suppressed with decreasing the wire width and the force pulling the VW along the width gradient is increased.

Influence of the Arrangement of the HRs

By arranging the HRs in different symmetries we investigate the interaction of the VWs with always an opposite magnetic charge, but sometimes equal and sometimes opposite chirality. The opposite magnetic charge is the consequence of the arrangement of the HRs with their vertices toward each other and a global field direction. The chirality depends on the direction of the curvature and since the nucleation of the domain walls only occurs in the wider part of the HR, in the HR pairs with axis symmetry VWs with the same chirality are generated while in the point symmetry arrangement in the HRs VWs with opposite chirality are nucleated. HR6, the counterpart with point symmetry of HR5 which has line symmetry, is shown alongside HR5 in Fig. 5.12. Here we even do not see stripes any more, but just features resembling enhanced noise. This is because the frequency of the changes of the pathway is only slightly lower than the scan frequency. The frequency of the changes between the pathways is higher if the chirality of the VWs is opposite. The same holds if you compare HR1 (Fig. 5.10) and HR2 (Fig. 5.15). In principle this behaviour could be just sample specific due to different pinning centres and not directly related to the different geometrical arrangement of the HRs. However, from

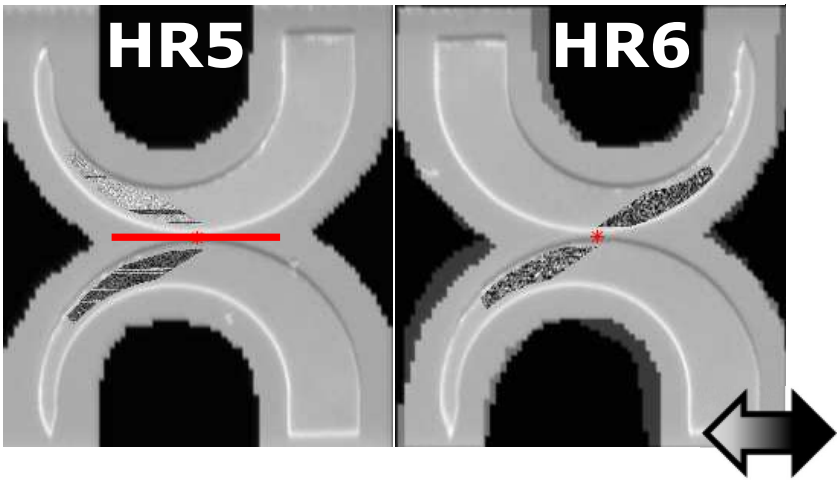

Figure 5.12: Topographic images of HR5 and HR6. The overlay shows the single scan SEMPA x-component magnetic images after integration over all 75 time frames of this scan. For HR5 the HRs are arranged in axis symmetry, for HR6 in point symmetry. The symmetry axis/ point are drawn in red. Abrupt contrast jumps indicate the changes between the pathways.

previous work we know that at finite temperatures around room temperature automotion does set in for geometries with a width gradient as in HR1&2 [181]. Here we observe in the experimental imaging and also in the simulations HRS1 and HRS2 that the VWs stop at the vertex.
Micromagnetic simulations of single HRs show that the nucleation dynamics is the same and automotion only occurs for the HR with the higher width gradient (Fig. 5.13a)). This is visible in the switched left half of the HR at the time t_6 during the second pulse, while in the case of the lower width gradient (Fig. 5.13b)) no significant automotion occurred. However the simulations are performed without considering thermal activation, that can assist the DWs to unpin and move towards the tapered end of the wire. If the HRs are paired the opposite magnetic charge of the DWs accelerates the motion of the nucleated VW towards the HR vertex and suppresses automotion [104]. This is shown in Fig. 5.14, where the VW in the single HR moves more slowly towards the vertex of the HR than the corresponding VW in the paired HR, but overtakes it after the field is released.
The reasons for the different probabilities to change between the pathways in the experimental HR samples might be sample-specific, but there are also smaller energy contributions to the stray field that are dependent on the polarity of the vortex cores and further contributions due to different positions of the half antivortices at the wire edge that could play a role. The polarity of the vortex cores, however, could not be directly resolved by our SEMPA measurements. Further the coupling of the pathways in the upper and lower HRs indicates a significant contribution of the interaction of the VWs. All samples showed this coupled behaviour. If a VW unpins and travels towards the

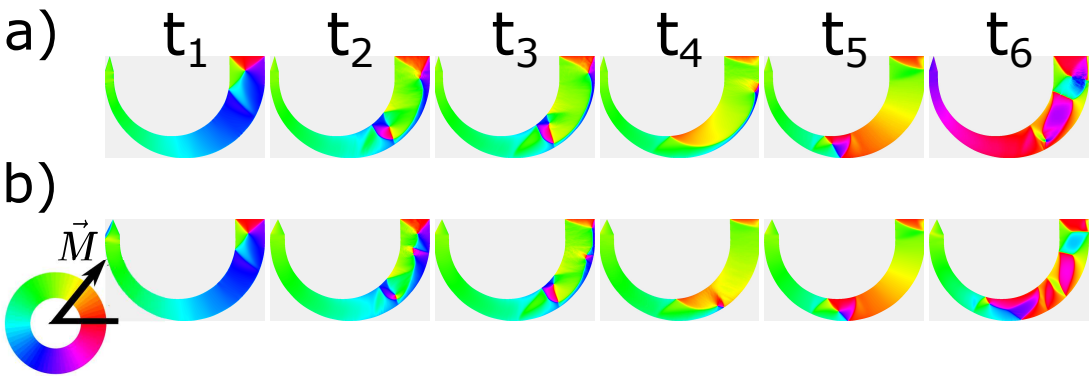

Figure 5.13: Micromagnetic simulations of single HRs with **a)** 300 nm and **b)** 500 nm width at the narrowest part due to different width gradients. The times are indicated in Fig. 5.8b).

tapered end it drags the other adjacent wall. If the attractive interaction is not strong enough to release the other VW from the pinning potential, it is very likely that synchronization happens after the next pulse, since the probability for automotion for a single VW is strongly increased. The overall attractive interaction of the VWs results in a synchronization of the switching pathway of the upper and the lower HRs. We observe a coupling of the switching pathways in HR1 and also in HR5. From the disentangled movies of HR1 shown in Fig. 5.10 we can deduce that the upper and lower HRs switch simultaneously following the same pathway - either pathway 1 or 2 - with a very high probability. However, the relative probabilities for pathway 1 and 2 are not the same if you compare the upper and lower HR of the point symmetric samples at 340 K, as shown at the end of this chapter in Tab. 5.3. This either indicates a reduced coupling for adjacent VWs with opposite chirality or - more probably - it is just a result of the fact that the vertices of the inner perimeters of the HRs are not at the same x position and therefore the distance between the VWs is slightly larger, which reduces the attraction.

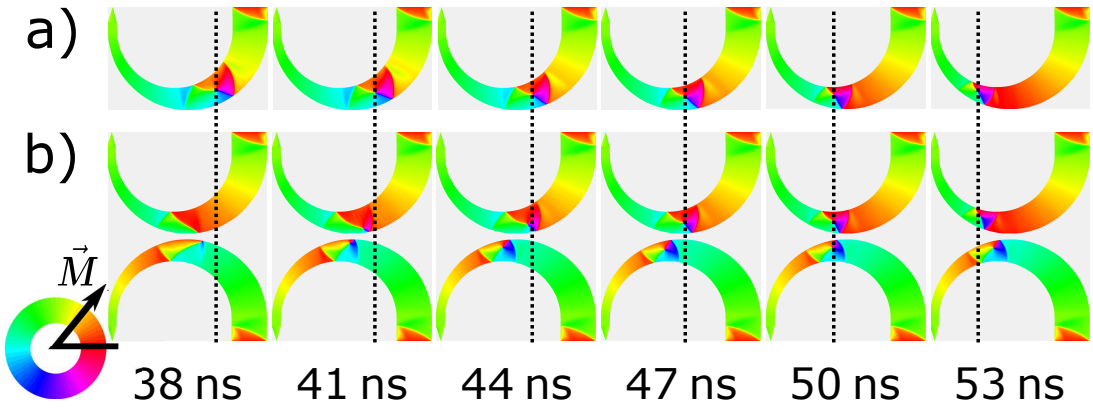

Figure 5.14: Comparison of micromagnetic simulations of **a)** a single HR and **b)** a paired HR with 300 nm width at the narrowest part. The VW in the single HR moves more slowly towards the HR vertex than in the paired geometry, but catches up and even overtakes when no field is applied. The punctuated line indicates the x position of the vortex in the single HR for easier comparison.

Temperature Dependence of Pathway Switching

Finally the energy barrier of the kinetic pinning potential should be determined. To this end time-resolved SEMPA imaging was repeated for HR2 at a cryostat temperature of 158 K and compared to the measurement at 340 K. The magnetization dynamics did not show any significant changes.
Fig. 5.15a) shows single scan SEMPA images of HR2 acquired at 158 K and 340 K. The x-spin asymmetry in the narrower part of the ring is overlaid on the topography image. Again the jumps in contrast indicate a change between the pathways. In Fig. 5.15b) the line profiles indicated in Fig. 5.15a) are shown. As discussed above the line scan reveals the time scale of the changes. Here the time between changes is on the order of tens of ms. The frequency of changes was also determined. To this end, the x-asymmetry image was transformed into a binary image by setting the threshold to the centre between the maximum and minimum asymmetry values. Then the number of jumps in the shown ROI were counted for all acquired scans. Lines with a length of only one pixel have been considered as noise and have not been counted. This leads to an underestimation of the frequency of changes for the samples with a high frequency of changes in the range of one per millisecond. While the magnetization dynamics did not change, the frequency of changes between the two pathways clearly decreased as shown in Tab. 5.2. Knowing the dwell time per pixel and from the number of pixels in the ROI (n_{pixel}) and the number of scans (n_{scans}) the overall time for acquiring all these ROIs is calculated (t_{ROI}). Then one can know the number of cycles (n_{cycles}) fitting into this time. The number of contrast jumps in the upper 'U' and lower 'L' HR is given as $n_{\mathrm{change,U/L}}$ and the probability $P_{\mathrm{U/L}}$ of the event that leads to a change of the pathway by the ratio $n_{\mathrm{change,U/L}}/n_{\mathrm{cycles}}$.

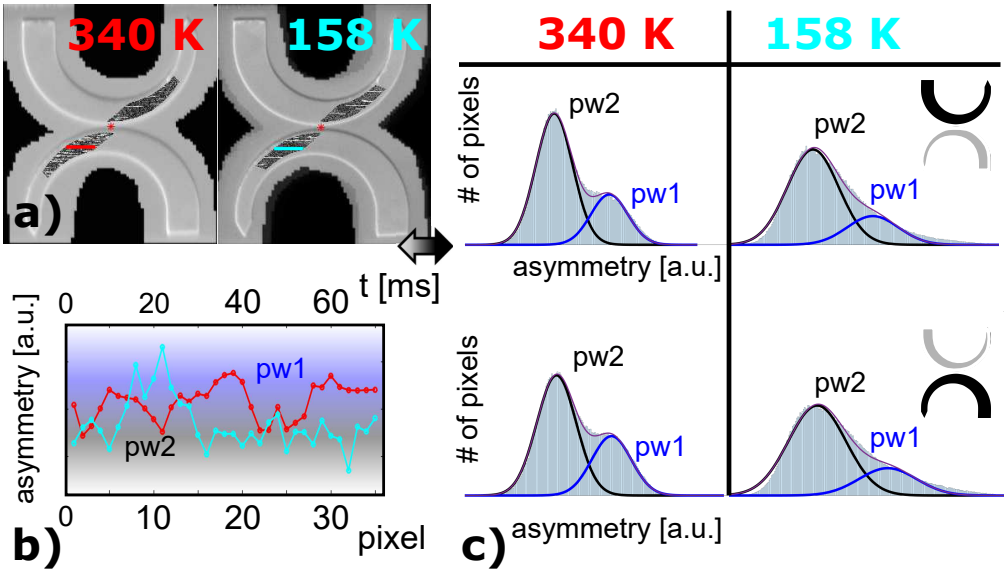

Figure 5.15: **a)** Single scan topography images with x-component SEMPA image overlay of HR2 at 340 K and 158 K. **b)** Line scan indicated in a) showing the different time scales (milliseconds *vs.* minutes compared to Fig. 5.10). Blue background corresponds to pathway 1 (pw1), black to pathway 2 (pw2). **c)** The overall relative occurrence of the two pathways was determined by fitting a double Gaussian function to the asymmetry values in the shown ROI of all scans.

The energy barrier can be calculated by using the Arrhenius law:

$$\tau = \tau_0 \cdot \exp(\Delta E / k_B T) \tag{5.1}$$

The attempt frequency τ_0 has a typical value of 10^{10} Hz in magnetic systems [306] and can be assumed to be independent of the temperature. Using the ratio of the measured probability values $P_{\mathrm{U/L}}$ given in Tab. 5.2 the energy barrier $\Delta E_{\mathrm{U/L}}$ can be determined:

$$\frac{\tau_{158\mathrm{K}}}{\tau_{340\mathrm{K}}} = \frac{P_{\mathrm{U/L},340\,\mathrm{K}}}{P_{\mathrm{U/L},158\,\mathrm{K}}} = \exp(\Delta E / k_B \cdot (\frac{1}{158\,\mathrm{K}} - \frac{1}{340\,\mathrm{K}})) \tag{5.2}$$

Rewriting the formula and inserting the values results in an energy barrier of 3.1×10^{-21} J for the upper HR and 3.0×10^{-21} J for the lower HR.

T [K]	n_{pixel}	n_{scans}	$t_{\mathrm{ROI}}[s]$	n_{cycles} $[10^9]$	$n_{\mathrm{change,U}}$	$n_{\mathrm{change,L}}$	P_{U} $[10^{-6}]$	P_{L} $[10^{-6}]$
340	1324	329	871	5.8	17641	28696	3.04	4.94
158	1103	382	843	5.6	7916	13233	1.41	2.36

Table 5.2: The values given here have been determined to calculate the probability of a change between the pathways and the energy barrier of the kinetic pinning potential.

HR	n_{scans}		$P_{\text{pw1}}/P_{\text{pw2}}$	error
1 (340 K)	326	U	4.43	-
		L	4.43	-
2 (340 K)	329	U	0.38	0.01
		L	0.49	0.01
2 (158 K)	382	U	0.30	0.02
		L	0.30	0.02
5 (339 K)	312	U	0.057	0.003
		L	0.055	0.003
6 (340 K)	298	U	0.40	0.02
		L	0.75	0.05

Table 5.3: The overall relative occurrence of pathway 1 compared to pathway 2 calculated by determining the area under the Gaussian curves for HR2,5,6 as shown in Fig. 5.15. The values corresponding to HR1 were determined by counting the scans with the respective pathway.

To conclude this section we again have a closer look at the probability and coupling of the two pathways. Fig. 5.15c) shows the temperature-dependent frequency of the pathways itself. In Tab. 5.3 the frequency ratio between pathway 1 and pathway 2 for all measured samples is listed. It is determined by plotting the number of pixels of every measured x asymmetry value in the ROI placed in the narrower part of the HR and fitting two superimposed Gaussian curves with the same width to the histogram as shown in Fig. 5.15c). The ratio of the areas below those Gaussian curves is a relative measure of the frequency of the pathways. For HR1 and HR5 both pathways have the same frequency in the upper and lower HR, confirming the prediction that the DWs in the HRs couple *via* stray field interaction. For HR2 and HR6 the measured values at 340 K for the upper and lower HR do not match within the error. Probably the interaction between the VWs is lower if the HRs are arranged in point symmetry and the attractive coupling is decreased for the reasons we described above. However the quantitative analysis of the low temperature measurement of HR2 indicates equalizing of the respective pathway frequency in both HRs. Stray field coupling dominates the dynamics with reduced thermal activation.

5.7 Summary and Significance

In conclusion this study of field-induced magnetization dynamics in permalloy half ring pairs employs a new analysis approach using time-resolved SEMPA imaging that allows in addition to nanosecond dynamic imaging for a quantification of the reliability of the magnetization dynamics. We showed for the first time experimentally the dynamics of chirality rectification in curved wires by dynamic imaging and demonstrated its high reliability compared to rectification at wire ends. These results could be of interest for

chirality-based logic devices and for the community investigating magnetism in planar curvilinear geometries. In addition, different possible pathways between the remnant magnetic states have been detected. With the help of micromagnetic simulations we discussed the origin of changes between the pathways and also quantified the frequency of those changes. Here the geometrical arrangement of the half rings as well as their width gradient play a crucial role. Thermal activation helps to overcome the energy barrier and leads to the pathway changes. By comparing the occurrence frequency of pathway changes at different temperatures the height of the energy barrier was determined. Considering the different options to vary the frequency *e.g. via* tuning the width gradient of the wire, the geometry might serve as a basic geometry for future stochastic unconventional computing devices [97].

6 Field-Angle- and Temperature-Dependent Switching in Asymmetric Rings

Magnetic rings are a promising basic geometry for a variety of device proposals such as magnetoresistive memory [332, 333], spin-based field effect transistors [92, 161], sensors [188] and logic elements [118]. The switching of symmetric magnetic rings in different sizes has been studied in detail in the past decades, as described in Section 1.4. The additional introduction of asymmetries allows for other switching pathways and a controlled selection of the pathway. Asymmetries have been introduced either by notches [331] or gradual width modulation [235]. Here vortex-to-onion switching and even chirality switching between two vortex states using static unidirectional fields could be demonstrated by time-resolved imaging [181, 236]. In this study we investigated field-angle dependent switching in asymmetric rings (ARs) with a gradual width modulation. We demonstrate that by tuning the angle reliably one vortex and both onion states can be obtained in this geometry. This could be of use for concepts like multi-level memories [178] or multi-valued logic [76]. Finally the magnetization dynamics was imaged at different temperatures to investigate the effect of temperature on the nucleation of the onion state and automotion of the domain walls.

6.1 Sample Fabrication, Experiment and Simulation

The samples are fabricated in the same way and with the same materials as the half rings described in Section 5.1. The magnetic asymmetric rings (AR) are placed on a stripline for Oersted field generation. A schematic drawing of the ring geometry is shown in Fig. 6.1. The outer diameter is 5.5 µm and the inner diameter 4 µm. The centre of the inner ring is shifted by 350 nm. Thus the narrowest part of the ring has a width of 400 nm. For the first asymmetric ring AR90 the symmetry axis is aligned parallel to the stripline with the angle between Oersted field and symmetry axis being 90°, for AR75 it is 15°, for AR60 60° and so on till AR0, which is symmetrical to the field axis. The field angle is defined in Fig. 6.1.

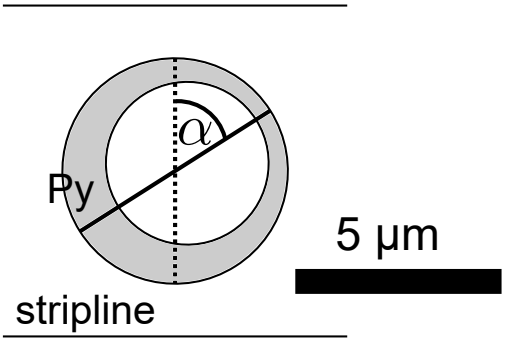

Figure 6.1: Schematic drawing of a permalloy (Py) ring on the stripline and definition of the field angle α..

The experiment is also very similar to the study of the half ring pairs inCh. 5, but we use a bipolar pulse, *i.e.* we have no delay between the first positive and the following reversed pulse. The pulse height is the same as we used in the experiment with the half rings, resulting in a maximum magnetic field of 15 mT. The pulse cycle with a period of 150 ns is again sampled into 75 frames with a length of 2 ns corresponding to the estimated temporal resolution for our SEMPA system (Fig. 3.5).
The time-resolved SEMPA movies of AR90, AR30 and AR0 were compared with micromagnetic simulations performed with Micromagnum [3]. In the first two cases a counter-clockwise vortex was chosen as the initial state, for the 90° tilted ring the dynamic measurement starts with an onion state where the magnetization points mainly in the positive y direction. The time steps in the simulation are 1 ns. In the case of AR90 and AR60 additional simulations have been performed starting with the second reversed pulse and an initial state corresponding to the experimentally observed state at this time. This is explained in the corresponding section. The simulations shown in this chapter have been performed with a damping value of 0.008 [181]. The damping of our permalloy films was determined experimentally using ferromagnetic resonance (FMR)[1]. Fig. 6.2 shows the dependency of the FWHM of the absorption peak on the excitation frequency f_{FMR}. The linewidth is given by

$$\Delta H = \Delta H_0 + 4\pi\gamma^{-1} f_{FMR}, \tag{6.1}$$

with ΔH_0 additional linewidth broadening due to sample and field inhomogeneities and two-magnon scattering. γ is the gyromagnetic ratio. Thus the damping α can be determined from the slope of the linear fit in Fig. 6.2. The value was $(6.5 \pm 0.1) \times 10^{-3}$ for pure Py grown on a naturally oxidized Si substrate. For Py grown on the stripline stack Ta(5 nm)/[CuN(20 nm)/Ta(5 nm)]×5 the damping was enhanced, being $(13.8 \pm 0.2) \times 10^{-3}$. Therefore additional simulations of the asymmetry rings with $\alpha = 0.014$ were compared to the simulations with $\alpha = 0.008$. More details regard-

[1]The author thanks A. Conca, University Kaiserslautern.

ing the general simulation parameters can be found in Section 5.3, since in the half ring study the same materials were used.

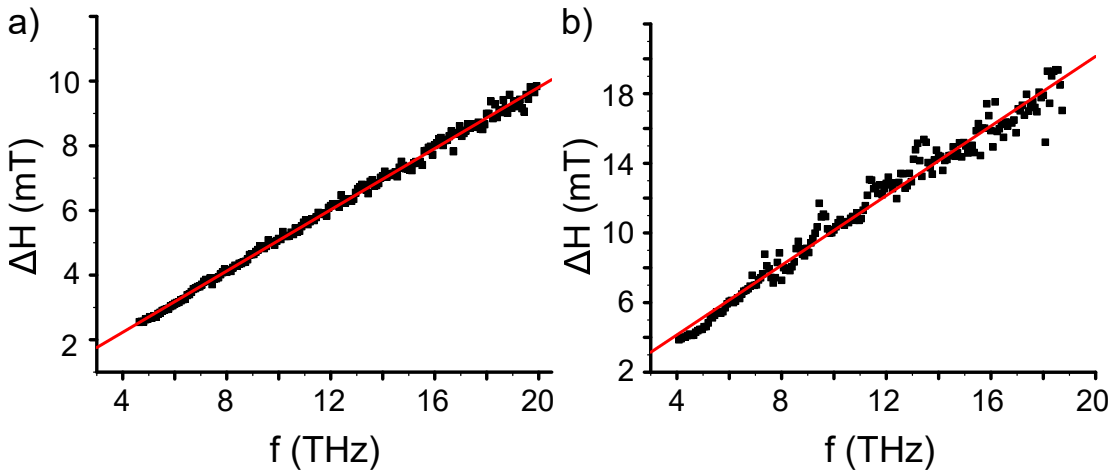

Figure 6.2: Dependence of the FWHM of the FMR absorption peak on the excitation frequency for **a)** a pure $Ni_{80}Fe_{20}$ (30 nm) film directly grown on a naturally oxidized Si substrate and **b)** $Ni_{80}Fe_{20}$ (30 nm) grown on the stripline stack of 3 repetitions Ta(4 nm)CuN(16 nm) capped with 4 nm of Ta. The red line is a linear fit and its slope is proportional to the damping. Note the different scale on the y axis.

6.2 Switching Pathway in Asymmetric Rings with Different Magnetic Field Angles

In this section we describe the influence of the field angle on the switching behaviour of asymmetric rings. First a static SEMPA overview image of the ARs was acquired to determine the as-grown magnetic configuration. The y component of the asymmetry images is shown in Fig. 6.3. Then single-period bursts of the bipolar excitation pulse were applied with opposite polarities and different amplitude. After each burst again an overview image was acquired. For a pulse amplitude that corresponds to a maximum field of 13 mT and positive polarity (up-down pulse) only the ARs with ccw chirality of the vortex state in the as-grown state have switched into a negative onion state. If the direction of the pulse is reversed (down-up), then the ccw vortex state switches into a positive onion state, while the ARs starting with a negative onion state (AR45 and AR0) show again their initial vortex state with the initial chirality. This is repeated with 19 mT maximum field. Here more rings show an onion state after the bipolar pulse burst. Taking also the overview images acquired after 15 mT pulses into account, it is striking that in particular the ARs with a low angle α switch for both pulse polarities into onion states. This hypothesis is confirmed by the lowest overview SEMPA measurement shown in Fig. 6.3 that is acquired during the continuous application of bipolar pulses

(up-down-off). The static SEMPA measurements after single excitation bursts indicate asymmetric switching fields for vortex-to-onion switching depending on the initial vortex state chirality if the symmetry axis is not aligned with the field.

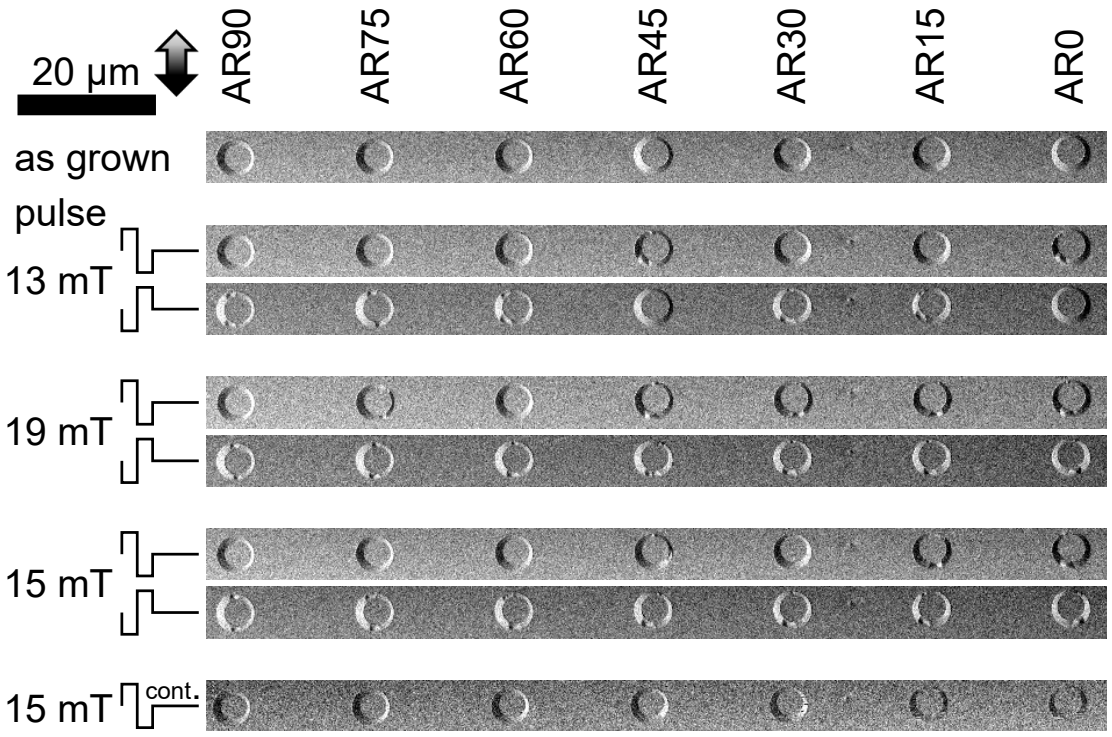

Figure 6.3: Initial static SEMPA measurements of the ARs on the stripline in the as-grown state showing the chirality of the initial vortex state, after single-period bipolar pulse excitations (13 mT, 19 mT and 15 mT with opposite polarities) and during continuous excitation of 15 mT.

To understand the underlying switching mechanism time-resolved SEMPA imaging was performed during continuous pulsing with a maximum field of 15 mT. Before starting the pulse train, all rings have been in the same magnetic vortex configuration with the same ccw chirality. Fig. 6.4a) shows selected time frame SEMPA images of the final movies of AR90, AR30 and AR0. The magnetization direction is colour-coded. The corresponding times are indicated in Fig. 6.4b), together with a plot of the measured excitation pulse. First it is striking that the magnetic states of AR30 and AR0 before the first pulse at t_1 are not equal to the initial vortex state but are negative onion states. We will explain this further down. All ARs have in common the nucleation of VWs during the first pulse and the formation of a positive onion state (t_2-t_4). If the symmetry axis of the AR is not equal to the field axis, then the wider side (in this case the left side) of the AR is energetically preferred for the nucleation process. In AR0 the nucleation is visible in both halves of the AR. The nucleation occurs *via* the formation of ripple-like

structures, as has been shown in [236]. The nucleated VWs travel to the upper and lower vertices of the ring. The field pushes the vortex cores of the walls towards the outer perimeter of the ring (t_3). When the field decreases the vortex cores relax back to a position in the centre of the wire (t_4), however, while the inner half antivortex is still at the vertex of the inner perimeter, the vortex cores stay in the left half of the ring for AR90 and AR30. Therefore the reverse field during the second pulse moves the VWs back into the wider part where they annihilate again (t_5). While AR90 stays in the ccw vortex state, in AR30 and AR90 VW nucleation is visible. AR30 indicates the formation of the ripple-like concertina pattern (t_6) and VW nucleation (t_7) in the side of the ring where no annihilation occurs. Note that compared to the nucleation process visible in t_2 the nucleation position is displaced a bit towards the wider part of the AR. In the case of AR90 the ring width in that other side is just too narrow to allow for VW nucleation. The demagnetization field energy here still dominates over the Zeeman energy term. This results in a steady-state equal to the initial ccw vortex state before starting the pulse train for AR90 and AR45. In contrast, the right half of AR30 and AR0 as shown in Fig. 6.4a) is wide enough to allow for re-nucleation of an onion state with the opposite direction. Therefore the steady-state for the rings where the field is applied in an angle of $\alpha \leq 30°$ is a negative onion state. AR90 is therefore a representative of vortex-to-onion-to-vortex switching, while AR0 represents onion-to-reversed onion-to-onion switching. For AR30 the field angle is just at the transition of these switching types, as we will show in the next section.

The experimental SEMPA results were compared with micromagnetic simulations. The advantages of simulations include the higher resolution and the possibility to start from defined steady-state magnetic configurations at any time during the excitation period, which is not possible in the experiment. In the following we will discuss the simulations and compare them for every single AR shown in Fig. 6.5. First we consider AR90. Here the choice of the initial state t_1 as ccw vortex state in the simulation is unambiguous. The dynamics during the first pulse match qualitatively the experimental observations. Both show the formation of a positive onion state. However, in the simulation 'sim. 1' the VWs move further than the upper vertex of the ring and annihilate in the right half of the ring during the second pulse. Therefore the wider left side of the ring is available for re-nucleation of VWs and the formation of an onion state with the opposite direction (t_7). The reduced pinning and the related stronger motion of the VWs in the simulations result from neglecting any material imperfections. To investigate the influence of the magnetic configuration of the AR after the first pulse at time t_4 on the switching dynamics, we started a second simulation 'sim. 2' with the onset of the second pulse. The initial state was chosen to be equal to the experimental state at t_4, where the VWs are still in the left half of the ring. Indeed the observed dynamics here match the experimental data, so that the annihilation occurs in the wider half of the AR and a ccw vortex state forms. The simulation of AR30 was also started with a ccw vortex state, although the experiment shows an onion-like state with two VWs placed in the right half of the ring at t_1. However, these VWs annihilate immediately with the onset of the first pulse in the SEMPA movie, so that we can neglect potential effects of the annihilation

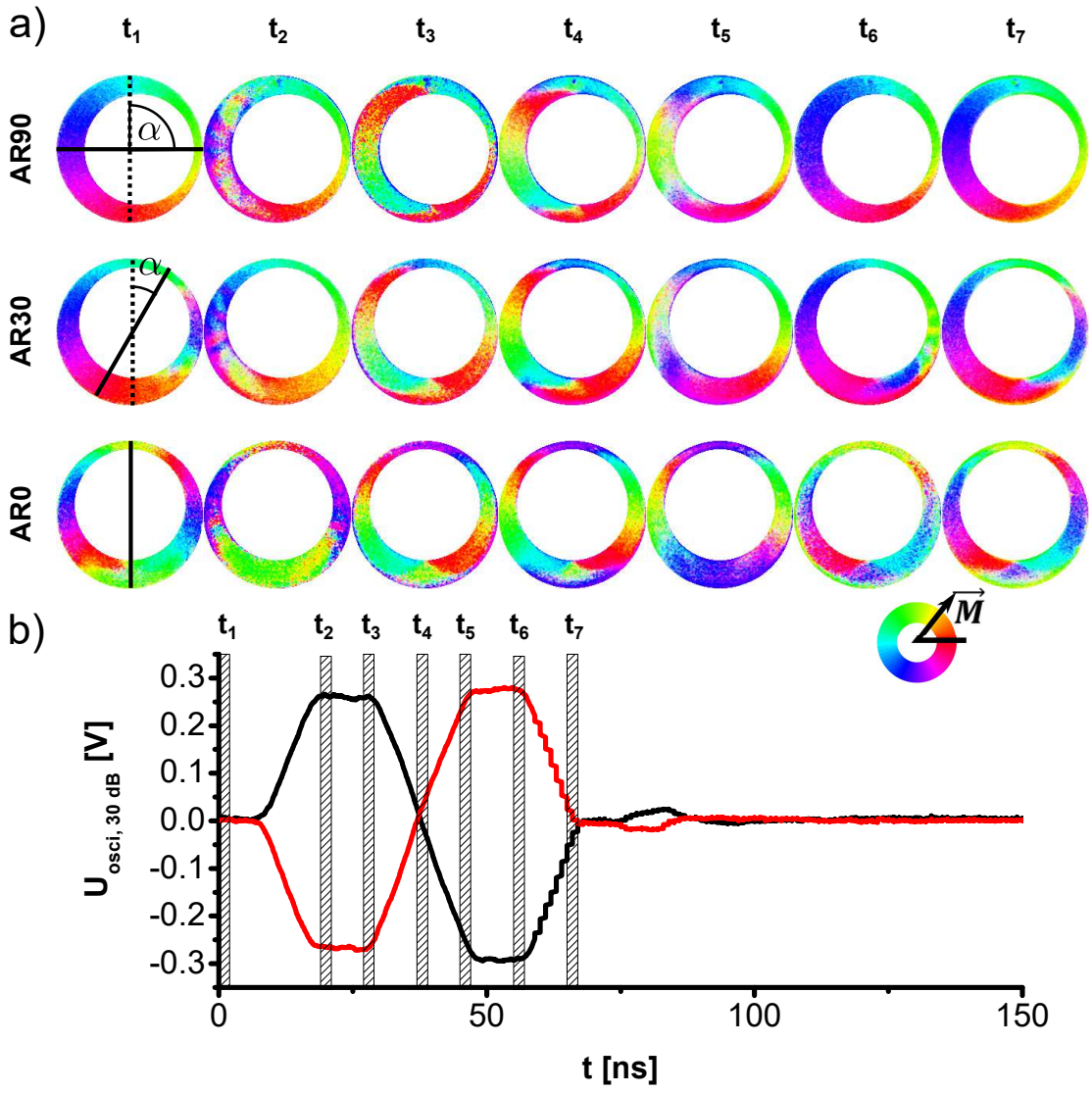

Figure 6.4: **a)** Selected time frames t_1-t_7 from the dynamic SEMPA movie for three different ARs with different field angles. The colour-coding of the images indicates the magnetization direction. **b)** Bipolar excitation pulse of the push-pull circuit. The two lines show the voltage attenuated by 30 dB before and after the sample. The time frames corresponding to the images shown in a) are indicated.

in the right side on the nucleation of new VWs in the left side. The nucleation of two VWs in the left side leads to a positive onion state as in the experiment. However, this match is only qualitative since especially the upper VW moves further into the right half of the ring in the simulation. Thus the dynamics during the second pulse were simulated twice, first as a continuation of 'sim. 1' and then starting at t_4 with another state comparable to the magnetic state visible in the SEMPA image. In 'sim. 1' the onion state undergoes 180° rotation during the second pulse. During this process one of the VWs splits up into a double vortex wall (t_7), which merges again. However for 'sim. 2', in contrast to AR90 and also in contrast to the experimental movie of AR30, during the second pulse only the VWs annihilate but no re-nucleation occurs in the right half. This indicates thermally assisted domain wall nucleation. Temperature effects are not considered in the micromagnetic simulations. Beside the field angle the temperature is another parameter to control the switching behaviour, as we will demonstrate in the next section. The mismatch between simulation and experimental direct imaging emphasizes the necessity of experimental determination of the switching pathways with real samples. The simulation of AR0 was initialized with a negative onion state. This initial state was generated by applying a field to the ring in the ccw vortex state. The position of the VWs is difficult to determine, because the SEMPA movie shows two superimposing pathways similar to the half ring study discussed in Ch. 5, as we will show further down. In the simulated AR one VW is trapped at the position where the ring width is the smallest, while the other domain wall is pushed by the field pulse *via* one of the ring halves towards the narrowest part, too. There both VWs annihilate. In the meantime new VWs are nucleated in the other ring half. For AR90 onion-to-reverse onion switching was observed in the experiment as well as in the simulation.

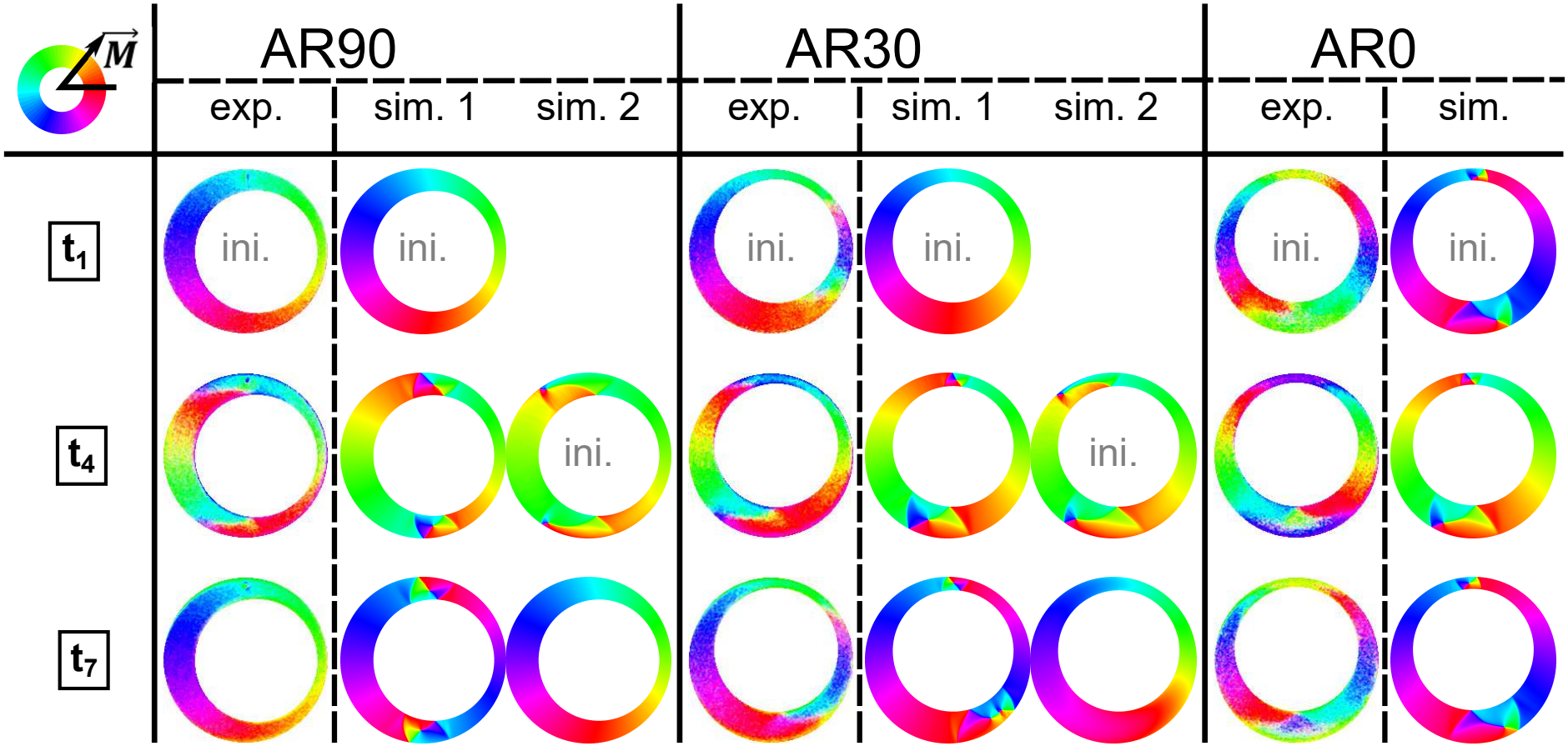

Figure 6.5: Measured and simulated magnetic states of AR90, AR30 and AR0 just before the first pulse (t_1), between both pulses (t_4) and after the second inverted pulse (t_7). For AR90 and AR30 two simulations have been performed since the simulation covering the full excitation period diverges from the observed dynamics in the SEMPA movies. 'sim. 1' starts with the onset of the first pulse while 'sim. 2' starts with an initial state corresponding to the experimentally observed magnetic configuration with the onset of the second pulse.

Another effect that becomes visible in all simulated rings due to reduced pinning is width-gradient driven automotion of the VWs. As a result of this effect the onion state is not stable in the simulated rings but relaxes *via* automotion into a vortex state. However, in the simulations that were performed with the enhanced damping values of $\alpha = 0.014$ and $\alpha = 0.016$, automotion was largely suppressed while the field-driven nucleation mechanism was the same. Fig. 6.6 shows for all damping values approximately the same magnetic state after the first pulse (t_4). At t_5 for $\alpha = 0.008$ the VWs move along the width gradient into the right half of the ring, while in the left half new DWs are nucleated. For $\alpha = 0.016$ no automotion into the narrower half of the AR occurs, but the DWs annihilate and the vortex cores of the VWs are expelled at the inner perimeter of the ring. For $\alpha = 0.014$ the upper VW is pinned and the lower one moves towards the right. The magnetic configuration at t_7 crucially depends on the occurrence of automotion. The experimental SEMPA movies show higher agreement with the simulations with enhanced damping values. This is also in accordance with the measured damping of the full thin film stack using FMR. Thus beside pinning due to sample imperfections a higher damping value can also be the reason for a reduced probability for gradient-driven automotion.

As mentioned before, it is impossible to determine the exact VW positions in AR0. This suggests the possibility of different superimposing pathways. Using the method developed in the last chapter we look again at the single scan images for indications of different pathways. Fig. 6.7a) shows the x asymmetry image of one scan for every imaged AR. AR90 and AR45, where the field axis is far from being parallel to the SR symmetry axis, show clear vortex states. In contrast, AR15 and AR0, where the field orientation is close to the AR symmetry axis, show a negative onion state. The most striking feature for the ARs with $\alpha \leq 30°$ is sudden contrast jumps between positive and negative asymmetry values at the ring vertices. These indicate different VW positions. The steady-state position of the VWs depends on the position where the VWs have been nucleated. If the nucleation takes place in the right half, then the VW stays at the right of the vertex and correspondingly for the left side. The apparent simultaneous nucleation of VWs in both ring halves in the SEMPA movie hides the fact that nucleation only occurs in one side of the ring during each pulse. In general the VWs do not move beyond the vertex - with rare exceptions leading to a change of the pathway, indicated by the abrupt contrast jumps. The relative occurrence of both pathways was estimated in the way as described in the last chapter. To this end the values of x asymmetry values in a symmetrically placed area at the lower vertex were plotted in a histogram, as shown in Fig. 6.5b). A superposition of two Gaussian curves was fit to the histogram. The ratio of the areas of those Gaussian curves is a measure for the relative occurrence of both pathways. The relative occurrence for AR15 was determined to be 60:40% and for AR0 55:45%. with an error (95% confidence interval determined from the Jacobian of the nonlinear least square curve fitting) of $< 0.3\%$. It is comparable due to the orientation of the symmetry axis compared to the field axis. Material imperfections and pinning centres lead to a preference of one pathway over the other. A change between pathways occurs every tens of milliseconds. For AR30 it is more difficult to analyse

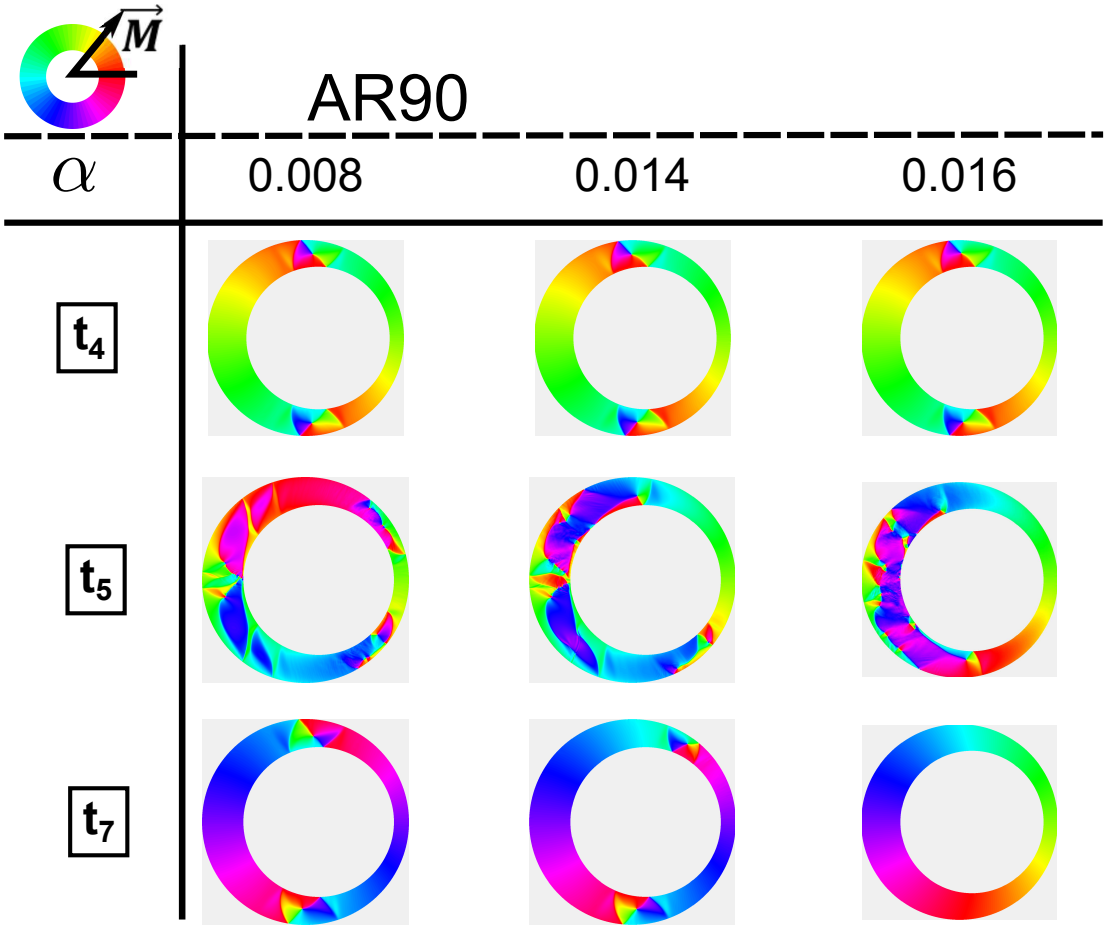

Figure 6.6: Micromagnetic simulations of AR90 with different damping values $\alpha = 0.008/0.014/0.016$. 3 time frames at the start (t_4), during (t_5) and after (t_7) the second pulse are shown. For higher damping values, automotion is suppressed.

the histogram properly. In this AR, automotion of the lower VW over a short distance is visible in the SEMPA movie and therefore the VW is usually displaced towards the right. Therefore the apparent magnetic configuration in Fig. 6.7a) is neither a clear onion nor a clear vortex state. It rather looks like a vortex state with discontinuities in the magnetization. This is also the reason for the apparent relative occurrence of 2:98%($\pm$1%). Indeed, the nucleation of VWs in the narrower half of the ring is expected to be suppressed, however due to the automotion the absolute values determined by the Gaussian fit have to be interpreted very carefully.

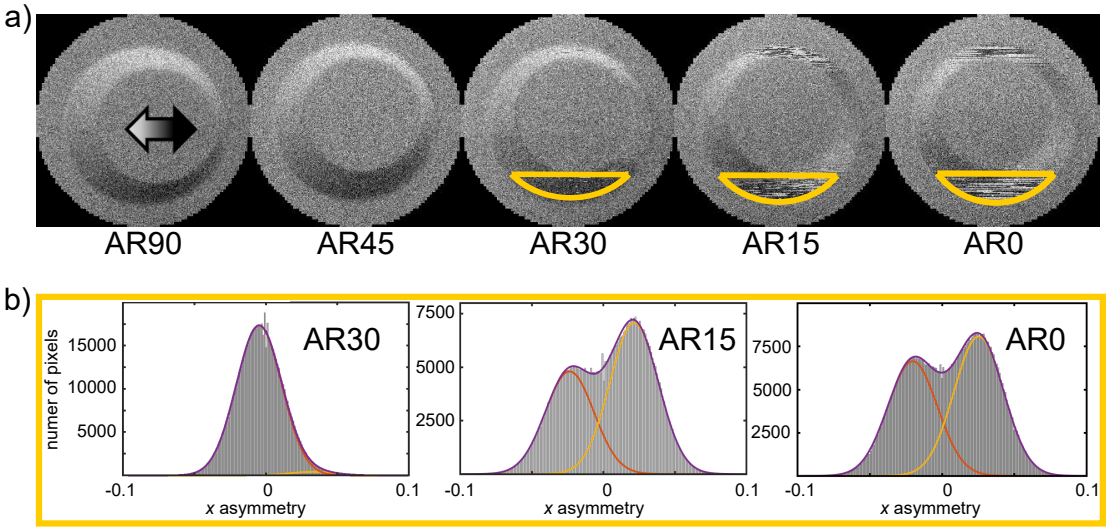

Figure 6.7: **a)** Single scans of the imaged ARs. A clear vortex state is visible in AR90 and AR45, in AR15 and AR0 the overall configuration is an onion state. Abrupt contrast changes at the vertices of the ARs with $\alpha \leq 30°$ indicate changes of the switching pathway. The area at the lower vertex (orange) was used to determine the relative occurrence of the pathways. **b)** Resulting histogram counting the number of pixels with the same x asymmetry values. Two superimposing Gaussian curves were fit to the histogram. From the area below the curves the relative occurrence of the pathways can be calculated. For this analysis all scans of the SEMPA acquisition were considered.

Overall, this study demonstrates the possibility to change the switching type and the magnetic states accessed in an AR system by tuning the field angle carefully. Further we have shown multiple possible pathways for ARs with their symmetry axis close to the field axis. However, the general magnetic states between the switching are the same, while details like the chirality of the domain walls will differ due to a curvature dependent chirality preference in the nucleation process and depending on the mechanism of switching (nucleation or rotation).

6.3 Temperature-Dependent Switching Pathway Probabilities in a Tilted Asymmetric Ring

By comparing the experimental SEMPA movies with the simulation results it is obvious that thermal excitations play a crucial role in the nucleation of VWs. AR30 was selected to be imaged at different temperatures due two reasons: First, for AR30 the field angle is just at the transition between vortex-to-onion-to-vortex switching and onion-to-reverse onion-to-onion switching and second, in this specific sample automotion has been observed for the lower VW. In this section we analyse the effect of temperature on automotion and the switching type. AR30 was imaged at a temperature of 340 K,

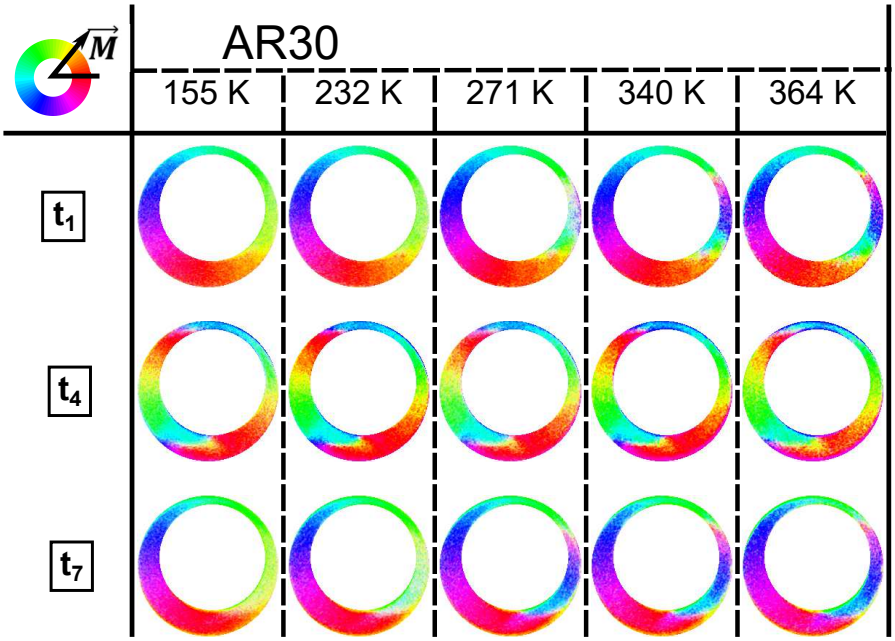

Figure 6.8: Measured magnetic states of AR30 at different temperatures (155 K, 232 K, 271 K, 340 K and 364 K) just before the first pulse (t_1), between both pulses (t_4) and after the second inverted pulse (t_7). The magnetization direction is colour-coded and the absolute value of the asymmetry $\sqrt{A_x^2 + A_y^2}$ indicated by the opacity of the colour.

232 K, 271 K, 155 K and 364 K (in this order) while applying the excitation as before. Fig. 6.8 shows the colour-coded magnetic states of AR30 at times t_1, t_4 and t_7 in the same table presentation as shown in Fig. 6.5. The magnetization configuration at t_4 after the first pulse is for all temperatures the same. However, for t_7 directly after the second pulse, for low temperatures a ccw vortex state is visible, while for high temperatures VWs have nucleated and reside in the right ring half. For low temperatures vortex-to-onion-to-vortex switching dominates as is the case in the corresponding simulation, where no thermal effects are considered, and with increasing temperature the probability for onion-to-reverse onion-to onion switching increases. The absolute asymmetry value $\sqrt{A_x^2 + A_y^2}$ is indicated by the opacity of the colour. It is proportional to the normalized reduced magnetization $M_{\text{red.}} = M_{x,y}/M_{\text{S}}$ and can serve as a measure of the in-plane component of the magnetization or under certain conditions, which we will explain later, as a measure of probability for two superimposing pathways. The difference in the opacity in the lower right quarter of the AR comparing t_1 and t_7 at 155 K, 232 K and 271 K is visible and demands an explanation.
To this end we look at the temporal evolution of the normalized reduced magnetization, which is shown exemplary for $T = 271$ K in Fig. 6.9a) starting immediately after the second pulse at 68 ns. The total asymmetry was determined from the scatter plot based on

the measured asymmetry values of the left, wider AR half, as described in Section 2.6.2. Here a grey scale representation is used where pixels with $\sqrt{A_x^2 + A_y^2} \geq 1$ are white and black indicates $\sqrt{A_x^2 + A_y^2} = 0$. The darkest features within the ring correspond to the VW positions. The lower one clearly moves over a small distance and then becomes pinned, which can be explained by width gradient-driven automotion. Furthermore, the area between the domain walls darkens with time. As already mentioned above, these images can be a measure of different pathway probabilities even if the dynamics is not recognized directly in the movie. Several assumptions are made to make this claim:

1. Based on the simulations and the other experimental results we assume that the dynamics in the left half of the ring is always the same to first approximation. This allows me to take the total asymmetry value determined in this area as a reference, where $P = 1$.

2. The two possible magnetic steady-states after the second pulse - a ccw vortex and a negative onion - have an anti-parallel magnetization direction. This allows for a simple estimation of the probability. In particular, only two superimposing magnetic states can be distinguished.

3. Based on the colour-coded SEMPA image one needs to judge carefully to which state the determined probability $P = P_{\text{meas}}$ belongs to. The other one then has the probability $P = 1 - P_{\text{meas}}$.

Fig. 6.9b) shows the average of these probabilities P_{onion}, measured in ROI 2 indicated in the SEM image and divided by the average probability in ROI 1 in the left AR half for all temperatures after the second pulse. The time where the magnetic field is still applied is hatched. The probability values determined during field application can not be compared to the values in the field free time due to shifts in the detector asymmetries. However, the other values are comparable and show a general trend of increasing probability of the onion state P_{onion} directly after the pulse with increasing temperature. The slightly reduced probability in the case of 340 K and 364 K might result from non-ideal placement of ROI 2 including also parts of the VW, where the exact position is not reliable. Another striking feature is the decreasing absolute value of the asymmetry[2]. This can be interpreted as gradient-driven automotion that changes the magnetic state from an onion back to a vortex. While in the majority of all cases the VWs become pinned at the positions indicated by the very dark pixels, sometimes automotion leads to annihilation of the VWs and results in a ccw vortex state. A higher probability for automotion with increasing temperature could be explained by thermally assisted depinning from shallow pinning potentials. The difficulty here is to explain the reduced automotion probability for 340 K and 364 K. One might suspect structural changes due to heating that lead to additional pinning centres, but this explanation is

[2] In the colour-coded images in Fig. 6.8 the opacity increases between t_7 and t_1, but here the vortex state is dominant and therefore the opacity corresponds to P_{vortex}. In the referred graph $P_{\text{onion}} = 1 - P_{\text{vortex}}$ is plotted.

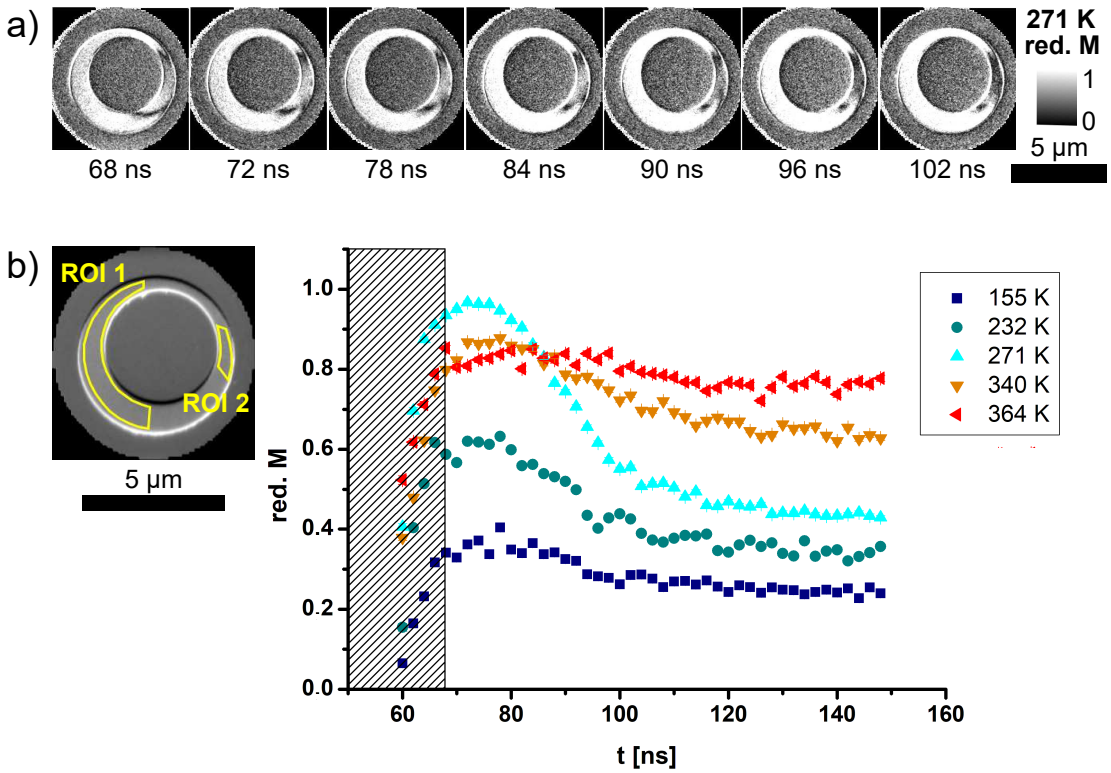

Figure 6.9: **a)** Grey scale images of the normalized reduced magnetization of AR30 at 271 K, serving as a measure of the probability of the observed magnetization dynamics. The reliability of the VW position is very low. The area in between the walls gets darker after the pulse, indicating automotion. **b)** The probability P_{onion} for an onion state inferred from the average pixel asymmetry value ratio of ROI 2 and ROI 1. The probability increases with increasing temperature. The probability for automotion including annihilation of the VWs peaks for this sample at 271 K.

not satisfying since the first measurement was performed at 340 K. Without a systematic investigation considering more samples the answer to this question must remain open at this stage.

6.4 Summary and Outlook

In this work we have shown field orientation dependent switching in asymmetric permalloy rings. If the field angle relative to the symmetry axis of the asymmetric ring is high, *i.e.* for our geometry and field $\alpha \leq 30°$, the magnetization switches from a vortex state to an onion state and back, otherwise onion-to-reverse onion switching was observed. In the latter case again two different pathways could be seen using the analysis ap-

proach described in Ch. 5, however the overall resulting remnant states do not change, which is advantageous for possible devices based on this geometry. Possible applications include multi-level computing devices, chirality dependent logic and stray-field based rotation sensors. The second part of this study investigated the temperature dependence of the switching with the field oriented 30° towards the symmetry axis. For lower temperatures vortex-to-onion-state switching was preferred, while at room temperature onion-to-onion switching was more probable due to thermally assisted domain wall nucleation. Recently emerging fields based on stochastic effects such as non-conventional computing could make use of these kind of thermally assisted transitions.

7 SEMPA Imaging of (Quasi-)Antiferromagnetic Heterostructures

While SEMPA is a strong imaging technique for ferromagnets, at first glance, it seems not to be interesting for the emerging field of antiferromagnetic spintronics. In antiferromagnets such as Mn_2Au the magnetic moments compensate and no magnetic signal is detected. However, for FeRh, a material with a transition temperature of 350 K between the antiferromagnetic and ferromagnetic phase, ferromagnetic domains have been observed at the surface even in the antiferromagnetic phase due to the extremely high surface sensitivity of SEMPA [330]. Konoto *et al.* successfully demonstrated SEMPA imaging of layered $La_{1.4}Sr_{1.6}Mn_2O_7$ antiferromagnetic stacks [149]. An artificial antiferromagnetic order can also be mimicked in a single layer. In Section 7.1 we investigated magnetic films with alternating magnetization direction in adjacent domains and therefore quasi-antiferromagnetic properties together with colleagues from Mainz and the Kyushu University [199, 329]. Another interesting approach is the use of rare-earth ferrimagnets to investigate the physics of antiferromagnets, since in this case the magnetic properties can be tuned *via* stoichiometry or temperature from ferromagnetic to antiferromagnetic properties at the compensation point, where the magnetic moments of the 3d ferromagnet and the rare earth compensate. For these materials one expects a magnetic signal in SEMPA images even at the compensation point, since SEMPA is mainly sensitive to the spin polarization from electrons in the transition metal d-bands while the strong inner shell magnetic moments of the localized rare earth ferromagnets are not detected [211]. This was shown in a study investigating TbFeCo thin films [7]. In Section 7.2 we show the feasibility of imaging skyrmion bubbles in GdFeCo. A last, albeit indirect, method to apply SEMPA for investigating antiferromagnetic materials is imaging a thin ferromagnetic layer that was deposited on top of the antiferromagnet and couples to it. This was demonstrated on imaging a Cr wedge covered with 1 nm Fe [294] and a NiO(001) surface covered with 0.9 nm Fe [180]. We applied this technique to the recently intensively investigated metallic antiferromagnetic material Mn_2Au (Section 7.3).

7.1 Quasi-Antiferromagnetic Layers Using Biquadratic Coupling

In 1996 it was found that a DC current flowing through an interface of a normal and a ferromagnetic layer can stimulate spin wave emission [271]. Such spin torque oscillators (STOs) can be used as microwave generators [23] or as an alternative to magnetoresistive sensors for the detection of the stray field of magnetic bits, since an external field shifts the oscillation frequency [36]. Besides high magnetic sensitivity and spatial resolution, a high measurement speed of these sensors is required. To this end the use of antiferromagnetic oscillators was proposed, since here the oscillation speed is several orders of magnitude higher than in ferromagnets [46]. While spin-transfer torque has been investigated theoretically [173, 209, 313] and experimentally [45, 192, 193, 296, 314], STOs have not been achieved yet, because the adjacent antiferromagnet atoms are strongly coupled *via* the exchange interaction. An intermediate step towards an antiferromagnetic STO is the use of a biquadratically coupled layer in a thin film stack [13]. Here the domains are alternating antiparallel and the stray field is reduced. Thus the oscillation frequency is expected to be higher than in conventional ferromagnetic multilayers. Due to the high surface sensitivity of SEMPA this technique has contributed significantly in the investigation of thin film systems [113]. Biquadratic coupling was shown by SEMPA imaging in trilayers such as Fe/Cr/Fe [225, 226] and Fe/Mn/Fe [227, 288]. In this work we focused on multilayers where the 90° coupling is mediated *via* an oxide layer. I performed the magnetic SEMPA imaging together with my colleague Pascal Krautscheid and the other experiments and simulations have been done by our Japanese colleagues. This chapter is based on the articles describing the joint research project [199, 329]. A subsequent publication focuses on the high frequency properties of the investigated stacks [115].

Samples

The thin film stacks investigated in this section were fabricated by our Japanese colleagues at Kyushu University [199, 329] and are shown in Fig. 7.1: a) Ta(5 nm)/Ru(2 nm)/$Ir_{22}Mn_{78}$(5 nm)/$Co_{90}Fe_{10}$[A](2 nm)/Fe-O(2 nm)/$Co_{90}Fe_{10}$[B](2 nm)/Cu(6 nm)/$Co_{90}Fe_{10}$[C](2.5 nm)/Cu(1 nm)/Ta(5 nm) and b) Ta(5 nm)/$(Ni_80Fe_20)Cr_40$(5 nm)/Co_90Fe_10(1 nm)/$Ir_{22}Mn_{78}$(5 nm)/$Co_{90}Fe_{10}$[A](2 nm)/Fe-O(2 nm)/$Co_{90}Fe_{10}$[B](2 nm)/Cu(6 nm)/$Co_{90}Fe_{10}$[C](2.5 nm)/Cu(1 nm)/Ta(5 nm). The stacks differ in their buffer layer grown on the thermally oxidized Si substrate. In one case, Ta/Ru, a typical buffer layer for fcc stacked layers was used and in the other case Ta/NiFeCr/CoFe. NiFeCr as buffer material increases the grain size of the films deposited on top [162]. On top of the buffer material antiferromagnetic IrMn provides the exchange bias for the pining of the fixed ferromagnetic layer [A]. The exchange bias direction was set by annealing the sample after deposition of all layers in a magnetic field of 4.1 kOe at 270°C for one hour. The second ferromagnetic layer [B] couples *via* Fe-O by 90° coupling [157]. For the fabrication of the oxide layer oxygen was pumped into the vacuum chamber after the deposition of Fe_3O_4. In the third ferromagnetic layer

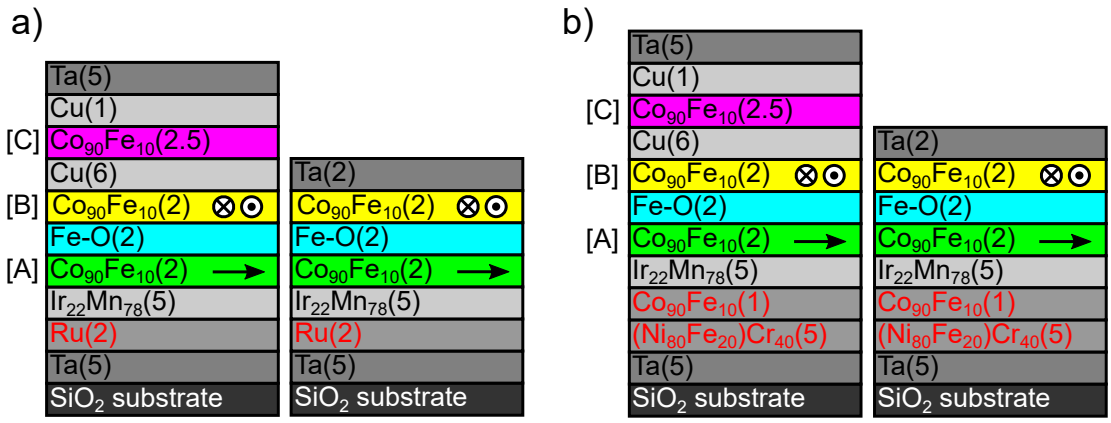

Figure 7.1: Schematic drawing of the investigated stacks with **a)** Ru buffer layer and **b)** NiFeCr buffer layer. For the SEMPA imaging of the quasi-antiferromagnetic layer (yellow) the reduced stack without ferromagnetic free layer (pink) was grown.

[C] the magnetization direction is free to rotate in an external field and can be used for magnetoresistance measurements. However, for SEMPA imaging reduced stacks without the third CoFe layer were grown (also shown in Fig. 7.1), since the interest was in the detailed domain pattern of the second CoFe layer [B].

Magnetic Hysteresis and Magnetoresistance Measurements

The full stacks were pre-characterized by vibrating sample magnetometry (VSM) [83] and magnetoresistance measurements. The results are shown in Fig. 7.2. The exchange bias field of IrMn can be determined from M-H measurements with the magnetic field direction parallel to the direction of the annealing field. As shown in Fig. 7.2a), in the stack with Ru buffer the exchange bias field is approximately 320 Oe and in the stack with the NiFeCr buffer it is 90 Oe. The 90° magnetic coupling energy was determined by M-H measurements perpendicular to the annealing field direction. Fig. 7.2e) shows schematically the magnetization direction in the three ferromagnetic layers at different stages in the magnetic field loop (i)-(iv) indicated in Fig. 7.2b) and d). For high magnetic fields in the y direction the magnetization is parallel to the applied field in all layers ((i) and (iii)). For lower fields the CoFe [A] layer aligns with the exchange bias field while the magnetization of the second layer [B] couples to it *via* 90°. The free layer´s magnetization follows the field direction. When the magnetization in the three layers is not orientated parallel, the MR ratio increases as shown in the lower graphs of Fig. 7.2a)-d). Both hysteresis and magnetoresistance measurements showed symmetric behaviour for positive and negative fields and thus 90° magnetic coupling between the layers [A] and [B] can be concluded. The coupling energy in the sample with Ru buffer corresponds to a magnetic field of 50 Oe, while the sample with the NiFeCr buffer has a stronger 90° coupling corresponding to a field of 100 Oe. At these fields the biquadratic coupling is

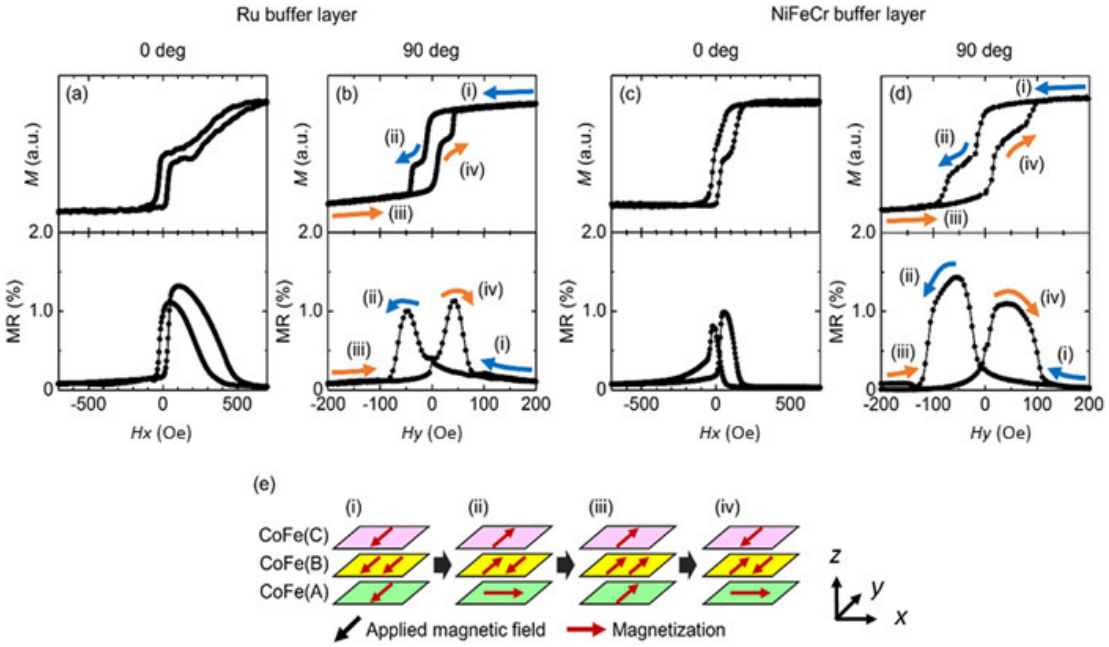

Figure 7.2: Magnetic hysteresis loops measured with VSM and corresponding magnetoresistance measurements of the stacks. The magnetic field is applied parallel to the annealing field in **a)** and **c)** to determine the exchange bias field and perpendicular to the annealing field in **b)** and **d)** to quantify the 90° coupling energy. In **e)** the magnetization switching of the three ferromagnetic layers for a perpendicular field loop is shown schematically. The pictures (i)-(iv) correspond to (i)-(iv) in b) and d). (Reprinted with permission from [199].)

broken.

Measurement of the Magnetization Direction with SEMPA

While the magnetoresistance and hysteresis loop measurements confirm the biquadratic coupling of the stacks, the detailed domain pattern can only be assessed *via* magnetic imaging. To this end the reduced stack without a free layer were used. The Ta(2 nm) capping, which was used to prevent oxidation of the CoFe layer, was removed using Ar milling with an energy of 1 kV. The milling time was 3 nm/hour. With this low rate damage of the layers should be avoided.
Fig. 7.3 shows SEMPA images of the reduced stacks with Ru and NiFeCr buffer layer. First we note the worm-like pattern in the sum image of the Ru buffer sample. This pattern was observed after electron beam exposure of the film. A clear difference of the topography can be seen depending on the exposure time in Fig. 7.4a). To exclude a magnetic origin of the contrast an overview image with the in-lens detector of the SEM was acquired after imaging a smaller area inside the FOV of the overview, as shown in Fig. 7.4b). This unintended structuring effect could be attributed to a still remaining

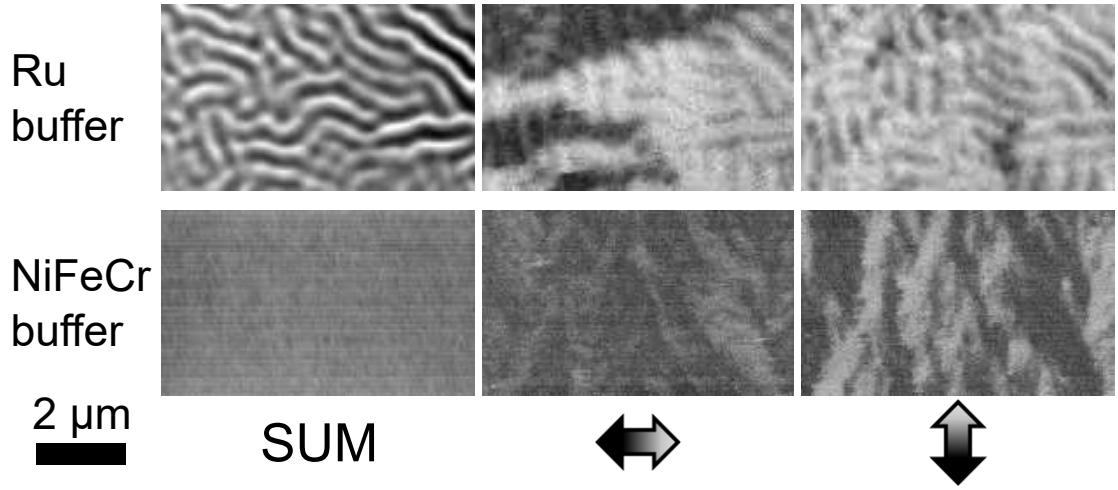

Figure 7.3: SEMPA images of $Co_{90}Fe_{10}$ [B] of the stack with Ru (upper row, $U_{\mathrm{EHT}} = 7.5\,kV$, $t_{\mathrm{dwell}} = 200\,ms$) and NiFeCr buffer layer (lower row, $U_{\mathrm{EHT}} = 7.5\,kV$, $t_{\mathrm{dwell}} = 10\,ms$). Sum and asymmetry ($x$ and y component) images are shown. The arrows indicate the magnetization direction.

very thin layer of Ta and bad adhesion on $Co_{90}Fe_{10}$. The same effect was observed during imaging of ferrimagnets, which were intentionally imaged through very thin layers of Pt to maintain the DMI (Section 7.2). For a deeper understanding of this effect other imaging techniques such as atomic force microscopy should be employed.
While the sum image changes, the overall domain pattern and the domain size does not change significantly. The other sample with NiFeCr buffer was probably milled further into the ferromagnetic layer and therefore this effect was not observed. First we compare the domain size of the CoFe [B] layers in both samples. The domains in the Ru buffer sample have a size of approximately 1 µm, while the domain size in the NiFeCr sample is roughly half of that size. Thus for stacks with NiFeCr buffer the stray field is reduced more strongly and higher oscillation frequencies are expected. Second, we focus on the magnetization orientation in the domains. Fig. 7.5 shows the colour-coded images of the magnetization orientation that correspond to Fig. 7.3. The magnetization in the domains is oriented along the elongation orientation of the domains and the M_x components of adjacent domains in the Ru sample and correspondingly the M_y components in the NiFeCr sample clearly point towards opposite directions. The image in the centre displays the in-plane magnetization. In general we expect the magnetization of our film to be fully in-plane and use this assumption to perform the vectorial *i.e.* colour-coded image analysis. Thus the M_{IP}/M_S image should exhibit a homogeneous grey value. However, there are some deviations visible: First, the emerging uneven topography in the Ru sample leads to artefacts. Second and more importantly, the domain walls are slightly darker. This could be either an indication of Bloch domain walls, where the magnetization rotates out of the plane from one domain to the other,

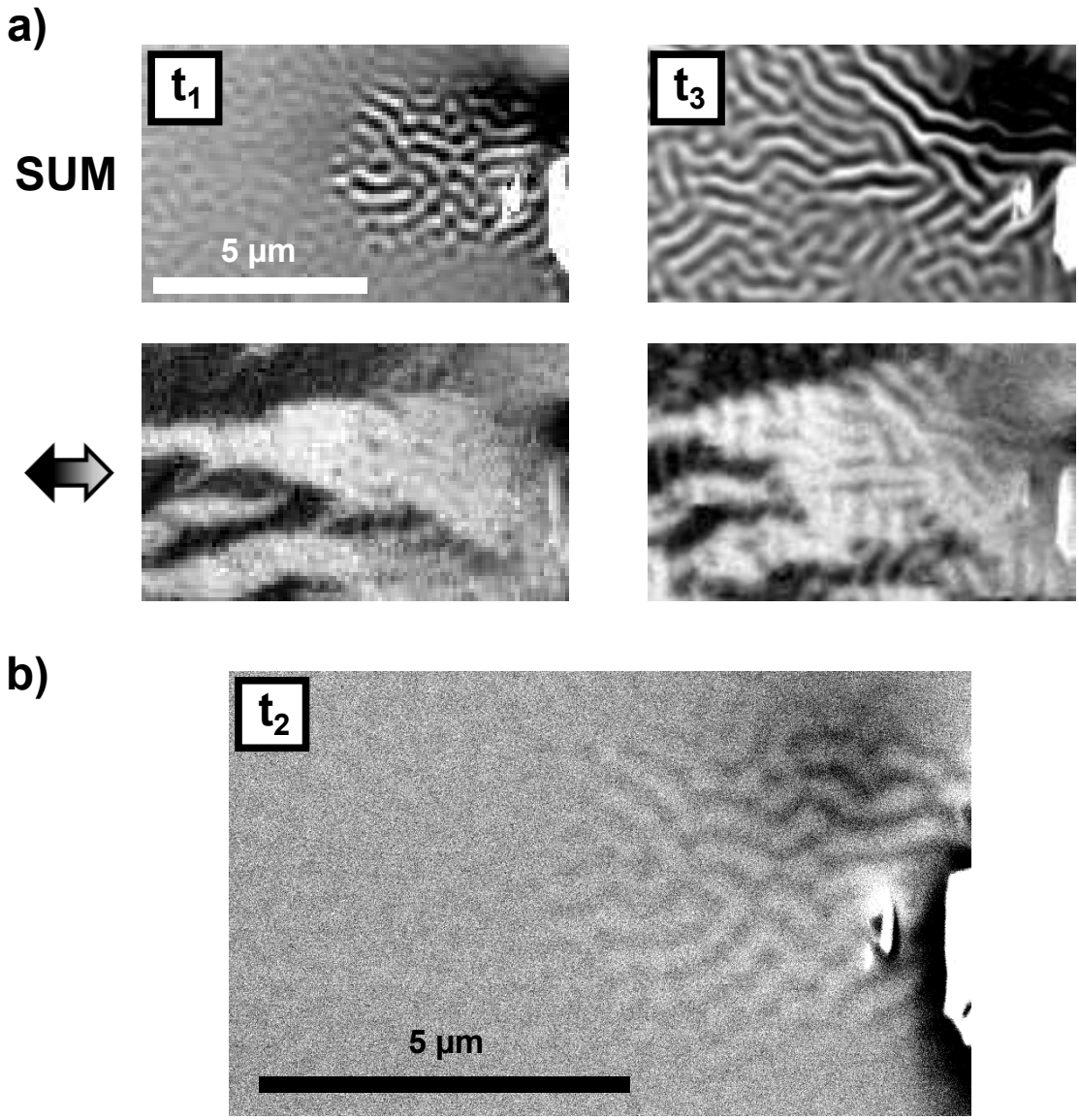

Figure 7.4: **a)** SPLEED sum and horizontal component asymmetry images showing the sensitivity of the topography to electron beam exposure and the overall similar domain pattern despite exposure at different times $t_1 \leq t_3$. **b)** SEM micrograph using the in-lens detector at t_2 ($t_1 \leq t_2 \leq t_3$).

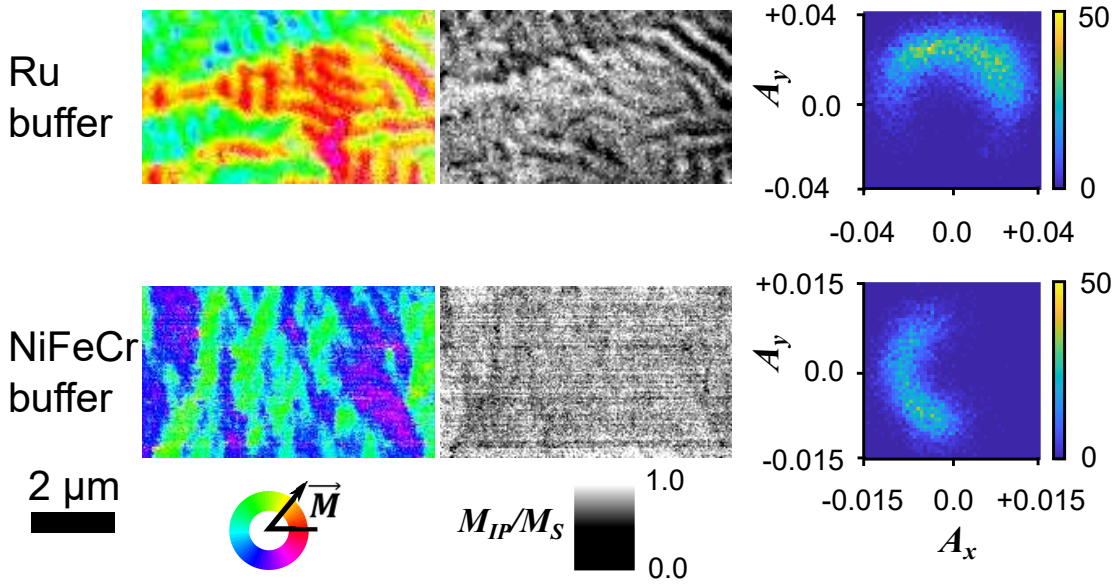

Figure 7.5: SEMPA image analysis. The colour-coded image at the left contains the vectorial magnetization direction information, the grey scale image in the centre shows the in-plane orientation of the magnetization M_{IP}/M_S and a two-dimensional histogram plotting the number of pixels with their horizontal and vertical asymmetry components $A_{x,y}$.

or an effect of the finite spatial resolution in combination with a strong gradient of the in-plane magnetization angle. The scatter plot in the right of Fig. 7.5 provides a quantitative measure of the polarization. Interestingly for the Ru sample the polarization is higher by about a factor of two, despite the ferromagnetic material in both cases being the same. This could be explained by stronger oxidation or over-milling in the case of the NiFeCr sample. The elongation of the domains is apparently different comparing both samples. While in the Ru sample the domains are elongated along the x axis they are elongated along the y axis in the NiFeCr sample. From the scatter plot also the orientation of the exchange bias field can be determined. For an ideal 90°-coupled film one would expect just two point clouds at opposing $A_{x,y}$ position. In reality we observe the $A_{x,y}$ pairs distributed over an angle of about 180°. The orientation of this half ring indicates the direction of the exchange bias field and shows that the samples have been rotated by around 90° towards each other. Another important observation is the stronger accumulation of $A_{x,y}$ pairs in the direction of the exchange field in the Ru sample compared to the NiFeCr stack. This indicates the stronger biquadratic coupling with NiFeCr as buffer layer. This asks for an explanation since the biquadratic coupling is mediated *via* the oxide layer in between the ferromagnetic layers [A] and [B], which is the same for both samples.
The SEMPA measurements were backed up with polarized neutron reflectivity (PNR) measurements by our Japanese colleagues, as described in [329]. The samples were mea-

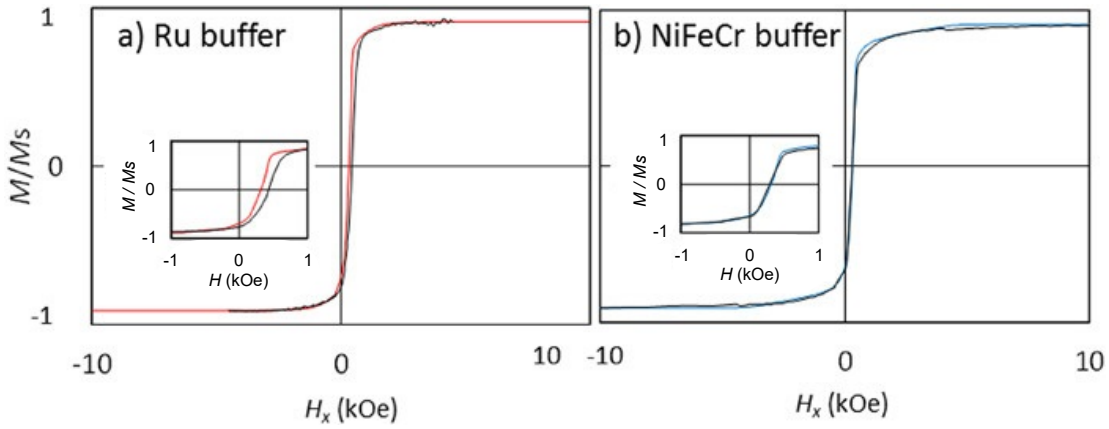

Figure 7.6: SQUID hysteresis loop (black) and simulated hysteresis curve (red and blue) for **a)** the Ru buffer sample and **b)** the NiFeCr buffer sample. (Reprinted with permission from [199].)

sured at SHARAKU (BL17) in the Materials and Life Science Experimental Facility (MLF), Japan Proton Accelerator Research Complex (J-PARC) [119, 200]. The structural parameters such as layer thickness, atomic density and roughness of each layer were determined by x-ray reflectometry in advance to reduce the free parameters for the fitting of the PNR curves. In PNR the wave vector transfer of the incoming and reflected neutron wave function reveals the depth profile of the magnetic structure [12]. The measurements were carried out under external fields of -2.8 mT, +2.9 mT and +100 mT for the Ru sample and -4.5 mT, +3.2 mT and +100 mT for the NiFeCr sample. From the fit the average magnetization orientation of the layers could be determined. The average magnetization angles in the domains of CoFe [B] were ±39 degrees for the Ru buffer sample and ±53 degrees for the NiFeCr buffer sample. The angles are measured with reference to the magnetization orientation in the CoFe [A] layer. These results agree very well with the SEMPA images and analysis.

Quantitative Determination of the Bilinear and Biquadratic Coupling Coefficients

Before we provide an explanation for the differing biquadratic coupling strengths in both samples, we summarize the results of a quantitative determination of the bilinear (A_{12}) and biquadratic (B_{12}) coupling strengths provided in [199]. The magnetic coupling energy is given, following Equation 1.57 [73], as

$$E = -\frac{A_{12}}{|\vec{M}_1| \cdot |\vec{M}_2|}(\vec{M}_1 \cdot \vec{M}_2) - \frac{B_{12}}{|\vec{M}_1| \cdot |\vec{M}_2|}(\vec{M}_1 \cdot \vec{M}_2)^2. \tag{7.1}$$

A_{12} and B_{12} can be estimated from fitting the SQUID experimental hysteresis loops with Landau-Lifshits-Gilbert (LLG) simulations, when the magnetic field is applied along

the exchange bias field direction. The calculation of the simulation of a trilayer stack CoFe [A] (2 nm)/Fe-O (2 nm)/ CoFe [B] (2 nm) is described in detail in [199]. The effective field $\vec{H_{eff}}$ in the LLG equation contains beside the external field, stray field, anisotropy field also the bilinear and biquadratic fields proportional to A_{12} and B_{12}. One element in the simulation was $10 \times 10 \times 2$ nm and the full simulation had $560 \times 560 \times 3$ volume elements. The anisotropy field was set to 3.5 mT, the saturation magnetization to 1450 emu/cm^3, the Gilbert damping $\alpha = 0.01$, the exchange constant $A = 10^{-6}$ erg/cm, the gyromagnetic ratio $1.76 \times 10^{11}\, 1/(\mathrm{T} \cdot \mathrm{s})$. The exchange bias field of CoFe [A] was assumed to be 40 mT. The external magnetic field was applied along the exchange bias field orientation from -1 T to 1 T with a sweep time of 200 ns. The calculation steps of the simulation were 10 fs. A_{12} scales with the magnetization jump while B_{12} scales with the slope of the hysteresis curve and therefore with the magnitude of magnetization rotation. The hysteresis loop for positive fields contains not only the magnetization motion for the CoFe [B] layer but also for the CoFe [A] layer, as shown in Fig. 7.2. Therefore the M–H curve was fitted to determine the energy coupling coefficients. The experimental SQUID data is plotted with black and the fit in red and blue for the Ru sample and the NiFeCr sample in Fig. 7.6. A_{12} was varied from 0 to 1.0 mJ/m^2 and B_{12} from -0.6 to -0.1 mJ/m^2 in 0.1 mJ/m^2 steps. For the sample with the Ru buffer the resulting values are $A_{12} = 0.4$ mJ/m^2 and $B_{12} = -0.3$ mJ/m^2, for the sample with NiFeCr buffer layer $A_{12} = 0.6$ mJ/m^2 and $B_{12} = -0.6$ mJ/m^2. The coupling energy values were plotted in a phase diagram (Fig. 7.7, similar to Fig. 1.21) and compared to other reported values with metallic spacer layers such as Al [90, 100], Au [90] and Cu [106] (black dots) and with a NiO spacer [300] (black circle). The biquadratic coupling in the Ru (red dot) as well in the NiFeCr sample (blue dot) is stronger than in the other samples, especially those with metallic spacer layer. However, there have been reported high values of B_{12} for Mn and Cr intermediate layers[81, 309] (not shown in Fig. 7.7).
The simulation of the domain structure agreed with the SEMPA images in terms of the domain size, as shown in Fig. 7.8. In the NiFeCr sample the domains have about half the width of the domains in the Ru sample. The magnetization in the DWs rotates within the plane, indicating that the best explanation for the reduced M_{IP}/M_S value at the DWs observed in Fig. 7.5 is related to the finite spatial resolution of the imaging technique. However, one needs to keep in mind that a rather large volume element size was used in the simulations, compared to the exchange length $l_{ex} = \sqrt{\frac{2A}{\mu_0 M_s^2}} \approx 2$ nm in CoFe.

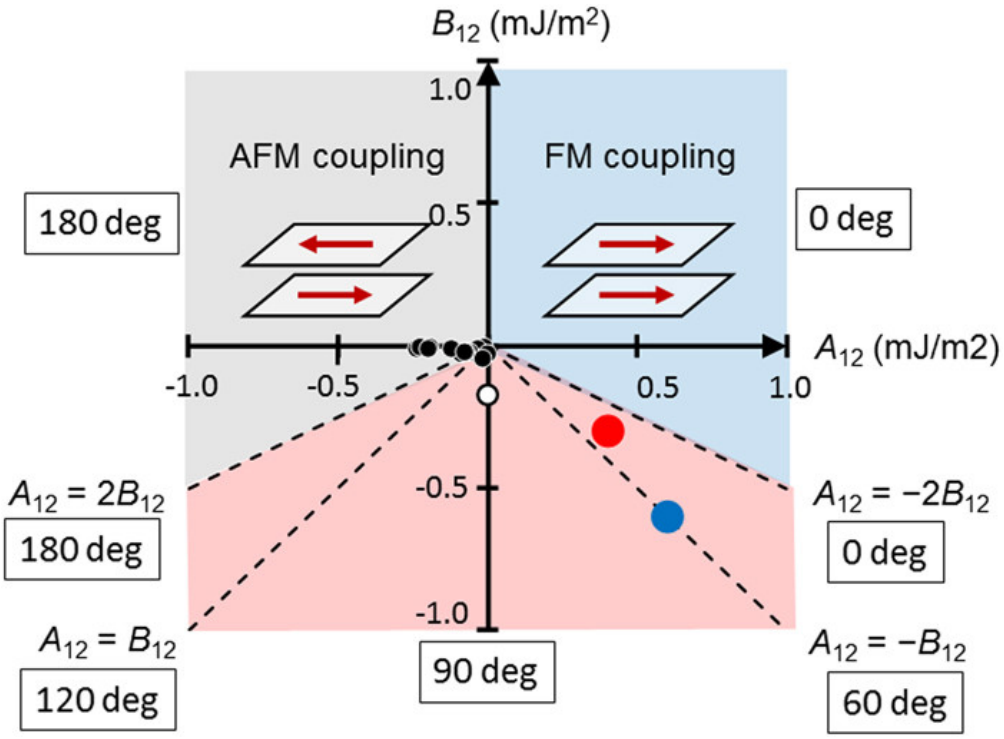

Figure 7.7: Magnetic coupling phase diagram of CoFe [A] and CoFe [B] layers with the ferromagnetic phase in blue, antiferromagnetic phase in grey and the intermediate phase including the 90° coupling phase in red. The results of prior research are included: black dots indicate stacks with nonmagnetic metal spacer [90, 100, 106], the circle a stack with NiO spacer [300] and the red and blue dot the Ru spacer sample and the NiFeCr spacer sample in the current work. (Reprinted with permission from [199].)

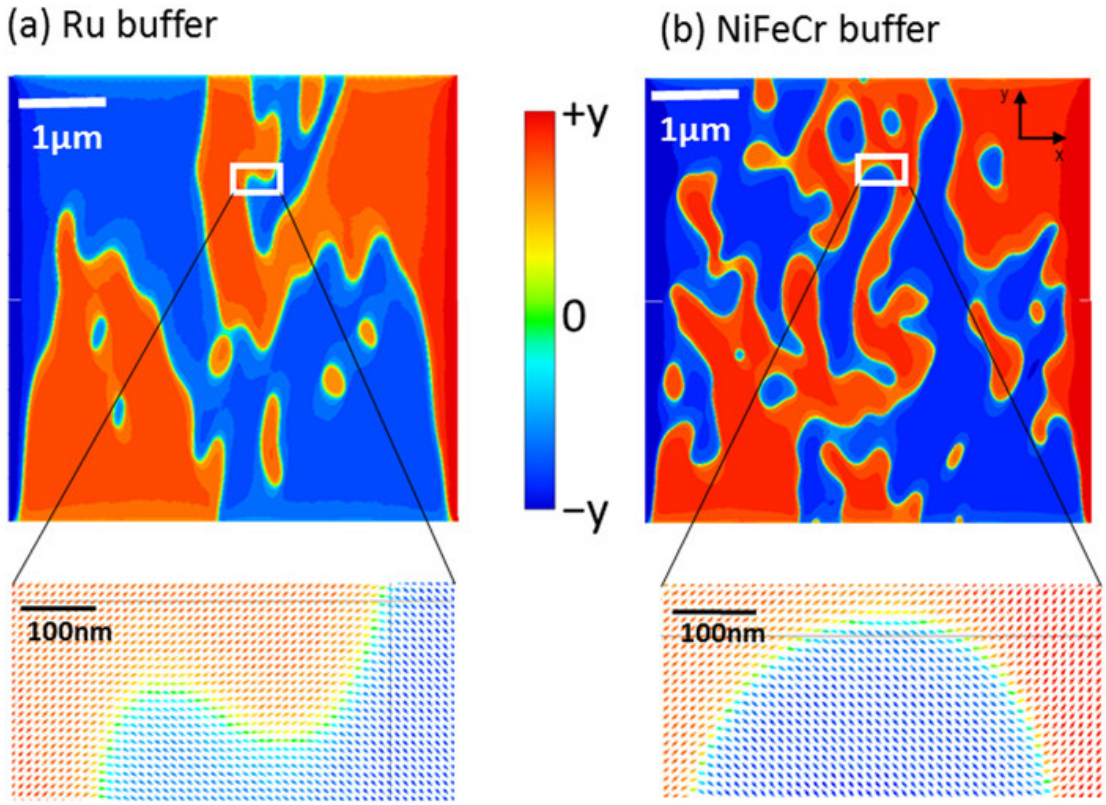

Figure 7.8: Micromagnetic simulation of the domain shape in **a)** the Ru buffer and **b)** the NiFeCr buffer sample. (Reprinted with permission from [199].)

Transmission Electron Microscopy

To investigate the reason for the different coupling strengths of both stacks, cross-sectional transmission electron microscopy images were performed. The main interest is in the roughness of the Fe-O since this layer mediates the coupling. Indeed, while for the Ru sample the roughness is about 2 nm the roughness of the Fe-O layer in the NiFeCr sample is 10× lower. X-ray reflectometry (XRR) measurements also indicated high differences between the roughness of the Fe-oxide layer [329]. For the XRR fit the oxide layer was assumed to be a double layer of FeO/Fe_2O_3 because this had the best fit results. The roughness determined by XRR was 0.70 nm for FeO and 0.50 nm for Fe_2O_3 in the case of the Ru buffer sample and 0.02 nm for FeO and 0.01 nm for Fe_2O_3 in the case of the NiFeCr buffer sample.
In general the size of the columnar crystalline grains determines the roughness of a sputtered magnetic layer on SiO_2. This leads to an additional contribution to the ferromagnetic coupling energy by the so-called orange peel coupling, given in Equation 1.56

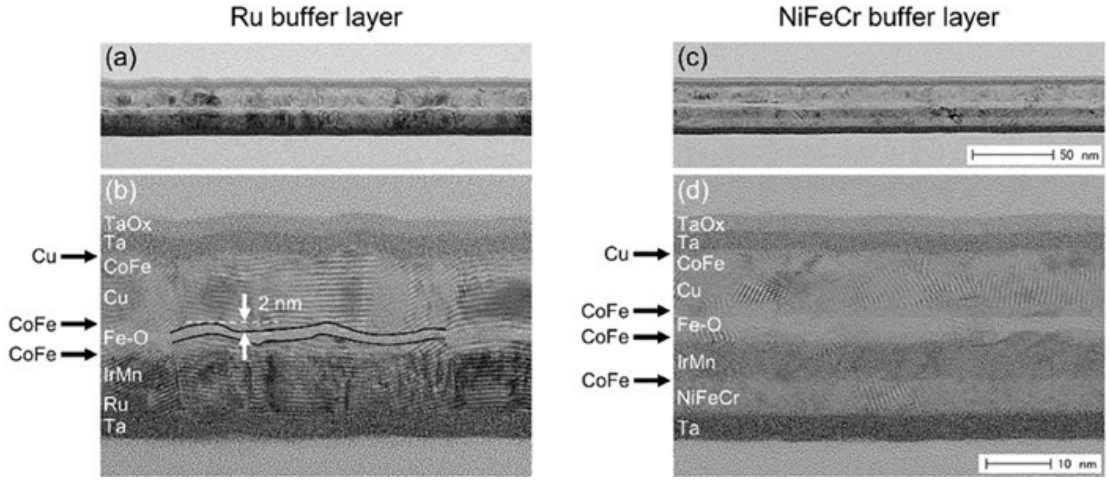

Figure 7.9: Cross-sectional TEM images of the sample stack with Ru buffer layer (left side, **a)** and **c)**) and NiFeCr buffer layer (right side, **b)** and **d)**). The magnification for the lower images is $4\times$ higher than for the upper images. (Reprinted with permission from [199].)

as

$$A_{12,\mathrm{OP}} = \frac{\pi^2}{\sqrt{2}} \frac{\delta_s^2}{\lambda} \mu_0 M_s^2 \exp(-\frac{\pi}{\sqrt{2}} \frac{t_s}{\lambda}). \tag{7.2}$$

δ_s indicates the amplitude and λ the wavelength of the roughness, t_s is the thickness of the intermediate oxide layer. An increased roughness δ_s results in an increased ferromagnetic coupling and the 90°-coupling is effectively reduced. A NiFeCr buffer increases the grain size of subsequently deposited layers [162]. The grain size of the CoFe [A] layer was 50 nm in the NiFeCr sample and 15 nm in the Ru sample [199].

Summary

We investigated multilayer stacks with oxide intermediate layers with strong 90°- coupling compared to stacks using metallic spacer layers. We further demonstrated with our work the possibility to tune the biquadratic coupling *via* the roughness of the layers. SEMPA imaging of samples with Ru and NiFeCr buffer layers showed different domain sizes and a differing magnetization orientation in adjacent domains. Strong biquadratic coupling could be employed in fast quasi-antiferromagnetic STOs due to reduced stray fields. A subsequent study using the investigated stack with the NiFeCr buffer layer already has confirmed increased FMR frequencies for quasi-antiferromagnetically coupled CoFe layers compared to conventional CoFe [115].

7.2 Chiral Domain Walls in Ferrimagnets

Changing and detecting the magnetization state in antiferromagnets is difficult because there is no net magnetic moment and thus they are by far not as sensitive to magnetic fields as ferromagnets [126]. Ferrimagnets based on rare-earth (RE) and transition metal (TM) compounds [25] are an ideal test system to investigate antiferromagnetic spintronics because they have in general a remaining net moment and therefore they can be investigated with the same techniques as ferromagnets. The net magnetic moment can be tuned by changing the stoichiometry and the temperature and thus specific antiferromagnetic properties such as fast dynamics [133] and straight skyrmion motion [110, 134] without a skyrmion Hall angle [168] can potentially be obtained. Here we demonstrate the feasibility of SEMPA imaging of the RE-TM ferrimagnet GdCoFe. For a strong interfacial DMI we need a material with strong spin-orbit coupling such as a heavy metal interface to the ferrimagnetic layer. This is disadvantageous for our highly surface-sensitive imaging technique. However, we succeeded in acquiring images across a thin Pt layer and measure the detailed DW spin structure and width.

Sample Fabrication and Preparation

The multilayer stack Ta(5 nm)/Ir(5 nm)/Fe(0.3 nm)/$Gd_{26.1}Fe_{65.5}Co_{8.3}$(8 nm)/Pt(5 nm) was deposited by Boris Seng at the Institut Jean Lamour in Nancy using magnetron sputtering under a base pressure of $3.2 \cdot 10^{-8}$ mbar. The ferrimagnetic layer was grown by co-sputtering from multiple targets. The subscripts indicate the stoichiometry of the RE-TM ferrimagnet. The composition is estimated from the deposition rates of the respective target. The stack is drawn schematically in Fig. 7.10. The ferrimagnet-heavy metal were arranged so that the interfaces should have a DMI constant with opposite sign, enhancing the net interfacial DMI with the $D_{\mathrm{Co-Pt}}$ and $D_{\mathrm{Fe-Pt}}$ being negative and $D_{\mathrm{Co-Ir}}$ and $D_{\mathrm{Fe-Ir}}$ being positive [127]. To further enhance the net positive DMI of the lower interface, a thin layer of Fe was deposited on Ir before co-sputtering the ferrimagnet, since $D_{\mathrm{Co-Ir}} < D_{\mathrm{Fe-Ir}}$. However, different calculations resulted in different sign for the DMI and it probably depends on the interface properties [21, 143,

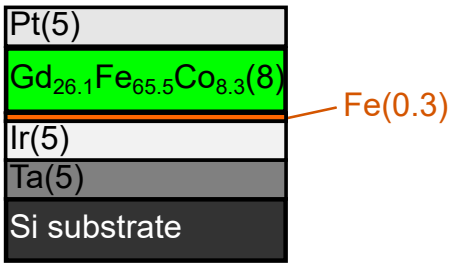

Figure 7.10: GdFeCo multilayer stack. For SEMPA imaging a few nanometre of the Pt cap were removed to be able to image the spin structure in the underlying GdFeCo.

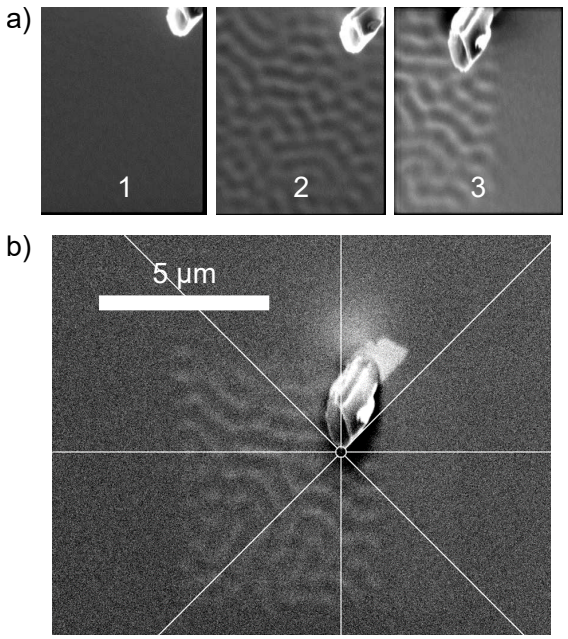

Figure 7.11: Topographic changes related to electron-beam exposure: **a)** SEMPA sum images acquired subsequently with the SPLEED detector (1: $t_{\mathrm{dwell}} = 49\,\mathrm{ms}$; 2: $t_{\mathrm{dwell}} = 195\,\mathrm{ms}$; 3: $t_{\mathrm{dwell}} = 50\,\mathrm{ms}$) and **b)** SEM images acquired with the in-lens detector. The scale bar is valid for all images. ($U_{\mathrm{EHT}} = 7.5\,kV$)

262]. Recently, a non-negligible bulk DMI was reported in the RE-TM ferrimagnet GdFeCo [132], which also contributes to the overall DMI in the system.
The high thickness of the top Pt layer is not necessary for the interfacial DMI but is used to prevent oxidation during the sample transfer from the fabrication to the measurement UHV chamber. To image with SEMPA, part of the cap layer was milled away with Ar^+ ions. If not enough Pt is removed, no magnetic contrast is seen [154]. However, if we milled too much, we observed increasing changes of the film surface with increasing exposure time, as shown in Fig. 7.11 for a sample with slightly different stoichiometry ($Gd_{22.6}Fe_{69.7}Co_{7.7}$). After milling 1.2 nm Pt was left nominally on top of the ferrimagnetic layer. In Fig. 7.11a) three subsequent SEMPA sum images are shown with $t_{\mathrm{dwell}} = 49\,\mathrm{ms}$ (1), $t_{\mathrm{dwell}} = 195\,\mathrm{ms}$ (2) and $t_{\mathrm{dwell}} = 50\,\mathrm{ms}$ (3). In the third image the FOV is shifted by approximately 2 µm to the right. The worm-like pattern gets clearly more pronounced with increasing exposure time. The area, which has not been scanned in the third image does not show the pattern. The pattern does not only appear in the images acquired with the SPLEED detector but also with the in-lens SEM detector, as shown in Fig. 7.11b). This confirms the topographic origin of the signal, which is similar to the changes observed in Fig. 7.4. Typical indications for charging such as drifts and wobbling were not observed. Further investigation using atomic force microscopy could be instructive.

This effect was seen for several samples even if not for all and might be related to a bad adhesion of the cap layer to the ferrimagnet or a redistribution of Pt atoms. For samples with a nominal cap layer thickness of 1.5 nm the described changes have not been observed even after very long exposure times with $t_{\mathrm{dwell}} > 1\,\mathrm{s}$. The images were acquired in the multi-scan mode, scanning the FOV with a scan frequency of 1000 px/s. We imaged a FOV of $5 \times 6.25\,\mu\mathrm{m}$ with a pixel size of 300×376 pixel to exploit fully the spatial resolution of our SEMPA system and thus to be able to resolve the narrow DWs in the otherwise out-of-plane magnetized film. The acquisition including the processing time took about 30 hours for one static image. This is due to the reduced signal due to the quite thick Pt cap layer. In the FOV a clear topographic feature needs to be visible to allow for cross-correlation with high precision in the post-processing. The multi-scan approach is based on the assumption that the spin structures are pinned and do not diffuse thermally [325]. No field was applied during the acquisition and the temperature was 296 K.

Result and Discussion

In Fig. 7.12 the SEMPA image results are shown. Fig. 7.12a) is the sum image with a clear topographic feature in the upper left edge, which was used for drift correction during post-processing. Fig. 7.12b-c) contains the SEMPA asymmetry images $A_{x,y}$ showing multiple bubble domains of a size of 500 nm to 3 µm. The irregular domain shapes and the fact that integration of the images over hours results in clear domain wall images, indicates a strong DW pinning. In the A_x image the DWs at the right side of the bubbles appear bright and the DWs at the left side dark, while in the A_y image this is the case for the upper and lower DWs. This holds for all visible bubbles and indicates already a fixed chirality with a strong Néel component. The domain shape is nicely seen in Fig. 7.12d), where the normalized total asymmetry $\sqrt{A_x^2 + A_y^2}$ is shown, which is in this case proportional to the in-plane component of the magnetization. In general, the magnetization is out-of-plane, but in the DWs there is due to the rotation of the magnetization an in-plane component and thus the DWs are brighter in the $M_{\mathrm{IP}}/M_{\mathrm{s}}$ image. Based on this image a binary mask just containing the DWs is generated by hand. In Fig. 7.12e) the asymmetry value pairs (A_x, A_y) of all pixels, which belong to the DWs, are plotted in a scatter plot. While for an in-plane magnetized film of Fe asymmetry values of about 5% are measured, as shown for example in Fig. 7.17, here the effectively measured asymmetry being approximately 0.3% is more than one order of magnitude lower. The obvious reason for this is the high contribution of unpolarized secondary electrons that are emitted from the top Pt layer and mainly contribute to the signal. However, it is still possible to calculate a magnetization vector image based on this scatter plot, as shown in Fig. 7.12f). The result is consistent with the observation we made already based on the gray-scale asymmetry images. All DWs have the same chirality and are of Néel type with no significant Bloch component.
Next we determine the DW width. Another reason besides the cap layer influence for the measured extremely low asymmetry could be a very narrow DW width. If the DW

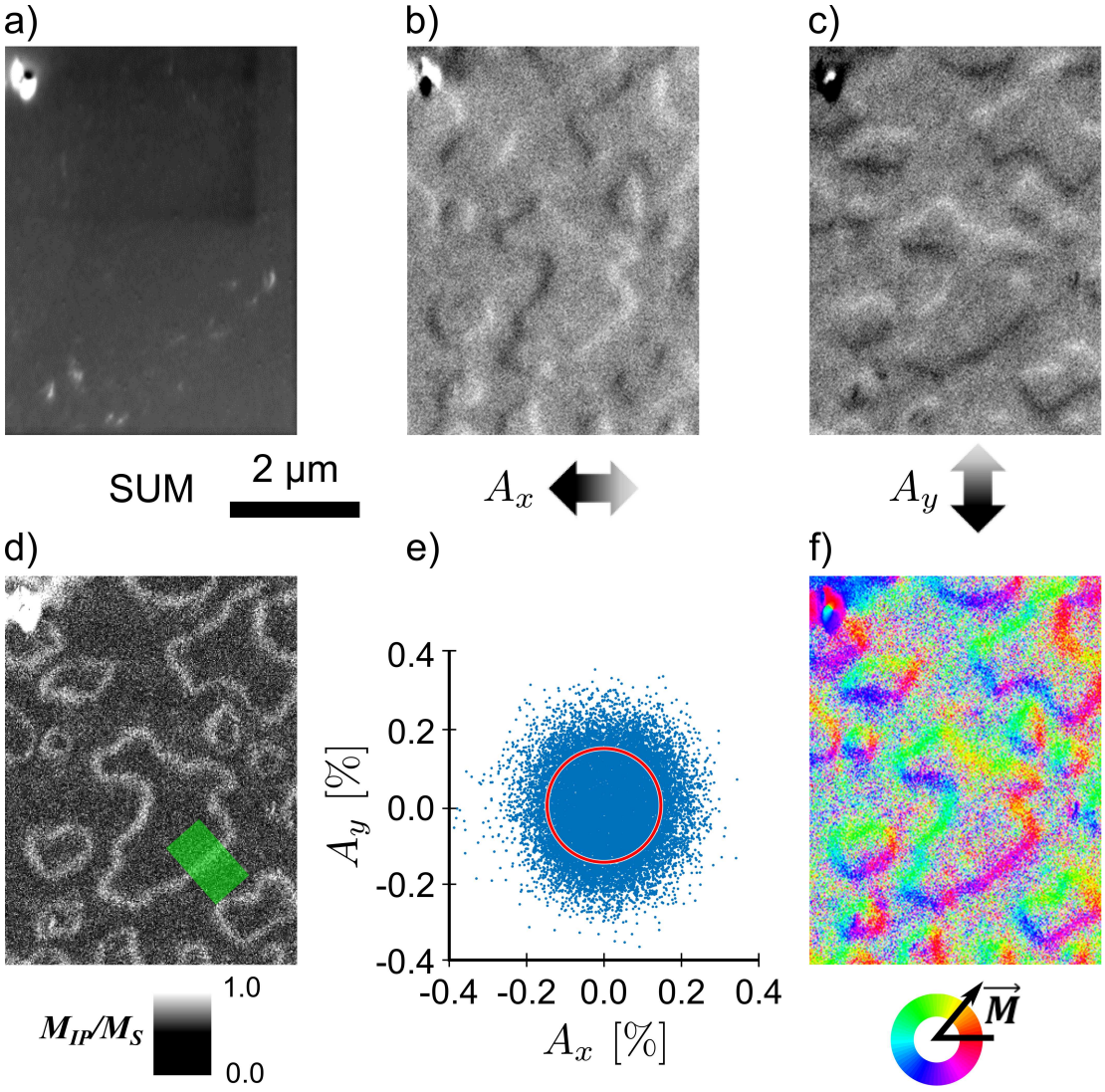

Figure 7.12: **a)** SEMPA sum image. **b)** SEMPA A_x asymmetry image. **c)** SEMPA A_y asymmetry image. **d)** Normalized absolute asymmetry image ($\propto M_{\mathrm{IP}}/M_{\mathrm{s}}$) indicating the DW position. **e)** Scatter plot of the asymmetry value pairs measured in the DWs. The radius of the fitted ring is a rough estimate of the effective asymmetry being around 0.3%. **f)** Colour-coded magnetization vector image showing a fixed chirality of the Néel type DWs.

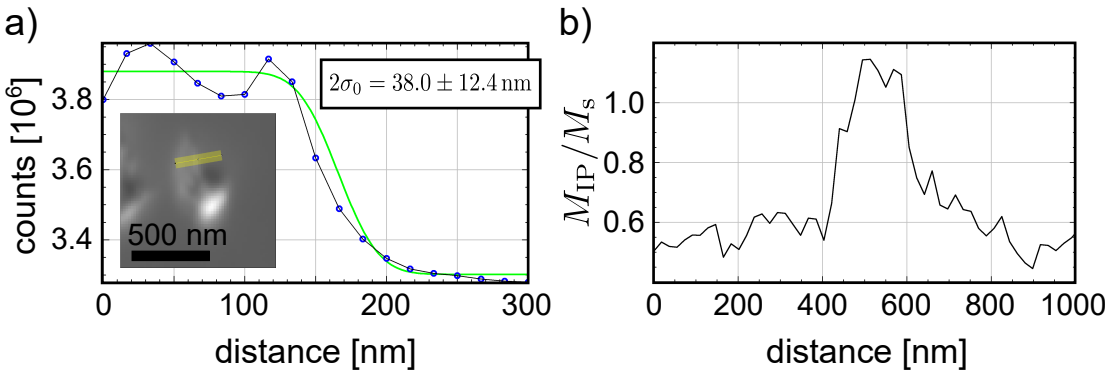

Figure 7.13: **a)** Determination of spatial resolution in the acquired image using a flake particle edge. The profile plot is averaged over a width of 4 pixels. The spatial resolution determined by the distance between 20% and 80% of the step height with a Gaussian edge fit is 38.0 ± 12.4 nm. **b)** DW profile along the line indicated in Fig. 7.12d), averaged over a width of 40 pixels. The DW width is approximately 150 nm.

width is below the spatial resolution of our system, the measured asymmetry will be reduced compared to the asymmetry measured in an in-plane magnetized film of the same magnetic material. Therefore we first need to determine the spatial resolution in our acquired image. To do so, we determine the edge width of the flake particle by fitting a Gauss function to it. Fig. 7.13a) shows the area of the flake particle with higher magnification and also the line corresponding to the profile plot. The measured spatial resolution was 38.0 ± 12.4 nm. This is slightly lower than the possible spatial resolution that can be obtained with our system. A possible reason for this is imperfect matching of the FOV scans during the drift correction. A plot of the DW profile indicated in Fig. 7.12d) is shown in Fig. 7.13b). The low signal-to-noise ratio due to the low asymmetry required averaging over a width of 40 pixels. The DW width is approximately 150 nm, which is significantly higher than the previously determined resolution[1]. Thus we conclude that the reduced asymmetry is mainly an effect of the Pt cap layer and not affected by the limited spatial resolution. The wide DWs further indicate that the system is close to the spin reorientation temperature at 296 K and the perpendicular magnetic anisotropy is already reduced.
Finally, we want to quantify the Néel and Bloch component of the DW. To this end, we generate manually a skeleton image based on Fig. 7.12d) which is shown in Fig. 7.14a) as an overlay on the colour-coded magnetization image. Then the domain contours were divided into 29 separate contour intervals that could be expressed by polynomial functions. The degree of the polynomial was chosen between 3 and 16 so that it fitted nicely

[1] A detailed image analysis by B. Seng has revealed an experimental DW width of 175±5 nm according to the definition in Ref. [164] and additional with SQUID magnetometry he measured an effective anisotropy $K_{\text{eff}} = 2.6\,\text{kJ/m}^3$ and an exchange stiffness of $A = 8.0\,\text{pJ/m}$, which is in the range of literature values [40].

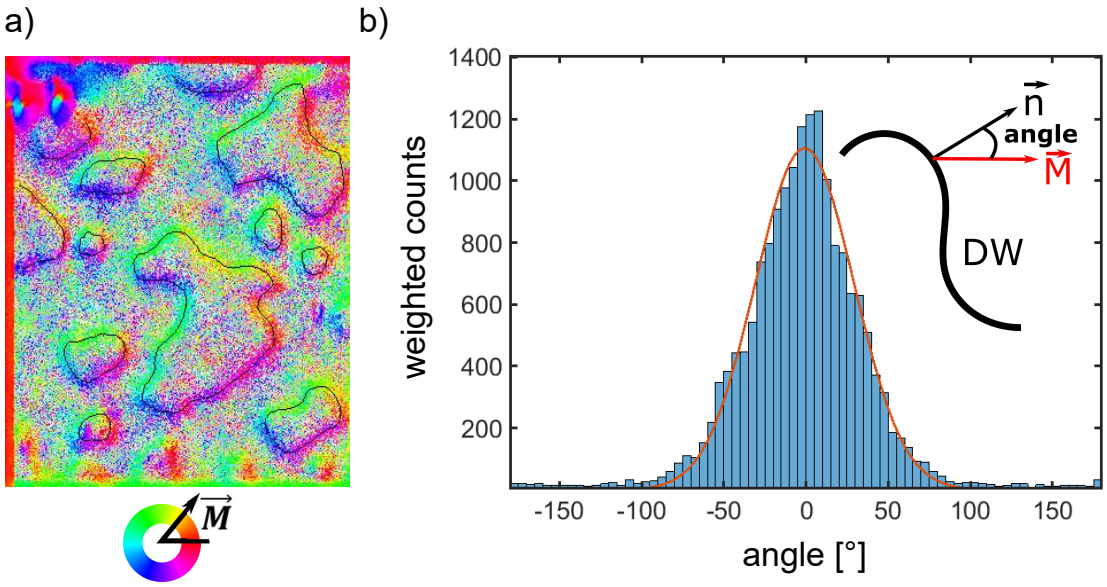

Figure 7.14: **a)** Colour-coded SEMPA magnetization angle image with skeleton overlay (black). The red edge is an artefact resulting from misalignments of the individual scans before post-processing. **b)** Histogram of the magnetization angle compared to the DW normal (see inset). The orange line shows the Gaussian function fit to determine the Néel and Bloch component.

the skeleton segment. Next, the tangent and normal equation at every pixel position belonging to the DW is determined. For the determination of the magnetization angle with respect to the DW normal (Fig. 7.14b)) we assume a DW width of 150 nm. The magnetization vectors of all pixels that are cut by the DW normal and are within the DW width are added to determine the mean value. These angles are not equally contributing to the resulting mean angle, but were weighted using the absolute asymmetry value of the respective pixel (Fig. 7.12d)) so that the pixels in the centre of the DW were taken more into account. The average angles of all DW normals were plotted in a histogram, shown in Fig. 7.14b), where a clear peak is visible. The histogram was fitted with a Gaussian function $g(\theta) = A/(\sigma_A \cdot \sqrt{2\pi}) \cdot \exp((\theta - \theta_\mathrm{m})/(2\sigma_A^2))$ to determine the overall spin orientation in the DWs. We observed pure Néel DWs with $\theta_\mathrm{m} = (-0.8 \pm 0.5)$ degree with a negligible Bloch component at room temperature in this thin film stack. The Néel nature of the DWs indicates a strong DMI even after removing 3.5 nm of the Pt cap layer.

Conclusion and Outlook

We demonstrated the feasibility of imaging narrow Néel DWs in RE-TM ferrimagnets using SEMPA. The ongoing study, which is followed up by Boris Seng, will investigate the effect of temperature, stoichiometry and stack materials on the spin structure. By

tilting the sample with respect to the detector plane also the out-of-plane direction of the magnetization in the domains will be determined and the sign of the effective DMI will be measurable with SEMPA. Additional measurement techniques such as bubble expansion [159] could be used to confirm the measurements. From a thorough analysis of the DW width and further complementary magnetic measurements the exchange stiffness and the DMI could be quantified.

7.3 Indirect SEMPA Imaging of Antiferromagnetic Domains Using an Exchange-Coupled Ferromagnetic Layer

Imaging of antiferromagnets has been done extensively at synchrotrons with XMLD-PEEM [16, 31, 246, 251]. Recently, lab-based techniques such as magneto-optical imaging [254, 319] and spin Seebeck imaging [96] have been successfully exploited for imaging of antiferromagnets. In general antiferromagnetic domains can not be detected using SEMPA due to the compensated sublattice spins. However, there is a possible approach to make them visible using a ferromagnetic layer that is exchange-coupled to the surface spins of the antiferromagnet. Thus the approach is analogous to the contrast enhancing mirror layer [303]. Earlier studies of antiferromagnet/ ferromagnet bilayers using XMCD and XMLD-PEEM found that the antiferromagnetic and ferromagnetic domains match because of the interfacial exchange coupling [208, 212]. In our study we investigated Mn_2Au/Fe. Mn_2Au is a layered collinear antiferromagnet with in-plane anisotropy and the magneto-crystalline easy axes [110] and [1$\bar{1}$0], as described in Ch. 1. A schematic drawing of the crystal structure is shown in Fig. 1.5. In an earlier study of the bilayer Mn_2Au/Fe a broadening of the hysteresis loop has been found indicating a coupling of the Fe spins to the Mn spins at the interface [245, 247]. Nolting *et al.*[208] explained the collinear coupling between the antiferromagnetic and ferromagnetic moments by uncompensated spins at the antiferromagnet's surface [280] that can even induce a local exchange bias averaging to zero macroscopically. The crystallographic symmetry of Mn_2Au with two magnetic sublattices forming inversion partners and a locally broken structural inversion asymmetry led to the prediction of current-induced Néel order switching [307]. The so-called Néel spin-orbit torque was demonstrated experimentally first for CuMnAs, the only other known antiferromagnet with the required symmetry [308]. Further experiments detected the effect also in Mn_2Au [30, 31, 184]. The high Néel temperature well above 1000 K [18], the lack of toxic elements and a good conductivity makes Mn_2Au a promising candidate for antiferromagnetic spintronics. The samples of this study were fabricated by Stanislav Bodnar. The project is continued by Satya Prakash Bommanaboyena. Both contributed to the discussion of the imaging results.

Sample Fabrication

The multilayer stacks investigated in this project were deposited *via* RF magnetron sputtering by S. Bodnar and S. Prakash. We follow here a detailed description of sample fabrication and characterization that was published in [32]. We used $10 \times 10 \times 0.53$ mm (1-102) r-plane sapphire substrates with one side polished (CrysTec GmbH). Before the deposition the substrates were outgassed in UHV at 550°C for 30 min to remove adsorbed water and organic materials. The base pressure of the UHV chamber was 1.5×10^{-8} mbar. Then a 13 nm thick epitaxial Ta (001) buffer layer was sputtered onto the substrate while maintaining a temperature of 450°C. Body-centred cubic Ta (001) is ideal as a buffer layer for Mn_2Au (001) because its lattice constant of 3.30 Å has only a very small mismatch of 0.6% compared to the cell size of the tetragonal structure of

Mn_2Au (a = 3.32 Å, c = 8.53 Å). In the next step 45 nm Mn_2Au were deposited *via* RF sputtering from a stoichiometric Mn_2Au target at 300°C and 0.1 mbar Ar pressure. The deposition rate was 0.75 Å/s. As ferromagnet 4.25 nm Fe was chosen because of its high spin polarization which is advantageous for SEMPA imaging. Finally the stack was capped with 4 nm Al to prevent oxidation. This layer was removed in the SEMPA UHV system before imaging by Ar^+ ion milling with 1 kV. The full stack used for investigation *via* SEMPA imaging is shown in Fig. 7.15. We investigated two samples. One has been exposed to a high magnetic field of 60 T along the [110] direction at the High Magnetic Field Laboratory of the Helmholtz-Zentrum Dresden-Rossendorf (HZDR). The other one has been imaged in the as-grown state where equally distributed domains along the two in-plane easy axes directions are expected.

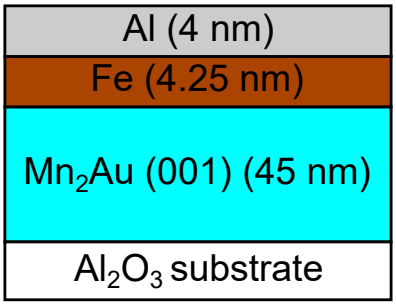

Figure 7.15: The investigated stack: Ta(001) serves as a buffer layer on an r-plane Al_2O_3 substrate, followed by the Mn_2Au(45 nm)/Fe(4.25 nm) bilayer, capped with 4 nm Al.

SEMPA Imaging of Mn_2Au/Fe

First we looked at the sample that was exposed to the high field, because the expected domain pattern is very specific and thus indicates if the Fe is exchange-coupled to the Mn_2Au. The SEMPA images are shown in Fig. 7.16a)-e). From earlier XMLD-PEEM imaging we know the very characteristic domain shape of Mn_2Au [246], as shown in Fig. 7.16f). The FOV of all images is 10 µm. The high roughness of the sputtered sample reported in [32] is visible in the sum image. The y asymmetry image (Fig. 7.16c)) is, as expected, very similar to the XMLD-PEEM image (Fig. 7.16f)) showing small worm-like domains/ domain walls on an otherwise homogeneous background. The average size of the areas between the narrow features being approximately 1-2 µm matches, too. Here the Néel vector of the Mn_2Au is expected to be oriented perpendicular to the applied spin-flop field [246]. While the XMLD signal does not change sign if the Néel vector is rotated by 180° and only the orientation axis can be detected, we can detect the magnetization angle of the Fe coupled to the Mn_2Au using SEMPA imaging. The x asymmetry image (Fig. 7.16b)) provides valuable information in addition to the XMLD-PEEM images. We can not only determine the orientation but also the direction of the Néel vector in the domains. In Fig. 7.16d) again the x asymmetry is shown, but with an overlay of the worm-like domains from the y asymmetry image (green). The dark small

domains separate large domains with opposite x magnetization component of the Fe layer, indicating antiparallel Néel vectors of the underlying Mn_2Au. The colour-coded image, however, reveals that the Fe magnetization is not perpendicular to the spin-flop field, but tilted by 45° towards the direction of the spin-flop field.

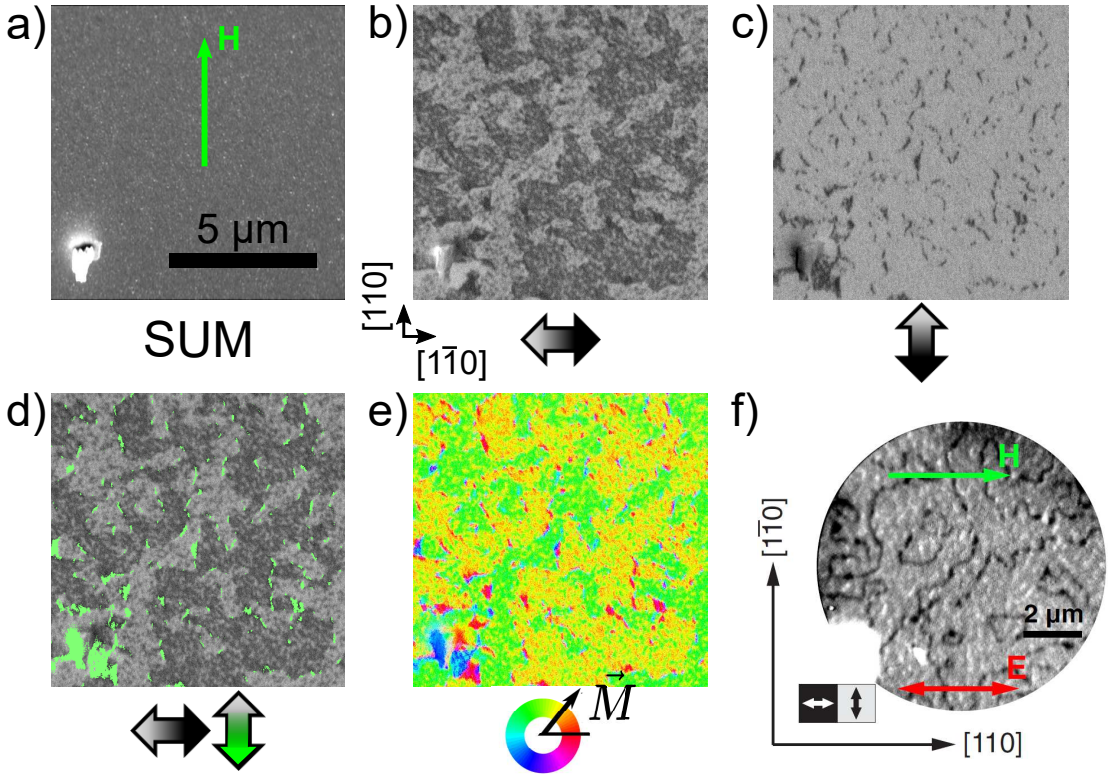

Figure 7.16: **a)** Sum image of Mn_2Au/Fe after 30 min Ar^+ milling ($U_{\mathrm{EHT}} = 7.5\,kV$, $t_{\mathrm{dwell}} = 24\,ms$). The green arrow indicates the direction of the spin-flop field. **b)** x asymmetry and **c)** y asymmetry SEMPA images. **d)** x asymmetry images as in b), but with the small domains from c) overlayed. **e)** Colour-coded magnetization angle image. **f)** Reference XMLD-PEEM image of Mn_2Au only with the same FOV size. Note the different orientation. The green arrow indicates the direction of the spin-flop field, the red arrow indicates the linear polarization axis of the x-ray beam. (Adapted from [246] with permission.)

Next we look at the as-grown sample, as shown in Fig. 7.17. These images are acquired after 55 minutes of ion milling with the same parameters as for the field-exposed sample. However, it took longer before magnetic contrast was visible. The reason for this is probably the different amount of oxidation of the Al cap layer. We will discuss the milling in more detail further down. The domain pattern is clearly different compared to Fig. 7.16. While from the x and y asymmetry images it is not immediately evident, the scatter plot in Fig. 7.17d) and the colour-coded magnetization image in Fig. 7.17e) indicate clearly the expected fourfold magneto-crystalline anisotropy of the underlying

Mn_2Au mirrored by the top Fe layer.

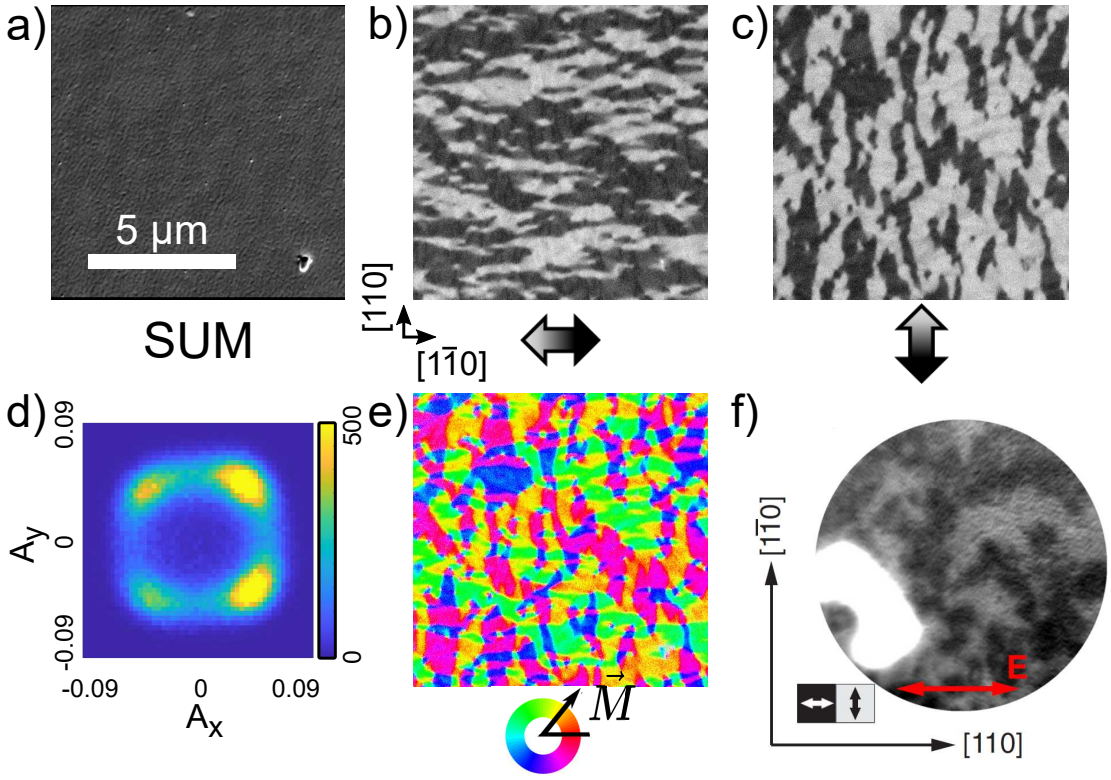

Figure 7.17: **a)** Sum image of the as-grown Mn_2Au/Fe after 55 min Ar^+ milling ($U_{EHT} = 7.5\,kV$, $t_{dwell} = 14\,ms$). **b)** x asymmetry and **c)** y asymmetry SEMPA images. **d)** Scatter plot indicating the fourfold magnetic anisotropy and the 45° angle of the Fe magnetization compared to the easy axes of Mn_2Au. The number of pixels in the 2D histogram is colour-coded. **e)** Colour-coded magnetization angle image. **f)** Reference XMLD-PEEM image of Mn_2Au only with the same FOV size. The red arrow indicates the linear polarization axis of the x-ray beam. (Adapted from [246] with permission.)

However, the magnetization direction in the Fe domains is again tilted by 45° compared to the easy axes orientations of Mn_2Au, as observed already before in Fig. 7.16. This is recognizable from the prevalent domain colours yellow, green, pink and blue in the colour-coded magnetization image and from the scatter plot with the maximum densities clearly not on the x or y axes, but in the centre of each quadrant. This confirms earlier MOKE hysteresis investigations of Mn_2Au/Fe published in [245]. The magnetization in Fe exchange-coupled to the Mn spin does not align parallel to the Néel vector in the $\langle 110 \rangle$ axis but along the $\langle 100 \rangle$ axis. This tilt can either have a crystallographic origin if Fe is grown epitaxially on Mn_2Au or indicates biquadratic coupling between the antiferromagnetic and ferromagnetic layers [241]. In the as-grown Mn_2Au we expect due to the fourfold anisotropy a similar amount of domains for every of the four mag-

netization directions. Here the scatter plot does not show an equal distribution of the four magnetization directions (Fig. 7.17d)), which might be attributed to the limited FOV. The 45° coupling of Fe complicates the analysis of this indirect method to image antiferromagnetic domains. Soft magnetic materials such as $Ni_{80}Fe_{20}$ could be an option to overcome this disadvantage.

Finally we have to consider the preparation of the sample before SEMPA imaging. Fig. 7.18 shows the SEMPA images of the field-exposed and as-grown sample after different times of Ar^+ ion milling. The times are given in minutes (’). In addition the average asymmetry value $\sqrt{A_x^2 + A_y^2}$ that is determined by the average distance of the points in the scatter plot is provided in percent (%). It serves as an estimate for the milling progress. For the field-exposed sample we start to see magnetic contrast after 19 minutes of milling. For the as-grown sample 40 minutes of milling were needed. As discussed before, probably the amount of oxidation of the samples differed strongly and resulted in different milling rates. For both samples, the measured asymmetry is still very low when magnetic contrast appears, since we are still looking through a remaining thin Al layer and therefore only a small fraction of secondary electrons are polarized. The asymmetry value increases up to $> 5\%$ as expected for Fe and decreases with further milling again when secondaries also from the Mn_2Au layer are emitted. While this is the observation we expected, surprisingly the magnetic domain pattern changes with the milling time. First we consider the field-exposed sample: As discussed above, the x asymmetry image acquired after 30 min ion milling clearly shows magnetic domains. The y component shows the narrow worm-like domains expected from the XMLD-PEEM images of Mn_2Au only. With additional milling the magnetic contrast disappeared (44’). However, after 10 to 15 more minutes the contrast re-appeared. That excludes the possibility of having removed the full Fe layer before. Note that the images from 30’ till 70’ were acquired always at the same position. Even more surprisingly the x asymmetry is inverted now. While the domain shape in general is the same comparing the images acquired after 30 and 60 min, dark and bright areas are now reversed. The detector orientation was not changed during the measurement series. With longer milling time the worm-like features in the y asymmetry component disappeared. The as-grown sample also shows changes depending on the milling time. More milling increases the domain size significantly until no magnetic contrast is visible any more.

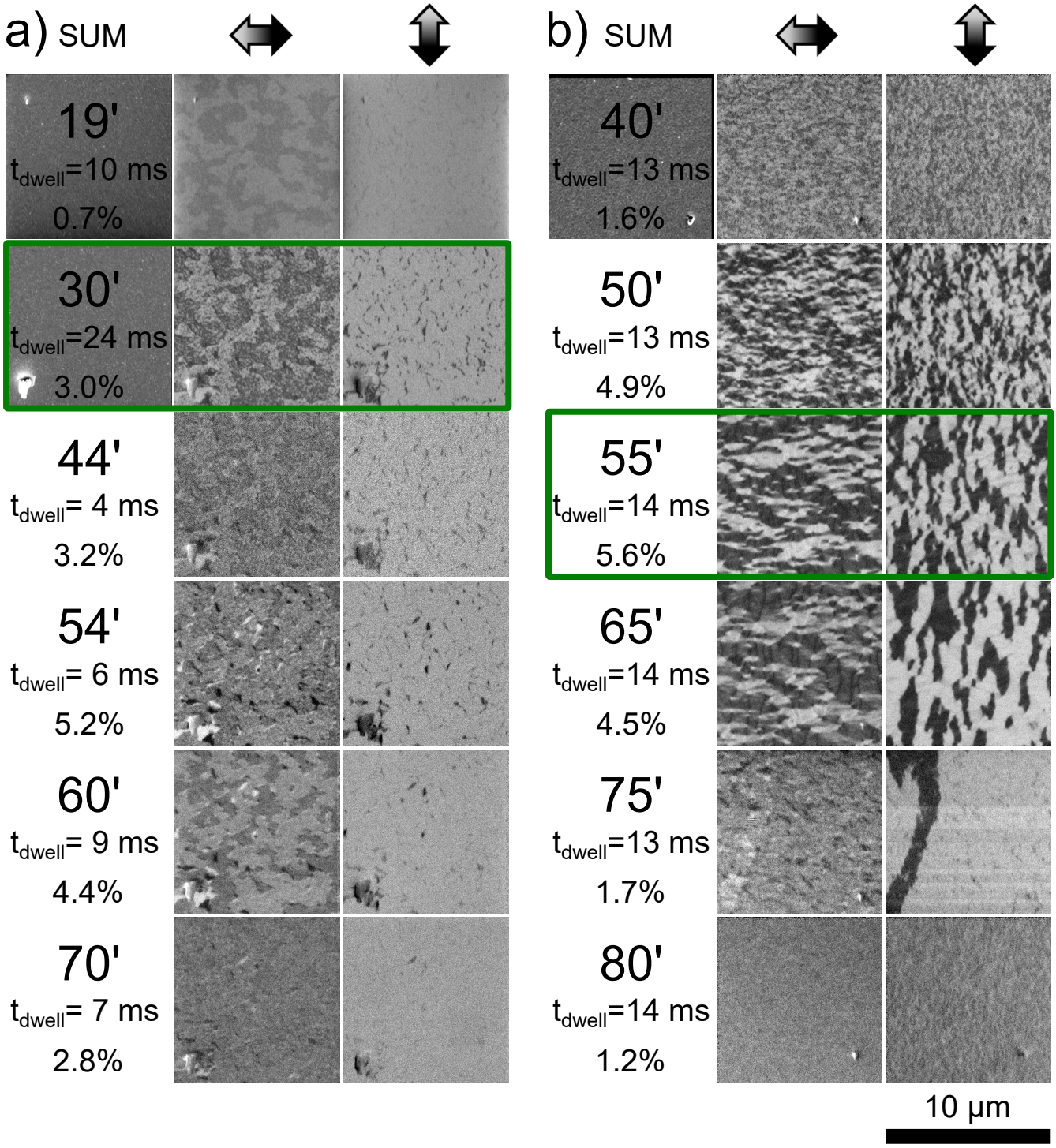

Figure 7.18: **a)** SEMPA images of the field-exposed sample at different stages of Ar^+ ion milling. The area imaged is always the same with the exception of the first row (19'). **b)** SEMPA images of the as-grown sample. The time of Ar^+ ion milling is given in minutes ('), the scan dwell time t_{dwell} is given in milliseconds, the measured asymmetry is given in % and serves as an estimate how much material has been removed by milling. The images with a green frame are discussed in detail above. ($U_{\mathrm{EHT}} = 7.5\,kV$)

Thus either the coupling of Fe to Mn_2Au depends strongly on its thickness or the high energetic ions affect the interlayer exchange coupling. For a better understanding one needs to investigate the domain pattern for stacks with varying Fe thickness. Further, if possible, the ion energy during milling should be decreased or milling even fully avoided by looking across the cap layer, as demonstrated for Pt in [154].

Conclusion and Outlook

The results of this indirect imaging method by using a ferromagnetic layer on top of the antiferromagnet indicate a promising route towards high resolution magnetic imaging of antiferromagnets in the lab, but also reveal difficulties that complicate drawing unambiguous conclusions about the magnetic state of the antiferromagnet. Therefore further research is required to understand the nature of the coupling between the layers and the impact of the sample preparation before imaging. For a better understanding of the coupling, the exchange coupling of Mn_2Au to soft polycrystalline ferromagnets such as $Ni_{80}Fe_{20}$ should be investigated. Furthermore, one could fabricate samples with ferromagnetic layers of different thickness and compare their domain pattern. The impact of ion milling on the magnetization could be investigated by varying the milling energy or by reducing the cap layer thickness and long-time acquisitions without any milling.

8 Conclusion and Outlook

With the new developments for the SEMPA system enabling time-resolved measurements we are able to address many open scientific questions in the field of spintronics with lab-based instrumentation where previously large facility instruments would have been required. The demonstrated time resolution below 2 ns and a five times enhanced SNR using phase-sensitive detection (PSD) allow for magnetic imaging of magnetization dynamics and detecting small oscillatory magnetization changes. We employed SEMPA imaging for different tasks and presented in this thesis, alongside the new scientific findings, the limitations and prospects of this magnetic imaging technique.
We attempted to image current-induced surface spin accumulation due to the spin-Hall and inverse spin-galvanic effects with conventional SEMPA imaging. In this case it was revealed that the inhomogeneous sample voltages due to the applied current have a strong impact on the measured asymmetry values, thereby hampering the interpretation of results. Using the improved signal to noise ratio afforded by the PSD approach, we could detect a signal correlated to the current excitation, but we observed also an unexpected signal when no current was flowing. The results are therefore promising and further supports the potential utility of the new PSD imaging mode for SEMPA. Yet the ambiguity of the findings calls for future studies and theoretical modelling of the signals expected for such emitted secondary electrons. Hence for now, despite their own challenges, other techniques such as magneto-optical Kerr and X-ray-based imaging are ahead of SEMPA if pure spin currents should be detected directly.
Next we demonstrated reliable field-induced vortex wall nucleation with a well defined chirality in curved $Ni_{80}Fe_{20}$ wires. The mechanism of chirality rectification was imaged directly with time-resolved SEMPA. Due to its high reliability, it is a promising mechanism that could find use in chirality-based domain wall logic devices. Using a novel analysis scheme we found different competing switching pathways in the paired half ring geometry and determined their probability. We were even able to determine the origin of changes between these pathways using micromagnetic simulations and quantified their frequency. Considering the different options to vary the frequency e.g. via tuning the width gradient of the wire, the geometry might serve as a basic geometry for future stochastic unconventional computing devices. It could also be exploited further by investigating the coupling of the DWs in dependence on the distance of the half rings. The used analysis scheme with its capability to detect rare events occurring only every one millionth cycle could be of use for the investigation of other systems and possibly even the reliability assessment of devices. It could be employed for a comparative study to determine quantitatively the reliability of different chirality rectification methods including edges, wire ends and notches.
Furthermore, we observed an angular dependence in the field-induced switching be-

haviour in asymmetric rings. If the field is oriented along the symmetry axis of the ring, onion-to-onion state switching takes place whereas if the component of the field perpendicular to the ring symmetry axis increases, the probability for vortex-to-onion-to-vortex state switching increases. The switching depends on the probability of domain wall nucleation and can be tuned also via varying the temperature. If the angle between the field and symmetry axes was small, again two possible switching pathways were observed, however, the resulting overall magnetic configuration after the field pulse was always the same. This angle-dependent switching could be exploited for rotation sensors while thermally assisted changes in the switching could be of use for unconventional computing devices.

In the last part of this thesis we demonstrated the applicability of SEMPA for more advanced material systems with (quasi-)antiferromagnetic properties. First we investigated the strength of biquadratic coupling mediated by an oxide layer depending on the film smoothness and its effect on the domain shape of the biquadratically coupled ferromagnetic film. We imaged the upper CoFe layer in the stack Ta/buffer/IrMn/CoFe/FeO/CoFe. Depending on the buffer layer, Ru or NiFeCr/CoFe, the smoothness of the oxide layer varied and for smoother films a higher biquadratic coupling was found that was revealed by smaller domain sizes and larger angles between the magnetization of adjacent domains. Progress in thin film deposition techniques and a broader buffer material survey will allow for the fabrication of very smooth films so that the effective biquadratic coupling in heterostructures could be enhanced. Strong biquadratic coupling could be employed in quasi-antiferromagnetic spin-torque oscillators with frequencies exceeding those of conventional STOs due to reduced stray fields. We were able to image the detailed spin structure of skyrmion bubbles in thick GdFeCo (8 nm) and found pure Néel walls at room temperature. From a thorough analysis of the domain wall width and further complementary SQUID magnetometry the exchange stiffness and the effective anisotropy could be determined. Based on these values the DMI could be quantified. Further static and dynamic SEMPA measurements at different temperatures will reveal the static and dynamic properties of this ferrimagnetic system. Measuring the skyrmion sizes and velocities would allow to estimate the magnetic and angular momentum compensation temperatures in the ferrimagnet. Other parameters that could be varied are the stoichiometry of the ferrimagnet and the selection of DMI-generating heavy metals. Furthermore, other material stacks and even multilayers consisting of very thin films could be investigated using SEMPA due to its inherent surface sensitivity.

Finally we imaged the domains of the antiferromagnet Mn_2Au via an exchange-coupled Fe layer. The observed domain pattern is very characteristic for Mn_2Au and indicates a clear coupling between the antiferromagnet and the ferromagnetic mirror layer. Since magnetic imaging of antiferromagnets has been mainly limited to XMLD X-ray imaging at large scale facilities, this is a very promising way forward for lab-based investigation of metallic and even nonmetallic antiferromagnets via imaging. However, some detailed question about the coupling nature are still unsolved and need further investigation. Further studies should investigate the coupling of Mn_2Au to soft ferromagnets such as $Ni_{80}Fe_{20}$ and relate the exchange coupling strength to the thickness of

the ferromagnetic layer. Furthermore, supplementary XMCD and XMLD PEEM of the Mn_2Au/ferromagnet bilayers would be highly instructive as an additional confirmation of the coupling. With a thorough understanding of the coupling patterned Mn_2Au samples with an exchange-coupled top ferromagnetic layer could be used to investigate Néel spin-orbit torques and correlate the observed changes in the domain pattern to resistance changes.

Overall, we extended the applicability of SEMPA magnetic imaging and employed it to investigate a broad range of material systems and scientific challenges and demonstrated the benefit for the continuously growing research field of spintronics. The work has shown that SEMPA can compete with top-end X-ray synchrotron facilities and even provide certain additional functionalities, while being available in a convenient lab-based setting with increased access.

Appendix

8.1 Acronyms

2D	2-Dimensional.
AC	Alternating Current.
AFM	Atomic Force Microscopy.
AHE	Anomalous Hall Effect.
AR	Asymmetric Ring.
AWG	Arbitrary Waveform Generator.
CAD	Computer-Aided Design.
ccw	counterclockwise.
cw	clockwise.
DAQ	Data Acquisition.
DC	Direct Current.
DLL	Dynamic Link Library.
DMI	Dzyaloshinskii-Moriya Interaction.
DUT	Device Under Test.
DW	Domain Wall.
EBL	Electron Beam Lithography.
EHT	Electron High Tension.
FIFO	First In–First Out (buffer).
FM	Ferromagnet.
FMR	Ferromagnetic Resonance.
FOV	Field of View.
FPGA	Field Programmable Gate Array.
FWHM	Full Width at Half Maximum.
GPIB	General Purpose Interface Bus.
HR	Half Ring.

ISGE	Inverse Spin-Galvanic Effect.
ISHE	Inverse Spin-Hall Effect.
LEDS	Low Energy Diffusive Scattering.
LEED	Low Energy Electron Diffraction.
LLG	Landau-Lifshitz-Gilbert.
LTEM	Lorentz Transmission Electron Microscopy.
MBE	Molecular Beam Epitaxy.
MFM	Magnetic Force Microscopy.
MIBK	Methyl Isobutyl Ketone.
MMA	Methyl Methacrylate.
MRAM	Magnetic Random Access Memory.
NEP	N-Ethylpyrrolidone.
PEEM	Photo Emission Electron Microscopy.
PMA	Perpendicular Magnetic Anisotropy.
PMMA	Poly Methyl Methacrylate.
PMN-PT	Lead Magnesium Niobate-Lead Titanate.
PNR	Polarized Neutron Reflectometry.
PSD	Phase Sensitive Detection.
Py	Permalloy ($Ni_{80}Fe_{20}$).
RE	Rare Earth.
RF	Radio Frequency.
RKKY	Ruderman–Kittel–Kasuya–Yosida (coupling).
ROI	Region of Interest.
SEM	Scanning Electron Microscope.
SEMPA	Scanning Electron Microscope with Polarization Analysis.
SHE	Spin-Hall Effect.
SMA	Sub-Miniature-A (connector).
SMC	SubMiniature-C (connector).
SNR	Signal-to-Noise Ratio.
SOT	Spin-Orbit Torque.
SP	Spin Pumping.
SPLEED	Spin-Polarized Low Energy Electron Diffraction.
STO	Spin Torque Oscillator.
STXM	Scanning Transmission X-Ray Microscopy.

TDC	Time-to-Digital Converter.
TDR	Time Domain Reflectometry.
TM	Transition Metal.
TW	Transverse (Domain) Wall.
UHV	Ultrahigh Vacuum.
VC	Vortex Core.
VSM	Vibrating Sample Magnetometry.
VW	Vortex (Domain) Wall.
XMCD	X-ray Magnetic Circular Dichroism.
XMLD	X-ray Magnetic Linear Dichroism.
XRR	X-Ray Reflectometry.
YIG	Yttrium Iron Garnet.

8.2 Details of Sample Fabrication

The samples investigated in Ch. 3, Ch. 5 and Ch. 6 were fabricated by me, while the sputter deposition of the spin-Hall materials Pt, Ta, Cu in Ch. 4 was done by J. Henrizi, J. Cramer, M. Vafaee and S. Jaiswal in the Singulus Rotaris system. For all those samples naturally oxidized undoped Si substrates with a resistivity of $> 1000\,\Omega$cm (CrysTec GmbH) were used. For the lift-off process I used NEP. For a better lift-off I placed the sample alternately in hot and cold NEP. Larger structures (e.g. the striplines) were lifted with the help of ultrasound.

Electron-Beam Lithography

We used two different electron-beam lithography lift-off recipes for the sample fabrication depending on the structure requirements. Electron-beam lithography was performed with the 'Süss Micro Tec's LabSpin Platform' and the Raith Pioneer system in the cleanroom lab in Mainz. The PMMA (950K A4) is PMMA 950K A11 (which is obtained commercially) diluted in anisole (by S. Kauschke). MMA EL6 is commercially available.

Double-layer positive resist MMA/PMMA

This recipe[1] was used for larger structures with a maximum thickness up to 100 nm such as the contact and the stripline fabrication in Ch. 3, Ch. 4, Ch. 5 and Ch. 6.

- Cleaning procedure
  - acetone 60 s
  - isopropanol 60 s
  - high-purity water 60 s
  - blow-dry the sample with nitrogen gun
  - hotplate > 120°C for 1 min (water desorption)
  - cool down substrate 1 min
- Coating procedure
  - methyl methacrylate MMA (8.5) MAA EL6 0.1 ml
  - pre-spin 2 s at 500 rpm/ Acc.:500
  - spin 60 s at 3000 rpm/ Acc.: 3000
  - 5 min pause
  - soft-bake: 180°C for 90 s
  - cool down substrate 5 min
  - poly methyl methacrylate (PMMA) 950k A4% 0.1 ml
  - pre-spin 1 s at 500 rpm/ Acc.: 500
  - spin 45 s at 3000 rpm/ Acc.: 3000
  - 5 min pause
  - soft-bake: 180°C for 90 s

[1] Recipe from the group wiki, developed by Stefan Kauschke and André Löscher (7th November 2020)

  - cool down substrate 5 min

- Exposure
  - EHT: 10 kV
  - aperture: 30 - 60 µm
  - working distance: 9 mm
  - step size: 20 - 100 nm
  - area dose: 160 µC/cm^2
  - vector mode: meander

- Development
  - MIBK:IPA dive development 30 s
  - development break: 30 s isopropanol
  - blow-dry with nitrogen

Single-layer positive resist PMMA

This recipe[2] was used for thinner nanoscale structures (max. 60 nm) such as the spin-Hall wires in Ch. 4 and the $Ni_{80}Fe_{20}$ structures in Section 2.6, Ch. 5 and Ch. 6.

- Cleaning procedure (as in the previous recipe)

- Coating procedure
  - PMMA 950k A4% 0.1 ml
  - pre-spin 2 s at 500 rpm/ Acc.: 500
  - Spin 60 s at 4000 rpm/ Acc.: 4000 (resist thickness approx. 200 nm)
  - 5 min pause
  - soft-bake: 180°C for 90 s
  - cool down substrate 5 min

- Exposure
  - EHT: 20 kV
  - aperture: 7.5 or 10 µm
  - working distance: 8.2 mm
  - step size: 5 nm
  - area dose: 360 µC/cm^2
  - vector mode: meander

- Development
  - MIBK:IPA(1:3) dive development 45 s
  - development break: 30 s isopropanol
  - blow-dry with nitrogen

[2]Recipe from the group wiki, developed by Stefan Kauschke and Alexander Pfeiffer (7th November 2020)

Material Deposition and Preparation of the Investigated SHE-Samples

The contact pads of these samples were sputtered in the small contact sputter chamber in Mainz (base pressure: low 10^{-7} mbar). First Cr(5 nm) was deposited as an adhesion layer, followed by 55 nm Au. The spin-Hall materials were deposited in the Singulus sputter machine. Target position, sputter power and Ar flow are given in Tab. 8.2, as well as the Ar milling time before SEMPA imaging. The samples were milled in the SEMPA preparation chamber with Ar^+ ions (1 kV, 10 mA).

Material Deposition and Preparation of the Samples Investigated in Ch. 5 and Ch. 6

The stripline was deposited in the Singulus sputter chamber:
02/20/19 Ta(4 nm)[CuN(16 nm))Ta(4 nm)]×3 deposition in Singulus (JC068); target positions: Ta RSM1.4, CuN RSM2.4
The ferromagnetic structures were deposited using thermal evaporation in the small MBE:
05/02/19 thermal evaporation of $Ni_{80}Fe_{20}$ in the small MBE chamber:

- position: $z = 430\,\text{mm}; y = 5\,\text{mm}; x = 20\,\text{mm}$
- chamber pressure: base pressure $2.9 \cdot 10^{-9}$ mbar; evaporation pressure $6 \cdot 10^{-9}$ mbar
- deposition parameters: $U_{\text{HV}} = 960 - 1003\,\text{V}$; $I_{\text{filament}} = 2.15\,\text{A}$; 90°/minute rotation in the first 20 minutes; rate $\approx 6\,\text{nm/h}$
- quartz crystal thickness monitor settings (Inficon SQM-160): $\rho = 8.69\,\text{g/cm}^3$; tooling= 50; z-factor= 0.33

After loading the sample, the sample was milled on the preparation stage with Ar^+ ions (1 kV, 10mA). The base pressure was $< 2 \cdot 10^{-9}$ mbar, the working pressure $5.0 \cdot 10^{-6}$ to $7.5 \cdot 10^{-6}$ mbar. Then 0.5 nm Fe were deposited *via* thermal evaporation *in situ* on the sample to enhance the SEMPA contrast (Fig. 2.10). The filament current was 2.0 A and the high voltage 510 V resulting in a deposition rate of 6 nm per hour. With the middle evaporator in the preparation chamber we can not monitor the thickness and have the sample at a good position for material deposition at the same time. Thus we first monitor the evaporation rate until it is stable (detector position 14.4 mm; quartz crystal thickness monitor settings (Inficon SQM-160): $\rho = 7.86\,\text{g/cm}^3$; tooling= 100; z-factor= 0.35) while the sample is retracted. After reaching a constant evaporation rate the detector is retracted (13 mm) and the sample is placed at the same position by moving the transfer stick forward and tilting it so that the sample surface is facing the evaporator.
Before SEMPA imaging we applied a high current through the stripline because then the carbonization due to e-beam exposure was observed to be smaller.

Material	geometry	Singulus: position, power, Ar flow	d_{dep} [nm]	$\mathrm{date}_{\mathrm{dep}}$	t_{mill} [min]	Δd_{mill} [nm]	$\mathrm{date}_{\mathrm{mill}}$	Fig.	$\mathrm{date}_{\mathrm{SEMPA}}$
Pt	U	RSM2.3, 0.8 kW, 60 sccm	25	10/20/15	30	6.3	12/04/15	Fig. 4.1,Fig. 4.2	12/08/15
Ta	U	RSM1.4, 0.8 kW	10	10/21/15	30	2.8 [179]	01/11/16	Fig. 4.2	08/08/16
Pt	U	RSM1.5, 0.8 kW, 60 sccm	20	08/04/16	15	3.2	08/08/16	Fig. 4.3	08/08/16
Pt	S	RSM1.5, 0.8 kW, 60 sccm	20	08/04/16	15	3.2	08/12/16	Fig. 4.4	08/12/16
Cu	S	RSM1.5, 0.8 kW	25	07/01/16	30	11.5 [179]	09/08/16	Fig. 4.5	09/10/16
Pt	I	RSM1.12, 0.8 kW, 60 sccm	20	10/20/16	20	4.2	11/16/16	Fig. 4.6	11/16/16
Pt	I	RSM1.12, 0.8 kW, 60 sccm	20	10/20/16	15	3.2	08/14/20	Fig. 4.8	09/10/20

Table 8.2: Material deposition and sample preparation parameters for the samples investigated in Ch. 4. The milling rate was calibrated for Pt, the values provided for Ta and Cu are based on Ref. [179].

8.3 Detailed SEMPA Measurement Procedure

Connection of the Time-to-Digital Converter

The four channeltron lines are connected to the first four stop inputs of the TDC. Then there are two reference signals. The first one is provided by the DAQ card and is synchronous to the scan frequency. It is connected to the 'pixel tag' input. The second needed reference synchronizes the TDC to the excitation signal. Here two connection options are available:

1. 'start input': To use this option, in the initialization file 'tdc_gpx3.ini' the 'StartCounter' variable must be set to 'YES' ('StartCounter = YES'). In general, the 'start input' of the ACAM chip accepts only frequencies between 100 kHz and 7 MHz, for higher frequencies the 'Start_Divider' variable in 'tdc_gpx3.ini' must be increased (e.g. 'Start_Divider=4'). The reference pulse is provided by the AWG and has an amplitude of 2.5 Vpp and a width of about 20 ns with a rise/ fall time as short as possible.
2. 5th 'stop input' (Fig. 8.1): To use this option, in the initialization file (min. 100 kHz, max. 7 MHz). 'tdc_gpx3.ini' the 'StartCounter' variable must be set to 'NO' ('StartCounter = NO'). If a static measurement is done, the pixel tag from the DAQ card can be fanned and fed into this channel, since here also frequencies lower than 100 kHz work.

Figure 8.1: Surface Concept TDC with the 5th stop input used as reference input. Alternatively the 'start input' can be used. A schematic drawing of the complete experimental setup is provided in Ch. 3 in Fig. 3.2.

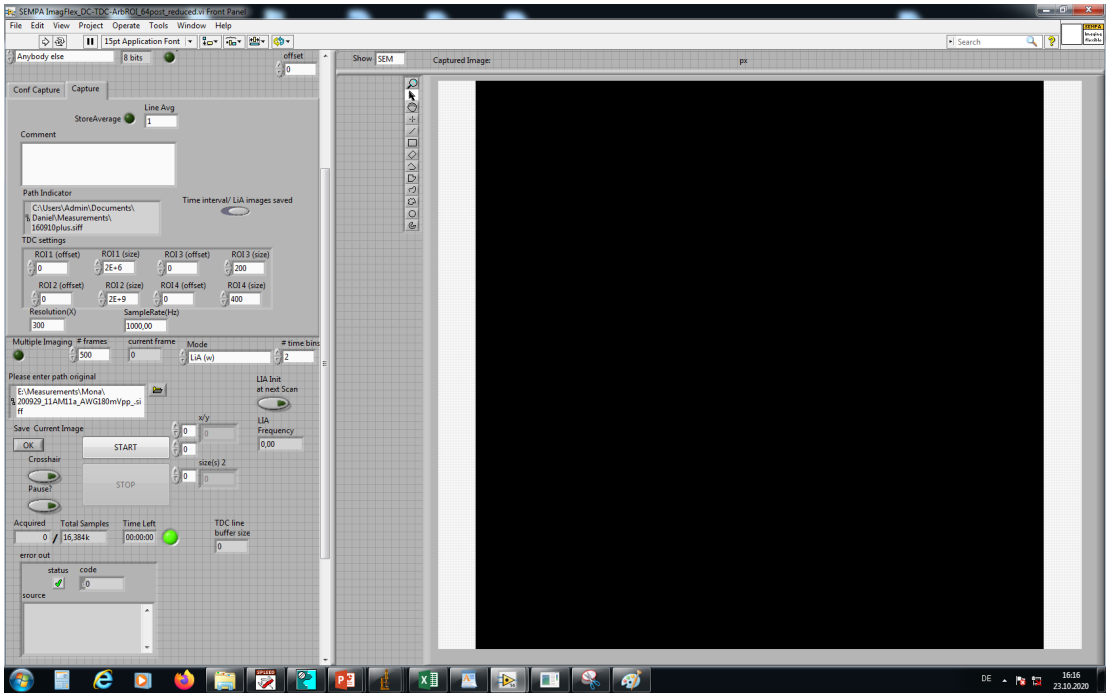

Figure 8.2: Screenshot of the graphical user interface of the LabVIEW measurement software in the 'capture' mode. At the left side the parameters for the acquisition can be set, the right part shows the live scan line by line. At the upper left side of the scan window the ROI tools are placed (rectangle, circle, annulus,...).

Typical Measurement Procedure and Parameters

1. Focussing using the SmartSEM software. Typical beam parameters: EHT=3-10 kV, 3 nA; the working distance typically around 10.8 mm. The FOV is chosen depending on the spatial resolution needed. Typical values are between 10 and 40 µm.
2. Optimization of the channeltron countrates by varying the deflector voltages ('EIS' software or 'TDC_demo.exe').
3. Overview image in the LabVIEW software scanning the full FOV with short dwell time. Then a ROI with one of the ROI selection tools must be selected (rectangle, circle, annulus or arbitrary shape ROI). If multi-scan imaging is required, the option 'Multiple Imaging' is activated. Depending on the sample drift, the ROI must be chosen to be considerably smaller than the full FOV to allow for the adaption of the deflection voltages. Further, for multi-scan imaging a clear topographic feature must be visible in the ROI.
4. Image acquisition in the 'Capture Mode' (Fig. 8.2). For a single scan image, the scan frequency can be as low as desired to achieve a reasonable SNR. In the multi-scan mode the acquisition time for one scan should be < 1 minute to avoid image

distortions within one scan. The pixel size of the image is typically chosen so that the spatial resolution of approximately 20 nm is oversampled by a factor of 2 (typical pixel width about 300 pixel). In the 'Multiple Imaging' mode after the first scan a dialogue window pops up, where the user needs to select an image region in the ROI that should be used for pattern recognition. Then the software subsequently scans the ROI until the desired number of scans is reached.
Besides scan frequency and pixel size the user needs to choose the time interval with respect to the reference frequency. Here two options are available by a slider switch under the 'Capture' tab:

a) 'LIA images saved': Selection of the number of time bins with equal length ('# time bins'). For every time bin and detector channel an image is saved.
b) 'Time interval images saved': 4 time intervals ('ROI0-3') can be set specifically by determining the delay to the reference pulse ('offset') and the length of the time interval ('size').

A detailed instruction of the measurement procedure is provided in the group wiki.

Bibliography

[1] Bruker Sharp Nitride Lever (SNL) probes.
URL https://www.brukerafmprobes.com/p-3693-snl-10.aspx.

[2] URL http://gwyddion.net/.

[3] URL http://micromagnum.informatik.uni-hamburg.de/.

[4] URL https://www.minicircuits.com/pdfs/LZY-22+.pdf.

[5] FOCUS FERRUM & SPINSwitch, 2018.
URL https://www.focus-gmbh.com/resources/UHV-Instruments/Spectroscopy/Spin-Detection/FERRUM/FOCUS_FERRUMFlyer2018Rev3WEB.pdf.

[6] acam messelektronik GmbH.
TDC-GPX multifunctional High-end Time-to-Digital Converter.
URL http://www.acam.de/products/time-to-digital-converters/tdc-gpx/.

[7] M. Aeschlimann, M. Scheinfein, J. Unguris, F. J. A. M. Greidanus, and S. Klahn.
Magnetic-Field-modulated Written Bits in TbFeCo Thin Films: Transmission Electron Microscopy Lorentz and Scanning Electron Microscopy with Polarization Analysis Studies.
J. Appl. Phys., 68(9):4710–4718, 1990.
doi:10.1063/1.346151.

[8] A. Aharoni.
Complete Eigenvalue Spectrum for the Nucleation in a Ferromagnetic Prolate Spheroid.
Phys. Rev., 131:1478–1482, Aug 1963.
doi:10.1103/PhysRev.131.1478.

[9] R. Allenspach.
Spin-Polarized Scanning Electron Microscopy.
IBM J. Res. Develop., 44(4):553–570, 2000.
doi:10.1147/rd.444.0553.

[10] D. A. Allwood, G. Xiong, C. C. Faulkner, D. Atkinson, D. Petit, and R. P. Cowburn.
Magnetic Domain-Wall Logic.

Science, 309(5741):1688–1692, 2005.
ISSN 0036-8075.
doi:10.1126/science.1108813.

[11] K. Ando, S. Takahashi, J. Ieda, Y. Kajiwara, H. Nakayama, T. Yoshino, K. Harii, Y. Fujikawa, M. Matsuo, S. Maekawa, and E. Saitoh.
Inverse Spin-Hall Effect Induced by Spin Pumping in Metallic System.
J. Appl. Phys., 109(10):103913, 2011.
doi:10.1063/1.3587173.

[12] J. F. Ankner and G. P. Felcher.
Polarized-Neutron Reflectometry.
J. Magn. Magn. Mater., 200(1):741 – 754, 1999.
ISSN 0304-8853.
doi:10.1016/S0304-8853(99)00392-3.

[13] D. Aravinthan, P. Sabareesan, and M. Daniel.
Spin Transfer Torque Switching in Pentalayer Nanopillar with Biquadratic Coupling.
J. Supercond. Nov. Magn., 31(8):2567–2572, 2018.
doi:10.1007/s10948-017-4517-3.

[14] P. N. Argyres.
Theory of the Faraday and Kerr Effects in Ferromagnetics.
Phys. Rev., 97:334–345, Jan 1955.
doi:10.1103/PhysRev.97.334.

[15] M. N. Baibich, J. M. Broto, A. Fert, F. Nguyen Van Dau, F. Petroff, P. Etienne, G. Creuzet, A. Friederich, and J. Chazelas.
Giant Magnetoresistance of (001)Fe/(001)Cr Magnetic Superlattices.
Phys. Rev. Lett., 61:2472–2475, Nov 1988.
doi:10.1103/PhysRevLett.61.2472.

[16] L. Baldrati, O. Gomonay, A. Ross, M. Filianina, R. Lebrun, R. Ramos, C. Leveille, F. Fuhrmann, T. R. Forrest, F. Maccherozzi, S. Valencia, F. Kronast, E. Saitoh, J. Sinova, and M. Kläui.
Mechanism of Néel Order Switching in Antiferromagnetic Thin Films Revealed by Magnetotransport and Direct Imaging.
Phys. Rev. Lett., 123:177201, Oct 2019.
doi:10.1103/PhysRevLett.123.177201.

[17] V. Baltz, A. Manchon, M. Tsoi, T. Moriyama, T. Ono, and Y. Tserkovnyak.
Antiferromagnetic Spintronics.
Rev. Mod. Phys., 90:015005, Feb 2018.
doi:10.1103/RevModPhys.90.015005.

[18] V.M.T.S. Barthem, C.V. Colin, H. Mayaffre, M.-H. Julien, and D. Givord.
Revealing the Properties of Mn_2Au for Antiferromagnetic Spintronics.
Nat. Commun., 4(1):1–7, 2013.
doi:10.1038/ncomms3892.

[19] R. P. Beardsley, S. Bowe, D. E. Parkes, C. Reardon, K. W. Edmonds, B. L. Gallagher, S. A. Cavill, and A. W. Rushforth.
Deterministic Control of Magnetic Vortex Wall Chirality by Electric Field.
Sci. Rep., 7(1):7613, 2017.

[20] E. Beaurepaire, J.-C. Merle, A. Daunois, and J.-Y. Bigot.
Ultrafast Spin Dynamics in Ferromagnetic Nickel.
Phys. Rev. Lett., 76:4250–4253, May 1996.
doi:10.1103/PhysRevLett.76.4250.

[21] A. Belabbes, G. Bihlmayer, F. Bechstedt, S. Blügel, and A. Manchon.
Hund's Rule-Driven Dzyaloshinskii-Moriya Interaction at $3d$−$5d$ Interfaces.
Phys. Rev. Lett., 117:247202, Dec 2016.
doi:10.1103/PhysRevLett.117.247202.

[22] L. Berger.
Low-Field Magnetoresistance and Domain Drag in Ferromagnets.
J. Appl. Phys., 49(3):2156–2161, 1978.
doi:10.1063/1.324716.

[23] L. Berger.
Emission of Spin Waves by a Magnetic Multilayer Traversed by a Current.
Phys. Rev. B, 54:9353–9358, Oct 1996.
doi:10.1103/PhysRevB.54.9353.

[24] G. Binasch, P. Grünberg, F. Saurenbach, and W. Zinn.
Enhanced Magnetoresistance in Layered Magnetic Structures with Antiferromagnetic Interlayer Exchange.
Phys. Rev. B, 39:4828–4830, Mar 1989.
doi:10.1103/PhysRevB.39.4828.

[25] M. Binder, A. Weber, O. Mosendz, G. Woltersdorf, M. Izquierdo, I. Neudecker, J. R. Dahn, T. D. Hatchard, J.-U. Thiele, C. H. Back, and M. R. Scheinfein.
Magnetization Dynamics of the Ferrimagnet CoGd near the Compensation of Magnetization and Angular Momentum.
Phys. Rev. B, 74:134404, Oct 2006.
doi:10.1103/PhysRevB.74.134404.

[26] A. Bisig, M. Stärk, M.-A. Mawass, C. Moutafis, J. Rhensius, J. Heidler, F. Büttner, M. Noske, M. Weigand, S. Eisebitt, T. Tyliszczak, B. Van Waeyenberge, H. Stoll, G. Schütz, and M. Kläui.

Correlation between Spin Structure Oscillations and Domain Wall Velocities.
Nat. Commun., 4(1):1–8, 2013.
doi:10.1038/ncomms3328.

[27] A. Bisig, M.-A. Mawass, M. Stärk, C. Moutafis, J. Rhensius, J. Heidler, S. Gliga, M. Weigand, T. Tyliszczak, B. Van Waeyenberge, H. Stoll, G. Schütz, and M. Kläui.
Dynamic Domain Wall Chirality Rectification by Rotating Magnetic Fields.
Appl. Phys. Lett., 106(12):122401, 2015.
doi:10.1063/1.4915256.

[28] F. Bitter.
Experiments on the Nature of Ferromagnetism.
Phys. Rev., 41:507–515, Aug 1932.
doi:10.1103/PhysRev.41.507.

[29] S. Blundell.
Magnetism in Condensed Matter.
Oxford Master Series in Condensed Matter Physics. Oxford University Press, 2001.
ISBN 9780198505914.

[30] S. Y. Bodnar, L. Šmejkal, I. Turek, T. Jungwirth, O. Gomonay, J. Sinova, A. A. Sapozhnik, H.-J. Elmers, M. Kläui, and M. Jourdan.
Writing and Reading Antiferromagnetic Mn_2Au by Néel Spin-Orbit Torques and Large Anisotropic Magnetoresistance.
Nat. Commun., 9(1):1–7, 2018.
doi:10.1038/s41467-017-02780-x.

[31] S. Y. Bodnar, M. Filianina, S. P. Bommanaboyena, T. Forrest, F. Maccherozzi, A. A. Sapozhnik, Y. Skourski, M. Kläui, and M. Jourdan.
Imaging of Current Induced Néel Vector Switching in Antiferromagnetic Mn_2Au.
Phys. Rev. B, 99:140409, Apr 2019.
doi:10.1103/PhysRevB.99.140409.

[32] S. P. Bommanaboyena, T. Bergfeldt, R. Heller, M. Kläui, and M. Jourdan.
High Quality Epitaxial Mn_2Au (001) Thin Films Grown by Molecular Beam Epitaxy.
J. Appl. Phys., 127(24):243901, 2020.
doi:10.1063/5.0009566.

[33] S. Bonetti, R. Kukreja, Z. Chen, D. Spoddig, K. Ollefs, C. Schöppner, R. Meckenstock, A. Ney, J. Pinto, R. Houanche, J. Frisch, J. Stöhr, H. A. Dürr, and H. Ohldag.
Microwave Soft X-Ray Microscopy for Nanoscale Magnetization Dynamics in the 5–10 GHz Frequency Range.
Rev. Sci. Instrum., 86(9):093703, 2015.

doi:10.1063/1.4930007.

[34] B. Borie, M. Voto, L. Lopez-Diaz, H. Grimm, M. Diegel, M. Kläui, and R. Mattheis.
Reliable Propagation of Magnetic Domain Walls in Cross Structures for Advanced Multiturn Sensors.
Phys. Rev. Applied, 8:044004, Oct 2017.
doi:10.1103/PhysRevApplied.8.044004.

[35] S. R. Bowden, K. K. L. Ahmed, and U. J. Gibson.
Longitudinal Magneto-Optic Kerr Effect Detection of Latching Vortex Magnetization Chirality in Individual Mesoscale Rings.
Appl. Phys. Lett., 91(23):232505, 2007.
doi:10.1063/1.2822814.

[36] P. M. Braganca, B. A. Gurney, B. A. Wilson, J. A. Katine, S. Maat, and J. R. Childress.
Nanoscale Magnetic Field Detection using a Spin Torque Oscillator.
Nanotechnology, 21(23):235202, may 2010.
doi:10.1088/0957-4484/21/23/235202.

[37] J. Brandão, R. L. Novak, H. Lozano, P. R. Soledade, A. Mello, F. Garcia, and L. C. Sampaio.
Control of the Magnetic Vortex Chirality in Permalloy Nanowires with Asymmetric Notches.
J. Appl. Phys., 116(19):193902, 2014.
doi:10.1063/1.4902008.

[38] D. Braun and A. Libchaber.
Computer-Based Photon-Counting Lock-in for Phase Detection at the Shot-Noise Limit.
Opt. Lett., 27(16):1418–1420, 2002.
doi:10.1364/OL.27.001418.

[39] C. Brüne, A. Roth, E. Novik, M. König, H. Buhmann, E. M. Hankiewicz, W. Hanke, J. Sinova, and L. W. Molenkamp.
Evidence for the Ballistic Intrinsic Spin Hall Effect in HgTe Nanostructures.
Nature Phys., 6(6):448–454, 2010.
doi:10.1038/nphys1655.

[40] F. Büttner, I. Lemesh, and Geoffrey S. D. Beach.
Theory of Isolated Magnetic Skyrmions: From Fundamentals to Room Temperature Applications.
Sci. Rep., 8(1):1–12, 2018.
doi:10.1038/s41598-018-22242-8.

[41] J. N. Chapman and M. R. Scheinfein.
Transmission Electron Microscopies of Magnetic Microstructures.
J. Magn. Magn. Mater., 200(1):729–740, 1999.
doi:10.1016/S0304-8853(99)00317-0.

[42] J.-Y. Chauleau, R. Weil, A. Thiaville, and J. Miltat.
Magnetic Domain Walls Displacement: Automotion Versus Spin-Transfer Torque.
Phys. Rev. B, 82:214414, Dec 2010.
doi:10.1103/PhysRevB.82.214414.

[43] C. Chen, D. Tian, H. Zhou, D. Hou, and X. Jin.
Generation and Detection of Pure Spin Current in an H-Shaped Structure of a Single Metal.
Phys. Rev. Lett., 122:016804, Jan 2019.
doi:10.1103/PhysRevLett.122.016804.

[44] H.-B. Chen and Y.-Q. Li.
Electric-Field-Controlled Suppression of Walker Breakdown and Chirality Switching in Magnetic Domain Wall Motion.
Appl. Phys. Express, 9(7):073004, jun 2016.
doi:10.7567/apex.9.073004.

[45] X. Z. Chen, R. Zarzuela, J. Zhang, C. Song, X. F. Zhou, G. Y. Shi, F. Li, H. A. Zhou, W. J. Jiang, F. Pan, and Y. Tserkovnyak.
Antidamping-Torque-Induced Switching in Biaxial Antiferromagnetic Insulators.
Phys. Rev. Lett., 120:207204, May 2018.
doi:10.1103/PhysRevLett.120.207204.

[46] R. Cheng, M. W. Daniels, J.-G. Zhu, and D. Xiao.
Ultrafast Switching of Antiferromagnets via Spin-Transfer Torque.
Phys. Rev. B, 91:064423, Feb 2015.
doi:10.1103/PhysRevB.91.064423.

[47] A. Chernyshov, M. Overby, X. Liu, J. K. Furdyna, Y. Lyanda-Geller, and L. P. Rokhinson.
Evidence for Reversible Control of Magnetization in a Ferromagnetic Material by Means of Spin–Orbit Magnetic Field.
Nature Phys., 5(9):656–659, 2009.
doi:10.1038/nphys1362.

[48] G. Chrobok and M. Hofmann.
Electron Spin Polarization of Secondary Electrons Ejected From Magnetized Europium Oxide.
Physics Letters A, 57(3):257 – 258, 1976.
ISSN 0375-9601.
doi:10.1016/0375-9601(76)90056-6.

[49] S.-H. Chung, D. T. Pierce, and J. Unguris.
Simultaneous Measurement of Magnetic Vortex Polarity and Chirality Using Scanning Electron Microscopy with Polarization Analysis (SEMPA).
Ultramicroscopy, 110(3):177 – 181, 2010.
ISSN 0304-3991.
doi:10.1016/j.ultramic.2009.11.002.

[50] R. Coehoorn.
Period of Oscillatory Exchange Interactions in Co/Cu and Fe/Cu Multilayer Systems.
Phys. Rev. B, 44:9331–9337, Nov 1991.
doi:10.1103/PhysRevB.44.9331.

[51] J. M. D. Coey.
Magnetism and Magnetic Materials.
Cambridge University Press, 2010.
doi:10.1017/CBO9780511845000.

[52] J. Cramer.
Propagation, Manipulation and Detection of Magnonic Spin Currents in Magnetic Oxides and Metals.
Univ., Mainz, 2018.
URL `http://nbn-resolving.org/urn:nbn:de:hebis:77-diss-1000024133`.

[53] K. De, A. Klimentov, T. Maeno, R. Mashinistov, P. Nilsson, D. Oleynik, S. Panitkin, E. Ryabinkin, and T. Wenaus.
Accelerating Science Impact through Big Data Workflow Management and Supercomputing.
EPJ Web Conf., 108:01003, 2016.
doi:10.1051/epjconf/201610801003.

[54] P.G. De Gennes.
Inelastic Magnetic Scattering of Neutrons at High Temperatures.
J. Phys. Chem. Solids, 4(3):223 – 226, 1958.
ISSN 0022-3697.
doi:https://doi.org/10.1016/0022-3697(58)90120-3.

[55] A. De Lucia, B. Krüger, O. A. Tretiakov, and M. Kläui.
Multiscale model approach for magnetization dynamics simulations.
Phys. Rev. B, 94:184415, Nov 2016.
doi:10.1103/PhysRevB.94.184415.

[56] S. Demokritov, E. Tsymbal, P. Grünberg, W. Zinn, and I. K. Schuller.
Magnetic-Dipole Mechanism for Biquadratic Interlayer Coupling.
Phys. Rev. B, 49:720–723, Jan 1994.
doi:10.1103/PhysRevB.49.720.

[57] S. O. Demokritov.
Biquadratic Interlayer Coupling in Layered Magnetic Systems.
J. Phys. D: Appl. Phys., 31(8):925–941, apr 1998.
doi:10.1088/0022-3727/31/8/003.

[58] K. Di, V. L. Zhang, H. S. Lim, S. C. Ng, M. H. Kuok, J. Yu, J. Yoon, X. Qiu, and H. Yang.
Direct Observation of the Dzyaloshinskii-Moriya Interaction in a Pt/Co/Ni Film.
Phys. Rev. Lett., 114:047201, Jan 2015.
doi:10.1103/PhysRevLett.114.047201.

[59] M. Diegel, S. Glathe, R. Mattheis, M. Scherzinger, and E. Halder.
A New Four Bit Magnetic Domain Wall Based Multiturn Counter.
IEEE Trans. Magn., 45(10):3792–3795, Oct 2009.
ISSN 1941-0069.
doi:10.1109/TMAG.2009.2024426.

[60] B. Dieny, I. L. Prejbeanu, K. Garello, P. Gambardella, P. Freitas, R. Lehndorff, W. Raberg, U. Ebels, S. O. Demokritov, J. Akerman, A. Deac, P. Pirro, C. Adelmann, A. Anane, A. V. Chumak, A. Hirohata, S. Mangin, S. O. Valenzuela, M. Cengiz Onbaşlı, M. d'Aquino, G. Prenat, G. Finocchio, L. Lopez-Diaz, R. Chantrell, O. Chubykalo-Fesenko, and P. Bortolotti.
Opportunities and Challenges for Spintronics in the Microelectronics Industry.
Nat. Electron., 3(8):446–459, 2020.
doi:10.1038/s41928-020-0461-5.

[61] J. Ding, W. Zhang, M. B. Jungfleisch, J. E. Pearson, H. Ohldag, V. Novosad, and A. Hoffmann.
Direct Observation of Spin Accumulation in Cu Induced by Spin Pumping.
Phys. Rev. Research, 2:013262, Mar 2020.
doi:10.1103/PhysRevResearch.2.013262.

[62] G. F. Dionne.
Origin of Secondary-Electron-Emission Yield-Curve Parameters.
J. Appl. Phys., 46(8):3347–3351, 1975.
doi:10.1063/1.322061.

[63] T. H. DiStefano.
Technology for Detecting Small Magnetic Domains and Beam-Addressed Memory Therewith.
IBM Tech. Disc. Bull., 20:4212–4215, 1978.

[64] C. Donnelly and V. Scagnoli.
Imaging Three-Dimensional Magnetic Systems with X-Rays.
J. Phys. Condens. Matter, 32(21):213001, feb 2020.
doi:10.1088/1361-648x/ab5e3c.

[65] C. Donnelly, S. Finizio, S. Gliga, M. Holler, A. Hrabec, M. Odstrčil, S. Mayr, V. Scagnoli, L. J. Heyderman, M. Guizar-Sicairos, and J. Raabe.
Time-Resolved Imaging of Three-Dimensional Nanoscale Magnetization Dynamics.
Nat. Nanotechnol., 15(5):356–360, 2020.
doi:10.1038/s41565-020-0649-x.

[66] V. Drchal, J. Kudrnovský, I. Turek, and P. Weinberger.
Interlayer Magnetic Coupling: The Torque Method.
Phys. Rev. B, 53:15036–15044, Jun 1996.
doi:10.1103/PhysRevB.53.15036.

[67] C. Durkan and M. E. Welland.
Electronic Spin Detection in Molecules Using Scanning-Tunneling-Microscopy-Assisted Electron-Spin Resonance.
Appl. Phys. Lett., 80(3):458–460, 2002.
doi:10.1063/1.1434301.

[68] M.I. Dyakonov and V.I. Perel.
Current-Induced Spin Orientation of Electrons in Semiconductors.
Phys. Lett. A, 35(6):459 – 460, 1971.
ISSN 0375-9601.
doi:https://doi.org/10.1016/0375-9601(71)90196-4.

[69] M.I. Dyakonov and V.I. Perel.
Soviet Phys. Solid State, USSR, 13(13):3023, 1972.

[70] I. Dzyaloshinsky.
A Thermodynamic Theory of "Weak" Ferromagnetism of Antiferromagnetics.
J. Phys. Chem. Solids, 4(4):241 – 255, 1958.
ISSN 0022-3697.
doi:10.1016/0022-3697(58)90076-3.

[71] K. Eason, M. Patricia Rouelli Garcia Sabino, M. Tran, and Y. Fook Liew.
Origins of Magnetic Damping Measurement Variations Using Ferromagnetic Resonance for Nano-Sized Devices.
Appl. Phys. Lett., 102(23):232405, 2013.
doi:10.1063/1.4811146.

[72] P. Eaton and P. West.
Atomic Force Microscopy.
Oxford University Press, 2010.

[73] D. M. Edwards and A. Umerski.
Exchange Coupling in Magnetic Multilayers, chapter 12.
Wiley, 2007.
ISBN 9780470022184.
doi:10.1002/9780470022184.hmm115.

[74] D. M. Edwards, J. M. Ward, and J. Mathon.
Intrinsic and Secondary Mechanisms for Biquadratic Exchange Coupling in Magnetic Trilayers.
J. Magn. Magn. Mater., 126(1):380 – 383, 1993.
ISSN 0304-8853.
doi:10.1016/0304-8853(93)90631-B.

[75] R. J. Elliott.
Theory of the Effect of Spin-Orbit Coupling on Magnetic Resonance in Some Semiconductors.
Phys. Rev., 96:266–279, Oct 1954.
doi:10.1103/PhysRev.96.266.

[76] G. Epstein, G. Frieder, and D. C. Rine.
The Development of Multiple-Valued Logic as Related to Computer Science.
Computer, 7(9):20–32, 1974.
doi:10.1109/MC.1974.6323304.

[77] M. Escher, N. B. Weber, M. Merkel, L. Plucinski, and C. M. Schneider.
FERRUM: A New Highly Efficient Spin Detector for Electron Spectroscopy.
e-J. Surf. Sci. Nanotech., 9:340–343, 2011.
doi:10.1380/ejssnt.2011.340.

[78] J. Fabian and S. D. Sarma.
Spin Relaxation of Conduction Electrons.
J. Vac. Sci. Technol. B, 17(4):1708–1715, 1999.
doi:10.1116/1.590813.

[79] T. Favaloro, J.-H. Bahk, and A. Shakouri.
Characterization of the Temperature Dependence of the Thermoreflectance Coefficient for Conductive Thin Films.
Rev. Sci. Instrum., 86(2):024903, 2015.
doi:10.1063/1.4907354.

[80] A. Fert, N. Reyren, and V. Cros.
Magnetic Skyrmions: Advances in Physics and Potential Applications.
Nat. Rev. Mater., 2(7):1–15, 2017.
doi:10.1038/natrevmats.2017.31.

[81] M. E. Filipkowski, J. J. Krebs, G. A. Prinz, and C. J. Gutierrez.
Giant Near-90° Coupling in Epitaxial CoFe/Mn/CoFe Sandwich Structures.
Phys. Rev. Lett., 75:1847–1850, Aug 1995.
doi:10.1103/PhysRevLett.75.1847.

[82] D. J. Flannigan and A. H. Zewail.
4D Electron Microscopy: Principles and Applications.

Acc. Chem. Res., 45(10):1828–1839, 2012.
URL 10.1021/ar3001684.

[83] S. Foner.
Versatile and Sensitive Vibrating-Sample Magnetometer.
Rev. Sci. Instrum., 30(7):548–557, 1959.
doi:10.1063/1.1716679.

[84] C. A. Fowler Jr. and E. M. Fryer.
Magnetic Domains by the Longitudinal Kerr effect.
Phys. Rev., 94(1):52, 1954.
doi:10.1103/PhysRev.94.52.

[85] R. Freeman, A. Zholud, Z. Dun, H. Zhou, and S. Urazhdin.
Evidence for Dyakonov-Perel-like Spin Relaxation in Pt.
Phys. Rev. Lett., 120:067204, Feb 2018.
doi:10.1103/PhysRevLett.120.067204.

[86] F. Freimuth, S. Blügel, and Y. Mokrousov.
Anisotropic Spin Hall Effect from First Principles.
Phys. Rev. Lett., 105:246602, Dec 2010.
doi:10.1103/PhysRevLett.105.246602.

[87] R. Frömter, H. P. Oepen, and J. Kirschner.
A Miniaturized Detector for High-Resolution SEMPA.
Applied Physics A, 76(6):869–871, 2003.
doi:10.1007/s00339-002-1966-7.

[88] R. Frömter, S. Hankemeier, H. P. Oepen, and J. Kirschner.
Optimizing a Low-Energy Electron Diffraction Spin-Polarization Analyzer for Imaging of Magnetic Surface Structures.
Rev. Sci. Instrum., 82(3):033704, 2011.
doi:10.1063/1.3534832.

[89] R. Frömter, F. Kloodt, S. Rößler, A. Frauen, P. Staeck, D. R. Cavicchia, L. Bocklage, V. Röbisch, E. Quandt, and H. P. Oepen.
Time-Resolved Scanning Electron Microscopy with Polarization Analysis.
Appl. Phys. Lett., 108(14):142401, 2016.
doi:10.1063/1.4945053.

[90] A. Fuß, S. Demokritov, P. Grünberg, and W. Zinn.
Short- and Long Period Oscillations in the Exchange Coupling of Fe across Epitaxially Grown Al- and Au-Interlayers.
J. Magn. Magn. Mater., 103(3):L221 – L227, 1992.
ISSN 0304-8853.
doi:10.1016/0304-8853(92)90192-Q.

[91] A. Fuß, J. A. Wolf, and P. A. Grünberg.
Exchange of Fe Layers across Interlayers with Good Match.
Phys. Scr., T45:95–98, jan 1992.
doi:10.1088/0031-8949/1992/t45/020.

[92] P. Gallo, A. Arnoult, T. Camps, E. Havard, C. Fontaine, L. Lombez, T. Amand, X. Marie, and A. Bournel.
Self-Aligned and Stray-Field-Free Electrodes for Spintronics: An Application to a Spin Field Effect Transistor.
J. Appl. Phys., 101(2):024322, 2007.
doi:10.1063/1.2422710.

[93] P. Gambardella and I. M. Miron.
Current-Induced Spin-Orbit Torques.
Philos. Trans. R. Soc. A, 369(1948):3175–3197, 2011.
doi:10.1098/rsta.2010.0336.

[94] S. D. Ganichev, E. L. Ivchenko, V. V. Bel'Kov, S. A. Tarasenko, M. Sollinger, D. Weiss, W. Wegscheider, and W. Prettl.
Spin-Galvanic Effect.
Nature, 417(6885):153–156, 2002.
doi:10.1038/417153a.

[95] K. Garello, F. Yasin, and G. S. Kar.
Spin-Orbit Torque MRAM for Ultrafast Embedded Memories: From Fundamentals to Large Scale Technology Integration.
In *2019 IEEE 11th International Memory Workshop (IMW)*, pages 1–4, 2019.
doi:10.1109/IMW.2019.8739466.

[96] I. Gray, T. Moriyama, N. Sivadas, G. M. Stiehl, J. T. Heron, R. Need, B. J. Kirby, D. H. Low, K. C. Nowack, D. G. Schlom, D. C. Ralph, T. Ono, and G. D. Fuchs.
Spin Seebeck Imaging of Spin-Torque Switching in Antiferromagnetic Pt/NiO Heterostructures.
Phys. Rev. X, 9:041016, Oct 2019.
doi:10.1103/PhysRevX.9.041016.

[97] J. Grollier, D. Querlioz, K.Y. Camsari, K. Everschor-Sitte, S. Fukami, and M. D. Stiles.
Neuromorphic Spintronics.
Nat. Electron., pages 360–370, 2020.
doi:10.1038/s41928-019-0360-9.

[98] N. D. Guise, S. D. Fallek, H. Hayden, C. S. Pai, C. Volin, K. R. Brown, J. T. Merrill, A. W. Harter, J. M. Amini, L. M. Lust, K. Muldoon, D. Carlson, and J. Budach.

In-Vacuum Active Electronics for Microfabricated Ion Traps.
Rev. Sci. Instrum., 85(6):063101, 2014.
doi:10.1063/1.4879136.

[99] G. Y. Guo, S. Murakami, T.-W. Chen, and N. Nagaosa.
Intrinsic Spin Hall Effect in Platinum: First-Principles Calculations.
Phys. Rev. Lett., 100:096401, Mar 2008.
doi:10.1103/PhysRevLett.100.096401.

[100] C.J. Gutierrez, J.J. Krebs, M.E. Filipkowski, and G.A. Prinz.
Strong Temperature Dependence of the 90° Coupling in Fe/Al/Fe(001) Magnetic Trilayers.
J. Magn. Magn. Mater., 116(3):L305 – L310, 1992.
ISSN 0304-8853.
doi:10.1016/0304-8853(92)90106-X.

[101] E. H. Hall.
XVIII. On the "Rotational Coefficient" in Nickel and Cobalt.
Philos. Mag., 12(74):157–172, 1881.
doi:10.1080/14786448108627086.

[102] I. Hashim, H. S. Joo, and H. A. Atwater.
Structural and Magnetic Properties of Epitaxial $Ni_{80}Fe_{20}$ Thin Films on Cu/Si.
Surf. Rev. Lett., 02(04):427–437, 1995.
doi:10.1142/S0218625X95000388.

[103] M. Hayashi, L. Thomas, C. Rettner, R. Moriya, and S. S. P. Parkin.
Direct Observation of the Coherent Precession of Magnetic Domain Walls Propagating along Permalloy Nanowires.
Nat. Phys., 3(1):21–25, 2007.
doi:10.1038/nphys464.

[104] T. J. Hayward, M. T. Bryan, P. W. Fry, P. M. Fundi, M. R. J. Gibbs, M.-Y. Im, P. Fischer, and D. A. Allwood.
Pinning Induced by Inter-Domain Wall Interactions in Planar Magnetic Nanowires.
Appl. Phys. Lett., 96(5):052502, 2010.
doi:10.1063/1.3275752.

[105] B. Heinrich and J. F. Cochran.
Ultrathin Metallic Magnetic Films: Magnetic Anisotropies and Exchange Interactions.
Adv. Phys., 42(5):523–639, 1993.
doi:10.1080/00018739300101524.

[106] B. Heinrich, Z. Celinski, J. F. Cochran, A. S. Arrott, K. Myrtle, and S. T. Purcell.
Bilinear and Biquadratic Exchange Coupling in bcc Fe/Cu/Fe Trilayers: Ferromagnetic-Resonance and Surface Magneto-Optical Kerr-Effect Studies.

Phys. Rev. B, 47:5077–5089, Mar 1993.
doi:10.1103/PhysRevB.47.5077.

[107] S. Heinze, K. Von Bergmann, M. Menzel, J. Brede, A. Kubetzka, R. Wiesendanger, G. Bihlmayer, and S. Blügel.
Spontaneous Atomic-Scale Magnetic Skyrmion Lattice in Two Dimensions.
Nature Phys., 7(9):713–718, 2011.
doi:10.1038/nphys2045.

[108] M. Henini.
Molecular Beam Epitaxy: from Research to Mass Production.
Newnes, 2012.

[109] Y. Hirata, D.-H. Kim, T. Okuno, T. Nishimura, D.-Y. Kim, Y. Futakawa, H. Yoshikawa, A. Tsukamoto, K.-J. Kim, S.-B. Choe, and T. Ono.
Correlation Between Compensation Temperatures of Magnetization and Angular Momentum in GdFeCo Ferrimagnets.
Phys. Rev. B, 97:220403, Jun 2018.
doi:10.1103/PhysRevB.97.220403.

[110] Y. Hirata, D.-H. Kim, S. K. Kim, D.-K. Lee, S.-H. Oh, D.-Y. Kim, T. Nishimura, T. Okuno, Y. Futakawa, H. Yoshikawa, A. Tsukamoto, Y. Tserkovnyak, Y. Shiota, T. Moriyama, S.-B. Choe, K.-J. Lee, and T. Ono.
Vanishing Skyrmion Hall Effect at the Angular Momentum Compensation Temperature of a Ferrimagnet.
Nat. Nanotechnol., 14(3):232–236, 2019.
doi:10.1038/s41565-018-0345-2.

[111] J. E. Hirsch.
Spin Hall Effect.
Phys. Rev. Lett., 83:1834–1837, Aug 1999.
doi:10.1103/PhysRevLett.83.1834.

[112] A. Hoffmann.
Spin Hall Effects in Metals.
IEEE Trans. Magn., 49(10):5172–5193, 2013.
doi:10.1109/TMAG.2013.2262947.

[113] H. Hopster and H. P. Oepen.
SEMPA Studies of Thin Films, Structures,and Exchange Coupled Layers.
In Hans Peter Oepen and Herbert Hopster, editors, *Magnetic Microscopy of Nanostructures*, chapter 7, pages 137–167. Springer-Verlag, Heidelberg, 2006.
doi:10.1007/b137837.

[114] H. Hopster, R. Raue, E. Kisker, G. Güntherodt, and M. Campagna.
Evidence for Spin-Dependent Electron-Hole-Pair Excitations in Spin-Polarized Secondary-Electron Emission from Ni(110).

Phys. Rev. Lett., 50:70–73, Jan 1983.
doi:10.1103/PhysRevLett.50.70.

[115] S. Horiike, G. Nagashima, Y. Kurokawa, Y. Zhong, K. Yamanoi, T. Tanaka, K. Matsuyama, and H. Yuasa.
Magnetic Dynamics of Quasi-Antiferromagnetic Layer Fabricated by 90° Magnetic Coupling.
Jpn. J. Appl. Phys., 59(SG):SGGI02, feb 2020.
doi:10.7567/1347-4065/ab5d62.

[116] A. Hubert and R. Schäfer.
Magnetic Domains: The Analysis of Magnetic Microstructures.
Springer-Verlag Berlin Heidelberg, 1998.
ISBN 9783540850540.
doi:10.1007/978-3-540-85054-0.

[117] S. Hunklinger.
Festkörperphysik.
De Gruyter Oldenbourg, Berlin, Boston, 2017.
ISBN 978-3-11-056775-5.
doi:https://doi.org/10.1515/9783110567755.

[118] A. Imre, L. Zhou, A. Orlov, G. Csaba, G. H. Bernstein, W. Porod, and V. Metlushko.
Application of Mesoscopic Magnetic Rings for Logic Devices.
In *4th IEEE Conference on Nanotechnology, 2004.*, pages 137–139, 2004.
doi:10.1109/NANO.2004.1392275.

[119] Y. Inamura, T. Nakatani, J. Suzuki, and T. Otomo.
Development Status of Software "Utsusemi" for Chopper Spectrometers at MLF, J-PARC.
J. Phys. Soc. Jpn., 82(Suppl.A):SA031, 2013.
doi:10.7566/JPSJS.82SA.SA031.

[120] M. M. Irvine.
Early Digital Computers at Bell Telephone Laboratories.
IEEE Ann. Hist. Comput., 23(3):22–42, 2001.
doi:10.1109/85.948904.

[121] S. Jain and A. O. Adeyeye.
Probing the Magnetic States in Mesoscopic Rings by Synchronous Transport Measurements in Ring-Wire Hybrid Configuration.
Appl. Phys. Lett., 92(20):202506, 2008.
doi:10.1063/1.2936089.

[122] H. Jaksch and J. P. Martin.

High-Resolution, Low-Voltage SEM for True Surface Imaging and Analysis.
Fresenius J. Anal. Chem., 353(3):378–382, Jan 1995.
doi:10.1007/BF00322073.

[123] X. Jiang, L. Gao, J. Z. Sun, and S. S. P. Parkin.
Temperature Dependence of Current-Induced Magnetization Switching in Spin Valves with a Ferrimagnetic CoGd Free Layer.
Phys. Rev. Lett., 97:217202, Nov 2006.
doi:10.1103/PhysRevLett.97.217202.

[124] B.D. Josephson.
Possible New Effects in Superconductive Tunnelling.
Phys. Lett., 1(7):251 – 253, 1962.
ISSN 0031-9163.
doi:10.1016/0031-9163(62)91369-0.

[125] M. Julliere.
Tunneling Between Ferromagnetic Films.
Phys. Lett. A, 54(3):225 – 226, 1975.
ISSN 0375-9601.
doi:https://doi.org/10.1016/0375-9601(75)90174-7.

[126] T. Jungwirth, X. Marti, P. Wadley, and J. Wunderlich.
Antiferromagnetic Spintronics.
Nature Nanotechnology, 11(3):231–241, 2016.
doi:10.1038/nnano.2016.18.

[127] V. Kashid, T. Schena, B. Zimmermann, Y. Mokrousov, S. Blügel, V. Shah, and H. G. Salunke.
Dzyaloshinskii-Moriya Interaction and Chiral Magnetism in $3d-5d$ Zigzag Chains: Tight-Binding Model and Ab Initio Calculations.
Phys. Rev. B, 90:054412, Aug 2014.
doi:10.1103/PhysRevB.90.054412.

[128] Y. K. Kato, R. C. Myers, A. C. Gossard, and D. D. Awschalom.
Observation of the Spin Hall Effect in Semiconductors.
Science, 306(5703):1910–1913, 2004.
ISSN 0036-8075.
doi:10.1126/science.1105514.

[129] J. Kessler.
Polarized Electrons, volume 1.
Springer Science & Business Media, 2013.

[130] J. M. Kikkawa and D. D. Awschalom.
Lateral Drag of Spin Coherence in Gallium Arsenide.

Nature, 397(6715):139–141, 1999.
doi:10.1038/16420.

[131] A. L. D. Kilcoyne, T. Tyliszczak, W. F. Steele, S. Fakra, P. Hitchcock, K. Franck, E. Anderson, B. Harteneck, E. G. Rightor, G. E. Mitchell, A. P. Hitchcock, L. Yang, T. Warwick, and H. Ade.
Interferometer-Controlled Scanning Transmission X-Ray Microscopes at the Advanced Light Source.
J. Synchrotron Radiat., 10(2):125–136, Mar 2003.
doi:10.1107/S0909049502017739.

[132] D.-H. Kim, M. Haruta, H.-W. Ko, G. Go, H.-J. Park, T. Nishimura, D.-Y. Kim, T. Okuno, Y. Hirata, Y. Futakawa, H. Yoshikawa, W. Ham, S. Kim, H. Kurata, A. Tsukamoto, Y. Shiota, T. Moriyama, S.-B. Choe, K.-J. Lee, and T. Ono.
Bulk Dzyaloshinskii–Moriya Interaction in Amorphous Ferrimagnetic Alloys.
Nat. Mater., 18(7):685, 2019.
doi:10.1038/s41563-019-0380-x.

[133] K.-J. Kim, S. K. Kim, Y. Hirata, S.-H. Oh, T. Tono, D.-H. Kim, T. Okuno, W. S. Ham, S. Kim, G. Go, Y. Tserkovnyak, A. Tsukamoto, T. Moriyama, K.-J. Lee, and T. Ono.
Fast Domain Wall Motion in the Vicinity of the Angular Momentum Compensation Temperature of Ferrimagnets.
Nature Mater., 16(12):1187–1192, 2017.

[134] S. K. Kim, K.-J. Lee, and Y. Tserkovnyak.
Self-Focusing Skyrmion Racetracks in Ferrimagnets.
Phys. Rev. B, 95:140404, Apr 2017.
doi:10.1103/PhysRevB.95.140404.

[135] T. Kimura, Y. Otani, T. Sato, S. Takahashi, and S. Maekawa.
Room-Temperature Reversible Spin Hall Effect.
Phys. Rev. Lett., 98:156601, Apr 2007.
doi:10.1103/PhysRevLett.98.156601.

[136] J. Kirschner and K. Koike.
Spin Polarization of Secondary Electrons from Fe(110) Excited by Unpolarized Primary Electrons.
Surf. Sci., 273(1):147 – 159, 1992.
ISSN 0039-6028.
doi:10.1016/0039-6028(92)90283-C.

[137] E. Kisker, W. Gudat, and K. Schröder.
Observation of a High Spin Polarization of Secondary Electrons from Single Crystal Fe and Co.
Solid State Commun., 44(5):591 – 595, 1982.

ISSN 0038-1098.
doi:https://doi.org/10.1016/0038-1098(82)90561-0.

[138] C. Kittel.
On the Theory of Ferromagnetic Resonance Absorption.
Phys. Rev., 73:155–161, Jan 1948.
doi:10.1103/PhysRev.73.155.

[139] M. Kläui.
Head-to-Head Domain Walls in Magnetic Nanostructures.
J. Phys. Condens. Matter, 20(31):313001, jul 2008.
doi:10.1088/0953-8984/20/31/313001.

[140] M. Kläui, J. Rothman, L. Lopez-Diaz, C. A. F. Vaz, J. A. C. Bland, and Z. Cui.
Vortex Circulation Control in Mesoscopic Ring Magnets.
Appl. Phys. Lett., 78(21):3268–3270, 2001.
doi:10.1063/1.1361282.

[141] M. Kläui, C. A. F. Vaz, J. A. C. Bland, T. L. Monchesky, J. Unguris, E. Bauer, S. Cherifi, S. Heun, A. Locatelli, L. J. Heyderman, and Z. Cui.
Direct Observation of Spin Configurations and Classification of Switching Processes in Mesoscopic Ferromagnetic Rings.
Phys. Rev. B, 68:134426, Oct 2003.
doi:10.1103/PhysRevB.68.134426.

[142] M. Kläui, C. A. F. Vaz, L. J. Heyderman, U. Rüdiger, and J. A. C. Bland.
Spin Switching Phase Diagram of Mesoscopic Ring Magnets.
J. Magn. Magn. Mater., 290-291:61 – 67, 2005.
ISSN 0304-8853.
doi:10.1016/j.jmmm.2004.11.226.

[143] F. Kloodt-Twesten, S. Kuhrau, H. P. Oepen, and R. Frömter.
Measuring the Dzyaloshinskii-Moriya Interaction of the Epitaxial Co/Ir(111) Interface.
Phys. Rev. B, 100:100402, Sep 2019.
doi:10.1103/PhysRevB.100.100402.

[144] M. Kläui, C.A.F. Vaz, W. Wernsdorfer, E. Bauer, S. Cherifi, S. Heun, A. Locatelli, G. Faini, E. Cambril, L.J. Heyderman, and J.A.C. Bland.
Domain Wall Behaviour at Constrictions in Ferromagnetic Ring Structures.
Physica B Condens. Matter, 343(1):343 – 349, 2004.
ISSN 0921-4526.
doi:https://doi.org/10.1016/j.physb.2003.08.067.

[145] T. Kohashi, M. Konoto, and K. Koike.
A Spin Rotator for Spin-Polarized Scanning Electron Microscopy.

Rev. Sci. Instrum., 75(6):2003–2007, 2004.
doi:10.1063/1.1753102.

[146] K. Koike.
Spin-Polarized Scanning Electron Microscopy.
Microscopy, 62(1):177–191, 2013.
doi:10.1093/jmicro/dfs092.

[147] K. Koike and K. Hayakawa.
Scanning Electron Microscope Observation of Magnetic Domains Using Spin-Polarized Secondary Electrons.
Jpn. J. Appl. Phys., 23(3A):L187, 1984.
doi:10.1143/JJAP.23.L187.

[148] K. Koike and J. Kirschner.
Primary Energy Dependence of Secondary Electron Polarization.
J. Phys. D: Appl.Phys., 25(7):1139–1141, jul 1992.
doi:10.1088/0022-3727/25/7/017.

[149] M. Konoto, T. Kohashi, K. Koike, T. Arima, Y. Kaneko, T. Kimura, and Y. Tokura.
Direct Imaging of Temperature-Dependent Layered Antiferromagnetism of a Magnetic Oxide.
Phys. Rev. Lett., 93:107201, Sep 2004.
doi:10.1103/PhysRevLett.93.107201.

[150] J. C. S. Kools, W. Kula, D. Mauri, and T. Lin.
Effect of Finite Magnetic Film Thickness on Néel Coupling in Spin Valves.
J. Appl. Phys., 85(8):4466–4468, 1999.
doi:10.1063/1.370376.

[151] P. Krautscheid, R. M. Reeve, M. Lauf, B. Krüger, and M. Kläui.
Domain Wall Spin Structures in Mesoscopic Fe Rings Probed by High Resolution SEMPA.
J. Phys. D, 49(42):425004, 2016.
doi:10.1088/0022-3727/49/42/425004.

[152] P. Krautscheid, R. M. Reeve, D. Schönke, I. Boventer, A. Conca, A. V. Chumak, B. Hillebrands, J. Ehrler, J. Osten, J. Fassbender, and M. Kläui.
Direct Observation of Spin Diffusion Enhanced Nonadiabatic Spin Torque Effects in Rare-Earth-Doped Permalloy.
Phys. Rev. B, 98:214406, Dec 2018.
doi:10.1103/PhysRevB.98.214406.

[153] S. Kuhrau.
Surface-Sensitive Magnetic Imaging of Polycrystalline and Epitaxial Ultrathin Cobalt Films with a Perpendicular Magnetic Anisotropy.

PhD thesis, Universität Hamburg, Von-Melle-Park 3, 20146 Hamburg, 2019.
URL `http://ediss.sub.uni-hamburg.de/volltexte/2019/10013`.

[154] S. Kuhrau, F. Kloodt-Twesten, C. Heyn, H. P. Oepen, and R. Frömter.
Cap-Layer-Dependent Oxidation of Ultrathin Cobalt Films and its Effect on the Magnetic Contrast in Scanning Electron Microscopy with Polarization Analysis.
Appl. Phys. Lett., 113(17):172403, 2018.
doi:10.1063/1.5052305.

[155] R. Kukreja, S. Bonetti, Z. Chen, D. Backes, Y. Acremann, J. A. Katine, A. D. Kent, H. A. Dürr, H. Ohldag, and J. Stöhr.
X-Ray Detection of Transient Magnetic Moments Induced by a Spin Current in Cu.
Phys. Rev. Lett., 115:096601, Aug 2015.
doi:10.1103/PhysRevLett.115.096601.

[156] H. Kurebayashi, J. Sinova, D. Fang, A. C. Irvine, T. D. Skinner, J. Wunderlich, V. Novák, R. P. Campion, B. L. Gallagher, E. K. Vehstedt, L. P. Zârbo, K. Výborný, A. J. Ferguson, and T. Jungwirth.
An Antidamping Spin–Orbit Torque Originating from the Berry Curvature.
Nat. Nanotechnol., 9(3):211–217, 2014.
doi:10.1038/nnano.2014.15.

[157] C.-H. Lai and K. H. Lu.
Biquadratic Coupling through Nano-Oxide Layers in Pinned Layers of IrMn-based Spin Valves.
J. Appl. Phys., 93(10):8412–8414, 2003.
doi:10.1063/1.1558099.

[158] M. Laufenberg, D. Bedau, H. Ehrke, M. Kläui, U. Rüdiger, D. Backes, L. J. Heyderman, F. Nolting, C. A. F. Vaz, J. A. C. Bland, T. Kasama, R. E. Dunin-Borkowski, S. Cherifi, A. Locatelli, and S. Heun.
Quantitative Determination of Domain Wall Coupling Energetics.
Appl. Phys. Lett., 88(21):212510, 2006.
doi:10.1063/1.2207220.

[159] R. Lavrijsen, D. M. F. Hartmann, A. van den Brink, Y. Yin, B. Barcones, R. A. Duine, M. A. Verheijen, H. J. M. Swagten, and B. Koopmans.
Asymmetric Magnetic Bubble Expansion Under In-Plane Field in Pt/Co/Pt: Effect of Interface Engineering.
Phys. Rev. B, 91:104414, Mar 2015.
doi:10.1103/PhysRevB.91.104414.
URL `https://link.aps.org/doi/10.1103/PhysRevB.91.104414`.

[160] M. Lederman, R. O'Barr, and S. Schultz.

Experimental Study of Individual Ferromagnetic Sub-Micron Cylinders.
IEEE Trans. Magn., 31(6):3793–3795, Nov 1995.
ISSN 1941-0069.
doi:10.1109/20.489774.

[161] J. H. Lee, S. N. Holmes, B. Hong, P. E. Roy, M. D. Mascaro, T. J. Hayward, D. Anderson, K. Cooper, G. A. C. Jones, M. E. Vickers, C. A. Ross, and C. H. W. Barnes.
Magnetic Remanent States and Quasistatic Switching Behavior of Fe Split-Rings for Spin Field-Effect-Transistor Applications.
Appl. Phys. Lett., 95(17):172505, 2009.
doi:10.1063/1.3257360.

[162] W.-Y. Lee, M. F. Toney, P. Tameerug, E. Allen, and D. Mauri.
High Magnetoresistance Permalloy Films Deposited on a Thin NiFeCr or NiCr Underlayer.
J. Appl. Phys., 87(9):6992–6994, 2000.
doi:10.1063/1.372908.

[163] W. Legrand, D. Maccariello, F. Ajejas, S. Collin, A. Vecchiola, K. Bouzehouane, N. Reyren, V. Cros, and A. Fert.
Room-Temperature Stabilization of Antiferromagnetic Skyrmions in Synthetic Antiferromagnets.
Nat. Mater., 19(1):34–42, 2020.
doi:10.1038/s41563-019-0468-3.

[164] I. Lemesh, F. Büttner, and G. S. D. Beach.
Accurate Model of the Stripe Domain Phase of Perpendicularly Magnetized Multilayers.
Phys. Rev. B, 95:174423, May 2017.
doi:10.1103/PhysRevB.95.174423.

[165] J. E. Lennard-Jones.
On the Determination of Molecular Fields. II. From the Equation of State of Gas.
Proc. Roy. Soc. A, 106:463–477, 1924.
doi:10.1098/rspa.1924.0082.

[166] J. Li, L. R. Shelford, P. Shafer, A. Tan, J. X. Deng, P. S. Keatley, C. Hwang, E. Arenholz, G. van der Laan, R. J. Hicken, and Z. Q. Qiu.
Direct Detection of Pure AC Spin Current by X-Ray Pump-Probe Measurements.
Phys. Rev. Lett., 117:076602, Aug 2016.
doi:10.1103/PhysRevLett.117.076602.

[167] Y. Li, Z. Lu, C. Chen, M. Cheng, H. Yin, W. Wang, C. Li, Y. Liu, R. Xiong, and J. Shi.

Dynamics of Vortex Domain Walls in Ferromagnetic Nanowires – A Possible Method for Chirality Manipulation.
J. Magn. Magn. Mater., 456:341 – 345, 2018.
ISSN 0304-8853.
doi:10.1016/j.jmmm.2018.02.041.

[168] K. Litzius, I. Lemesh, B. Krüger, P. Bassirian, L. Caretta, K. Richter, F. Büttner, K. Sato, O. A. Tretiakov, J. Förster, R. M. Reeve, M. Weigand, I. Bykova, H. Stoll, G. Schütz, G. S. D. Beach, and M. Kläui.
Skyrmion Hall Effect Revealed by Direct Time-Resolved X-Ray Microscopy.
Nature Phys., 13(2):170–175, 2017.
doi:10.1038/nphys4000.

[169] L. Liu, T. Moriyama, D. C. Ralph, and R. A. Buhrman.
Spin-Torque Ferromagnetic Resonance Induced by the Spin Hall Effect.
Phys. Rev. Lett., 106:036601, Jan 2011.
doi:10.1103/PhysRevLett.106.036601.

[170] L. Liu, C.-F. Pai, Y. Li, H. W. Tseng, D. C. Ralph, and R. A. Buhrman.
Spin-Torque Switching with the Giant Spin Hall Effect of Tantalum.
Science, 336(6081):555–558, 2012.
doi:10.1126/science.1218197.

[171] S. Lloyd.
Least Squares Quantization in PCM.
IEEE Trans. Inf. Theory, 28(2):129–137, 1982.
doi:10.1109/TIT.1982.1056489.

[172] F. Lofink, S. Hankemeier, R. Frömter, J. Kirschner, and H. P. Oepen.
Long-Time Stability of a Low-Energy Electron Diffraction Spin Polarization Analyzer for Magnetic Imaging.
Rev. Sci. Instrum., 83(2):023708, 2012.
doi:10.1063/1.3685629.

[173] A. H. MacDonald and M. Tsoi.
Antiferromagnetic Metal Spintronics.
Philos. Trans. R. Soc. A, 369(1948):3098–3114, 2011.
doi:10.1098/rsta.2011.0014.

[174] S. Maekawa, S. O. Valenzuela, E. Saitoh, and T. Kimura.
Spin Current.
Oxford University Press, 2017.

[175] G. Malinowski, O. Boulle, and M. Kläui.
Current-Induced Domain Wall Motion in Nanoscale Ferromagnetic Elements.
J. Phys. D Appl. Phys., 44(38):384005, sep 2011.
doi:10.1088/0022-3727/44/38/384005.

[176] C. Marrows.
Addressing an Antiferromagnetic Memory.
Science, 351(6273):558–559, 2016.
ISSN 0036-8075.
doi:10.1126/science.aad8211.

[177] X. Marti, I. Fina, C. Frontera, J. Liu, P. Wadley, Q. He, R. J. Paull, J. D. Clarkson, J. Kudrnovský, I. Turek, J. Kuneš, D. Yi, J-H. Chu, C. T. Nelson, L. You, E. Arenholz, S. Salahuddin, J. Fontcuberta, T. Jungwirth, and R. Ramesh.
Room-Temperature Antiferromagnetic Memory Resistor.
Nat. Mater., 13(4):367–374, 2014.
doi:10.1038/nmat3861.

[178] S. Matsunaga, K. Hiyama, A. Matsumoto, S. Ikeda, H. Hasegawa, K. Miura, J. Hayakawa, T. Endoh, H. Ohno, and T. Hanyu.
Standby-Power-Free Compact Ternary Content-Addressable Memory Cell Chip Using Magnetic Tunnel Junction Devices.
Appl. Phys. Express, 2:023004, feb 2009.
doi:10.1143/apex.2.023004.

[179] N. Matsunami, Y. Yamamura, Y. Itikawa, N. Itoh, Y. Kazumata, S. Miyagawa, K. Morita, R. Shimizu, and H. Tawara.
Energy Dependence of the Ion-Induced Sputtering Yields of Monatomic Solids.
Atomic Data and Nuclear Data Tables, 31(1):1 – 80, 1984.
ISSN 0092-640X.
doi:10.1016/0092-640X(84)90016-0.

[180] H. Matsuyama, C. Haginoya, and K. Koike.
Microscopic Imaging of Fe Magnetic Domains Exchange Coupled with Those in a NiO(001) Surface.
Phys. Rev. Lett., 85:646–649, Jul 2000.
doi:10.1103/PhysRevLett.85.646.

[181] M.-A. Mawass, K. Richter, A. Bisig, R. M. Reeve, B. Krüger, M. Weigand, H. Stoll, A. Krone, F. Kronast, G. Schütz, and M. Kläui.
Switching by Domain-Wall Automotion in Asymmetric Ferromagnetic Rings.
Phys. Rev. Applied, 7:044009, Apr 2017.
doi:10.1103/PhysRevApplied.7.044009.

[182] J. McCord.
Progress in Magnetic Domain Observation by Advanced Magneto-Optical Microscopy.
J. Phys. D: Appl. Phys., 48(33):333001, jul 2015.
doi:10.1088/0022-3727/48/33/333001.

[183] R. D. McMichael and M. J. Donahue.

Head to Head Domain Wall Structures in Thin Magnetic Strips.
IEEE Trans. Magn., 33(5):4167–4169, 1997.
doi:10.1109/20.619698.

[184] M. Meinert, D. Graulich, and T. Matalla-Wagner.
Electrical Switching of Antiferromagnetic Mn_2Au and the Role of Thermal Activation.
Phys. Rev. Applied, 9:064040, Jun 2018.
doi:10.1103/PhysRevApplied.9.064040.

[185] J. Mennig, F. Matthes, D. E. Bürgler, and C. M. Schneider.
Observation and Implications of Magnetic Domains in Lateral spin valves.
J. Appl. Phys., 111(7):07C504, 2012.
doi:10.1063/1.3671415.

[186] P. A. Midgley and R. E. Dunin-Borkowski.
Electron Tomography and Holography in Materials Science.
Nature Mater., 8(4):271–280, 2009.
doi:10.1038/nmat2406.

[187] G. Mihajlovic, J. E. Pearson, M. A. Garcia, S. D. Bader, and A. Hoffmann.
Negative Nonlocal Resistance in Mesoscopic Gold Hall Bars: Absence of the Giant Spin Hall Effect.
Phys. Rev. Lett., 103:166601, Oct 2009.
doi:10.1103/PhysRevLett.103.166601.

[188] M. M. Miller, G. A. Prinz, S.-F. Cheng, and S. Bounnak.
Detection of a Micron-Sized Magnetic Sphere Using a Ring-Shaped Anisotropic Magnetoresistance-Based Sensor: A Model for a Magnetoresistance-Based Biosensor.
Appl. Phys. Lett., 81(12):2211–2213, 2002.
doi:10.1063/1.1507832.

[189] I. M. Miron, K. Garello, G. Gaudin, P.-J. Zermatten, M. V. Costache, S. Auffret, S. Bandiera, B. Rodmacq, A. Schuhl, and P. Gambardella.
Perpendicular Switching of a Single Ferromagnetic Layer Induced by In-Plane Current Injection.
Nature, 476(7359):189–193, 2011.
doi:10.1038/nature10309.

[190] G. E. Moore.
Cramming more Components onto Integrated Circuits, Reprinted from Electronics, volume 38, number 8, April 19, 1965, pp.114 ff.
Electronics, 38(8):114, 1965.

[191] C. Moreau-Luchaire, C. Moutafis, N. Reyren, J. Sampaio, C. A. F. Vaz, N. Van Horne, K. Bouzehouane, K. Garcia, C. Deranlot, P. Warnicke, P. Wohlhüter, J.-M. George, M. Weigand, J. Raabe, V. Cros, and A. Fert.
Additive Interfacial Chiral Interaction in Multilayers for Stabilization of Small Individual Skyrmions at Room Temperature.
Nat. Nanotechnol., 11(5):444–448, 2016.
doi:10.1038/nnano.2015.313.

[192] T. Moriyama, S. Takei, M. Nagata, Y. Yoshimura, N. Matsuzaki, T. Terashima, Y. Tserkovnyak, and T. Ono.
Anti-Damping Spin Transfer Torque through Epitaxial Nickel Oxide.
Appl. Phys. Lett., 106(16):162406, 2015.
doi:10.1063/1.4918990.

[193] T. Moriyama, M. Kamiya, K. Oda, K. Tanaka, K.-J. Kim, and T. Ono.
Magnetic Moment Orientation-Dependent Spin Dissipation in Antiferromagnets.
Phys. Rev. Lett., 119:267204, Dec 2017.
doi:10.1103/PhysRevLett.119.267204.

[194] O. Mosendz, G. Mihajlovic, J. E. Pearson, P. Fischer, M.-Y. Im, S. D. Bader, and A. Hoffmann.
Imaging of Lateral Spin Valves with Soft X-Ray Microscopy.
Phys. Rev. B, 80:104439, Sep 2009.
doi:10.1103/PhysRevB.80.104439.

[195] O. Mosendz, J. E. Pearson, F. Y. Fradin, G. E. W. Bauer, S. D. Bader, and A. Hoffmann.
Quantifying Spin Hall Angles from Spin Pumping: Experiments and Theory.
Phys. Rev. Lett., 104:046601, Jan 2010.
doi:10.1103/PhysRevLett.104.046601.

[196] N. F. Mott and N. H. D. Bohr.
The Scattering of Fast Electrons by Atomic Nuclei.
Proc. R. Soc. A, 124(794):425–442, 1929.
doi:10.1098/rspa.1929.0127.

[197] S. Mühlbauer, B. Binz, F. Jonietz, C. Pfleiderer, A. Rosch, A. Neubauer, R. Georgii, and P. Böni.
Skyrmion Lattice in a Chiral Magnet.
Science, 323(5916):915–919, 2009.
doi:10.1126/science.1166767.

[198] N. Nagaosa, J. Sinova, S. Onoda, A. H. MacDonald, and N. P. Ong.
Anomalous Hall effect.
Rev. Mod. Phys., 82:1539–1592, May 2010.
doi:10.1103/RevModPhys.82.1539.

[199] G. Nagashima, Y. Kurokawa, Y. Zhong, S. Horiike, D. Schönke, P. Krautscheid, R. Reeve, M. Kläui, Y. Inagaki, T. Kawae, T. Tanaka, K. Matsuyama, K. Ohnishi, T. Kimura, and H. Yuasa.
Quasi-Antiferromagnetic Multilayer Stacks with 90 Degree Coupling Mediated by Thin Fe Oxide Spacers.
J. Appl. Phys., 126(9):093901, 2019.
doi:10.1063/1.5117869.

[200] K. Nakajima, Y. Kawakita, S. Itoh, J. Abe, K. Aizawa, H. Aoki, H. Endo, M. Fujita, K. Funakoshi, W. Gong, et al.
Materials and Life Science Experimental Facility (MLF) at the Japan Proton Accelerator Research Complex II: Neutron Scattering Instruments.
Quantum Beam Sci., 1(3):9, 2017.
doi:10.3390/qubs1030009.

[201] L. Néel.
Propriétés d'un ferromagnétique cubique en grains fins.
C. R. Acad. Sci., 224:1488–1490, 1947.
URL `https://hal.archives-ouvertes.fr/hal-02878474/file/Doc.pdf`.

[202] L. Néel.
Anisotropie Magnétique Superficielle et Surstructures d'Orientation.
J. Phys. Radium, 15(4):225–239, 1954.
doi:10.1051/jphysrad:01954001504022500.

[203] L. Néel.
Magnetisme - sur un nouveau mode de couplage entre les animantations de deux couches minces ferromagnetiques.
C. r. hebd. séances Acad. sci., 255(15):1676, 1962.

[204] L. Néel.
Magnetism and the Local Molecular Field.
Nobel Lect. Phys., pages 1963–1970, 1970.

[205] H. T. Nembach, J. M. Shaw, M. Weiler, E. Jué, and T. J. Silva.
Linear Relation Between Heisenberg Exchange and Interfacial Dzyaloshinskii–Moriya Interaction in Metal Films.
Nature Phys., 11(10):825–829, 2015.
doi:10.1038/nphys3418.

[206] D. E. Nikonov, S. Manipatruni, and I. A. Young.
Automotion of Domain Walls for Spintronic Interconnects.
J. Appl. Phys., 115(21):213902, 2014.
doi:10.1063/1.4881061.

[207] Nobel Media AB 2020.

Louis Néel – Facts. NobelPrize.org.
URL `https://www.nobelprize.org/prizes/physics/1970/neel/facts/`.

[208] F. Nolting, A. Scholl, J. Stöhr, J. W. Seo, J. Fompeyrine, H. Siegwart, J.-P. Locquet, S. Anders, J. Lüning, E. E. Fullerton, M. F. Toney, M. R. Scheinfein, and H. A. Padmore.
Direct Observation of the Alignment of Ferromagnetic Spins by Antiferromagnetic Spins.
Nature, 405(6788):767–769, 2000.
doi:10.1038/35015515.

[209] A. S. Núñez, R. A. Duine, P. Haney, and A. H. MacDonald.
Theory of Spin Torques and Giant Magnetoresistance in Antiferromagnetic Metals.
Phys. Rev. B, 73:214426, Jun 2006.
doi:10.1103/PhysRevB.73.214426.

[210] L. O'Brien, D. Petit, H. T. Zeng, E. R. Lewis, J. Sampaio, A. V. Jausovec, D. E. Read, and R. P. Cowburn.
Near-Field Interaction between Domain Walls in Adjacent Permalloy Nanowires.
Phys. Rev. Lett., 103:077206, Aug 2009.
doi:10.1103/PhysRevLett.103.077206.

[211] Hans Peter Oepen and Robert Frömter.
Scanning Electron Microscopy with Polarisation Analysis, volume 3, chapter 4.
Wiley Online Library, Chichester, 2007.

[212] H. Ohldag, T. J. Regan, J. Stöhr, A. Scholl, F. Nolting, J. Lüning, C. Stamm, S. Anders, and R. L. White.
Spectroscopic Identification and Direct Imaging of Interfacial Magnetic Spins.
Phys. Rev. Lett., 87:247201, Nov 2001.
doi:10.1103/PhysRevLett.87.247201.

[213] Y. Ohno, D. K. Young, B. Beschoten, F. Matsukura, H. Ohno, and D. D. Awschalom.
Electrical Spin Injection in a Ferromagnetic Semiconductor Heterostructure.
Nature, 402(6763):790–792, 1999.
doi:10.1038/45509.

[214] K. Olejník, T. Seifert, Z. Kašpar, V. Novák, P. Wadley, R. P. Campion, M. Baumgartner, P. Gambardella, P. Němec, J. Wunderlich, J. Sinova, P. Kužel, M. Müller, T. Kampfrath, and T. Jungwirth.
Terahertz Electrical Writing Speed in an Antiferromagnetic Memory.
Sci. Adv., 4(3), 2018.
doi:10.1126/sciadv.aar3566.

[215] A. B. Oliveira, S. M. Rezende, and A. Azevedo.

Magnetization Reversal in Permalloy Ferromagnetic Nanowires Investigated with Magnetoresistance Measurements.
Phys. Rev. B, 78:024423, Jul 2008.
doi:10.1103/PhysRevB.78.024423.

[216] K. Omari, R. C. Bradley, T. J. Broomhall, M. P. P. Hodges, M. C. Rosamond, E. H. Linfield, M.-Y. Im, P. Fischer, and T. J. Hayward.
Ballistic Rectification of Vortex Domain Wall Chirality at Nanowire Corners.
Appl. Phys. Lett., 107(22):222403, 2015.
doi:10.1063/1.4936565.

[217] K. A. Omari and T. J. Hayward.
Chirality-Based Vortex Domain-Wall Logic Gates.
Phys. Rev. Applied, 2:044001, Oct 2014.
doi:10.1103/PhysRevApplied.2.044001.

[218] K. A. Omari, T. J. Broomhall, R. W. S. Dawidek, D. A. Allwood, R. C. Bradley, J. M. Wood, P. W. Fry, M. C. Rosamond, E. H. Linfield, M.-Y. Im, P. J. Fischer, and T. J. Hayward.
Toward Chirality-Encoded Domain Wall Logic.
Adv. Funct. Mater., 29(10):1807282, 2019.
doi:10.1002/adfm.201807282.

[219] T. Ono, H. Miyajima, K. Shigeto, K. Mibu, N. Hosoito, and T. Shinjo.
Propagation of a Magnetic Domain Wall in a Submicrometer Magnetic Wire.
Science, 284(5413):468–470, 1999.
ISSN 0036-8075.
doi:10.1126/science.284.5413.468.

[220] C.-F. Pai, L. Liu, Y. Li, H.-W. Tseng, D. C. Ralph, and R. A. Buhrman.
Spin Transfer Torque Devices Utilizing the Giant Spin Hall Effect of Tungsten.
Appl. Phys. Lett., 101(12):122404, 2012.
doi:10.1063/1.4753947.

[221] S. S. P. Parkin, N. More, and K. P. Roche.
Oscillations in Exchange Coupling and Magnetoresistance in Metallic Superlattice Structures: Co/Ru, Co/Cr, and Fe/Cr.
Phys. Rev. Lett., 64:2304–2307, May 1990.
doi:10.1103/PhysRevLett.64.2304.

[222] S. S. P. Parkin, M. Hayashi, and L. Thomas.
Magnetic Domain-Wall Racetrack Memory.
Science, 320(5873):190–194, 2008.
ISSN 0036-8075.
doi:10.1126/science.1145799.

[223] M. Pernpeintner, A. Kamra, S. T. B. Goennenwein, and H. Huebl.
Characterizing Spin Transport: Detection of Spin Accumulation via Magnetic Stray Field.
arXiv preprint arXiv:1709.01820, 2017.

[224] R. J Phillips.
Digital Technology and Institutional Change from the Gilded Age to Modern Times: The Impact of the Telegraph and the Internet.
J. Econ. Issues, 34(2):267–289, 2000.
doi:10.1080/00213624.2000.11506266.

[225] D. T. Pierce, J. A. Stroscio, J. Unguris, and R. J. Celotta.
Influence of Cr Growth on Exchange Coupling in Fe/Cr/Fe(100).
Phys. Rev. B, 49:14564–14572, May 1994.
doi:10.1103/PhysRevB.49.14564.

[226] D. T. Pierce, J. Unguris, R. J. Celotta, and M. D. Stiles.
Effect of Roughness, Frustration, and Antiferromagnetic Order on Magnetic Coupling of Fe/Cr Multilayers.
J. Magn. Magn. Mater., 200(1):290 – 321, 1999.
ISSN 0304-8853.
doi:10.1016/S0304-8853(99)00319-4.

[227] D. T. Pierce, A. D. Davies, J. A. Stroscio, D. A. Tulchinsky, J. Unguris, and R. J. Celotta.
Non-Collinear Exchange Coupling in Fe/Mn/Fe(001): Insight from Scanning Tunneling Microscopy.
J. Magn. Magn. Mater., 222(1):13 – 27, 2000.
ISSN 0304-8853.
doi:10.1016/S0304-8853(00)00551-5.

[228] S. Pizzini, J. Vogel, S. Rohart, L. D. Buda-Prejbeanu, É. Jué, O. Boulle, I. M. Miron, C. K. Safeer, S. Auffret, G. Gaudin, and A. Thiaville.
Chirality-Induced Asymmetric Magnetic Nucleation in Pt/Co/AlO_x Ultrathin Microstructures.
Phys. Rev. Lett., 113:047203, Jul 2014.
doi:10.1103/PhysRevLett.113.047203.

[229] S. Prosandeev, I. Ponomareva, I. Kornev, and L. Bellaiche.
Control of Vortices by Homogeneous Fields in Asymmetric Ferroelectric and Ferromagnetic Rings.
Phys. Rev. Lett., 100:047201, Jan 2008.
doi:10.1103/PhysRevLett.100.047201.

[230] J. Puebla, J. Kim, K. Kondou, and Y. Otani.
Spintronic Devices for Energy-Efficient Data Storage and Energy Harvesting.

Commun. Mater., 1(1):1–9, 2020.
doi:10.1038/s43246-020-0022-5.

[231] F. Radu and H. Zabel.
Exchange Bias Effect of Ferro-/Antiferromagnetic Heterostructures, pages 97–184.
Springer Berlin Heidelberg, Berlin, Heidelberg, 2008.
ISBN 978-3-540-73462-8.
doi:10.1007/978-3-540-73462-8_3.

[232] R. M. Reeve, C. Mix, M. König, M. Foerster, G. Jakob, and M. Kläui.
Magnetic Domain Structure of $La_{0.7}Sr_0.3MnO_3$ Thin-Films Probed at Variable Temperature with Scanning Electron Microscopy with Polarization Analysis.
Appl. Phys. Lett., 102(12):122407, 2013.
doi:10.1063/1.4798538.

[233] R. M. Reeve, H.-J. Elmers, F. Büttner, and M. Kläui.
Magnetic Imaging and Microscopy.
arXiv preprint arXiv:1806.07767, 2018.
URL `https://arxiv.org/abs/1806.07767`.

[234] R. M. Reeve, M. Vafaee, and M. Kläui.
Magnetization Configurations and Reversal in Small Magnetic Elements.
J. Mater. Sci. Technol., pages 1–53, 2019.
doi:10.1002/9783527603978.mst0465.

[235] K. Richter, A. Krone, M.-A. Mawass, B. Krüger, M. Weigand, H. Stoll, G. Schütz, and M. Kläui.
Local Domain-Wall Velocity Engineering via Tailored Potential Landscapes in Ferromagnetic Rings.
Phys. Rev. Applied, 5:024007, Feb 2016.
doi:10.1103/PhysRevApplied.5.024007.

[236] K. Richter, A. Krone, M.-A. Mawass, B. Krüger, M. Weigand, H. Stoll, G. Schütz, and M. Kläui.
Localized Domain Wall Nucleation Dynamics in Asymmetric Ferromagnetic Rings Revealed by Direct Time-Resolved Magnetic Imaging.
Phys. Rev. B, 94:024435, Jul 2016.
doi:10.1103/PhysRevB.94.024435.

[237] P. Riego, S. Vélez, J. M. Gomez-Perez, J. A. Arregi, L. E. Hueso, F. Casanova, and A. Berger.
Absence of Detectable Current-Induced Magneto-Optical Kerr Effects in Pt, Ta, and W.
Appl. Phys. Lett., 109(17):172402, 2016.
doi:10.1063/1.4966276.

[238] S. Rößler.
Magnetic Imaging of Static and Dynamic States in Systems of Reduced Dimensions.
Ph.D. thesis, Universität Hamburg, Institut für Angewandte Physik, April 2015.

[239] J. Rothman, M. Kläui, L. Lopez-Diaz, C. A. F. Vaz, A. Bleloch, J. A. C. Bland, Z. Cui, and R. Speaks.
Observation of a Bi-Domain State and Nucleation Free Switching in Mesoscopic Ring Magnets.
Phys. Rev. Lett., 86:1098–1101, Feb 2001.
doi:10.1103/PhysRevLett.86.1098.

[240] N. Rubiano da Silva, M. Möller, A. Feist, H. Ulrichs, C. Ropers, and S. Schäfer.
Nanoscale Mapping of Ultrafast Magnetization Dynamics with Femtosecond Lorentz Microscopy.
Phys. Rev. X, 8:031052, Aug 2018.
doi:10.1103/PhysRevX.8.031052.

[241] M. Rührig, R. Schäfer, A. Hubert, R. Mosler, J. A. Wolf, S. Demokritov, and P. Grünberg.
Domain Observations on Fe-Cr-Fe Layered Structures. Evidence for a Biquadratic Coupling Effect.
Phys. Status Solidi A, 125(2):635–656, 1991.
doi:10.1002/pssa.2211250225.

[242] E. Sagasta, Y. Omori, M. Isasa, M. Gradhand, L. E. Hueso, Y. Niimi, Y. Otani, and F. Casanova.
Tuning the Spin Hall Effect of Pt from the Moderately Dirty to the Superclean Regime.
Phys. Rev. B, 94:060412, Aug 2016.
doi:10.1103/PhysRevB.94.060412.

[243] E. Sagasta, Y. Omori, S. Vélez, R. Llopis, C. Tollan, A. Chuvilin, L. E. Hueso, M. Gradhand, Y. Otani, and F. Casanova.
Unveiling the Mechanisms of the Spin Hall Effect in Ta.
Phys. Rev. B, 98:060410, Aug 2018.
doi:10.1103/PhysRevB.98.060410.

[244] E. Saitoh, M. Ueda, H. Miyajima, and G. Tatara.
Conversion of Spin Current into Charge Current at Room Temperature: Inverse Spin-Hall Effect.
Appl. Phys. Lett., 88(18):182509, 2006.
doi:10.1063/1.2199473.

[245] A. Sapozhnik.

Magnetic Properties of Antiferromagnetic Mn2Au: Exchange Interaction and Domain Manipulation.
PhD thesis, Johannes Gutenberg-Universität Mainz, 2018.
URL `https://openscience.ub.uni-mainz.de/handle/20.500.12030/1176`.
Dissertation.

[246] A. A. Sapozhnik, M. Filianina, S. Y. Bodnar, A. Lamirand, M.-A. Mawass, Y. Skourski, H.-J. Elmers, H. Zabel, M. Kläui, and M. Jourdan.
Direct Imaging of Antiferromagnetic Domains in Mn_2Au Manipulated by High Magnetic Fields.
Phys. Rev. B, 97:134429, Apr 2018.
doi:10.1103/PhysRevB.97.134429.

[247] A. A. Sapozhnik, M. Jourdan, H. Zabel, M. Kläui, and H.-J. Elmers.
Exchange bias in epitaxial Mn_2Au (0 0 1)/Fe (0 0 1) bilayers.
J. Phys. D: Appl. Phys., 52(46):465003, sep 2019.
doi:10.1088/1361-6463/ab3966.

[248] M. Schäfer, S. Demokritov, S. Müller-Pfeiffer, R. Schäfer, M. Schneider, P. Grünberg, and W. Zinn.
Investigation of 90°Coupling in Fe/Ag/Fe Structures: "Loose Spins" and Fluctuation Mechanism.
J. Appl. Phys., 77(12):6432–6438, 1995.
doi:10.1063/1.359117.

[249] M. R. Scheinfein, D. T. Pierce, J. Unguris, J. J. McClelland, R. J. Celotta, and M. H. Kelley.
Improved Low-Energy Diffuse Scattering Electron-Spin Polarization Analyzer.
Rev. Sci. Instrum., 60(1):1–11, 1989.
doi:10.1063/1.1140575.

[250] M. R. Scheinfein, J. Unguris, M. H. Kelley, D. T. Pierce, and R. J. Celotta.
Scanning Electron Microscopy with Polarization Analysis (SEMPA).
Rev. Sci. Instrum., 61(10):2501–2527, 1990.
doi:10.1063/1.1141908.

[251] A. Scholl, J. Stöhr, J. Lüning, J. W. Seo, J. Fompeyrine, H. Siegwart, J.-P. Locquet, F. Nolting, S. Anders, E. E. Fullerton, M. R. Scheinfein, and H. A. Padmore.
Observation of Antiferromagnetic Domains in Epitaxial Thin Films.
Science, 287(5455):1014–1016, 2000.
doi:10.1126/science.287.5455.1014.

[252] G. Schönhense and H. C. Siegmann.
Transmission of Electrons through Ferromagnetic Material and Applications to Detection of Electron Spin Polarization.

Ann. Phys., 505(5):465–474, 1993.
doi:https://doi.org/10.1002/andp.19935050504.

[253] D. Schönke, A. Oelsner, P. Krautscheid, R. M. Reeve, and M. Kläui.
Development of a Scanning Electron Microscopy with Polarization Analysis System for Magnetic Imaging with ns Time Resolution and Phase-Sensitive Detection.
Rev. Sci. Instrum., 89(8):083703, 2018.
doi:10.1063/1.5037528.

[254] F. Schreiber, L. Baldrati, C. Schmitt, R. Ramos, E. Saitoh, R. Lebrun, and M. Kläui.
Concurrent Magneto-Optical Imaging and Magneto-Transport Readout of Electrical Switching of Insulating Antiferromagnetic Thin Films.
Appl. Phys. Lett., 117(8):082401, 2020.
doi:10.1063/5.0011852.

[255] H. W. Schumacher, C. Chappert, P. Crozat, R. C. Sousa, P. P. Freitas, J. Miltat, J. Fassbender, and B. Hillebrands.
Phase Coherent Precessional Magnetization Reversal in Microscopic Spin Valve Elements.
Phys. Rev. Lett., 90:017201, Jan 2003.
doi:10.1103/PhysRevLett.90.017201.

[256] K. Schwab.
The Fourth Industrial Revolution.
World Economic Forum, Geneva, Switzerland, 2016.

[257] A. Schwarz and R. Wiesendanger.
Magnetic Sensitive Force Microscopy.
Nano Today, 3(1):28–39, 2008.
doi:10.1016/S1748-0132(08)70013-6.

[258] M. P. Seah, I. S. Gilmore, and S. J. Spencer.
Signal Linearity in XPS Counting Systems.
J. Electron Spectrosc. Relat. Phenom., 104(1):73 – 89, 1999.
ISSN 0368-2048.
doi:10.1016/S0368-2048(98)00317-X.

[259] T. Seifert, S. Jaiswal, U. Martens, J. Hannegan, L. Braun, P. Maldonado, F. Freimuth, A. Kronenberg, J. Henrizi, I. Radu, E. Beaurepaire, Y. Mokrousov, P. M. Oppeneer, M. Jourdan, G. Jakob, D. Turchinovich, L. M. Hayden, M. Wolf, M. ünzenberg, M. Kläui, and T. Kampfrath.
Efficient Metallic Spintronic Emitters of Ultrabroadband Terahertz Radiation.
Nat. Photonics, 10(7):483, 2016.
doi:10.1038/nphoton.2016.91.

[260] S. Serrano-Guisan, K. Rott, G. Reiss, J. Langer, B. Ocker, and H. W. Schumacher.
Biased Quasiballistic Spin Torque Magnetization Reversal.
Phys. Rev. Lett., 101:087201, Aug 2008.
doi:10.1103/PhysRevLett.101.087201.

[261] K. Seshan and D. Schepis.
Handbook of Thin Film Deposition.
Elsevier, 2018.
ISBN 978-0-12-812311-9.

[262] K. Shahbazi, J.-V. Kim, H. T. Nembach, J. M. Shaw, A. Bischof, M. D. Rossell, V. Jeudy, T. A. Moore, and C. H. Marrows.
Domain-wall Motion and Interfacial Dzyaloshinskii-Moriya Interactions in Pt/Co/Ir(t_{Ir})/Ta Multilayers.
Phys. Rev. B, 99:094409, Mar 2019.
doi:10.1103/PhysRevB.99.094409.

[263] D.-F. Shao, G. Gurung, S.-H. Zhang, and E. Y. Tsymbal.
Dirac Nodal Line Metal for Topological Antiferromagnetic Spintronics.
Phys. Rev. Lett., 122:077203, Feb 2019.
doi:10.1103/PhysRevLett.122.077203.

[264] D.-F. Shao, S.-H. Zhang, G. Gurung, W. Yang, and E. Y. Tsymbal.
Nonlinear Anomalous Hall Effect for Néel Vector Detection.
Phys. Rev. Lett., 124:067203, Feb 2020.
doi:10.1103/PhysRevLett.124.067203.

[265] T. Shinjo, T. Okuno, R. Hassdorf, † K. Shigeto, and T. Ono.
Magnetic Vortex Core Observation in Circular Dots of Permalloy.
Science, 289(5481):930–932, 2000.
doi:10.1126/science.289.5481.930.

[266] S. A. Siddiqui, J. Sklenar, K. Kang, M. J. Gilbert, A. Schleife, N. Mason, and A. Hoffmann.
Metallic Antiferromagnets.
J. Appl. Phys., 128(4):040904, 2020.
doi:10.1063/5.0009445.

[267] J. Sinova, D. Culcer, Q. Niu, N. A. Sinitsyn, T. Jungwirth, and A. H. MacDonald.
Universal Intrinsic Spin Hall Effect.
Phys. Rev. Lett., 92:126603, Mar 2004.
doi:10.1103/PhysRevLett.92.126603.

[268] J. Sinova, S. O. Valenzuela, J. Wunderlich, C. H. Back, and T. Jungwirth.
Spin Hall Effects.
Rev. Mod. Phys., 87:1213–1260, Oct 2015.
doi:10.1103/RevModPhys.87.1213.

[269] J. C. Slonczewski.
Fluctuation Mechanism for Biquadratic Exchange Coupling in Magnetic Multilayers.
Phys. Rev. Lett., 67:3172–3175, Nov 1991.
doi:10.1103/PhysRevLett.67.3172.

[270] J. C. Slonczewski.
Origin of Biquadratic Exchange in Magnetic Multilayers (Invited).
J. Appl. Phys., 73(10):5957–5962, 1993.
doi:10.1063/1.353483.

[271] J. C. Slonczewski.
Current-driven Excitation of Magnetic Multilayers.
J. Magn. Magn. Mater., 159(1):L1 – L7, 1996.
ISSN 0304-8853.
doi:10.1016/0304-8853(96)00062-5.

[272] C. Stamm, C. Murer, M. Berritta, J. Feng, M. Gabureac, P. M. Oppeneer, and P. Gambardella.
Magneto-Optical Detection of the Spin Hall Effect in Pt and W Thin Films.
Phys. Rev. Lett., 119:087203, Aug 2017.
doi:10.1103/PhysRevLett.119.087203.

[273] C. D. Stanciu, A. V. Kimel, F. Hansteen, A. Tsukamoto, A. Itoh, A. Kirilyuk, and Th. Rasing.
Ultrafast Spin Dynamics Across Compensation Points in Ferrimagnetic GdFeCo: The Role of Angular Momentum Compensation.
Phys. Rev. B, 73:220402, Jun 2006.
doi:10.1103/PhysRevB.73.220402.

[274] M. Stepanova and S. Dew.
Nanofabrication: Techniques and Principles.
Springer Science & Business Media, 2012.
ISBN 978-3-7091-0424-8.
doi:10.1007/978-3-7091-0424-8.

[275] M. D. Stiles.
Interlayer Exchange Coupling.
In J. Anthony C. Bland and Bretislav Heinrich, editors, *Ultrathin Magnetic Structures III: Fundamentals of Nanomagnetism*, pages 99–142. Springer, 2005.
doi:10.1007/3-540-27163-5.

[276] J. Stöhr, Y. Wu, B. D. Hermsmeier, M. G. Samant, G. R. Harp, S. Koranda, D. Dunham, and B. P. Tonner.
Element-Specific Magnetic Microscopy with Circularly Polarized X-Rays.
Science, 259:658–661, 1993.

doi:10.1126/science.259.5095.658.

[277] E. C. Stoner.
Collective Electron Ferronmagnetism.
Proc. Math. Phys. Eng. Sci., 165(922):372–414, 1938.
doi:10.1098/rspa.1938.0066.

[278] E. C. Stoner and E. P. Wohlfarth.
A Mechanism of Magnetic Hysteresis in Heterogeneous Alloys.
Philos. Trans. Roy. Soc. A, 240(826):599–642, 1948.
doi:10.1098/rsta.1948.0007.

[279] Y. Su, H. Wang, J. Li, C. Tian, R. Wu, X. Jin, and Y. R. Shen.
Absence of Detectable MOKE Signals from Spin Hall Effect in Metals.
Appl. Phys. Lett., 110(4):042401, 2017.
doi:10.1063/1.4974044.

[280] K. Takano, R. H. Kodama, A. E. Berkowitz, W. Cao, and G. Thomas.
Interfacial Uncompensated Antiferromagnetic Spins: Role in Unidirectional Anisotropy in Polycrystalline $Ni_{81}Fe_{19}$/CoO Bilayers.
Phys. Rev. Lett., 79:1130–1133, Aug 1997.
doi:10.1103/PhysRevLett.79.1130.

[281] O. Takeuchi, M. Aoyama, R. Oshima, Y. Okada, H. Oigawa, N. Sano, H. Shigekawa, R. Morita, and M. Yamashita.
Probing Subpicosecond Dynamics Using Pulsed Laser Combined Scanning Tunneling Microscopy.
Appl. Phys. Lett., 85(15):3268–3270, 2004.
doi:10.1063/1.1804238.

[282] T. Tanaka, H. Kontani, M. Naito, T. Naito, D. S. Hirashima, K. Yamada, and J. Inoue.
Intrinsic Spin Hall Effect and Orbital Hall Effect in 4d and 5d Transition Metals.
Phys. Rev. B, 77(16):165117, 2008.

[283] A. Tange, C. L. Gao, B. Y. Yavorsky, I. V. Maznichenko, C. Etz, A. Ernst, W. Hergert, I. Mertig, W. Wulfhekel, and J. Kirschner.
Electronic Structure and Spin Polarization of the Fe(001)$-p(1 \times 1)$O Surface.
Phys. Rev. B, 81:195410, May 2010.
doi:10.1103/PhysRevB.81.195410.

[284] A. Thiaville.
Extensions of the Geometric Solution of the Two Dimensional Coherent Magnetization Rotation Model.
J. Magn. Magn. Mater., 182(1):5 – 18, 1998.
ISSN 0304-8853.
doi:https://doi.org/10.1016/S0304-8853(97)01014-7.

[285] A. Thiaville, S. Rohart, É. Jué, V. Cros, and A. Fert.
Dynamics of Dzyaloshinskii Domain Walls in Ultrathin Magnetic Films.
Europhys. Lett., 100(5):57002, 2012.
doi:10.1209/0295-5075/100/57002.

[286] R. Tomasello, E. Martinez, R. Zivieri, L. Torres, M. Carpentieri, and G. Finocchio.
A Strategy for the Design of Skyrmion Racetrack Memories.
Sci. Rep., 4:6784, 2014.
doi:10.1038/nnano.2013.210.

[287] Q. Tseng.
`https://sites.google.com/site/qingzongtseng/template-matching-ij-plugin` and `https://github.com/qztseng/imagej_plugins/tree/master/current`.

[288] D. A. Tulchinsky, J. Unguris, and R. J. Celotta.
Growth and Magnetic Oscillatory Exchange Coupling of Mn/Fe(001) and Fe/Mn/Fe(001).
J. Magn. Magn. Mater., 212(1):91 – 100, 2000.
ISSN 0304-8853.
doi:10.1016/S0304-8853(99)00814-8.

[289] F. Tyler.
XLIX. The Magnetization-Temperature Curves of Iron, Cobalt, and Nickel.
Phil. Mag., 11(70):596–602, 1931.
doi:10.1080/14786443109461711.

[290] K. Uchida, S. Takahashi, K. Harii, J. Ieda, W. Koshibae, K. Ando, S. Maekawa, and E. Saitoh.
Observation of the Spin Seebeck Effect.
Nature, 455(7214):778–781, 2008.
doi:10.1038/nature07321.

[291] W. C. Uhlig, M. J. Donahue, D. T. Pierce, and J. Unguris.
Direct Imaging of Current-Driven Domain Walls in Ferromagnetic Nanostripes.
J. Appl. Phys., 105(10):103902, 2009.
doi:10.1063/1.3125526.

[292] J. Unguris, D. T. Pierce, A. Galejs, and R. J. Celotta.
Spin and Energy Analyzed Secondary Electron Emission from a Ferromagnet.
Phys. Rev. Lett., 49:72–76, Jul 1982.
doi:10.1103/PhysRevLett.49.72.

[293] J. Unguris, R. J. Celotta, and D. T. Pierce.
Observation of Two Different Oscillation Periods in the Exchange Coupling of Fe/Cr/Fe(100).

Phys. Rev. Lett., 67:140–143, Jul 1991.
doi:10.1103/PhysRevLett.67.140.

[294] J. Unguris, R. J. Celotta, and D. T. Pierce.
Magnetism in Cr Thin Films on Fe(100).
Phys. Rev. Lett., 69:1125–1128, Aug 1992.
doi:10.1103/PhysRevLett.69.1125.

[295] J. Unguris, R. J. Celotta, and D. T. Pierce.
Oscillatory Exchange Coupling in Fe/Au/Fe(100).
J. Appl. Phys., 75(10):6437–6439, 1994.
doi:10.1063/1.356954.

[296] S. Urazhdin and N. Anthony.
Effect of Polarized Current on the Magnetic State of an Antiferromagnet.
Phys. Rev. Lett., 99:046602, Jul 2007.
doi:10.1103/PhysRevLett.99.046602.

[297] S. O. Valenzuela and M. Tinkham.
Direct Electronic Measurement of the Spin Hall Effect.
Nature, 442(7099):176, 2006.
doi:10.1038/nature04937.

[298] S. O. Valenzuela and M. Tinkham.
Electrical Detection of Spin Currents: The Spin-Current Induced Hall Effect (Invited).
J. Appl. Phys., 101(9):09B103, 2007.
doi:10.1063/1.2710794.

[299] T. Valet and A. Fert.
Theory of the Perpendicular Magnetoresistance in Magnetic Multilayers.
Phys. Rev. B, 48:7099–7113, Sep 1993.
doi:10.1103/PhysRevB.48.7099.

[300] P. A. A. van der Heijden, C. H. W. Swüste, W. J. M. de Jonge, J. M. Gaines, J. T. W. M. van Eemeren, and K. M. Schep.
Evidence for Roughness Driven 90° Coupling in Fe_3O_4/NiO/Fe_3O_4 Trilayers.
Phys. Rev. Lett., 82:1020–1023, Feb 1999.
doi:10.1103/PhysRevLett.82.1020.

[301] A. Vansteenkiste, J. De Baerdemaeker, K. W. Chou, H. Stoll, M. Curcic, T. Tyliszczak, G. Woltersdorf, C. H. Back, G. Schütz, and B. Van Waeyenberge.
Influence of Domain Wall Pinning on the Dynamic Behavior of Magnetic Vortex Structures: Time-Resolved Scanning X-Ray Transmission Microscopy in NiFe Thin Film Structures.

Phys. Rev. B, 77:144420, Apr 2008.
doi:10.1103/PhysRevB.77.144420.

[302] O. M. J. vant Erve, A. T. Hanbicki, K. M. McCreary, C. H. Li, and B. T. Jonker.
Optical Detection of Spin Hall Effect in Metals.
Appl. Phys. Lett., 104(17):172402, 2014.
doi:10.1063/1.4874328.

[303] T. VanZandt, R. Browning, and M. Landolt.
Iron Overlayer Polarization Enhancement Technique for Spin-Polarized Electron Microscopy.
J. Appl. Phys., 69(3):1564–1568, 1991.
doi:10.1063/1.347250.

[304] D. Vasilyev, C. Tusche, F. Giebels, H. Gollisch, R. Feder, and J. Kirschner.
Low-Energy Electron Reflection from Au-Passivated Ir(001) for Application in Imaging Spin-Filters.
J. Electron Spectrosc., 199:10 – 18, 2015.
ISSN 0368-2048.
doi:10.1016/j.elspec.2014.12.006.

[305] C. A. F. Vaz, C. Athanasiou, J. A. C. Bland, and G. Rowlands.
Energetics of Magnetic Ring and Disk Elements: Uniform Versus Vortex State.
Phys. Rev. B, 73:054411, Feb 2006.
doi:10.1103/PhysRevB.73.054411.

[306] C. Vouille, A. Thiaville, and J. Miltat.
Thermally Activated Switching of Nanoparticles: A Numerical Study.
J. Magn. Magn. Mater., 272-276:E1237 – E1238, 2004.
ISSN 0304-8853.
doi:10.1016/j.jmmm.2003.12.1353.
Proceedings of the International Conference on Magnetism (ICM 2003).

[307] J. Železný, H. Gao, K. Výborný, J. Zemen, J. Mašek, A. Manchon, J. Wunderlich, J. Sinova, and T. Jungwirth.
Relativistic Néel-Order Fields Induced by Electrical Current in Antiferromagnets.
Phys. Rev. Lett., 113:157201, Oct 2014.
doi:10.1103/PhysRevLett.113.157201.

[308] P. Wadley, B. Howells, J. Železný, C. Andrews, V. Hills, R. P. Campion, V. Novák, K. Olejník, F. Maccherozzi, S. S. Dhesi, S. Y. Martin, T. Wagner, J. Wunderlich, F. Freimuth, Y. Mokrousov, J. Kuneš, J. S. Chauhan, M. J. Grzybowski, A. W. Rushforth, K. W. Edmonds, B. L. Gallagher, and T. Jungwirth.
Electrical Switching of an Antiferromagnet.
Science, 351(6273):587–590, 2016.
ISSN 0036-8075.

doi:10.1126/science.aab1031.

[309] H. Wang, A. Sato, K. Saito, S. Mitani, K. Takanashi, and K. Yakushiji.
Oscillatory Interlayer Exchange Coupling in Epitaxial Co_2MnSi/Cr/Co2MnSi Trilayers.
Appl. Phys. Lett., 90(14):142510, 2007.
doi:10.1063/1.2719606.

[310] H. L. Wang, C. H. Du, Y. Pu, R. Adur, P. C. Hammel, and F. Y. Yang.
Scaling of Spin Hall Angle in 3d, 4d, and 5d Metals from $Y_3Fe_5O_{12}$/Metal Spin Pumping.
Phys. Rev. Lett., 112:197201, May 2014.
doi:10.1103/PhysRevLett.112.197201.

[311] L. Wangenheim.
Aktive Filter und Oszillatoren.
Springer-Verlag, Berlin, Heidelberg, 2008.
ISBN 978-3-540-71739-3.
doi:10.1007/978-3-540-71739-3.

[312] R. K. Wangsness.
Sublattice Effects in Magnetic Resonance.
Phys. Rev., 91:1085–1091, Sep 1953.
doi:10.1103/PhysRev.91.1085.

[313] Z. Wei, A. Sharma, A. S. Núñez, P. M. Haney, R. A. Duine, J. Bass, A. H. MacDonald, and M. Tsoi.
Changing Exchange Bias in Spin Valves with an Electric Current.
Phys. Rev. Lett., 98:116603, Mar 2007.
doi:10.1103/PhysRevLett.98.116603.

[314] Z. Wei, A. Sharma, J. Bass, and M. Tsoi.
Point-Contact Search for Antiferromagnetic Giant Magnetoresistance.
J. Appl. Phys., 105(7):07D113, 2009.
doi:10.1063/1.3059615.

[315] E. Weiss.
Konrad Zuse Obituary.
IEEE Ann. Hist. Comput., 18(2):3–, 1996.
doi:10.1109/MAHC.1996.489747.

[316] R. J. H. Wesselink, K. Gupta, Z. Yuan, and P. J. Kelly.
Calculating Spin Transport Properties from First Principles: Spin Currents.
Phys. Rev. B, 99:144409, Apr 2019.
doi:10.1103/PhysRevB.99.144409.

[317] R. Wiesendanger.
Spin Mapping at the Nanoscale and Atomic Scale.
Rev. Mod. Phys., 81:1495–1550, Nov 2009.
doi:10.1103/RevModPhys.81.1495.

[318] E.-S. Wilhelm, D. McGrouther, L. Heyne, A. Bisig, and M. Kläui.
Vortex Domain Wall Chirality Rectification due to the Interaction with End Domain Spin Structures in Permalloy Nanowires.
Appl. Phys. Lett., 95(25):252501, 2009.
doi:10.1063/1.3275576.

[319] J. Xu, C. Zhou, M. Jia, D. Shi, C. Liu, H. Chen, G. Chen, G. Zhang, Y. Liang, J. Li, W. Zhang, and Y. Wu.
Imaging Antiferromagnetic Domains in Nickel Oxide Thin Films by Optical Birefringence Effect.
Phys. Rev. B, 100:134413, Oct 2019.
doi:10.1103/PhysRevB.100.134413.

[320] W. Yan, E. Sagasta, M. Ribeiro, Y. Niimi, L. E. Hueso, and F. Casanova.
Large Room Temperature Spin-to-Charge Conversion Signals in a Few-Layer Graphene/Pt Lateral Heterostructure.
Nat. Commun., 8(1):1–7, 2017.
doi:10.1038/s41467-017-00563-y.

[321] H. Yang, A. Thiaville, S. Rohart, A. Fert, and M. Chshiev.
Anatomy of Dzyaloshinskii-Moriya Interaction at Co/Pt Interfaces.
Phys. Rev. Lett., 115:267210, Dec 2015.
doi:10.1103/PhysRevLett.115.267210.

[322] K. V. Yershov, V. P. Kravchuk, D. D. Sheka, O. V. Pylypovskyi, D. Makarov, and Y. Gaididei.
Geometry-Induced Motion of Magnetic Domain Walls in Curved Nanostripes.
Phys. Rev. B, 98:060409, Aug 2018.
doi:10.1103/PhysRevB.98.060409.

[323] D. Yu, C. Math, M. Meier, M. Escher, G. Rangelov, and M. Donath.
Characterisation and Application of a SPLEED-Based Spin Polarisation Analyser.
Surf. Sci., 601(24):5803–5808, 2007.
doi:10.1016/j.susc.2007.06.061.

[324] X. Z. Yu, Y. Onose, N. Kanazawa, J. H. Park, J. H. Han, Y. Matsui, N. Nagaosa, and Y. Tokura.
Real-Space Observation of a Two-Dimensional Skyrmion Crystal.
Nature, 465(7300):901–904, 2010.
doi:10.1038/nature09124.

[325] J. Zázvorka, F. Jakobs, D. Heinze, N. Keil, S. Kromin, S. Jaiswal, K. Litzius, G. Jakob, P. Virnau, D. Pinna, K. Everschor-Sitte, L. Rózsa, A. Donges, U. Nowak, and M. Kläui.
Thermal Skyrmion Diffusion Used in a Reshuffler Device.
Nat. Nanotechnol., 14(7):658–661, 2019.
doi:10.1038/s41565-019-0436-8.

[326] H. J. Zhang, S. Yamamoto, Y. Fukaya, M. Maekawa, H. Li, A. Kawasuso, T. Seki, E. Saitoh, and K. Takanashi.
Current-Induced Spin Polarization on Metal Surfaces Probed by Spin-Polarized Positron Beam.
Sci. Rep., 4:4844, 2014.
doi:10.1038/srep04844.

[327] S. Zhang.
Spin Hall Effect in the Presence of Spin Diffusion.
Phys. Rev. Lett., 85:393–396, Jul 2000.
doi:10.1103/PhysRevLett.85.393.

[328] X. Zhang, Y. Zhou, and M. Ezawa.
Antiferromagnetic Skyrmion: Stability, Creation and Manipulation.
Sci. Rep., 6:24795, 2016.
doi:10.1038/srep24795.

[329] Y. Zhong, Y. Kurokawa, G. Nagashima, S. Horiike, T. Hanashima, D. Schönke, P. Krautscheid, R. M. Reeve, M. Kläui, and H. Yuasa.
Determination of Fine Magnetic Structure of Magnetic Multilayer with Quasi Antiferromagnetic Layer by Using Polarized Neutron Reflectivity Analysis.
AIP Advances, 10(1):015323, 2020.
doi:10.1063/1.5130445.

[330] X. Zhou, F. Matthes, D. E. Bürgler, and C. M. Schneider.
Magnetic Surface Domain Imaging of Uncapped Epitaxial FeRh(001) Thin Films across the Temperature-Induced Metamagnetic Transition.
AIP Advances, 6(1):015211, 2016.
doi:10.1063/1.4940758.

[331] F. Q. Zhu, G. W. Chern, O. Tchernyshyov, X. C. Zhu, J. G. Zhu, and C. L. Chien.
Magnetic Bistability and Controllable Reversal of Asymmetric Ferromagnetic Nanorings.
Phys. Rev. Lett., 96:027205, Jan 2006.
doi:10.1103/PhysRevLett.96.027205.

[332] J.-G. Zhu, Y. Zheng, and G. A. Prinz.
Ultrahigh Density Vertical Magnetoresistive Random Access Memory.
J. Appl. Phys., 87(9):6668–6673, 2000.

doi:10.1063/1.372805.

[333] X. Zhu and J.-G. Zhu.
A Vertical MRAM Free of Write Disturbance.
IEEE Trans. Magn., 39(5):2854–2856, 2003.
doi:10.1109/TMAG.2003.816244.

[334] B. Zimmermann, K. Chadova, D. Ködderitzsch, S. Blügel, H. Ebert, D. V. Fedorov, N. H. Long, P. Mavropoulos, I. Mertig, Y. Mokrousov, and M. Gradhand.
Skew Scattering in Dilute Ferromagnetic Alloys.
Phys. Rev. B, 90:220403, Dec 2014.
doi:10.1103/PhysRevB.90.220403.

[335] Zurich Instruments AG.
Principles of Lock-in Detection and the State of the Art.
URL `https://www.zhinst.com/applications/principles-of-lock-in-detection`.

Anhänge gemäß Prüfungsordnung

Eidesstattliche Erklärung

Hiermit erkläre ich an Eides statt, dass ich meine Dissertation selbständig und ohne fremde Hilfe verfasst und keine anderen als die von mir angegebenen Quellen und Hilfsmittel zur Erstellung meiner Dissertation verwendet habe. Die Arbeit ist in vorliegender oder ähnlicher Form bei keiner anderen Prüfungsbehörde zur Erlangung eines Doktorgrades eingereicht worden.

Mainz, den

Eigener Beitrag zur Thematik

Removed in the electronic version of this thesis due to data protection regulations.
In der elektronischen Version entfernt aufgrund datenschutzrechtlicher Bestimmungen.

Lebenslauf

Removed in the electronic version of this thesis due to data protection regulations.
In der elektronischen Version entfernt aufgrund datenschutzrechtlicher Bestimmungen.

Publikationen

Wissenschaftliche Aufsätze

- P. Krautscheid, R. M. Reeve, **D. Schönke**, I. Boventer, A. Conca, A. V. Chumak, B. Hillebrands, J. Ehrler, J. Osten, J. Fassbender, und M. Kläui. "Direct observation of spin diffusion enhanced nonadiabatic spin torque effects in rare-earth-doped permalloy." *Phys. Rev. B* 98.21 (2018): 214406.

- **D. Schönke**, A. Oelsner, P. Krautscheid, R. M. Reeve, und M. Kläui. "Development of a Scanning Electron Microscopy with Polarization Analysis System for Magnetic Imaging with ns Time Resolution and Phase-Sensitive Detection." *Rev. Sci. Instrum.* 89.8 (2018): 083703.

- R. M. Reeve, A. Loescher, H. Kazemi, B. Dupé, M.-A. Mawass, T. Winkler, **D. Schönke**, J. Miao, K. Litzius, N. Sedlmayr, I. Schneider, J. Sinova, S. Eggert, und M. Kläui. "Scaling of Intrinsic Domain Wall Magnetoresistance with Confinement in Electromigrated Nanocontacts." *Phys. Rev. B* 99.21 (2019): 214437.

- G. Nagashima, Y. Kurokawa, Y. Zhong, S. Horiike, **D. Schönke**, P. Krautscheid, R. Reeve, M. Kläui, Y. Inagaki, T. Kawae, T. Tanaka, K. Matsuyama, K. Ohnishi, T. Kimura, und H. Yuasa. "Quasi-Antiferromagnetic Multilayer Stacks with 90 Degree Coupling Mediated by Thin Fe Oxide Spacers." *J. Appl. Phys.* 126.9 (2019): 093901.

- Y. Zhong, Y. Kurokawa, G. Nagashima, S. Horiike, T. Hanashima, **D. Schönke**, P. Krautscheid, R. M. Reeve, M. Kläui, und H. Yuasa. "Determination of Fine Magnetic Structure of Magnetic Multilayer with Quasi Antiferromagnetic Layer by Using Polarized Neutron Reflectivity Analysis." *AIP Adv.* 10.1 (2020): 015323.

- **D. Schönke**, R.M. Reeve, H. Stoll, M. Kläui. (2020) Magnetic State Control via Field-Angle-Selective Switching in Asymmetric Rings. *Phys. Rev. Applied* 14:3 (2020): 034028

- **D. Schönke**, R. M. Reeve, H. Stoll, und M. Kläui. "Quantification of Competing Magnetic States and Switching Pathways in Curved Nanowires by Direct Dynamic Imaging." *ACS Nano* 14:10 (2020): 13324-13332.

Konferenzbeiträge

- DPG Spring Meeting, Regensburg, Germany (07.-09.03.2016)

  Poster: "Magnetic Imaging of Domain Wall Spin Structures in Fe Rings using SEMPA", P. Krautscheid, **D. Schönke**, M. Lauf, B. Krüger, R. M. Reeve und M. Kläui.

- DPG Spring Meeting, Dresden, Germany (19.-24.03.2017)

  Poster: "SEMPA Imaging of Magnetic Spin Configurations and Manipulation by Spin Currents", **D. Schönke**, P. Krautscheid, M. Lauf, B. Krüger, R. M. Reeve und M. Kläui.

- MAINZ Summer School: New Directions in Spintronics Research Beijing, China (12.-19.08.18)

  Poster: "Development of a Novel SEMPA System for Magnetic Imaging with ns Time Resolution and Phase-Sensitive Detection", **D. Schönke**, A. Oelsner, P. Krautscheid, R. M. Reeve, und M. Kläui.

- Joint European Magnetic Symposia (JEMS), Mainz, Germany (03.-07.09.2018)

  Vortrag: "Spin Diffusion-Enhanced Non-Adiabatic Spin Torque in Rare-Earth-Doped Permalloy", P. Krautscheid , R. M. Reeve, **D. Schönke**, I. Boventer , A. Conca, A. V. Chumak , B. Hillebrands, J. Ehrler , J. Osten , J. Fassbender und M. Kläui

  Poster: "Development of a Novel SEMPA System for Magnetic Imaging with ns Time Resolution and Phase-Sensitive Detection", **D. Schönke**, A. Oelsner, P. Krautscheid, R. M. Reeve, und M. Kläui.

- DPG Spring Meeting Regensburg, Germany (01.-05.04.2019)

  Poster: "Imaging Domain Wall Motion Using Time-Resolved SEMPA", **D. Schönke**, A. Oelsner, P. Krautscheid, R. Reeve, und M. Kläui.

- Tohoku-Mainz-Lorraine Spintronic Workshop, Nancy, France (17.-20.09.19)

  Vortrag: "Imaging Spin-Structure Dynamics with SEMPA", R. M. Reeve, **D. Schönke**, A. Oelsner, H. Stoll, P. Krautscheid, und M. Kläui.

Danksagung

Removed in the electronic version of this thesis due to data protection regulations.
In der elektronischen Version entfernt aufgrund datenschutzrechtlicher Bestimmungen.